PSFC/RR-10-13

Phase Contrast Imaging Measurements and Modeling of Short Wavelength Turbulence in the DIII–D Tokamak

James R. Dorris

January 2010

Plasma Science and Fusion Center
Massachusetts Institute of Technology
Cambridge MA 02139 USA

Phase Contrast Imaging Measurements and Modeling of Short Wavelength Turbulence in the DIII–D Tokamak

by

James Robert Dorris III

B.S. (2001), Department of Applied and Engineering Physics
Cornell University

Submitted to the Department of Physics
in partial fulfillment of the requirements for the degree of

Doctor of Philosophy in Plasma Physics

at the

MASSACHUSETTS INSTITUTE OF TECHNOLOGY

January 2010

Author . . . .

Department of Physics
January 13, 2010

Certified by . . . .

Miklos Porkolab
Professor of Physics
Director, Plasma Science and Fusion Center
Thesis Supervisor

Accepted by . . . .

Krishna Rajagopal
Professor of Physics, Associate Department Head for Education

Phase Contrast Imaging Measurements and Modeling of Short Wavelength Turbulence in the DIII–D Tokamak

by

James Robert Dorris III

Abstract

The DIII–D phase contrast imaging (PCI) diagnostic has been upgraded and used to measure turbulence in the outer plasma region ($0.7 < r/a < 1$). These upgrades extended its operational range to high frequencies (10 kHz - 10 MHz), short wavelength (2 - 30 cm^{-1}), and improved the signal-to-noise ratio by 10X, as well as provided a novel rotating mask to measure turbulence as a function of propagation angle about the PCI chord. Turbulent fluctuations that propagate perpendicular to the magnetic field direction can be localized by making use of the variation of the magnetic field component perpendicular to the viewing chord as a function of chord height.

Long wavelength ($|k| \lesssim 12$ cm^{-1}) turbulence is shown to be a branch in frequency and wave-number space, and is localized to within the instrumental width of the last closed flux surface (LCFS) ($r/a \gtrsim 0.9$). Three classes of turbulence with finite (and theoretically unexpected) $k_{||}$ have been identified: (i) modes that are localized in wave-number and mask angle (the high-k and medium-k modes), (ii) a broad (in mask angle) background turbulence, and (iii) a low-k "wing" that smears the main branch structure. These modes are seen to propagate at angles as large as $k_{||}/k \sim 0.1 - 0.4$.

ECH heating is observed to increase the spectral power density in the high-k mode ($-24 < k < -18$ cm^{-1}), and the parallel wave-numbers are measured to be as large as $k_{||}/k \sim 0.15$. The applied heating is shown to *increase* the electron temperature gradient drive (inverse scale-length, $1/L_{Te}$) and *decrease* the ion temperature and density gradient drives ($1/L_{Ti}$ and $1/L_n$). Using a basic temperature gradient driven drift-wave model in slab geometry, it is shown that finite (and relatively high) $k_{||}$ modes could interact resonantly with ions through the ion cyclotron Doppler resonance terms $\zeta_{\pm 1i} = (\omega \mp \Omega_i)/(k_{||} v_{ti}) \sim 1$. These $m \neq 0$ terms in the dispersion relation are not included in the derivation of the gyrokinetic equations.

Thesis Supervisor: Miklos Porkolab
Title: Professor of Physics
Director, Plasma Science and Fusion Center

Acknowledgments

I would like to thank all the people who have helped me, both directly and indirectly, to complete this thesis. I will do my best to acknowledge as many of them as I can. The difficulties I encountered in this work were felt by many around me, and I want to offer my most sincere apology for the hardships this caused, especially to those closest to me.

My gratitude goes foremost to my thesis supervisor, Professor Miklos Porkolab and my research supervisor at General Atomics, Dr. Jon C. Rost for their contributions to, and discussions of the many physics topics relevant (and some not so relevant) to the success of the work contained in this thesis. They both provided me with encouragement and insights throughout the many years of this project, as well as the pushing and prodding needed for its completion. I am extremely grateful for their patience and support. I would also like to extend my heartfelt thanks to my thesis readers, Dr. Earl Marmar and Prof. John Belcher.

Early in my graduate career I was fortunate to work with Dr. Jan Egedal and fellow graduate students Jon Nazemi and Will Fox on the Versatile Toroidal Facility at MIT. Their contributions helped cultivate the laboratory skills that were critical for the success of this thesis work, I am grateful for all their patience and support.

I would like to thank General Atomics for hosting me, and providing support throughout the years. In particular, I would like to thank Dr. Jeff Candy for his patience and openness in discussing details of the GYRO code, Dr. Keith Burrell for being such an approachable and unbelievably comprehensive resource, Dr. Terry Rhodes for always welcoming discussion with the UCLA turbulence group. I would also like to thank Drs. Réjean Boivin, Craig Petty, Jim Deboo, Tony Taylor, and the entirety of the General Atomics DIII–D community for their generosity and oversight.

Plasma turbulence is a field of study where much of the modern theory relies on highly complex numerical simulations. I would like to thank Drs. Darin Ernst and John Wright for providing me access to the Marshall and Loki computational facilities at MIT, without which the GYRO simulations conducted in this work may not have

been possible.

I would also like to thank all the fellow graduate students that contributed to my work, happiness, and sanity over the years. Conducting my research away from a community graduate student peers could have been much more difficult had it not been for the following conversations and camaraderie. I wish to thank Eric Edlund and Liang Lin for the enjoyable collaboration I was fortunate to have with the MIT PCI group - conversations were illuminating, stress relieving, and always morale boosting. My office mates at General Atomics, Adam McLean and Morgan Shafer, were always helpful, enjoyable and always conducive to a productive work environment.

Having few fellow graduate students to commiserate with at General Atomics could have been isolating. However, many friends helped to sustain me during this work and in particular during the thesis writing process; I'd like to give special thanks to Susannah, Kristie, and Paul for their encouragement, confidence in my abilities, and willingness to involve themselves in my struggle. I would also like to thank Drs. Michael Grundmann and Brent Pryor for some of the best advice I received in my later years, "Don't worry about ..., just write it up." I would also like to thank Erica, Cleve, Wendy and Medy for their support and encouragement. Sometimes, the kindnesses and support that are most impactful come from the least expected places: Joanna, Jill, and Kate - your help, compassion, generosity and support during my most difficult struggles made a world of difference.

For me, the thesis process was filled with frustrations, struggles, and setbacks; I want to apologize to both Amanda and Katey for the difficulties and stress this caused them simply for being so involved in my life. I cannot thank you enough for being such meaningful people in my life, and for giving me so much love and support. I wish you both all the best - lives filled with love, fulfillment and abundance.

Finally, I would like to give special thanks my family and in particular to my mother and father; I know you will always be my biggest fans. I'm sorry that I was not more vulnerable about my struggles and frustrations during this process, and that living so far away has limited the time we were able to spend together. Thank

you for all the opportunities you have provided me over the years, I would not be in a position to write this thesis without so much support and sacrifice from you both.

THIS PAGE INTENTIONALLY LEFT BLANK

Contents

THIS PAGE INTENTIONALLY LEFT BLANK

List of Figures

17

19

24

List of Tables

THIS PAGE INTENTIONALLY LEFT BLANK

Chapter 1

Introduction

1.1 Fusion Energy

Fusion is the process that powers our Sun. It is the nuclear reaction by which light-weight atoms combine into heavier atoms, and release energy in the process because the product rest mass is lower than the reactants. The most attractive reaction for magnetically confined fusion as a source of energy is

$$^2_1D \; + \; ^3_1T \; \rightarrow \; ^4_2He \; + \; ^1_0n, \tag{1.1}$$

where D and T are the 1st and 2nd isotopes of hydrogen: deuterium and tritium. The D-T cross-section is fairly large (due to the isotope neutrons) and since they are hydrogen isotopes, the nuclei are only singly-charged, making the electrostatic repulsion minimum. The D-T reaction can generally occur at temperatures of 5-10 keV, meaning that the deuterium and tritium are in an ionized plasma state. This process releases a helium nuclei (or alpha particle) with 3.5 MeV of kinetic energy and a neutron with 14.1 MeV of kinetic energy. The alpha particle is charged and therefore cannot escape the magnetic confinement; it will collisionally damp on slower particles further heating the plasma fuel. The neutron is uncharged and will therefore escape the magnetic confinement where its energy can be captured and used to generate electricity.

Nuclear fusion has the advantages of being safe, sustainable, and environmentally attractive. The potential for catastrophic accident is less than in fission reactors because the risk of a runaway reaction is dramatically reduced. The helium product of the reaction is not radioactive and although the high energy neutrons will activate the structural materials, the resulting material half-lives tend to be on the order of 50-100 years instead of thousands of years as with the fission reaction. The technological overlap of fusion energy with nuclear weapons production is small relative to the technologies employed in fission reactors, and the dangers of nuclear weapons proliferation would therefore be significantly reduced. Finally, the fusion reaction produces no greenhouse gas byproducts making it an attractive alternative to fossil fuels on the basis of providing a carbon-free energy source to combat global climate change.

1.2   DIII–D Tokamak

A "tokamak" is a toroidal device used for confining hot plasma in a toroidally symmetric helical magnetic field. The term comes from a Russian acronym roughly meaning "toroidal chamber with magnetic coils". The magnetic field used to confine the plasma is dominated by the large toroidal field generated by the tan colored coils depicted in Fig. 1-1, however a smaller poloidal field generated by inducing current in the plasma itself is necessary for the equilibrium to be stable. In most modern devices, the plasma current is generated through transformer action by the ohmic coils which cannot provide steady-state operation. Therefore, various forms of RF current drive systems are being studied on many devices.

Tokamak performance is often specified through the Lawson Criterion [1] which defines the conditions needed for a plasma to reach ignition, where the self-heating of the plasma by the fusion reaction products is balanced against all losses, and therefore the plasma temperature is maintained without the need for applied power input. This criterion for achieving ignition is stated as a threshold value of the plasma triple product, namely density, temperature, and confinement time. For the
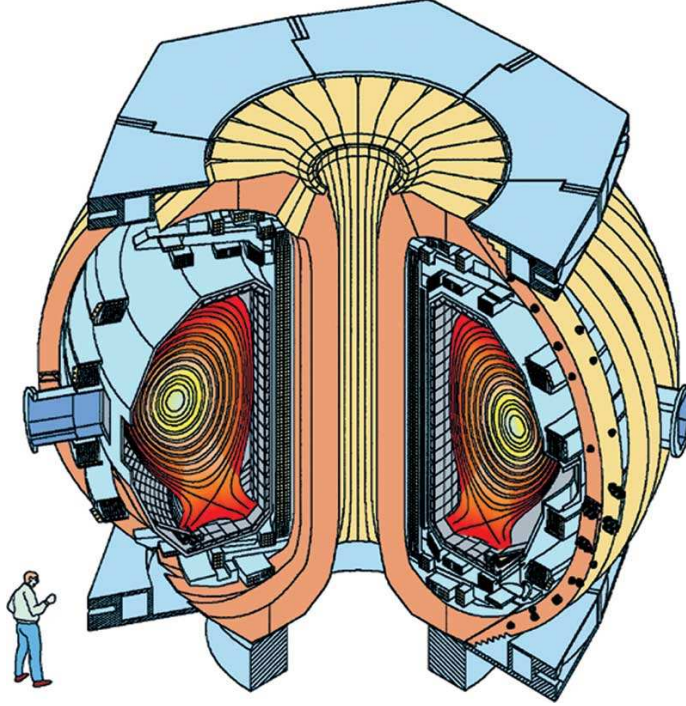
Figure 1-1: Artist depiction of the DIII–D tokamak showing the toroidal field coils colored in tan. Ohmic transformer coils loop toroidally around the inner wall, and many plasma shaping coils are also shown.

D-T reaction, ignition is achieved when

$$n_e T_i \tau_E \geq 10^{21} \text{ keV s/m}^3. \tag{1.2}$$

Over the last 40 years, tokamak performance has improved by nearly a factor of 10^7 and the first device to achieve a burning plasma ($Q > 10$) is planned to be ITER [2]. It is scheduled for first operation in 2018 and will provide the first facility that can be used to study a dominantly self-heated burning plasma regime. While not a condition for success, attempting to reach the igition threshold is planned for ITER.

The DIII–D National Fusion Facility, located at General Atomics in San Diego, CA, has made remarkable contributions to the world fusion program for more than 20 years. Particularly important contributions have been in the understanding of the role of cross-section shaping in plasma confinement and stability, determining the effectiveness of the poloidal divertor in exhausting heat and plasma impurities, identi-

fying and understanding modes of enhanced energy confinement, and developing the tools needed to manage the plasma profiles [3]. The DIII–D program now focuses on using the these results to develop scenarios for next step tokamaks and advanced reactor designs. The DIII–D program also includes the development of the GYRO code, providing some of the most rigorous computational simulations to study turbulence driven effects on confinement and transport [4]. Improving the predictive capacity of turbulence simulations is a major thrust of both the theoretical and experimental communities - this can only be achieved through validation of their performance against experimental measurement [5].

1.3   Challenge of Anomalous Transport

Universally, tokamak experiments show particle and energy transport that is large compared to that predicted by collisional theories [6]. This so-called anomalous transport is generally thought to arise from turbulent processes generated by micro-instabilities [7] and is considered to be the main factor limiting confinement of heat and particles in tokamak devices. Understanding the fundamental physics that govern these instabilities is therefore a major focus of the international fusion community. By understanding the mechanisms and relevance of turbulence driven transport processes, models with predictive capability can be used to study and improve confinement and ultimately to help design the next generation of reactor relevant devices.

Most modern turbulence theories focus on the drift-wave family of instabilities as the key mechanisms by which turbulence can drive transport; these include the Ion Temperature Gradient (ITG) mode ($k_\perp \rho_{si} \sim 0.1$), the Trapped Electron Mode (TEM) ($k_\perp \rho_{si} \lesssim 1$), and the Electron Temperature Gradient (ETG) mode ($k_\perp \rho_{si} > 1$). Here $k_\perp$ is the component of the fluctuating wave-vector perpendicular to the local magnetic field, $\rho_{si} = c_s/\omega_{ci}$ is the ion sound gyro-radius and c_s is the plasma sound speed. In the plasma core, simulations and measurements of long wavelength (ITG/TEM) turbulence generally agree that this mode can drive ion thermal and particle transport [8,9]. However, agreement between measurements and simulations

generally disagree closer to plasma edge $r/a \gtrsim 0.75$ [10, 11].

There is still controversy over the importance of short wavelength (ETG) modes [12]. Some simulations of short wavelength turbulence show substantial electron thermal transport due to ETG modes, while other simulations show essentially none. The simulations differ in computational technique (*e.g.* continuum vs. particle in cell) as well as physics effects included (*e.g.* adiabatic ions vs. kinetic ions) [13]. These electron scale simulations are computationally expensive and are in various stages of maturity; however, there has been little rigorous comparison to experimental measurements. Confinement losses through the electron channel will be especially important in reactor-relevant plasmas due to strong thermal coupling between electrons and ions, and because fusion energy will be transferred from fast alpha particles to electrons. Modern simulations must be validated and bench-marked against experimental measurements before they can confidently be used to study and predict transport levels to ultimately control electron transport and improve device confinement.

The drift-wave family of modes studied in modern turbulence theories assume a mode propagating nearly perpendicular to the local magnetic field. A small but finite parallel wave-number is needed for field continuity on non-rational flux surfaces and allows us to estimate the size to be $k_{||}/k_\theta \sim 10^{-4}$. This assumption of near perpendicular propagation is built into the gyrokinetic theory from the start of the derivation when the gyrokinetic ordering is imposed, setting an upper limit on the parallel wave-number of $k_{||}/k_\theta \sim 10^{-2}$. Such an assumption is generally agreed upon as valid throughout the community, and therefore the concept of short-wavelength turbulence with a significant wave-vector component along the magnetic field is generally thought to be irrelevant to transport. However, in this thesis research we find the existence of large parallel wave-number modes ($k_{||}/k_\theta \sim 0.1 - 0.4$), which begs the question of whether the gyrokinetic theory is complete. Throughout the thesis, we will refer to such large parallel wave-numbers as "finite parallel wave-number" or "finite $k_{||}$", while we refer to the small parallel wave-number drift-wave modes as "propagating near perpendicular" or "$k_{||} \sim 0$".

1.4 DIII–D Phase Contrast Imaging Diagnostic

Phase Contrast Imaging is a diagnostic technique that measures electron density fluctuations by probing the plasma using an infrared laser. It produces a measurement proportional to the fluctuating density amplitude in both time and space (across the PCI chord as detector elements map to individual chords). This 2-D measurement domain can be Fourier analyzed to obtain the spectral power density of fluctuations in both frequency and wave-number. The PCI is a complementary diagnostic to the DIII–D set of turbulence measurements including reflectometry [14], far infrared (FIR) scattering [15], beam emission spectroscopy (BES) [16], and the microwave backscattering [17]. Reflectometry can probe measurements of scales $0 - 5$ cm^{-1}, and BES from $0 - 5$ cm^{-1} - too small to be in the ETG range of spatial scales. While the microwave scattering diagnostics (FIR and backscattering) can operate to a higher wave-number, they provide only single wave-number measurements in three regions [18, 19] $k = 0 - 2$ cm$^{-1}, 7 - 12$ cm$^{-1}, 35 - 40$ cm^{-1}. In contrast, the PCI provides continuous measurements over the wave-number region, with a resolution proportional to the number of detector elements, and the range set by adjusting the imaging optics.

1.4.1 Enhanced Operational Regime

The work described in this thesis is focused toward a comparison between experimental measurements and the simulation of short-wavelength turbulence. Upgrades to the diagnostic sensitivity, operational range, and measurement capacity have been designed, fabricated, and implemented as part of this work. The upper limits of the PCI operational range have been extended from 1 MHz and 8 cm^{-1} to 10 MHz and 40 cm^{-1} through new high speed digitizers, and a re-designed optical layout. In addition, the diagnostic sensitivity has been improved by nearly 10X through numerous improvements to the system conditioning and data transfer electronics.

A new capacity of the DIII–D PCI has also been designed, fabricated, and implemented that takes advantage of the vertical variation of radial magnetic field to

make measurements as a function of propagation angle about the PCI chord. In the case of drift-wave turbulence propagating near perpendicular to the local magnetic field, this technique provides the capacity to make localized measurements along the PCI chord. This technique utilizes a motor driven rotating mask system to allow the localization of turbulence for $k \gtrsim 10 \text{ cm}^{-1}$. The design, procurement, installation, and calibration of this system was a major part of this thesis research. With this localization technique, the DIII–D PCI is now able to simultaneously measure density turbulence amplitude as a function of frequency, wave-number, and plasma location. If there are significant fluctuations with finite $k_{||}$, the rotating mask has the ability to make the first measurements of this phenomenon.

1.5   Thesis Outline

This thesis is divided into seven chapters.

Chapter 1, "Introduction", provides an overview of the basic concepts of fusion energy, and the tokamak devices used to magnetically confine the hot plasma. For motivation, the reader is introduced to the current state of limited understanding of the mechanisms of turbulence induced transport in tokamak devices and the relevance of such research to next step devices. Finally, phase contrast imaging (PCI), the experimental technique used for the studies in this thesis is briefly introduced.

Chapter 2, "Diagnostic Principle", provides an understanding of the PCI measurement and localization technique by developing a simple framework for a mathematically rigorous treatment of the laser-plasma scattering interaction relevant for PCI measurements. Analysis of the rotating mask technique reveals how it can be used to measure turbulence as a function of propagation angle about the PCI chord. Finally, we explain the assumptions necessary to interpret propagation angle measurements as measurements localized along the PCI chord.

Chapter 3, "PCI Implementation on DIII–D", describes the PCI hardware, optical system, upgrades, absolute calibration, and calibration and plasma tests of the masking system. These upgrades were implemented to increase the diagnostic fre-

quency and wave-number range as well as the system signal-to-noise ratio. Many of the diagnostic improvements were performed as original work for this thesis including optical analysis and design for larger scattering angles and rotating mask placement, circuit analysis, design and prototyping of the variable gain amplifiers and filters, contracting for rotating mask development and PCB fabrication, cylindrical lens technique and implementation, and the analysis and implementation of the fiber optic data transfer system now providing a low noise solution of transferring data from the DIII–D machine hall to the digitizers. Calibrations using ultrasonic waves in air confirm that this new capability provides measurements in the range $2 < k < 30$ cm^{-1}, 10 kHz $< f < 10$ MHz, and analysis of magnetic field mappings generally result in a radial range of $0.7 < r/a < 1$. Experimental determination of the mask response function show excellent agreement with the theoretical expectations.

Chapter 4, "Spectral Measurements of Turbulence with Upgraded PCI", provides the reader with an introduction to the spectral measurements made with the PCI diagnostic. Power spectra estimates exhibit features that are ubiquitous across many plasma conditions with the largest amplitude turbulence structure being a branch in wave-number (generally limited to $k \lesssim 15$) and frequency space with roughly constant phase velocity that decays monotonically with increasing frequency. This main branch feature is due to turbulence propagating near perpendicular to the magnetic field, and is localized to (within the diagnostic sensitivity) the last closed flux surface (LCFS) of the plasma.

Chapter 5, "Finite Parallel Wave-number Turbulence", presents data showing three classes of turbulence that propagate at angles too large to be interpreted as modes propagating near perpendicular to the local magnetic field. These modes are seen to propagate at large angles corresponding to $k_{||}/k \sim 0.1 - 0.4$.

Chapter 6, "Interpretation of Finite $k_{||}$ Modes", provides a brief review of gyrokinetic theory showing that modes with finite parallel wave-number are ordered out of the gyrokinetic equations. Plasma profile changes are presented to show that the electron temperature gradient is potentially a driver for at least one of the classes of finite $k_{||}$ turbulence measured. Finally, a basic slab model drift-wave theory of

34

temperature gradient driven turbulence is revisited to show a potentially important mechanism for which these modes can become unstable.

Chapter 7, "Conclusions and Future Work", provides a thesis summary, concluding remarks, and suggestions for future studies related to the work in this thesis.

THIS PAGE INTENTIONALLY LEFT BLANK

Chapter 2

PCI Technique

2.1 Diagnostic Principle

In fields such as biology, crystallography, turbulence studies, and others, it is often the case that one seeks to study an object that diffracts and scatters the probing beam but does not absorb significant power. Such an object is called a *phase object* because the object alters only the phase of the probe beam and not its amplitude. Many methods of detection are sensitive only to the intensity of radiation and therefore phase objects have been historically difficult to study. Early techniques to diagnose such objects include the schlieren, dark field, shadowgraph, and interferometric techniques [20].

The Phase Contrast technique was developed in the 1930s by Dutch physicist Frits Zernike for which he received the Nobel Prize in 1953 [21, 22]. His Phase Contrast Microscope was initially applied to cells and small organisms, and had the advantage of producing an intensity pattern that is proportional to the phase pattern introduced by the object. Phase Contrast Imaging (PCI), was first applied to the study of plasma physics at Yeshiva University [23] in the "observation of macroscopic moving tenuous objects, such as jets, shock waves, and plasmas." The technique was later applied to fusion plasmas on the TCA Tokamak to study density fluctuations with wavelengths above 3 mm using a CO_2 laser probe beam [24]. The Phase Contrast technique has been successfully deployed on a number of fusion plasma devices including the DIII–D Tokamak at General Atomics [25, 26], the Heliotron-E device at Kyoto University

[27,28], the TEXT-U tokamak at the University of Texas at Austin [29], the Alcator C-Mod tokamak at MIT [30–32], and the Large Helical Device at the National Institute for Fusion Science in Toki, Japan [33, 34].

As applied to the study of plasmas, PCI is a form of internal reference beam interferometry that measures phase variations in the incident laser that are introduced by the probed medium. Unlike traditional interferometry, the reference beam does not traverse a separate leg. In PCI, the incident laser is chosen of suitable wavelength so that the scattering is far forward or equivalently Raman-Nath [35]. In such a small-angle scattering regime, if the phase object fluctuation is small then its effect on the incident beam can be expressed in terms of scattered and unscattered beams. The entire beam is sent through the plasma; the reference is the component of the beam unscattered by the fluctuating media while the signal beam is generated through the interaction of the incident laser and the fluctuating plasma.
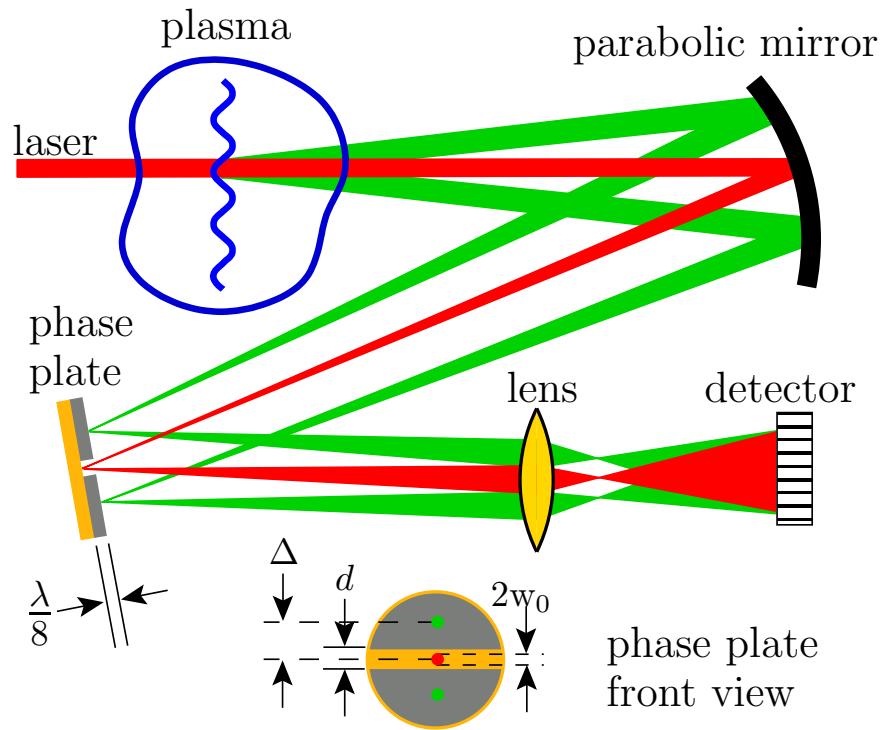
Figure 2-1: Depiction of PCI technique showing $\pi/2$ phase shift introduced by reflecting the unscattered beam off the *phase plate* groove

The unscattered reference beam is then phase shifted 90°. Finally, the signal and reference beams are combined through imaging optics and interfered on the detector.

With this technique, variations in the index of refraction of the probed medium are then converted to intensity variations at the imaging plane. Figure 2-1 depicts the phase contrast technique.

The following sections 2.1.1 and 2.1.3 detail the mathematical basis of PCI in terms of the laser-plasma scattering process and the PCI system response. The following analysis uses assumptions to simplify and illuminate the relevant physics. Table 2.1 lists the DIII–D PCI diagnostic parameter ranges that are used in the following sections to characterize operation.

Table 2.1: Typical DIII–D PCI diagnostic parameters assumed for derivation of PCI operation

Laser	
Type	CO_2 gas
Power	20 W
Wavelength (λ_0)	10.6 μm
Wave-number $(k_0 = 2\pi/\lambda_0)$	$\sim 6 \times 10^5$ m^{-1}
Angular Frequency (ω_0)	1.8×10^{14} rad/sec
Typical DIII–D Plasma Parameters	
Plasma minor radius (a)	~ 1 m
Density (n_0)	$1 - 5 \times 10^{19}$ m^{-3}
Magnetic Field (B_0)	1 - 2 T
Electron Temperature (T_e)	0.4 - 2 keV
Electron Thermal Velocity (v_{te})	$\sim 1 \times 10^7$ (m/s)
Electron Cyclotron Frequency (Ω_e)	$\sim 2 \times 10^{11}$ rad/sec
Plasma Frequency (ω_{pe})	$\sim 1.8 \times 10^{11}$ rad/sec
Fluctuation Amplitude $(\tilde{n}/n_0)$	$\sim 0.01 - 1.0$
Fluctuation Wave-number (k)	1 - 30 cm^{-1}
Fluctuation Frequency (f)	50 kHz - 1 MHz

2.1.1 Laser Plasma Interaction

The Phase Contrast Imaging technique uses an electromagnetic probe beam (often an infrared laser) to diagnose the fluctuations of the plasma electron density. Like many scattering techniques, the probe beam has the advantage of being completely non-perturbative and can penetrate into any region of the plasma. This section presents the formalism used to compute the interaction of the infrared probe beam with the

plasma.

We consider a plane wave source of electromagnetic radiation incident upon a quasi-neutral plasma with background magnetic field $\vec{B} = B_0 \hat{z}$. The incident wave electric field is of the form

$$\vec{E} = \vec{E}_0 e^{i(\vec{k}_0 \cdot \vec{r} - \omega_0 t)}, \tag{2.1}$$

where $\vec{E}_0$ describes the incident electric field polarization, $\vec{k}_0$ and ω_0 are the wave-vector and frequency of the incident beam respectively. The plasma is treated as an electrically charged macroscopic fluid in which current can flow but is otherwise governed by Maxwell's equations and an appropriate dielectric tensor. The cold plasma assumption is justified because the electromagnetic wave propagates at a phase velocity near the speed of light c in the plasma and $v_{te}/c \ll 1$. Because the frequency of the incident radiation is large compared to the characteristic frequencies of the plasma ($\omega_0 \gg \omega_{pe}, \Omega_e$), only the electron response is of importance as the ion contribution is negligible. The simplest approach starts with the wave electric field acting on a single electron - the field causes the electron to accelerate and we can calculate the induced current in the plasma. The current and incident electric field together specify the plasma conductivity, from which the dielectric tensor can be computed and the plasma index of refraction obtained. This procedure is well known and worked out in many texts [36, 37]. The single electron equation of motion is

$$m_e \dot{\vec{v}} = -e(\vec{E} + \vec{v} \times \vec{B}_0), \tag{2.2}$$

where v is the electron velocity response to the incident wave electric field $\vec{E}$. Assuming a harmonic response for v like that of Eq. 2.1, the above can be solved by Fourier analysis

$$
\begin{aligned}
v_x &= \frac{-ie}{\omega_0 m_e} \frac{1}{1 - \Omega_e^2/\omega_0^2} \left(E_x - i\frac{\Omega_e}{\omega_0} E_y \right), \\
v_y &= \frac{-ie}{\omega_0 m_e} \frac{1}{1 - \Omega_e^2/\omega_0^2} \left(E_y + i\frac{\Omega_e}{\omega_0} E_x \right), \\
v_z &= \frac{-ie}{\omega_0 m_e} E_z,
\end{aligned}
\tag{2.3}
$$

where $\Omega_e = eB_0/m_e$ is the electron cyclotron frequency. The current is simply $\vec{j} = -en_e\vec{v} = \overleftrightarrow{\sigma} \cdot \vec{E}$ and the dielectric tensor is $\overleftrightarrow{\epsilon} = \left(1 + \frac{1}{\omega_0\epsilon_0}\overleftrightarrow{\sigma}\right)$. Thus the dielectric tensor can be written

$$\overleftrightarrow{\epsilon} = \begin{bmatrix} 1 - \frac{\omega_{pe}^2}{\omega_0^2 - \Omega_e^2} & \frac{i\omega_{pe}^2\Omega_e}{\omega_0(\omega_0^2 - \Omega_e^2)} & 0 \\ \frac{-i\omega_{pe}^2\Omega_e}{\omega_0(\omega_0^2 - \Omega_e^2)} & 1 - \frac{\omega_{pe}^2}{\omega_0^2 - \Omega_e^2} & 0 \\ 0 & 0 & 1 - \frac{\omega_{pe}^2}{\omega_0^2} \end{bmatrix}. \tag{2.4}$$

In the limit that ($\omega_0 \gg \omega_{pe}$ and $\omega_0 \gg \Omega_e$) as is justified in Table 2.1, the dielectric tensor is diagonal and the plasma can be considered unmagnetized and therefore homogenous with

$$\epsilon = 1 - \frac{\omega_{pe}^2}{\omega_0^2}, \tag{2.5}$$

and the index of refraction is simply $N = \sqrt{\epsilon}$ or

$$N = \sqrt{1 - \frac{w_{pe}^2}{w_0^2}} \simeq \left(1 - \frac{w_{pe}^2}{2w_0^2}\right) = \left(1 - \frac{n_e q^2}{2m_e\epsilon_0 w_0^2}\right), \tag{2.6}$$

where q is the electron charge and m_e is electron mass. The plasma responds by very slightly modifying the phase velocity of the incident beam in a manner proportional to the electron density. This response is the basis for many kinds of diagnostics that use high frequency electromagnetic waves to probe the plasma.

To proceed in describing the interaction of the probe laser beam incident upon a plasma with a fluctuating index of refraction, the author notes the similarity with early work by Raman and Nath in which they were concerned with scattering of light by high frequency waves in a fluid medium [35, 38]. It should also be noted that the interaction of the PCI probe beam with the fluctuating plasma has great degree of similarity with the field of Acousto-Optics devices [39]. To the knowledge of the author, this approach has not previously been used to describe the Phase Contrast Technique and yields an easy to follow yet highly illustrative and complete analysis.

We consider a Gaussian laser beam with wave-vector k_0, frequency ω_0, and $1/e$

width w_0 propagating in the z-direction incident upon a plasma supporting plane-wave like density fluctuation structures. The plasma considered is as above, and we seek a solution to the scattering of the incident laser by a plane-wave density fluctuation $n_e(x, z, t) = n_0 + \tilde{n}\cos(kx - \omega t)e^{-\frac{\pi z^2}{L^2}}$, where n_0 is the background electron density, and the fluctuation is limited in spatial extent by a Gaussian envelope with effective width L. The fluctuation is, for now, assumed to be perpendicular to the incident beam, however we will relax this assumption in Sec. 2.1.2. This system is depicted in Fig. 2-2. Physically, L is the effective distance over which the amplitude
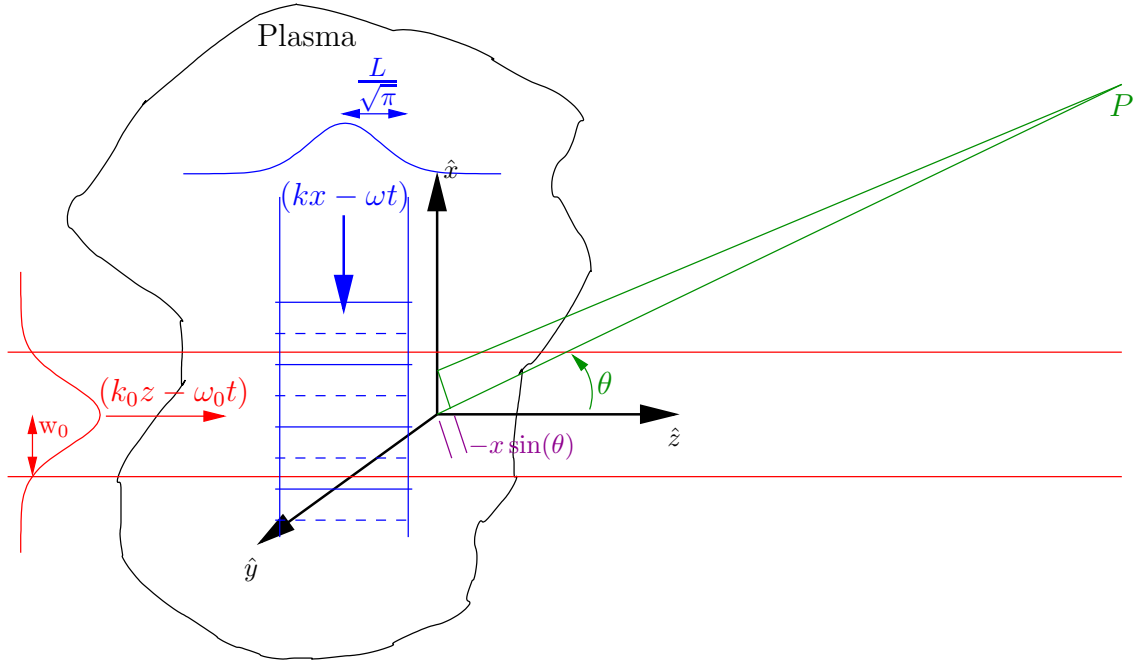
Figure 2-2: Scattering Diagram showing incident laser upon a plasma of effective length L supporting a plane wave Gaussian envelope density fluctuation, and the point P at a large distance away showing the geometrical phase difference $xl = -x\sin\theta$

of the plane-wave plasma fluctuation is significant. The response of the PCI will be shown to be linear, so a generalized plasma density fluctuation can be decomposed into a set of Fourier harmonics and treated as independent density waves of the form of Eq. 2.7.

The single Fourier mode density fluctuation causes a fluctuating index of refraction

$$N = \mu_0 + \tilde{\mu}\cos(kx - \omega t)e^{-\frac{\pi z^2}{L^2}} \tag{2.7}$$

$$\mu_0 = 1 - \frac{\overline{\omega_{pe}}^2}{2\omega_0^2} \tag{2.8}$$

$$\tilde{\mu} = -\frac{\overline{\omega_{pe}}^2}{2\omega_0^2}\frac{\tilde{n}}{n_0}, \tag{2.9}$$

where $\overline{\omega_{pe}}$ is the plasma frequency due to the background electron density (*i.e.* in the absence of the density fluctuation), and $\tilde{\mu}$ is the amplitude of the fluctuation in index of refraction. Initially, consider the plasma fluctuation to propagate perpendicular to the incident beam. The phase shift acquired by the incident laser as it exits the plasma due to the plasma fluctuation is then simply

$$\Phi(x,t) = k_0 \int dz (N - 1) = \tilde{\mu}k_0 L\cos(kx - \omega t), \tag{2.10}$$

where we have chosen to ignore the constant phase shift of the background plasma as this does not cause scattering of the incident beam. The incident laser electric field is considered a plane wave with Gaussian envelope (Gaussian beam at its waist). By using a scalar diffraction approach, the electric field at point P is then just given by the far field diffraction integral over the exiting beam aperture including the geometrical phase contribution $-x\sin\theta$, and the phase shift given by Eq. 2.10.

$$\vec{E}_P = \int_{-\infty}^{\infty} dx \vec{E}_0 e^{-i\omega_0 t} e^{-\frac{x^2}{w_0^2}} e^{ik_0 lx} e^{i\tilde{\mu}k_0 L\cos(kx - \omega t)}. \tag{2.11}$$

Here we have chosen to leave out the $e^{ik_0 z}$ term because we are propagating the electric field at the *exit* of the plasma, *i.e.* evaluating the field at $z = L$. We ignore the constant phase term $e^{ik_0 L}$. The scattered beam propagation direction will be determined from the angle θ in the far field. Using the Jacobi-Anger [40] expansion in terms of Bessel functions of the first kind J_n

$$e^{ia\cos\psi} = \sum_{n=-\infty}^{\infty} i^n J_n(a)e^{in\psi}, \tag{2.12}$$

equation 2.11 can be written

$$\vec{E}_P = \vec{E}_0 e^{-i\omega_0 t} \int_{-\infty}^{\infty} dx \, e^{-\frac{x^2}{w_0^2}} e^{ik_0 lx} \sum_{n=-\infty}^{\infty} i^n J_n(a) e^{in\psi}, \tag{2.13}$$

where $a = \tilde{\mu} k_0 L$ and $\psi = (kx - \omega t)$. The above equation produces scattered beams with amplitudes given by $J_n(a)$. Note that in the limit $a \to 0$, which implies $\tilde{\mu} \to 0$, the density fluctuation in the plasma ceases to exist. In this limit only the J_0 term is non-zero, and the incident laser propagates without any scattering. When a is non-zero, the amplitude of the J_0 beam is reduced, and this gives rise to the presence of the scattered beams for $n = \pm 1, \pm 2 ... \pm \infty$. Rearranging Eq. 2.13 and separating the x-dependence in ψ, we have

$$\vec{E}_P = \sum_{n=-\infty}^{\infty} i^n J_n(a) \vec{E}_0 e^{-i(\omega_0 + n\omega)t} \int_{-\infty}^{\infty} dx \, e^{-\frac{x^2}{w_0^2}} e^{i(k_0 l + nk)x}. \tag{2.14}$$

We can now see the asymmetry for positive and negative n in the sum over the Bessel functions. The terms $n < 0$ cause a down-shift in frequency while the terms $n > 0$ cause an up-shift in frequency. The $n = 0$ term is the "unscattered" beam, although its amplitude is reduced as power is coupled from the original beam into the scattered $n \neq 0$ beams. Because the electric field at point P has been computed by using a scalar diffraction approach, the small shift in the vector direction of the scattered beams is not included in this derivation. The integral is now easily performed as it is simply the Fourier Transform of a Gaussian,

$$\vec{E}_P = \sum_{n=-\infty}^{\infty} i^n J_n(a) \vec{E}_0 e^{-i(\omega_0 + n\omega)t} \sqrt{\pi} w_0 e^{-\frac{1}{4}(k_0 l + nk)^2 w_0^2}. \tag{2.15}$$

The nature of the scattered beams is hidden in the Gaussian term $e^{-\frac{1}{4}(k_0 l + nk)^2 w_0^2}$. The Gaussian term peaks when its argument is 0, therefore the peak of each scattered beam is given by $k_0 l + nk = 0$, again where $n < 0$ corresponds to the down-shifted beams and the $n > 0$ corresponds to the up-shifted beams. These peaks correspond

44

to beams scattered at the angles

$$\sin\theta = \frac{nk}{k_0}. \tag{2.16}$$

This is the Raman-Nath scattering response. Additionally, we can see that each beam expands as a Gaussian beam, centered about its peak scattering angle. The $1/e$ response of the Gaussian term is given by $\frac{1}{4}(k_0 l + nk)^2 w_0^2 = 1$ or

$$\sin\theta = \frac{nk}{k_0} - \frac{2}{k_0 w_0}. \tag{2.17}$$

The $1/e$ response is shifted from the peak angular response by $\Delta\theta \simeq \frac{2}{k_0 w_0}$. This is simply the expansion angle of a Gaussian laser as it expands from its waist as will be shown in Appendix A.2.

To summarize, an incident laser with wave-vector k_0, frequency ω_0, and a Gaussian beam profile is scattered into Gaussian expanding beams shifted in frequency by $n\omega$, and propagating at angles $\sin\theta = \frac{nk}{k_0}$. Considering the propagation angle, we see that the magnitude of the wave-vector of each scattered beam remains k_0, and the x-component is nk. Therefore the z-component of the scattered field is $k_n^z = \sqrt{k_0^2 - (nk)^2} \simeq k_0 \left(1 - \frac{(nk)^2}{2k_0^2}\right)$. The scattered wave-vector can thus be written

$$\vec{k}_n = k_0 \left(1 - \frac{(nk)^2}{2k_0^2}\right)\hat{z} + nk\hat{x}. \tag{2.18}$$

We can now write the full scattered field with explicit wave-vector dependence. The Gaussian envelope width expands as $w(s) = w_0\sqrt{1 + \left(\frac{2s}{k_0 w_0^2}\right)^2}$, where s is the distance perpendicular to each scattered beam. This gaussian expansion is dropped for simplicity at this point leaving the scattered electric field

$$\vec{E}(x,z,t) = \sum_{n=-\infty}^{\infty} i^n J_n(a)\vec{E}_0 e^{i\left[\vec{k}_n \cdot \vec{x} - (\omega_0 + n\omega)t\right]}. \tag{2.19}$$

The "unscattered" beam is the $n = 0$ term. It is a continuation of the incident beam, reduced in amplitude due to the coupling of energy to higher order scattered beams.

The phase between the $\pm n$ modes appears to be out of phase due to the i^n term. However, using the identity $J_{-n} = (-1)^n J_n$ we can re-write the three components as follows

$$\vec{E}_{\text{unscattered}} = J_0(a)\vec{E}_0 e^{i[k_0 z - \omega_0 t]}, \tag{2.20}$$

$$\vec{E}_{\text{up-shifted}} = \sum_{n=1}^{\infty} i^n J_n(a)\vec{E}_0 e^{i[k_n^z z + nkx - (\omega_0 + n\omega)t]}, \tag{2.21}$$

$$\vec{E}_{\text{down-shifted}} = \sum_{n=1}^{\infty} i^n J_n(a)\vec{E}_0 e^{i[k_n^z z - nkx - (\omega_0 - n\omega)t]}. \tag{2.22}$$

2.1.2 A Word About Non-Perpendicular Fluctuations

We consider the scattering response to a fluctuation propagating at an angle β from perpendicular to the incident laser. To do this, we will simply rotate the Gaussian profile and wave-vector of the fluctuation in the plasma, again following the approach of Raman and Nath. The index of refraction (Eq. 2.7) is now angled relative to the incident beam and can be written

$$N = \mu_0 + \tilde{\mu}\cos(kx\cos\beta + kz\sin\beta - \omega t)e^{-\frac{\pi(z\cos\beta - x\sin\beta)^2}{L^2}}, \tag{2.23}$$

where μ_0 and $\tilde{\mu}$ are previously defined in Eq. 2.8 and Eq. 2.9. We must now perform the integral along the beampath to compute the phase shift acquired by the incident beam after it passes though the density fluctuation of effective width L. Applying this index of refraction perturbation to Eq. 2.10 we get

$$\Phi(x,t) = k_0\tilde{\mu}\cos(kx\cos\beta - \omega t)\int_{-\infty}^{\infty} dz\cos(kz\sin\beta)e^{-\frac{\pi(z - x\tan\beta)^2}{(L\sec\beta)^2}}$$
$$- k_0\tilde{\mu}\sin(kx\cos\beta - \omega t)\int_{-\infty}^{\infty} dz\sin(kz\sin\beta)e^{-\frac{\pi(z - x\tan\beta)^2}{(L\sec\beta)^2}}. \tag{2.24}$$

46

Making the substitution $u = z - x \tan \beta$ and noting that x is constant over the integral, Eq. 2.24 can be written

$$\Phi(x,t) = k_0\tilde{\mu}\cos(kx\cos\beta - \omega t)\cos(kx\sin\beta\tan\beta)\int_{-\infty}^{\infty} du\cos(ku\sin\beta)e^{-\frac{\pi u^2}{(L\sec\beta)^2}}$$
$$- k_0\tilde{\mu}\cos(kx\cos\beta - \omega t)\sin(kx\sin\beta\tan\beta)\int_{-\infty}^{\infty} du\sin(ku\sin\beta)e^{-\frac{\pi u^2}{(L\sec\beta)^2}}$$
$$- k_0\tilde{\mu}\sin(kx\cos\beta - \omega t)\cos(kx\sin\beta\tan\beta)\int_{-\infty}^{\infty} du\sin(ku\sin\beta)e^{-\frac{\pi u^2}{(L\sec\beta)^2}}$$
$$- k_0\tilde{\mu}\sin(kx\cos\beta - \omega t)\sin(kx\sin\beta\tan\beta)\int_{-\infty}^{\infty} du\cos(ku\sin\beta)e^{-\frac{\pi u^2}{(L\sec\beta)^2}}.$$

$$(2.25)$$

The integrands that vary as $\sin(u)e^{-u^2}$ are odd, and therefore those integrals are zero. The integrands that vary as $\cos(u)e^{-u^2}$ can be recognized as being equivalent to the Fourier Transform of the Gaussian term. Therefore the Eq. 2.25 reduces to

$$\Phi(x,t) = \tilde{\mu}k_0 L\cos(kx\sec\beta - \omega t)\sec\beta e^{-\frac{(kL\tan\beta)^2}{4\pi}}. \qquad (2.26)$$

Therefore, the phase shift introduced by a plane-wave fluctuation with limited spatial extent L propagating at an angle β from perpendicular to the incident beam reduces the induced phase shift by $\sec\beta$ times a Gaussian. The wave-number of the measured response is increased to the *apparent* wave-number $k\sec\beta$. Comparing Eq. 2.26 with Eq. 2.10 we can see that the scattering analysis will proceed equivalently as before with the apparent wave-vector $k \rightarrow k\sec\beta$ and the Bessel function argument

$$a' = a\sec(\beta)e^{-\frac{(kL\tan\beta)^2}{4\pi}}, \qquad (2.27)$$

where $a = \tilde{\mu}k_0 L$ is the original argument of the Bessel functions, and β is the angle of the fluctuation from perpendicular to the incident beam. When $kL > 2\sqrt{\pi}$ the $\sec\beta$ term is nearly unity over the angular range of importance. In this case, the PCI

response peaks at $\beta = 0$ and decreases with a $1/e$ width in β given by

$$\beta_e = \tan^{-1}\left(\frac{2\sqrt{\pi}}{kL}\right). \tag{2.28}$$

Comparing this result to that of Raman and Nath [35, 38], we can generalize the angular response of the scattering process. In their paper, they assumed the fluctuation in the optical medium was a plane-wave with uniform amplitude over the width of the column L. The scattering response as a function of angle with the incident beam was determined to be $a' = a \sec \beta \sin(t)/t$. We can recognize the $\sin(t)/t$ as the Fourier Transform of the rectangular envelope they assumed. In fact, by repeating the analysis with arbitrary envelope function $G(z)$, we see that the response will be modified by $a' = a \sec(\beta)\mathcal{F}[G]$ where $\mathcal{F}$ denotes the Fourier Transform of the envelope function G. Thus, the choice of the envelope function is not particularly important, and the result is that the angular response of the PCI to modes propagating at finite angles from perpendicular is directly related to the effective width L over which the amplitude of mode is significant. As the width decreases, the response increases to higher angles from perpendicular.

For PCI in a typical sized tokamak, the scale of kL is bounded by practical considerations. The wave-numbers of the modes of interest are given in Table 2.1, and we can consider the effective width of the envelope function to be no larger than the size of the plasma and no smaller than the wavelength of the mode. Therefore, kL should be in the range of $2\pi < kL < 3000$. Table 2.2 lists the width β_e of the PCI angular response for several values of the scale of the fluctuation width kL. From Table 2.2 we can see that for fluctuations with effective width greater than approximately 10 times their wavelength ($L > 10\lambda$), the scattered beam power decreases by almost an order of magnitude within a few degrees from propagating perpendicular to the incident beam. This thesis will consider plasma turbulence in this regime where the PCI technique is described as responsive only to modes propagating perpendicular to the probe beam.

Table 2.2: Angle from perpendicular to the incident beam at which the fluctuation response falls to $1/e$

Angular Response vs. Fluctuation Scale	
kL	β_e **(deg)**
6	30.5
25	8.1
100	2.0
500	0.4
1000	0.2
3000	0.07

2.1.3 PCI System Response

The response of the Phase Contrast Imaging technique as applied to measuring plasma density fluctuations can be evaluated with only limited knowledge of the details of the imaging system used. The PCI uses optical components to create an imaging system, and a particular optic known as the *phase plate*. The phase plate spatially filters the scattered beams such that it only retards the phase of the $n = 0$ unscattered beam by $\pi/2$ relative to the scattered beams. An array of photodiode detector elements is placed at the image location of the optical system where, due to the spatial filtering of the phase plate, the signal intensity is proportional to the line-integrated plasma density (see Fig. 2-1). Because of the nature of such an imaging diagnostic, the system response only depends on the overall magnification (M) of the imaging system, assuming optical abberations are negligible and no clipping of the scattered radiation occurs.

Using the parameter estimates in Table 2.1, an upper limit on the amplitude of fluctuation of index of refraction of a single plane wave is $\tilde{\mu} \sim 5 \times 10^{-7}$. This is an extremely high estimate because it assumes fluctuation levels as measured at the edge of the plasma and assumes that the plasma fluctuation is a single plane wave. The fluctuation amplitude $(\tilde{n}/n_0)$ is really a statistical quantity of the fully developed turbulence which is composed of many modes. Therefore, the amplitude of a single mode would be markedly smaller, and a resonable upper limit of the argument of the Bessel Functions is $a \sim 2 \times 10^{-2} \ll 1$. The coupling from unscattered 0th beam to

the scattered beams is therefore weak, and the Bessel functions can be expanded in the small argument limit giving $J_n(a) \simeq \frac{1}{n!} \left(\frac{a}{2}\right)^n$. Keeping only terms to order $\mathcal{O}(a)$, the beams that contribute to the PCI response are $n = -1, 0, 1$, and the total electric field in the object plane is

$$\vec{E}_{\text{obj}}(x, z, t) = \vec{E}_0 e^{i[k_0 z - \omega_0 t]} \left[1 + i\frac{a}{2} \left(e^{i\left[-\frac{k^2}{2k_0}z + kx - \omega t\right]} + e^{i\left[-\frac{k^2}{2k_0}z - kx + \omega t\right]}\right)\right]. \quad (2.29)$$

After propagating through the PCI imaging system, the field in the region of the image plane will be modified only by the overall magnification in that the scattered beams will propagate through the system as geometrical rays and the wave-vector of the scattered beams modified as in Eq. A.7. In essence, the wave-vector of the scattered beams is rotated by the system magnification, understanding that $M < 0$ means the image is "upside down" relative to the object. In the image plane, the scattered beam wave-vectors are then

$$\vec{k}_{\pm n} = k_0 \left(1 - \frac{(nk)^2}{2M^2 k_0^2}\right) \hat{z} \pm \frac{nk}{M} \hat{x}. \quad (2.30)$$

Therefore, the field near the image plane $(z = 0)$ in the absence of the phase plate is

$$\vec{E}_{\text{img}}(x, z, t) = \vec{E}_0 e^{i\psi_0} \left[1 + i\frac{a}{2} \left(e^{i\psi_M} e^{-i\zeta} + e^{-i\psi_M} e^{-i\zeta}\right) + \mathcal{O}(a^2)\right], \quad (2.31)$$

where $\psi_0 = (k_0 z - \omega_0 t)$, $\psi_M = (\frac{k}{M}x - \omega t)$, and $\zeta = \frac{k^2}{2M^2 k_0}z$. The intensity of this field is

$$I_{\text{img}}(x, z, t) = |E_0|^2 \left[1 - 2a \cos(\psi_M) \sin(\zeta) + \mathcal{O}(a^2)\right]. \quad (2.32)$$

We can now see the need and purpose of the phase plate. At the precise image plane, $\zeta = 0$ and the response is $\mathcal{O}(a^2)$. When placed in the conjugate plane of the imaging system, the phase plate spatially filters the unscattered beam by requiring it to traverse an increased path of $\lambda/4$ (see Fig. 2-1), and thus retards the phase of the unscattered beam by $\pi/2$. The total electric field at the image plane is then

$$\vec{E}_{\text{img}}^{\text{PCI}}(x, z, t) = \vec{E}_0 e^{i\psi_0} \left[i + i\frac{a}{2} \left(e^{i\psi_M} e^{-i\zeta} + e^{-i\psi_M} e^{-i\zeta}\right) + \mathcal{O}(a^2)\right], \quad (2.33)$$

and the corresponding intensity profile is

$$I_{\text{img}}^{\text{PCI}}(x, z, t) = |E_0|^2 \left[1 + 2a \cos(\psi_M) \cos(\zeta) + \mathcal{O}(a^2)\right]. \tag{2.34}$$

The intensity at the image plane (defined by $z = 0, \zeta = 0$) is now directly proportional to the original density fluctuation in the plasma. This is the PCI operating under perfect conditions. Two factors that can alter the system response in the real world laboratory are the imperfect placement of the detector array such that they are not located exactly at the system image plane ($\zeta \neq 0$), and that the phase plate fabrication process is difficult and the phase plate groove isn't always exactly $\lambda/8$ deep (this will be discussed further in Sec. 3.1.2). A deviation of the phase plate groove depth will retard the phase of the unscattered by $ie^{-i\delta}$, where δ is the deviation in phase from $\pi/2$. This definition implies that for $\delta < 0$, the phase plate groove is too deep, and conversely for $\delta > 0$, the phase plate groove is too shallow. This mixes the responses of the PCI with and without the phase plate; after a little algebra the system response can be written as

$$I_{\text{img}}^{PCI}(x, z, t) = |E_0|^2 \left[1 + 2a \cos(\psi_M) \cos(\zeta + \delta) + \mathcal{O}(a^2)\right]. \tag{2.35}$$

The analysis of PCI operation presented in Sec. 2.1.1 and Sec. 2.1.3 makes assumptions that the scattering process is in the Raman-Nath regime, $i.e.$ that the effective length scale L of the fluctuation is small, and that $k/k_0 \ll 1$. The Klein-Cook Parameter [41] ($Q = \frac{k^2 L}{\mu_0 k_0}$) is used to demarcate the Raman-Nath ($Q \ll 1$) from the Bragg regime ($Q \gg 1$). For density waves with $kL \sim 60$ or $L \sim 10\lambda$, the Klein Cook parameter is between $0.01 - 0.3$ for fluctuation wave-numbers in the range specified in Table 2.1. This is a resonable estimate considering the plasma magnetic shear and that much of the PCI signal comes from the plasma edge (as will be discussed in Chapter 4). Additionally, this analysis ignores effects due to the finite propagation time of the laser through the plasma ($i.e.$ the retarded time does not factor into our integrals). This is a valid assumption when the laser transit time L/c is small compared to fluctuation time scale $1/f$, a good approximation for plasma turbulence but

not for RF waves. Under these conditions, Eq. 2.35 gives the PCI system response including defocusing effects (the Talbot Effect), and the effect of imperfect fabrication of the phase plate groove depth. We see that the imaged intensity is directly proportional to the plasma density fluctuation integrated along the beampath. The scattering process is linear, therefore an arbitrary density structure can be broken into a set of Fourier modes, each resulting in a response via Eq. 2.35. Each density mode would result in a Fourier mode in the imaged intensity, making the total intensity structure proportional to the original density structure in the plasma. In this sense, the PCI truly is an imaging diagnostic. Moving off the image plane (or equivalently, fluctuations generated off the object plane) causes the $n = 1$ and $n = -1$ modes to interfere with one another. This suggests a solution when the PCI is used to view extremely high wave-numbers; if the $n = -1$ beam is blocked, the destructive interference is removed. However, this solution has the side-effect of degrading the system response by a factor of 2. Blocking one of the scattered beams to remove interference caused by defocusing has been verified using ultrasonic waves in air during system calibration.

2.2 Measurement of Turbulence Propagation Direction

The DIII–D Phase Contrast Imaging diagnostic is accurately described as being sensitive primarily to modes propagating perpendicular to the probe beam. This was described in Sec. 2.1.1 by showing that the system response decreases rapidly for fluctuations propagating at an angle offset from perpendicular to the probe beam. In this section we will assume this to be the case - *i.e.* that the PCI measures modes propagating in the $x - y$ plane in Fig. 2-2. Here we will be concerned with what angle in the $x - y$ plane the mode propagates (*i.e.* what angle *about* the PCI chord the mode propagates). Using a simple rotating mask, it is possible to spatially filter the scattered beam so as to isolate the propagation direction of the turbulence being

measured. Section 2.2.1 will describe the 3-D nature of the scattering geometry and how this leads to a spatial separation of modes propagating at different angles in the conjugate planes of the imaging system. Section 2.2.2 will show that for modes propagating near perpendicular to magnetic field ($k_{||} \sim 0$), this propagation direction corresponds to the location along the probe beam at which the mode is propagating, and thus filtering in propagating direction leads to localization along the PCI chord.

2.2.1 Technique

The scattering of the PCI probe laser beam from turbulent plasma fluctuations is, in general, a 3-dimensional process. When PCI is used in a toroidal fusion device it is generally implemented in one of two orientations, vertical injection or tangential injection. For practical reasons, including the limited availability of port space, vertical injection is most common (*e.g.* both the DIII–D and Alcator C-Mod PCI diagnostics use this orientation). In both orientations, the 3-D nature of the scattering can be used to gain a more detailed diagnosis of the plasma. In a tangentially injected PCI, the scattering angle perpendicular to the probe beam shows where in (k_r, k_θ) space the turbulence is propagating. This information can most easily be gained from a 2-D detector array, or it can be gained from a rotating mask and rotating 1-D detector array. In a vertically injected PCI, the propagating angle around the probe beam shows where in $(k_\phi, k_\perp)$ space the turbulence is propagating, where $\hat{\phi}$ is the toroidal direction and $\perp$ refers to perpendicular to the PCI chord while still in the poloidal plane (k_R).

Since our PCI diagnostic is implemented in the vertical orientation, we now consider only this geometry and the segment of wave-vector space it diagnoses. In this orientation, the propagation angle ($\alpha \in [-\pi/2, \pi/2]$) is measured from the direction perpendicular to the chord in the poloidal plane. Therefore, at $\alpha = 0$, $k > 0$ is a mode propagating perpendicular to the probe beam in poloidal plane towards the outboard midplane, while $\alpha = 0$, $k < 0$ is a mode propagating towards the inboard midplane. Since we are only interested in small angles $|\alpha| < \pi/2$, we elect to choose the somewhat odd notation of both positive and negative wave-vectors (positive defined as

propagating towards the outboard direction $\hat{R}$, and negative defined as propagating towards the inboard direction $-\hat{R}$) and propagation angle defined over the domain $-\pi/2 < \alpha < \pi/2$ (as opposed to a cylindrical system).

Figure 2-3 depicts the 3-D nature of the scattering process. Here we focus on a vertically injected PCI and consider modes propagating at different angles about the PCI chord. The figure shows both positive $(k > 0)$ and negative $(k < 0)$ wave-numbers in solid and dashed lines respectively for values of α that span the appropriate range. The scattered beams are shown with exaggerated scattering angles for clarity. Each wave-vector produces $\pm 1^{\text{st}}$ order scattered beams, and the direction of propagation is determined at detection because the signal intensity at the detector array is proportional to the density in the plasma as shown in Eq. 2.35.

The filtering is accomplished by a rotating mask placed at a conjugate plane in the PCI imaging system where the scattered beams focus to their smallest size and the distance from the unscattered beam to the focused spot (Δ) is proportional to fluctuation wave-number. This distance and the spot $1/e$ half width (w_0) (see Fig. 2-1) are given by

$$\Delta = \frac{kf}{k_0} \qquad \text{and} \qquad \mathrm{w}_0 = \frac{2f}{k_0 \mathrm{w}}, \qquad (2.36)$$

where k and k_0 are the fluctuation and probe beam wave-numbers, f is the focal length of the first focusing optic, and w is the $1/e$ radius of the incident beam electric field in the plasma. The spots are focused in the plane made by the optical axis and the scattered beam, and therefore each spot focuses at the same angle α as the scattered beam. The scattered beams shown in Fig. 2-3 therefore focus to a minimum spot size in the conjugate plane at the angle equal to the value of the propagating direction α.

Figure 2-4 plots scattered beams (evaluated for $k = 30$ cm^{-1}) for the same propagation angles as was plotted in Fig. 2-3 in the first conjugate plane (where the phase plate is located) of the DIII–D PCI imaging system. In the left plot, the spots are shown focused on the phase plate, where the gold bar represents the phase plate
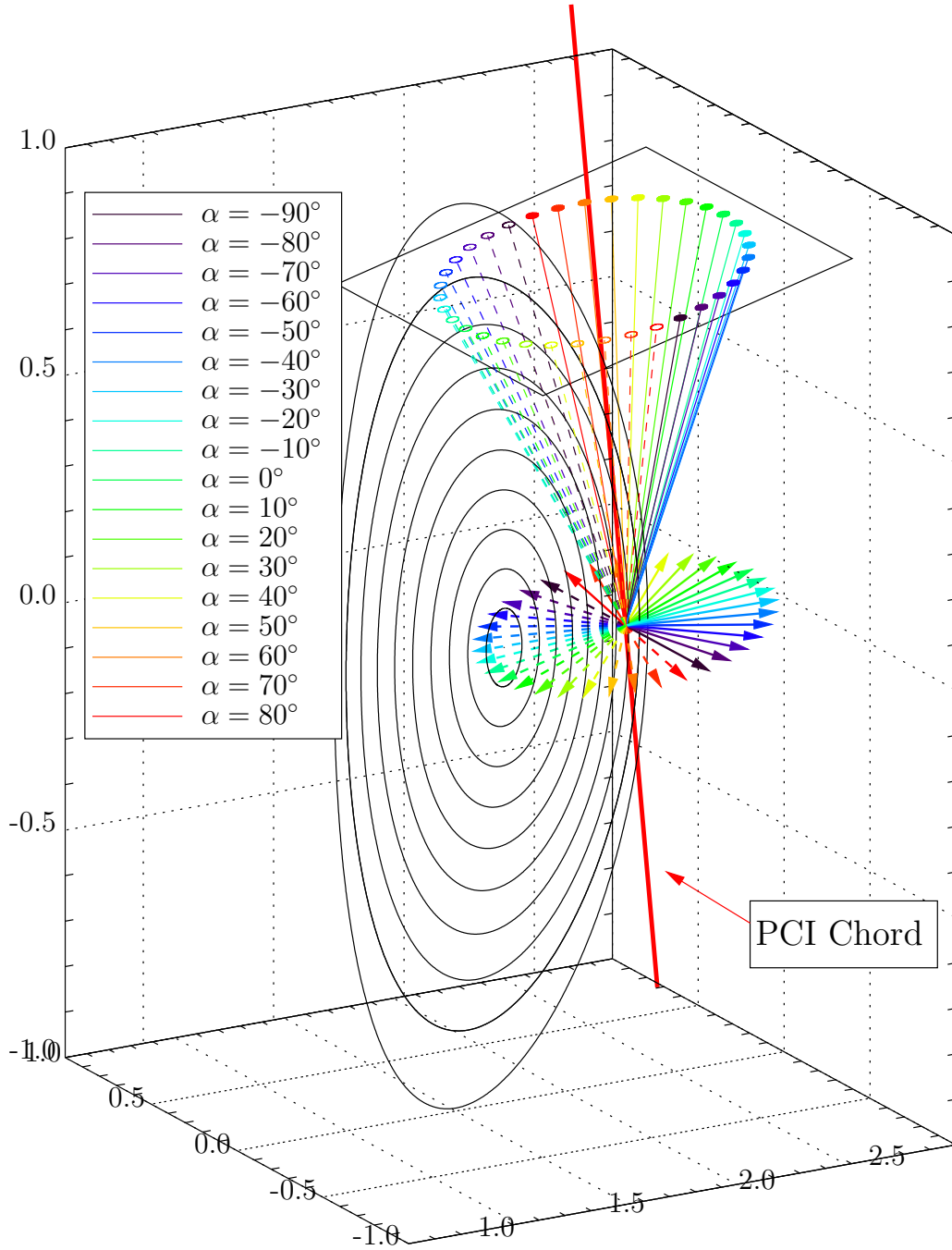
Figure 2-3: Diagram representing the PCI laser beam scattering off a set of possible fluctuations at the plasma midplane. Each arrow at the midplane represents the wave-vector of a different plasma fluctuation, and each colored line shows that path of the upshifted scattered radiation as a function of propagation angle α. Solid line wave-vectors all correspond to $k > 0$ as measured by the PCI while the dashed wave-vectors correspond to $k < 0$.
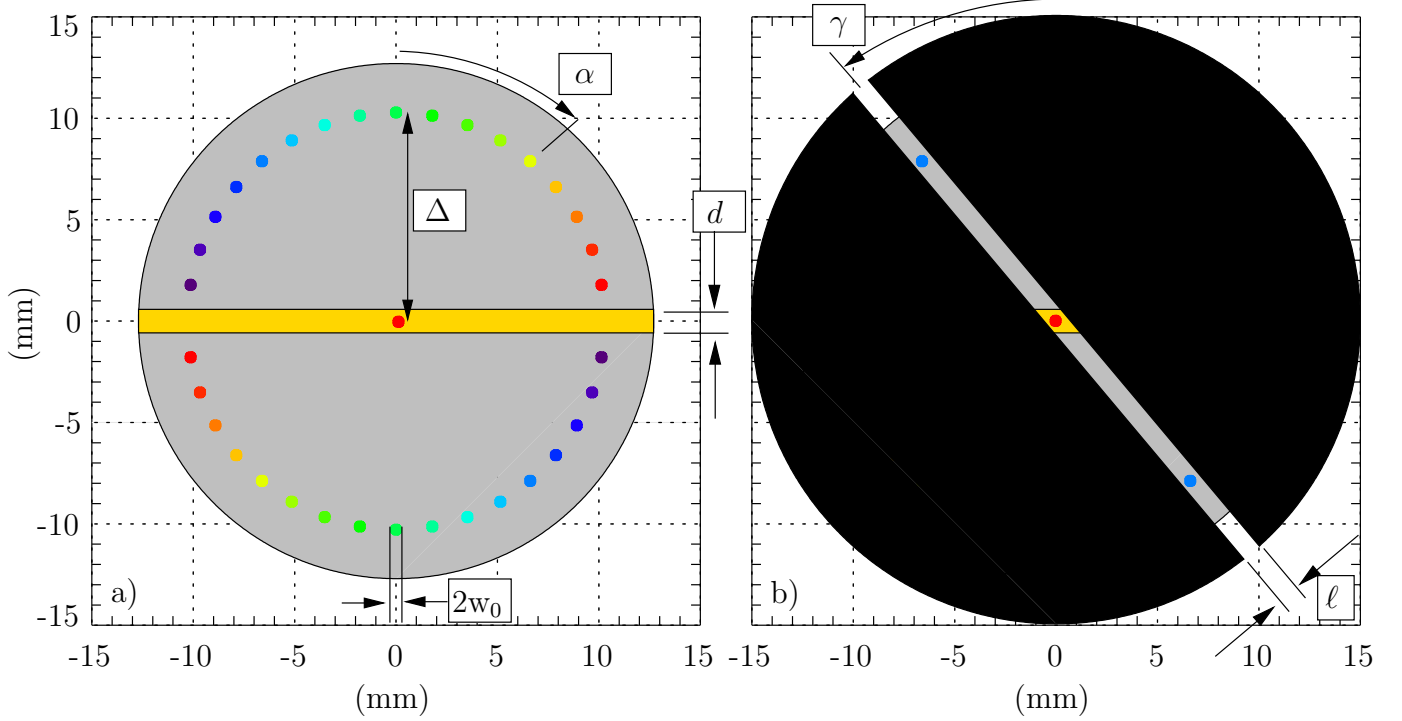
Figure 2-4: Diagram showing the scattered beams as focused at the phase plate (1st conjugate plane). a) Focused spots from example fluctuations propagating at the same angles (α) as shown in Fig. 2-3. b) The rotating mask (angle γ) with a thin slit selectively passes only modes propagating at specific propagation angles.

groove of width d. The phase plate is oriented so that perpendicular to the groove corresponds to a mode propagating in the poloidal plane ($\alpha = 0$). On the right plot, a mask with slit of width ℓ is depicted as blocking all scattered beams except for that at $\alpha = -40°$. The mask is made of a metal plate with a slit cut across its diameter. In this way the mask filters the scattered beams providing a measurement that is limited in the mode propagation angle.

In practice, the mask is mounted on a rotation stage and rotated during the experiment. It is assumed that the turbulence is stationary and fully developed, and that the mask rotates slowly compared to turbulence time scales while fast compared to changes in the plasma parameters. Under these conditions, a single mask sweep provides measurements as a function of propagation angle, and each sweep is a measurement in time modified by the evolving plasma conditions. If we consider turbulent modes as in Sec. 2.1.1, *i.e.* modes that propagate as plane waves with a envelope that

localizes the mode to a finite spatial location, then the measurements with a rotating mask produce the turbulence spectra

$$S(\gamma, k) = \int dz \int d\alpha \; S(\alpha, z, k) \; \mathcal{M}(\gamma - \alpha, k), \qquad (2.37)$$

where k is the wave-number of the mode as measured with the PCI, z is the height along the beampath, α is the propagation angle of turbulence as previously defined, γ is the angle of the rotating mask, and $\mathcal{M}$ is the "mask response function" or rotating mask transfer function. The mask response function can be understood as the system response to a single plane wave mode in the plasma. In this formulation, it represents the actual response of the system, including all physical effects such as diffraction of the beam through the narrow mask slit. Details of the model and experimental verification of $\mathcal{M}$ will be discussed further in Sec. 3.5.3, however the basic form is a peak at $\alpha = \gamma$ falling to zero in both directions with a width proportional to $1/k$. The PCI signal collected with a rotating mask is the normal chord-integrated signal along the beampath convolved against the mask response function. This convolution can be thought of as a filter in $\vec{k}$-space that selects modes propagating at an angle α from the poloidal plane.

In essence, the rotating mask system measures turbulence of different portions of wave-vector space. While it is fairly easy to imagine the rotating mask wave-vector selection in terms of a coordinate system (k_R, k_ϕ, k_Z), it is somewhat mind-numbing to imagine this selection of wave-vectors in the more meaningful $(k_r, k_{||}, k_\perp)$ space. The first coordinate system refers to a cylindrical system, where $\hat{R}$ is the direction towards the outboard side of the torus, $\hat{Z}$ is the vertical direction, and $\hat{\phi}$ is the toroidal direction. The second coordinate system is locally orthogonal, where $\hat{r}$ is normal to the flux surface, $||$ is parallel to the local magnetic field, and $\perp$ is perpendicular to the local magnetic field while still in the flux surface. In general, $(||, \perp)$ do not correspond to the toroidal coordinate directions $(\hat{\phi}, \hat{\theta})$ but are rotated in the flux surface due to the pitch of the magnetic field. In the limit $q \to \infty$, the poloidal field is zero, $|| \to \hat{\phi}$ and $\perp \to \hat{\theta}$.

Consider a PCI chord, near vertically injected in the poloidal plane, and rotated toward the inboard side at the top of the chord by an angle β_0. Such a chord is used in the DIII–D PCI Phase I Geometry, and depicted in Figs. 2-3 and 3-1. Consider the angle β as in Sec. 2.1.1 to be the angle from perpendicular of the fluctuation wave-vector relative to the incident beam. This creates a set of two spherical angles from which we can define any wave-vector in the plasma in terms of the cylindrical system (k_R, k_ϕ, k_Z)

$$
\begin{aligned}
\vec{k} &= k \cos(\beta + \beta_0) \cos(\alpha) \; \hat{R} \\
&+ k \sin(\alpha) \; \hat{\phi} \\
&+ k \sin(\beta + \beta_0) \cos(\alpha) \; \hat{Z},
\end{aligned} \tag{2.38}
$$

where $(\alpha, \beta) \in [-\pi/2, \pi/2]$, and k spans both positive and negative wave-numbers. This defines two hemispheres, one for $k > 0$ and the other for $k < 0$. The transformation into a local coordinates (k_r, k_ϕ, k_θ) is simply a rotation about the $\hat{\phi}$ axis. Because the (r, ϕ, θ) coordinate system is local, the rotation about the $\hat{\phi}$ axis is dependent on the location along the PCI chord at which the turbulence is propagating. This rotation angle (ν) is related to the slope of the flux surface. If we consider Miller geometry flux surfaces [42], then the rotation angle can be written

$$
\tan(\nu) = -\frac{dR}{dZ} = -\frac{B_R(s)}{B_Z(s)} = \frac{1}{\kappa} \sin\left[\theta + \sin^{-1}(\delta)\sin(\theta)\right]\left(\sec(\theta) + \sin^{-1}(\delta)\right), \quad (2.39)
$$

where κ is the elongation, δ is the triangularity, and θ is the Miller coordinate that parameterizes the flux surface. Of course, in the limit of a circular flux surface $(\delta \to 0, \kappa \to 1)$, we get the appropriate relation $\nu = \theta$. The general scattering wave-vector can now be expressed in terms of the toroidal coordinates (k_r, k_ϕ, k_θ).

$$
\begin{aligned}
\vec{k} &= k \cos(\alpha) \cos(\beta + \beta_0 - \nu) \; \hat{r} \\
&+ k \sin(\alpha) \; \hat{\phi} \\
&+ k \cos(\alpha) \sin(\beta + \beta_0 - \nu) \; \hat{\theta}.
\end{aligned} \tag{2.40}
$$

The coordinates of interest are those aligned with the local magnetic field. This is simply a rotation about the $\hat{r}$ axis. The rotation angle is given by the local magnetic field pitch $\chi = -\frac{B_\phi}{B_\theta}$ where χ is defined to be a kind of 'local' safety factor. With these definitions, a fluctuation in the plasma specified by (k, α, β) can be written in local magnetic field aligned coordinates where $\chi(z)$ and $\nu(z)$ depend on the local magnetic geometry,

$$
\begin{aligned}
k_r &= k \cos(\alpha) \cos(\beta + \beta_0 - \nu), \\
k_{||} &= \frac{k}{\sqrt{1 + \chi^2}} \left[\chi \sin(\alpha) + \cos(\alpha) \sin(\beta + \beta_0 - \nu) \right], \\
k_\perp &= \frac{k}{\sqrt{1 + \chi^2}} \left[\chi \cos(\alpha) \sin(\beta + \beta_0 - \nu) - \sin(\alpha) \right].
\end{aligned}
\tag{2.41}
$$

PCI measurements in the field aligned representation are most easily compared to theory since it is generally assumed that the turbulence spectrum peaks along $k_\perp/k = 1$. The PCI cannot measure modes propagating in this direction as shown in Fig. 2-5. The PCI can probe the dependency of turbulence amplitude with finite $k_{||}$ components. As the propagation angle α increases in either direction from $\alpha = 0$, the PCI is primarily measuring the dependence of a particular wave-vector in the $(k_r, k_\perp)$ plane as it rotates towards alignment with the magnetic field.

In summary, a rotating mask placed in one of the conjugate planes of the PCI imaging system can use a narrow masking slit to selectively pass scattered beams from fluctuations that propagate at a specific angle about the PCI chord. This technique allows measurements that probe regions of wave-vector space that are normally not isolated, $e.g.$ modes with finite $k_{||}$ components. The following section describes how this technique can be used for localizing turbulence along the PCI chord.

2.2.2 Localization Technique

In Tokamaks, transport caused by turbulence is often assumed to be dominated by drift-wave instabilities such as the Ion Temperature Gradient (ITG) [43, 44], the Trapped Electron (TEM) [45, 46], and Electron Temperature Gradient (ETG) [13, 47]
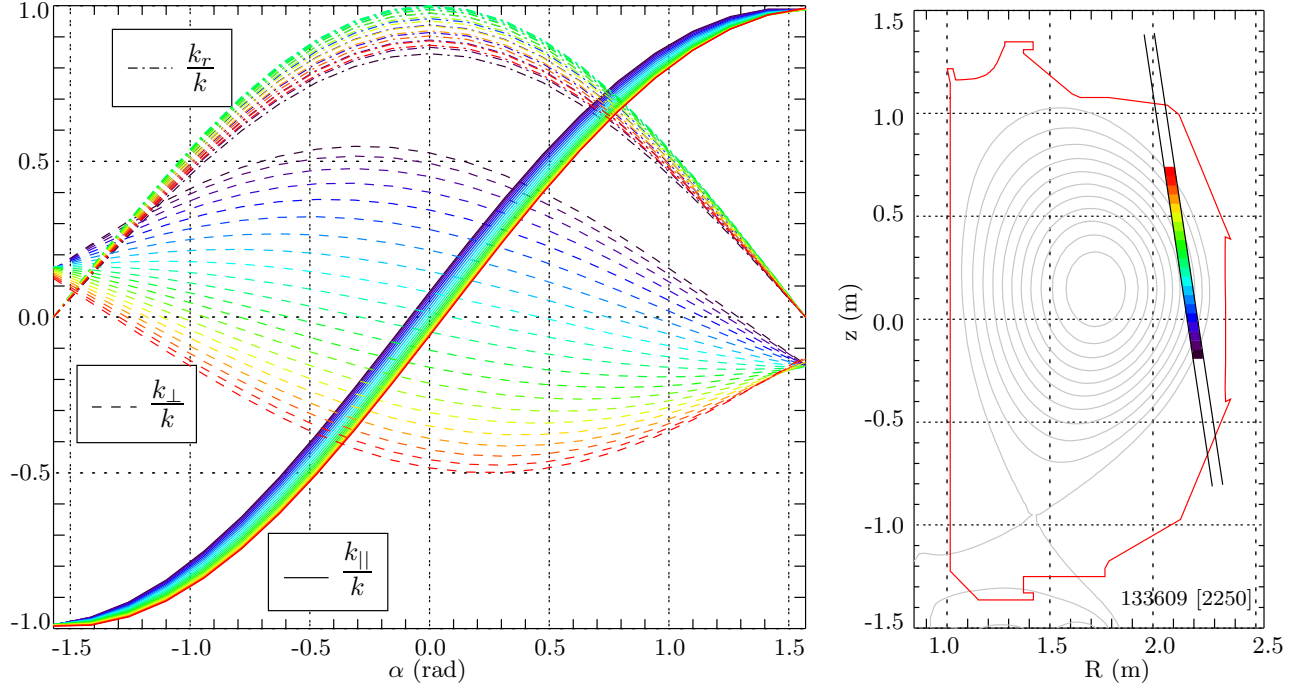
Figure 2-5: (left) Plot of the PCI measured wave-vectors as a function of propagation angle (α) and chord location (shown in different colors). Solid lines are the component of the wave-vector parallel to the magnetic field. Dashed lines are the component of the wave-vector perpendicular to the magnetic field, in the flux surface. Dash-dotted lines are the component of the wave-vector normal to the flux surface. (right) Plot of a typical L-Mode plasma flux surfaces showing the color corresponding to height along the PCI chord.

modes. These modes are assumed to be primarily electrostatic, and therefore $\vec{k}$ is parallel to $\vec{E}$, implying that any component of wave-vector along the local magnetic field would necessarily have a wave electric field along the local magnetic field. At drift-wave frequencies, the small electron mass means that their mobility along field lines is nearly infinite and electrons would short out any component of $\vec{E}$ along $\vec{B}$. Therefore, $k_{||} \sim 0$ for electrostatic drift-wave instabilities, and they propagate near perpendicular to the magnetic field. Note that high-k measurements on DIII–D image a small portion of the beam, so we can consider the magnetic field to be a constant across the beam.

If it is assumed that the dominant turbulence in a tokamak propagates nearly perpendicular to the local magnetic field, then we can exploit the magnetic geometry to gain localized measurements along the viewing chord [48]. This is possible because

the component of the magnetic field perpendicular to the viewing chord varies as a function of chord height. This is because the poloidal field reverses direction from the bottom of PCI chord to the top - the toroidal field is then tilted differently along the chord. As described in Sec. 2.1.1, PCI is only sensitive to fluctuations propagating perpendicular to the viewing chord ($\beta \sim 0$), and by assuming drift-wave turbulence with $k_{||} \sim 0$, the PCI can be viewed as measuring only specific wave-vectors. These two constraints imply that PCI only measures scattering from fluctuations that propagate perpendicular to both the viewing chord and the local magnetic field. Therefore, fluctuations from different plasma heights scatter at rotationally different angles about the PCI chord (their propagation angle α). This angle is a projection of the magnetic pitch angle onto a plane perpendicular to the PCI chord. We can verify this by setting $k_{||} = 0$ in Eq. 2.41 resulting in

$$
\begin{aligned}
\tan(\alpha) &= \frac{B_\theta}{B_\phi}\sin(\beta_0 - \nu) = \frac{B_R}{B_\phi}\cos(\beta_0) + \frac{B_Z}{B_\phi}\sin(\beta_0) \\
&= \frac{B_\theta^\perp(z)}{B_\phi(z)},
\end{aligned}
\tag{2.42}
$$

where $B_\theta^\perp$ is the component of the poloidal magnetic field perpendicular to the PCI chord and B_ϕ is the toroidal magnetic field. The location of the mode in the plasma is directly related to the propagation angle only if the turbulence has $k_{||} \sim 0$. This allows the rotating mask to selectively pass modes propagating from a limited region of the PCI chord, and thus localize the PCI measurement. The component of the poloidal magnetic field perpendicular to the PCI chord ($B_\theta^\perp$) and the associated wave-vectors that are measured are shown at both intersections of the chord and the last closed flux surface (LCSF) in Fig. 2-6.

When the scattered beams are focused in conjugate planes of the PCI imaging system, they appear as in Fig. 2-4 where the spot position can be described in terms of a polar coordinate system. The radial location of the focused spot (Δ given by Eq. 2.36) is a function of the fluctuation wave-number k. The consequence of $k_{||} \sim 0$ turbulence is that the angular position of the focused spot (α) is now a function of scattering height z. Thus, the rotating mask can yield a PCI signal that localizes
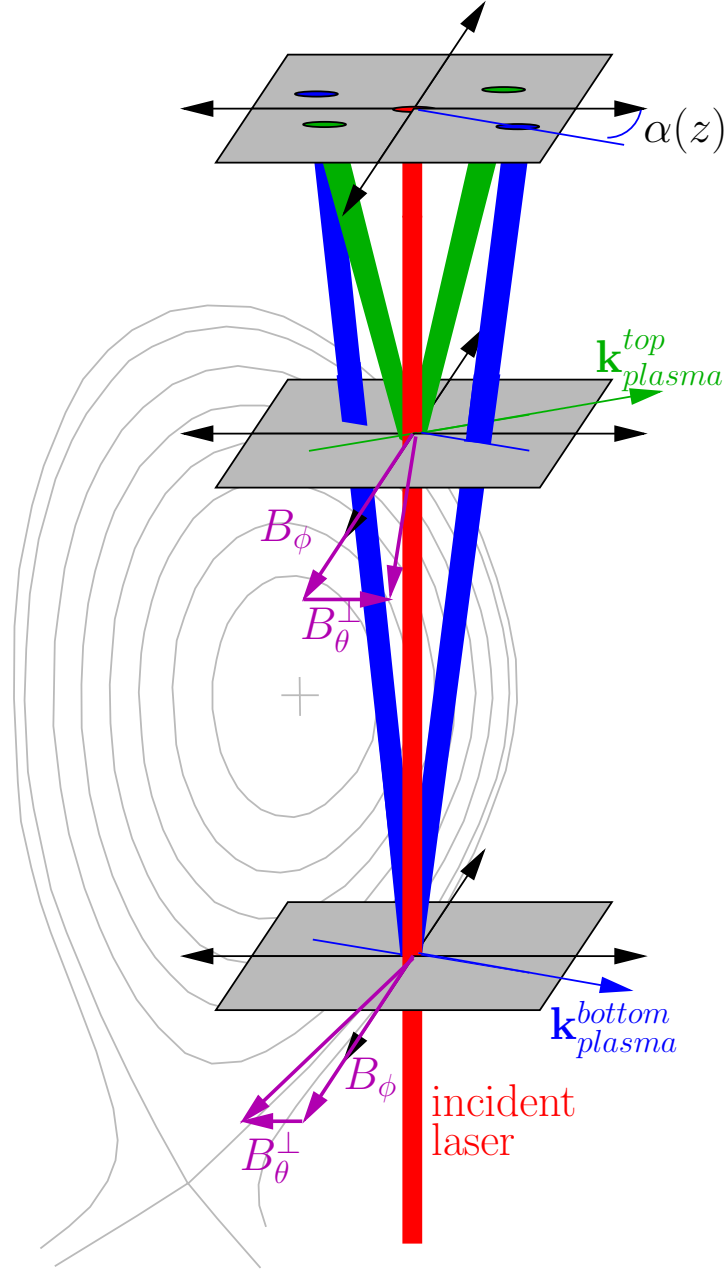
Figure 2-6: Diagram of magnetic field components perpendicular to the PCI chord and the measured plasma wave-vectors. Blue beams represent scattering from fluctuations at the bottom of the DIII–D PCI chord, while green beams represent scattering from fluctuations at the top of the chord. Scattering angles not to scale.

measurements of turbulence along the chord.

It is useful to introduce a Figure of Merit ($\mathcal{L}$) to estimate the effectiveness of a masking system for localized measurements. The minimum achievable resolution can be estimated by calculating the separation between points in the plasma that

map to distinguishable points in the focal plane (*e.g.* points that are separated by at least the diameter of the focused beam spot). The propagation angle separating distinguishable points at the conjugate plane is simply $\delta\alpha = 2w_0/\Delta = 4/kw$ and thus

$$\mathcal{L} = \frac{dz}{d\alpha}\delta\alpha \simeq \frac{4B_\phi}{kw}\left(\frac{dB_\theta^\perp}{dz}\right)^{-1}, \tag{2.43}$$

where z is the height along the PCI chord, and we have assumed an optimal slit width and tokamak magnetic field geometry. It can immediately be seen that PCI localization improves at higher k fluctuations. For a given plasma configuration, the only adjustment to the PCI that improves localization is to increase the size of the probe beam (w) in the plasma. An optimum probe beam diameter can be determined for the desired high k cutoff given the various apertures in the optical path.

The figure of merit described above is a good approximation of the localization capability of a PCI with a static masking slit. It is the plasma chord length-scale at which one can consider measurements separated by $\mathcal{L}$ (or equivalently $\delta\alpha$ in the conjugate plane) as independent. However, when the masking slit is rotated in time, a more rigorous analysis yields improved localization. The power spectrum as a function of mask angle can be related to the spectrum as a function of chord height (z) by combining Eq. 2.42 with Eq. 2.37

$$S(\gamma, k) = \int d\alpha \; \mathcal{M}(\gamma - \alpha, k) \int dz \; S(\alpha, z, k) \; \delta\left(z - z(\alpha)\right), \tag{2.44}$$

where the delta function is used so that the integral over z picks out only the correct value of propagation angle that is perpendicular to the local magnetic field. Performing the integral over the delta function and noting $S(z, k) \left|\frac{dz}{d\alpha}\right| = S(\alpha, k)$ so that spectral power density is conserved, we can write the power spectrum as measured with the rotating mask as

$$S(\gamma, k) = \int d\alpha \; S(z, k) \left|\frac{dz}{d\alpha}\right| \mathcal{M}(\gamma - \alpha; k), \tag{2.45}$$

where $S(z, k)$ is the turbulence power per unit z in the plasma chord, $S(\alpha, k)$ is the

turbulence power per unit propagation angle mapped to the conjugate plane, and $|dz/d\alpha|$ is the "mapping density". In practice, the mapping density tends to peak at the plasma chord edges, resulting in an artificial enhancement of edge turbulence. Again, the mask response function $\mathcal{M}$ is the rotating mask transfer function. The plasma fluctuation power spectra measured at the detector array is given by $S(\gamma, k)$, and γ is the mask slit angle. Note that because of the $k_{||} \sim 0$ assumption, the propagation angle α is limited in domain by tokamak magnetic geometry while γ represents the mask slit angle which is free to rotate through an entire revolution.

Within this framework, it can be seen that the interpretation of localized PCI measurements depends upon accurate knowledge of plasma magnetic geometry and the mask response function. Again, the form of the mask response function ($\mathcal{M}$) is a peak at $\alpha = \gamma$, falling to zero in both directions with a width proportional to $1/k$ (specifics of $\mathcal{M}$ are presented in Sec. 3.5.3). Thus, the contribution from a small region in z is broadened out into a finite range in mask angle (γ), limiting the resolution of the reconstruction. Equivalently, the convolution integral in Eq. 2.45 can be expressed as a multiplication in transform space, and thus the mask response function can also be thought of as a form of low-pass filter.

The analysis of these measurements is to deconvolve the measured spectra and map to plasma chord coordinates, yielding a localized measurement of turbulence power spectra. When interpreting these results, we must note that localized PCI measurements are not only spatially localized along the PCI chord but also in (k_r, k_θ) space. The sharp and narrow response of the PCI around $\beta = 0$ again implies a sensitivity only to fluctuations propagating perpendicular to the chord (e.g. $\vec{k}$ has finite components in both k_r, k_θ at the plasma edge but $\vec{k} = k_r \hat{r}$ where the chord is tangent to flux surfaces). It should be pointed out that this localization technique assumes turbulence with correlation lengths that are small compared to the localized chord segment $\mathcal{L}$. In the range of wave-numbers of interest for high-k measurements, $L_C < 1$ cm and $\mathcal{L} > 5$ cm. This insures that fluctuation spectral power will add incoherently, which is a reasonable assumption for high-k drift-wave turbulence. It should also be noted that for longer wavelength fluctuations (where the localization

technique is not used) L_C can become longer than 1 cm.

In summary, turbulent fluctuations from the drift-wave family propagate near perpendicular to the local magnetic field. Because the poloidal field varies with chord height, the propagation angle of $k_{||} \sim 0$ modes also depend on chord height. Using a rotating mask to selectively pass turbulence at a specific propagation angle amounts to selectively passing turbulence from a region of the PCI chord. The ability to localize improves at larger wave-numbers, and improves as the size of the probe beam in the plasma is increased.

THIS PAGE INTENTIONALLY LEFT BLANK

Chapter 3

PCI Implementation on DIII–D

3.1 Original Implementation

3.1.1 History

The DIII–D PCI was originally built by Stephano Coda in 1992 [26] to measure density fluctuations. At that time, access was through the R+1 and R-1 ports providing measurements in the outboard midplane region near the last closed flux surface (LCFS) [25]. The beam path was moved to the Phase I geometry (access via the R+2 and R-1 ports) in 2003 to cover the region $r/a > 0.7$ as shown in Fig. 3-1. Measurements were integrated along the beam chord and no spatial localization was available.

In these configurations, the PCI was responsible for making the first time-resolved measurements of correlation length and decorrelation time across the L-mode to H-mode transition [49, 50]. The differences between type I and type III ELMs were studied initially in DIII–D by the PCI system [51], and the time resolution was improved with wavelet analysis [52]. The PCI measurements suggesting zonal flows [53] were cited as early evidence for this phenomenon [54]. The PCI was the first diagnostic to measure the density fluctuation component of the edge harmonic oscillation (EHO) coincident with the quiescent H-mode (QH-mode) [55].

3.1.2 System Hardware

The majority of the PCI system is located on an optics table in the DIII–D machine hall. This optics table is turned on its side due to space limitations and houses most
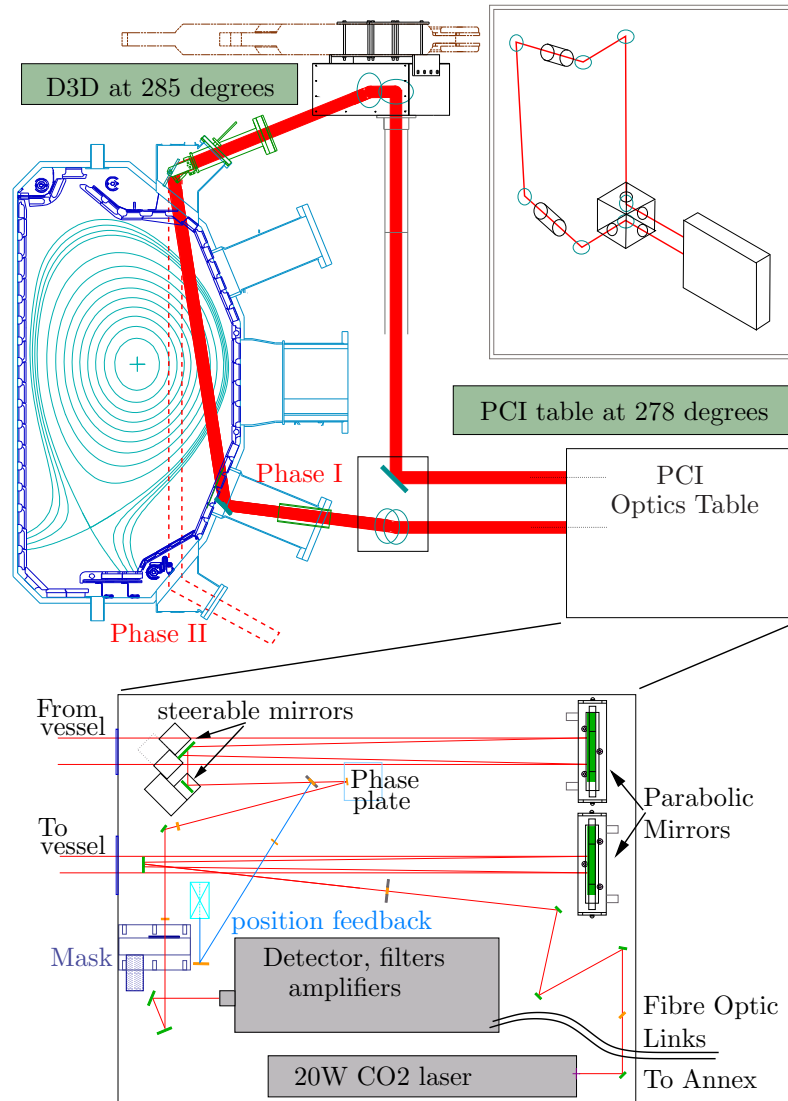
Figure 3-1: DIII–D PCI system overview with beam path in Phase I geometry (solid line) and current Phase II (dashed line) PCI chord geometry. Cylindrical focusing optics not shown for clarity. Upgraded amplifiers/filters condition the raw data and fiber optic links send data to the DIII–D annex where it is digitized.

of the system optics, laser, detectors, amplifiers, and the majority of the vibration compensation feedback system. The beam is generated and conditioned on the optics table, and then steered through the vessel and back to the optics table where the

imaging optics and system detectors reside. Data is collected and conditioned before being transported to the DIII–D annex where it is anti-alias filtered and digitized. A schematic of the DIII–D PCI system is shown in Fig. 3-1.

Laser

The CO_2 laser is a popular tool used in scattering based plasma diagnostics for its relatively high power, spectral and power stability, and low cost. The DIII–D PCI probe beam is generated by a continuous wave (CW) 20 W, 10.6 μm CO_2 laser firing in the TEM_{00} mode. This laser was manufactured by MPB Technologies, model GN-802-MP-20. To maintain stable power output, a Lansing 90.215 power stabilizer is

Figure 3-2: Photo of the DIII–D PCI laser and safety shutter.

used, and the laser is left on during the run day to avoid power fluctuations that occur during laser startup. To achieve this, the laser must have a safety shutter as well as a temperature control system. The operating temperature is kept constant during the run day by circulating water from a chiller, model RTE110-D from Neslab. The safety shutter, model LST400D manufactured by NM Laser Products, Inc. of Sunnyvale, CA is timed to the DIII–D shot cycle and acts as a beam dump when the diagnostic

is not in use to prevent unnecessary beam exposure to all DIII–D personnel. The laser and safety shutter are shown in Fig. 3-2.

Beam Conditioning and Steering

Directly after exiting the laser, the beam is combined with a 16 mW HeNe laser (633 nm wavelength) used for alignment, Melles-Griot model MG 05-LHR-981. The beam is then expanded and collimated using a 1" diameter, 10" focal length ZnSe lens and a 9" diameter, 81.75" focal length off-axis parabolic mirror. These two optics are used to prepare the beam to a diameter of 5 cm before leaving the optics table. The probe beam is collimated at a large diameter so that the gaussian expansion is negligible. The collimated beam is necessary so that the laser waist occurs at the proper phase plate location; this is discussed in further detail in Sec. 3.3.1. The beam is then steered into the vessel through the R-1 port where it is reflected off two in-vessel mirrors as depicted in Fig. 3-1. These in-vessel mirrors shake and vibrate with the vessel during plasma operations due to the large magnetic fields and eddy currents in the metal structure, and they are therefore a major source of noise introduced into the PCI system. The beam exits the vessel through the R+2 port, and is again steered back to the optics table where it is focused onto the phase plate by a symmetric 81.75" focal length off-axis parabolic mirror.

Phase Plate

The phase plate is the optical component used to introduce a $\lambda/4$ or $\pi/2$ phase shift in the unscattered (0th order) beam relative to the scattered (1st order) beams. It is made of an optical reflector with a $\lambda/8$ deep groove cut across the plate diameter. The central groove is generally left as uncoated ZnSe and therefore acts as a partial reflector with a reflection coefficient of 17%. This lowers the DC power on the detector to prevent saturation of the detector elements. The reflector coating is often chosen to be gold, which has a somewhat higher reflectivity at 10.6μm than aluminum or silver. Previous to 2008, the phase plates were manufactured via a deposition process with a masked central groove. The depth of the groove therefore relied on accurate knowledge
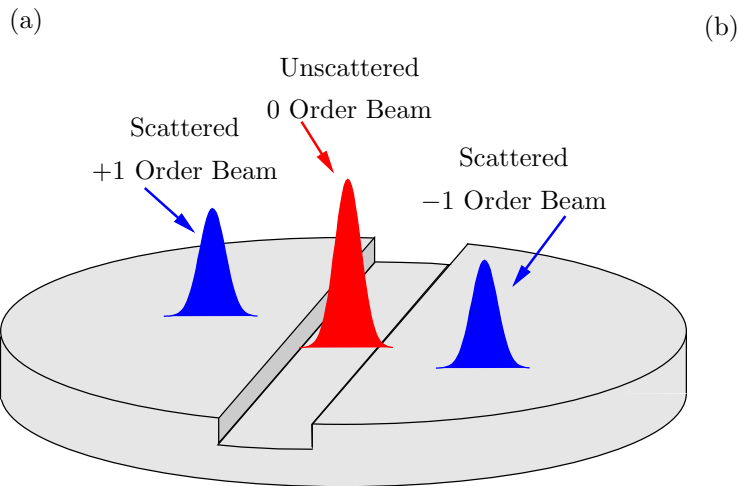
Figure 3-3: a) Schematic of phase plate with scattered and unscattered beams (groove depth exagerated for clarity). b) Picture of new phase plate fabricated by Bandwidth Semiconductor using the etching process.

of deposition rates. In 2008, a new generation of phase plates was needed for both the DIII–D and Alcator C-Mode PCI systems. A more robust fabrication process was developed by Bandwidth Semiconductor, Inc. (now Spire, Inc.) of Hudson NH using a an etching process similar to that used in the fabrication of printed circuit boards [56]. The new fabrication process results in a phase plate groove depth accurate to better than 10%, and is shown in Fig. 3-3.

Feedback System

As stated earlier, a major source of noise in the PCI system comes from vibrations introduced by the in-vessel mirrors. There is no way to avoid the use of these mirrors due to port geometry and access on DIII–D. Compensation for these vibrations is provided by using a feedback system comprised of two galvanometer-mounted steering mirrors, a quadrant position detector, and control circuitry. The galvanometers, shown in Fig. 3-4, are placed in the beam path $\sim 20"$ before the beam focus at the phase plate. A partial reflector is used to direct a fraction of the beam power into the quadrant detector which is positioned at an image of the phase plate - thus movement of the beam focus on the phase plate is proportional to that on the quadrant detector. The quadrant detector measures vibrational movement of the beam focus;
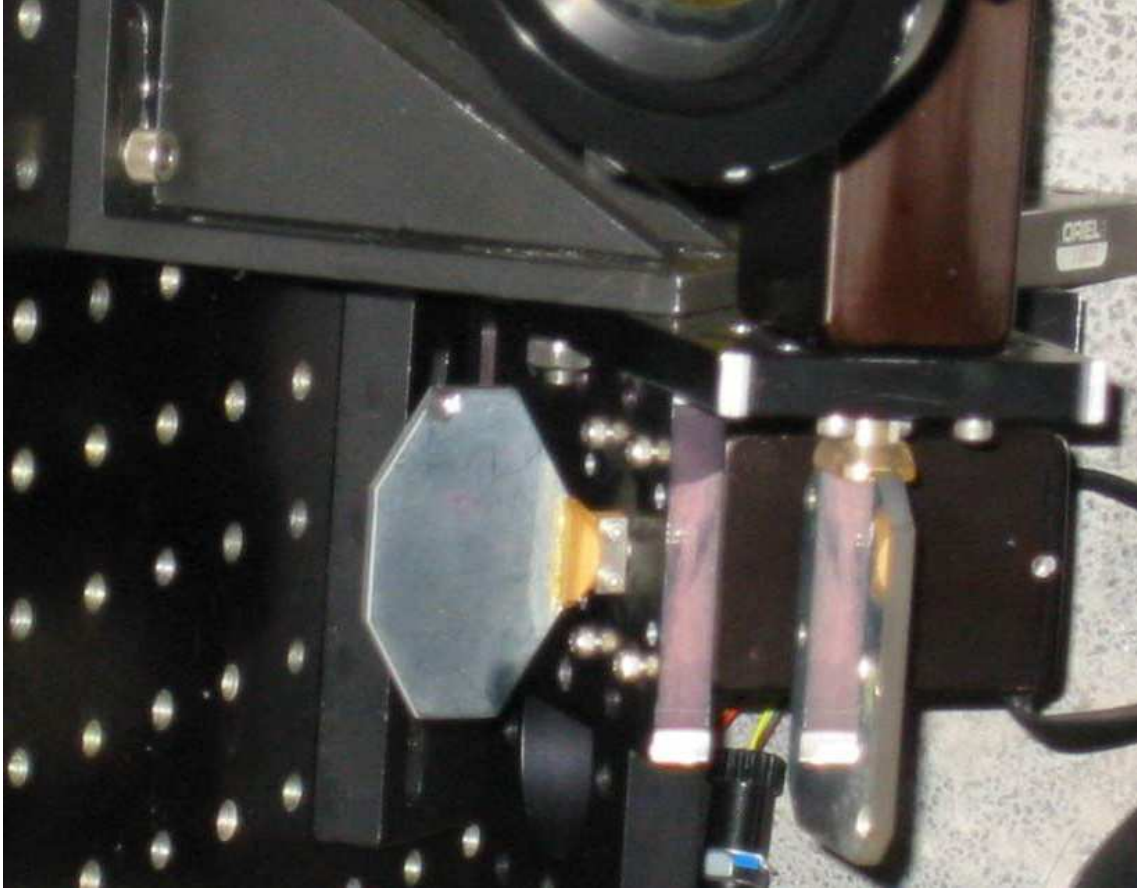
Figure 3-4: Feedback System Steering Mirrors

this is used to adjust the galvanometer mirror angles to maintain the phase plate focal spot position to an accuracy of 0.01 mm RMS over a bandwidth of approximately 1 kHz [26].

Imaging Optics

The PCI uses a two lens (in addition to the return parabolic mirror) imaging system that consists of plano-convex ZnSe optics manufactured by II-VI Incorporated, Saxonburg, PA. The lens diameters are constrained only in that they must be large enough to prevent clipping from occurring in the scattered beams. Thus, the lens diameters depend on the specific imaging layout itself. This layout will also set the system magnification and therefore the effective spacing of detector elements in the plasma. This provides the Nyquist wave-number k_{max}, and is chosen to select the

region in wave-number space to diagnose. It should also be noted that for a fixed probe beam diameter, the system S/N scales like $1/M^2$ where M is the system magnification. This is because the beam size at the detector will be proportional to M, and the beam power will be spread over a larger area for larger magnification - the power delivered to any single detector element is therefore reduced by a factor of $1/M^2$.

Detector

The PCI detector is a photovoltaic array of 16 HgMnTe elements having a manufacturer specified bandwidth greater than 10 MHz. The detector was fabricated by Semiconductor Diagnostics, model PV-10.6-L-16. The detector operates well within

Figure 3-5: DIII–D PCI detector is contained in a LN_2 dewar

its saturation limits, as the 17% reduction in unscattered beam power by the central groove of the phase plate reduces the DC load on the detector. The detector is shown in Fig. 3-5, and is housed in a liquid nitrogen filled dewar that keeps the photodiode elements cool, thereby lowering their thermal noise. The PCI measures only the fluctuating part of the plasma density, therefore the detector photodiodes are AC-coupled to the system preamplifiers, model 490 from Perry Amplifier of Brookline,

MA. The DIII–D detector is currently 15 years old and, as a result, the performance of channels 2, 5, 8, and 11 have either become degraded or are inoperable - this is easily seen by the absolute calibration measurements in Sec. 3.4.2. The detector array was fabricated using individual elements assembled on Flatpack 3R44M-1 from Mini Systems. Table 3.1 lists the DIII–D detector specifications as provided by the manufacturer. Tests have been performed to determine the present performance of the detector array and are discussed in Sec. 3.3.5.

Table 3.1: DIII–D Detector Manufacturer Specifications

Photodiode Material	HgMnTe
Number of elements	16
Element diameter (μm)	450
Center-center distance (μm)	700
Element impedance @ 0V bias (Ω)	20-80
Detectivity $D^\star$ $\left(\text{Jones}, \frac{\text{cm}\sqrt{Hz}}{W}\right)$	$\sim 2^{10}$
Responsivity $\left(\frac{A}{W}\right)$	1.6

Remaining PCI Hardware

The remaining hardware components used in the operation of the DIII–D PCI diagnostic are discussed in Sec. 3.3 as they were either upgraded or newly installed as part of the work performed for this thesis. These components include changes to the optical system including the use of cylindrical lenses for improved signal-to-noise ratio, the rotating mask system, the VGAF filter and amplifier circuits, the new fiber optic link system for data transmission, and the high frequency digitizers.

3.2   DIII–D Parameters and Turbulence Regime

DIII–D is a medium-size ($R = 1.66$ m, $a = 0.67$ m) diverted tokamak with a carbon first wall. Auxiliary heating is provided by neutral beams ($P_{\text{inj}} < 16$ MW), ICRF ($P_{\text{source}} < 6$ MW), and ECH ($P_{\text{source}} < 4$ MW) [3]. Typical ranges for plasma parameters are $B_0 = 1.5 - 2$ T, $I_p = 1 - 2$ MA, $\bar{n}_e = 1 - 5 \times 10^{19}$ m^{-3}, $T_{i0} = 2 - 10$ keV, and $T_{e0} = 1 - 4$ keV.

To estimate the regime of high-k ETG modes on DIII–D we take $T_e = 1$ keV, $L_n = L_{T_e} = a = 0.67$ m, $B_0 = 1.5$ T. Thus $v_{te} = 1.3 \times 10^7$ m/s and $\rho_e = 0.05$ mm. The strongest ETG growth is expected near $k_\perp \rho_e \sim 0.2$, which corresponds to roughly $k_\perp \sim 40$ cm^{-1} at $T_e = 1$ keV, though the parameters vary widely between different plasma discharges. Modeling predicts a frequency for ETG modes of $f \simeq 0.2(k_\perp \rho_e)v_{te}/(2\pi L_T)$ [13]. This is about 100 kHz near the peak growth, again assuming $L_T = a$. However, given that the high k spectrum peaks near the edge, L_T may be $0.1a$ or less, and the frequency would be 1 MHz even without Doppler shift.

3.3   High-k Upgrade

As described in Sec. 3.1.1, the PCI was originally used to study low-k (0.3 - 8 cm^{-1}) phenomena. During 2004-2006, the DIII–D PCI underwent hardware upgrades and a re-vamping to extend its functional regime to high-k fluctuations with wave-number to 40 cm^{-1}, and frequency to 10 MHz. This upgrade also included the installation of a rotating mask system that measures fluctuations as a function of propagation angle about the PCI viewing chord. As previously described in Sec. 2.2.2, this rotating mask system allows for localization of near perpendicularly propagating ($k_{||} \sim 0$) modes along the viewing chord. This localization technique improves with increasing wave-number. However, empirical data shows that PCI turbulence amplitude spectra falls as $1/k$ and therefore it is necessary that the diagnostic have adequate signal-to-noise for the full time dependent analysis to improve resolution beyond that defined by Eq. 2.43. Although the PCI technique is inherently very sensitive (it is used to measure density perturbations from RF waves on Alcator C–Mod [57]), electron-scale fluctuations appear to be one to two orders of magnitude smaller in amplitude than the ion-scale counterparts [58]. The DIII–D PCI has therefore received hardware upgrades over the past two years to improve the system signal-to-noise ratio. The following sections describe the hardware upgrades made over the 2004-2006 period.

3.3.1 Optical Considerations

Constraints on the Imaging System

To bring the DIII–D PCI into the short wavelength turbulence regime, several changes to the imaging system are required. The goal of the PCI upgrade was to extend the maximum wave-number range from 8 cm^{-1} to 40 cm^{-1} (roughly a factor of 5); therefore the imaging system must be refined to account for 3 effects:

1. The scattering angle is given by Eq. 2.16 and therefore increases as the turbulence wave-number increases. Keeping the imaging system the same, larger scattering angles require larger diameter lenses, windows and other optical components to ensure the scattered beams are not clipped.

2. It will be shown in Sec. 3.4.1 that the effective spacing of the detector elements in the plasma and thus the Nyquist maximum wave number is set by the system magnification. Therefore, the magnification of the imaging system must increase proportionally to the increase in wave-number to resolve the high-k modes.

3. The PCI response given by Eq. 2.35 shows that a defocused optical system reduces the signal intensity through the term $\cos(\zeta + \delta)$ (recall that $\zeta \propto k^2$). Thus, measuring high-k increases the system susceptibility to defocusing and therefore requires tighter tolerances on the placement of optical components to insure that the object plane occurs at the center of the plasma.

These three factors must be considered when designing the imaging system needed to extend PCI operation to a high-k regime.

Laser Beam Parallelism

As described in Appendix A, the definitions of the *image plane* and the *conjugate plane* are given by geometric optics. If we consider the object plane to be the center of the plasma-chord intersection, then the phase plate is placed in a corresponding conjugate plane. Recall from Sec. 2.2.1 that the resolution of measurements as a

function of propagation angle are optimized when the laser waist occurs at the conjugate/phase plate plane. The criterion for the laser waist to coincide with the phase plate (conjugate plane) is that there be a waist at the front of the first lens in the optical system, *i.e.* that the beam be parallel as it impinges the first lens (in the case of the DIII–D PCI, this would be the return parabolic mirror). Since the PCI beam is very large when inside the vessel, it is sufficient to determine that the PCI laser is not expanding as it travels through the machine. This places constraints on the beam generation optics such that the beam expansion and collimation be precise. Figure 3-6 shows a plot of two gaussian beams propagating through the DIII–D PCI optics; the blue beam is parallel at the object plane, while the green beam is expanding at an angle of $\theta \sim 0.02°$.
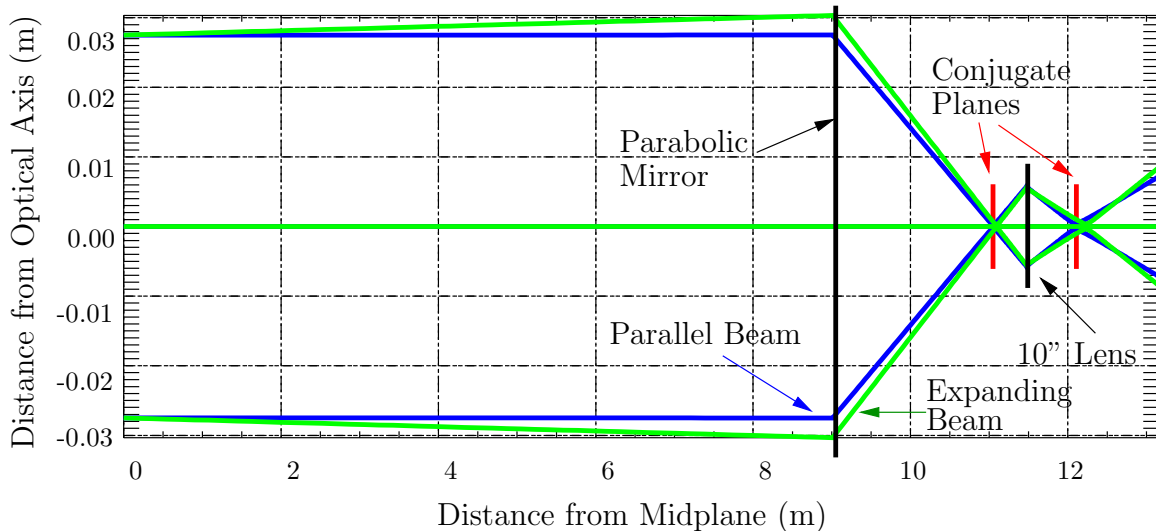
Figure 3-6: Diverging Beam at Object plane $\theta \sim 0.02°$

Figure 3-7 zooms in on the laser waist locations relative to the conjugate planes after the beam is focused by the return parabolic mirror. The non-expanding beam has its waists coincide with the conjugate planes (denoted by vertical red lines), however the expanding beam's waists are progressively further from the these locations as the beams propagate through each lens. Recall from Eq. 2.43 that the resolution of propagation angle measurements decrease with a larger spot size of the focused laser. For even such a small beam expansion angle of $\theta \sim 0.02°$, the resolution of any scattered component decreases by a factor of ~ 3. Such a degradation in performance

would render the propagation angle measurement using a rotating mask ineffective.
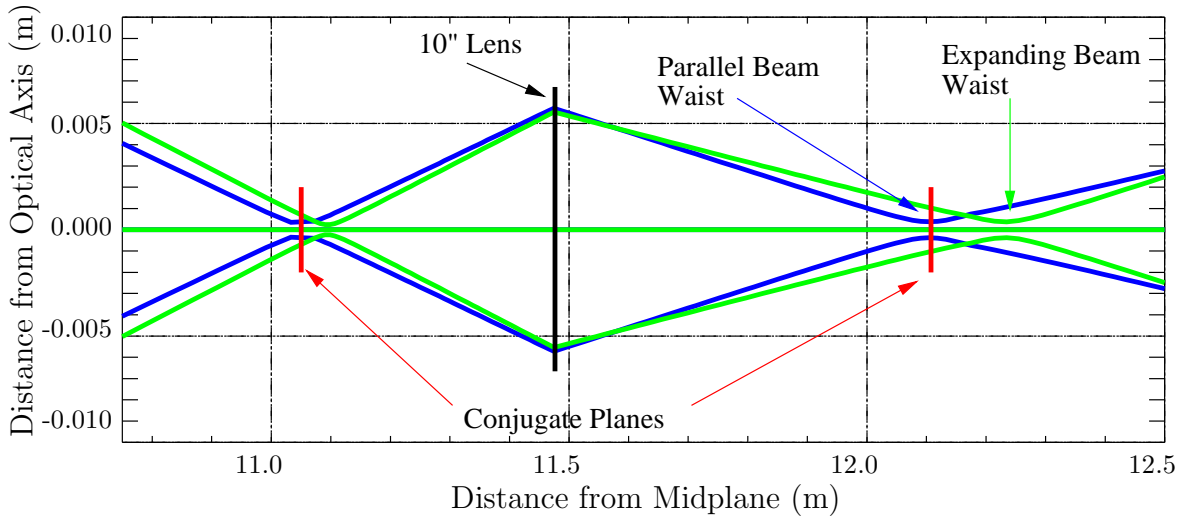
Figure 3-7: Error offsets between phase plate and waist location

The above consideration stresses the need for a high precision technique to ensure that the laser is parallel and collimated inside the vessel. After experimenting with new methods to measure the laser diameter when expanded to 2" (at low intensity) using temperature sensitive liquid crystal paper, a method was developed to measure the beam expansion based on the symmetry of the imaging system about the two parabolic mirrors. Because the parabolic mirrors focus off-axis, they are cut from the same reflector. This implies that they should have identical focal lengths. Thus, if the laser is properly collimated inside the vessel, the waists on either side of the parabolic mirrors should be equal in distance to their respective parabolic mirror. Using an old phase plate and a micrometer stage, we are able to measure the waist location to an accuracy of 0.5 cm. This gives a tolerance of the expansion of the beam inside the vessel less than $0.0015°$. The mask placement in the PCI optical system is dicussed in detail in Sec. 3.5.1.

3.3.2 Rotating Mask Hardware

Section 2.2 introduced the concept of using a rotating slit to mask only scattered beams from fluctuations propagating at a specific angle (the mask angle γ). The

rotating mask assembly, shown in Fig. 3-8, was designed and fabricated by Newmark Systems of Mission Viejo, CA and is mounted on a 2 inch inner bore high speed bearing driven by a motor at speeds up to 3000 RPM. This results in up to 100 scans along the chord per second, and the speed can be changed between shots from the DIII–D control room. Generally, the mask is spun at roughly 5-20 scans per second to assure a long enough time record to perform spectral analysis. The thin mask slit is cut into a removable plate which mounts to the rotation stage. This allows for slits of differing widths (currently 0.5, 1.0, 2.0 mm) that provide flexibility in system magnification, beam size in the plasma, and mask placement.
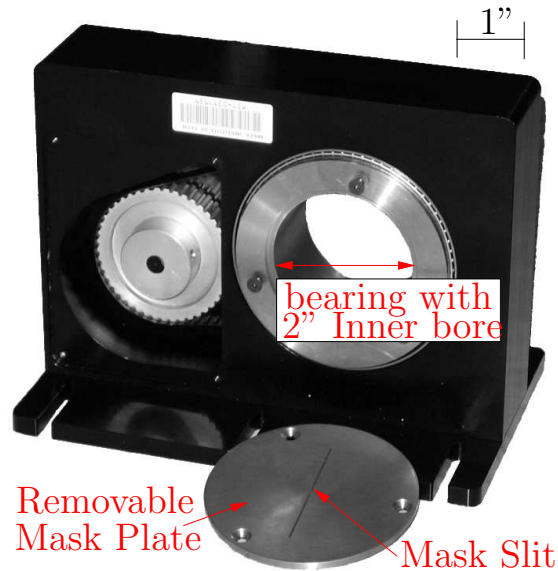
Figure 3-8: Rotating mask hardware assembly (removed from optics table for clarity). Removable mask plate has also been removed for clarity. The thin mask slit is cut into a removable plate so that the system can accommodate slits of different thicknesses.

3.3.3   Signal to Noise

Cylindrical Lenses

To improve DIII–D PCI signal-to-noise ratio, cylindrical lenses are used in the imaging system to compress the beam along the axis perpendicular to the detector array,

increasing signal intensity by a factor of 2 to 5 without affecting the imaging properties. This signal enhancing optical setup requires dual cylindrical lenses to break the imaging into independent orthogonal systems parallel and perpendicular to the detector array. Both axes must have image planes coincident with the detector array. This setup can be configured with a cylindrical lens focusing along each axis, or with both cylindrical lenses focusing along the same axis.

By using the configuration with both lenses focusing along the same axis, the lenses may be removed without the need to re-adjust the rest of the system optics to return to a traditional imaging configuration. This is highly desirable, and is therefore the configuration of choice. In this configuration, the PCI imaging system is determined to satisfy the traditional constraints as well as those constraints discussed in Sec. 3.3.1. Once the imaging system is determined in the absence of the cylindrical lenses, the $ABCD$ parameters discussed in Appendix A are known after the last focusing lens. With this information, the cylindrical lens position (z_1, z_2) can be determined given the focal lengths of the two cylindrical lenses (f_1, f_2) and the cylindrical gain factor g_c. The cylindrical gain factor is the measure of the magnification along the detector axis divided by the magnification along the axis perpendicular to the detector array.

Denote the $ABCD$ parameters after the last lens along the detector axis as $A_p B_p C_p D_p$ and the parameters after the last cylindrical lens along the axis perpendicular to the detector array as $A_c B_c C_c D_c$. Recalling the definition $z_{\text{image}} = -B^i/D^i$, the requirement that image planes must coincide along both axes can be written

$$-\frac{B_p}{D_p} = z_1 + z_2 - \frac{B_c}{D_c}. \tag{3.1}$$

The second constraint comes from the magnification given by $M = 1/D^i$ and the definition of the cylindrical gain factor, that is $D_c = g_c D_p$. The parameters B_c, D_c can be expressed in terms of $(z_1, z_2, f_1, f_2, B_p, D_p)$ leaving 2 equations for the 2 unknowns (z_1, z_2). Both constraints can be expressed as an equation in the form $(I_0 + I_1 z_1 + I_2 z_2 + I_3 z_1 z_2) = 0$, and solved simultaneously for the lens locations.

Low Noise Amplifier/Filter Circuits

The DIII–D PCI suffers from noise introduced by vibrations of the in-vessel mirrors. This vibrational noise is generally low frequency ($f \lesssim 10$ kHz) but is large in amplitude compared to the fluctuation signal. Avoidance of clipping the vibrational noise signal resulted in the fluctuation signal using only a small portion of the system dynamic range. To avoid this problem, a new set of low noise amplifiers and high-pass filters were developed using modern components and fabrication techniques. The filters are selectable with high-pass cutoffs at either 10 or 100 kHz, while the gain has a fixed gain of 10 (to achieve the lowest noise possible), followed by selection of 4 gain stages to activate. The additional stages have gains of (25, 10, 4, 2) and can be activated in any combination thereof. The circuit design, component selection, contracting for PCB layout and fabrication, and housing design were all performed as part of the work for this thesis. These Variable Gain and Filter (VGAF) circuits are built with two channels per board, and are housed in a 12 slot, 3U, VME backplane. The equivalent input noise of each channel is measured to be less than 2 nV$/\sqrt{\text{Hz}}$, which is very close to the thermal limit of a 50 Ω resistor - such performance requires surface mount technology, and express care in circuit design, PCB layout and trace selection. The full 12 slot housing is shown in Fig. 3-9 a) while an individual board is shown in Fig. 3-9 b). The VGAF circuits are generally used with a high pass cutoff of 10 kHz and a total gain of 1000.

Fiber Optic Links

The DIII–D PCI data transmission system sends the fluctuation signal from each of the 16 detector channels from the optics table in machine hall to the digitizers in the annex, located roughly 50 meters away. The previous system mixed the data signals onto an RF carrier and sent them to the annex via long runs of coax. This system had a usable dynamic range of 37 dB or roughly 6 bits.

This system was upgraded using fiber optic links model 732T/R designed by Analog Modules of Longwood, FL. These links increase dynamic range to 59 dB or
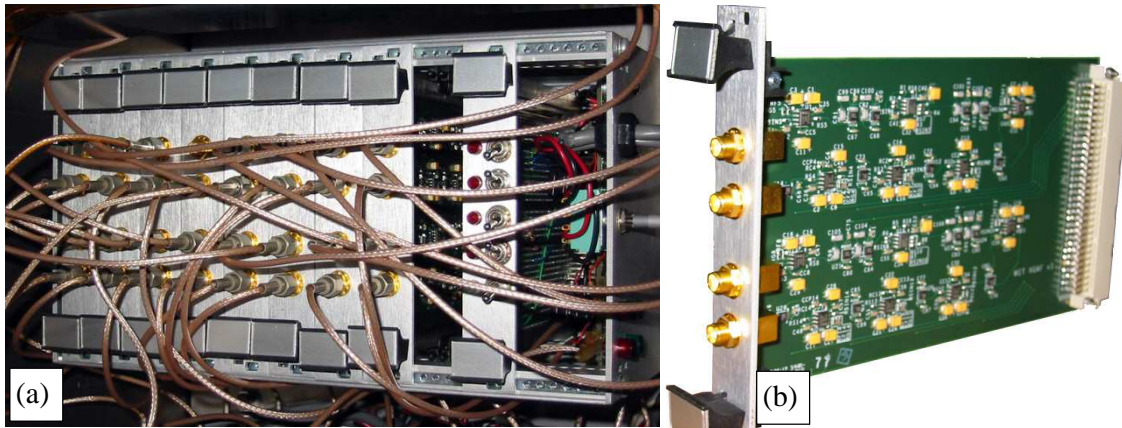
Figure 3-9: Variable Gain and Filter (VGAF) circuits are used to filter the low frequency noise induced into the PCI system by vibrations of the in-vessel mirrors. The right-most board in a) is used to control the gain and frequency cutoff.

almost 10 bits over a bandwidth of 10 MHz. The system-wide noise floor is now at the thermal limit of the HgMnTe detectors.

Figure 3-10: Top Shelf of the Fiber Optic Link Transmitters

3.3.4   High Frequency Digitizers

An important part of the upgrade was to extend the frequency response of the PCI diagnostic. This was achieved through the introduction of the VGAF amplifiers, the

Fiber Optic Links, and a high speed digitizer system model Dt-216 built by D-tAcq Solutions of Scotland, UK. The digitizer uses multiple 16 channel CPCI boards capable of 20 MSamples/s at 16 channels or 40 MS/s at 8 channels. Each channel has a differential input with a selectable range up to ±10 V. The data records are limited to roughly 24 MSamples at 16 channels or 48 MSamples at 8 channels. Utilizing 2 boards, the PCI generally collects roughly a 6 second time record with a Nyquist frequency limit of $f_{max} = 4$ MHz. This allows the DIII–D PCI to digitize an entire shot, however data records are then generally a cumbersome $1-1.5$ GB/shot. Digitizer programming/setup and data storage is managed by the MDSplus software and drivers written at MIT. Data storage capacity, disk I/O performance, and computational resources must all increase as a result.
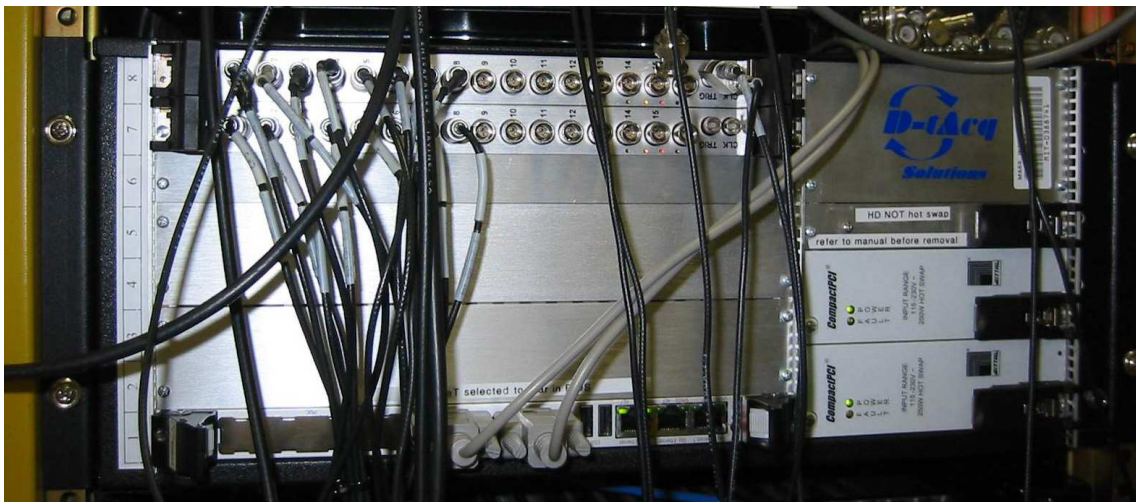
Figure 3-11: High frequency digitizers from D-tAcq Solutions showing two CPCI digitizer boards, each in an 8 channel configuration

3.3.5 Suggested and Future Upgrades

Measurements of the HgMnTe detector element I-V curves suggest that the detector elements do not respond to bias voltage as one would expect. The measured responsivity (see Sec. 3.4.2) suggests detector element resistances of 20-80 ohms, which is significantly lower than the manufacturer specification of roughly 250-350 ohms. This suggests that the performance of the detector elements has degraded over time, likely

due to high energy neutron bombardment. These measurements were performed with the use of a DC-coupled test amplifier from Perry Amplifier of Brookline, MA, and reveal that the detector $D^\star$ is roughly and order of magnitude lower than the original specification shown in Table 3.1. Additionally, channels 2,5,8,11 perform in a highly degraded or inoperable capacity. Therefore, a new HgCdTe (HCT) PV detector array would not only result in 16 fully operation channels, but would lower the system noise floor by up to factor 10. Due to changes in the market, PV HCT detector arrays are not available at a resonable price. HCT detector arrays operating in a photo-conductive (PC) mode are available, however, they suffer from reduced responsivity at high frequency (3 dB/octave roll-off starting around 500 kHz).

The PCI chord was in the Phase I geometry for the collection of all data used in this thesis and is shown in Fig. 3-1. However, an upgrade was performed in 2009 that moved the chord into the Phase II geometry using the R-2 port, shown by the dashed line in Fig. 3-1. This has given the PCI access to $r/a \sim 0.4$ and thus the foot of the internal transport barrier (ITB). It has been suggested by recent theoretical work [59] that to observe pure ETG modes one should look in the shear stabilized ITG regimes, such as in ITBs where the nonlinearly up-shifted ITG cascade modes would be stabilized by the strong E_r shear.

3.4   Absolute Calibration

Turbulence studies have matured greatly over the past 10-15 years as rigorous simulations have become computationally tractable to solve. In particular, the plethora of gyrokinetic simulations demonstrates just how much simulations have come to dominate the landscape of turbulence theory [13, 59–62]. Therefore, it has become important to be able to verify simulation results and validate them against experimental results. One of the basic quantities for comparison is the turbulence amplitude ($\tilde{n}/n_0$) as predicted by gyrokinetics and that observed in experiments. To use the DIII–D PCI for such a comparison, it must be calibrated absolutely using a well-defined test signal. The following sections extend the PCI response analysis beyond that of

Eq. 2.35 into a form suitable for absolute calibration, and detail the measurements of calibration using ultrasonic waves launched in air.

3.4.1 Theory

The PCI response as computed in Eq. 2.35 neglects a number of important features. These include the gaussian envelope of the beam profile, different magnifications along each axis due to the use of cylindrical focusing mirrors (as described in Sec. 3.3.3), the reflection coefficient of the unscattered beam at the phase plate from the uncoated ZnSe, and the overall optical efficiency of the system as a whole. Computing these effects are necessary for absolute calibration.

The DIII–D PCI detector array is AC coupled, and therefore only measures the fluctuating part of the signal. By including the additional physics described above, the fluctuating part of Eq. 2.35 can be written as

$$\tilde{I}_{\text{img}}^{PCI}(\vec{x}, t) = I_{\text{d}} e^{-\frac{x^2 + g_c^2 y^2}{M^2 w^2/2}} \cos\left(\frac{kx}{M}\cos\alpha + \frac{kg_c y}{M}\sin\alpha - \omega t\right) \cos\left(\frac{k^2}{2M^2 k_0}z + \delta\right) \quad (3.2)$$

$$I_{\text{d}} = \left(\frac{\tilde{n}}{n_0}\frac{k_0 L \overline{\omega}_{pe}^2}{\omega_0^2}\right)\left(\frac{2g_c}{\pi M^2 w^2}\right)\left(\eta_{\text{opt}} P_0 \sqrt{\mathcal{P}_r}\right), \quad (3.3)$$

where the x-axis is along the detector array, the y-axis is perpendicular, and the z-axis is the optical axis of the imaging system. The gaussian profile has a $1/e$ electric field radius of Mw or a $1/e$ intensity radius of Mw$/\sqrt{2}$, where as before M is the system magnification and w is the size of the beam in the plasma. The cylindrical lenses decrease the size of the beam in the direction perpendicular to the detector axis by the cylindrical gain factor, $g_c \geq 1$. If the beam is decreased in size along the y-axis to one-fourth of the original size then $g_c = 4$, if there are no cylindrical lenses in use, $g_c = 1$. The intensity at the detector array I_{d} is made up of three parts, the first parenthesis is the coupling factor (recognized as $2a$) between the turbulence mode and the incident beam, and scales proportional to the amplitude of the density fluctuation in the plasma. The second parenthesis is the normalization of the gaussian profile of the beam at the detector image plane. The third parenthesis is the laser power in

the fluctuating part of the laser intensity where $\mathcal{P}_r$ is the reflection coefficient of the unscattered beam off the uncoated ZnSe of the phase plate groove, η_{opt} is the optical efficiency of all mirrors, windows, and lenses in the imaging system, and P_0 is the laser power.

Equation 3.2 gives the PCI response including the effects described above necessary for absolute calibration. To compute the effect of the detection, amplification, and digitization of the signal, we must take into account the finite size of the detector elements, the detector channel responsivity (DIII–D detector channel responsivity is non-uniform), and the amplification and the digitization. To proceed, we assume that the DIII–D PCI system is properly aligned so that the optical axis (center of the gaussian envelope) is aligned with the center of the detector array.

The detection effects are computed by integrating Eq. 3.2 over a detector element centered at $x = \xi$. The detector elements are considered to have dimensions $2\epsilon_x \times 2\epsilon_y$, this allows for elliptical or rectangular detector elements or, in the case that $\epsilon_x = \epsilon_y$, circular or square detector elements (the Alcator C-Mod PCI diagnostic uses rectangular detector elements while the DIII–D PCI uses circular elements). Making the substitution $u = (x-\xi)/\epsilon_e$, $v = y/\epsilon_y$, the signal power to a single detector element can be written as

$$
\begin{aligned}
P(\xi) =& I_{\mathrm{d}}\epsilon_x\epsilon_y \cos(\zeta + \delta) \int_{-1}^{1} du \ e^{-\left(\frac{\epsilon_x}{r}\right)^2 (u + \frac{\xi}{\epsilon_x})^2} \\
& \times \int_{-\bar{u}}^{\bar{u}} dv \ e^{-\left(\frac{g_c \epsilon_y}{r}\right)^2 v^2} \cos(k_x\xi - \omega t + k_x\epsilon_x u + k_y\epsilon_y g_c v),
\end{aligned}
\tag{3.4}
$$

where $r = Mw/\sqrt{2}$ is the $1/e$ radius of the intensity profile at the detector, $k_x = k\cos\alpha/M$ and $k_y = k\sin\alpha/M$ are the components of the detected wave-vector parallel and perpendicular to the detector array, and ζ, δ are defined in Sec. 2.1.3. The style of detector (*e.g.* circular/elliptical vs. square/rectangular elements) depends on the limits of the dv integral, specifically, the value of $\bar{u}$. For circular or elliptical detector elements, $\bar{u} = \sqrt{1 - u^2}$), while for square or rectangular detector elements, $\bar{u} = 1$. The detector element half width $\epsilon_{x,y}$ is small compared to the beam radius r - this can be seen by considering $r \sim 2\xi_{\mathrm{max}}$. In this case, $\epsilon_x/r = \rho/2N_{\mathrm{ch}} \ll 1$, where

$N_{\rm ch}$ is the number of detector channels and $\rho = 2\epsilon_x/\Delta_x$ is the fraction of detector space used by the element (*i.e.* the detector element width divided by the channel to channel spacing). The cylindrical gain is generally less than a maximum value $g_c \lesssim 10$ for reasons that will be shown after the detector response is computed. In general, $\epsilon_x \sim \epsilon_y$, the exponentials can be expanded in terms of the small arguments. Keeping terms to $\mathcal{O}(\epsilon_x/r)$ and $\mathcal{O}((\epsilon_y g_c/r)^2)$, Eq. 3.4 can be written

$$P(\xi) = I_{\rm d} A_e \cos(\zeta + \delta) \ e^{-\left(\frac{\xi}{r}\right)^2} \left[\mathcal{D}_c \cos(k_x \xi - \omega t) - \mathcal{D}_s \frac{2\xi}{r} \sin(k_x \xi - \omega t) \right] \quad (3.5)$$

$$\mathcal{D}_c = \frac{\epsilon_x \epsilon_y}{A_e} \int_{-1}^{1} du \ \cos(k_x \epsilon_x u) \int_{-\bar{u}}^{\bar{u}} dv \ \left[1 - \left(\frac{\epsilon_y g_c}{r}\right)^2 v^2 \right] \cos(k_y \epsilon_y g_c v) \quad (3.6)$$

$$\mathcal{D}_s = \frac{\epsilon_x \epsilon_y}{A_e} \int_{-1}^{1} du \ \frac{\epsilon_x}{r} u \sin(k_x \epsilon_x u) \int_{-\bar{u}}^{\bar{u}} dv \ \left[1 - \left(\frac{\epsilon_y g_c}{r}\right)^2 v^2 \right] \cos(k_y \epsilon_y g_c v). \quad (3.7)$$

The coefficient $\mathcal{D}_s$ in Eq. 3.5 causes distortion of the detected wave by the factor $\xi \sin(k_x \xi - \omega t)$, which results in spreading in the wave-number spectra. This effect is generally negligible as it scales like the detector radius divided by the beam radius, for the DIII–D PCI in the high-k configuration $\epsilon_x/r = 2\%$. However, when diagnosing low-k turbulence, this effect can be of importance. In the high-k configuration, the term proportional to $(\epsilon_y g_c/r)^2$ is also negligible and the above integral can be performed explicitly for rectangular elements. The resulting PCI response is

$$P_{\rm rect}(\xi) = I_{\rm d} A_e \cos(\zeta + \delta) \cos(k_x \xi - \omega t) e^{-\left(\frac{\xi}{r}\right)^2} \frac{\sin(k_x \epsilon_x)}{k_x \epsilon_x} \frac{\sin(k_y g_c \epsilon_y)}{k_y g_c \epsilon_y}. \quad (3.8)$$

We can now justify that there is a maximum value for the cylindrical gain factor. The term $\sin(k_y g_c \epsilon_y)/k_y g_c \epsilon_y$ will reduce the signal by roughly a factor of 2 when its argument is equal to $\pi/2$. The maximum resolvable wave-number (the Nyquist wave-number) of the system is $k_{\rm max} \sim \pi \rho M/2\epsilon_x$. Using this wave-number and assuming $\epsilon_x \simeq \epsilon_y$, we get $g_{c,{\rm max}} \simeq 1/(\rho \sin\alpha)$. Using a cylindrical gain factor much larger than this will result in a reduction of signal intensity as the term $\sin(k_y g_c \epsilon_y)/k_y g_c \epsilon_y$ nears its 1st zero.

The response of finite sized detector elements is plotted in Fig. 3-12 assuming

that $\mathcal{D}_s = 0$ and that the imaging system is similar to that used in the DIII–D PCI high magnification configuration. In this configuration, $k_{\max} = 30$ cm^{-1}, and $\epsilon_x/r = 2\%$. The left plot shows the detector response vs. propagation angle (α)
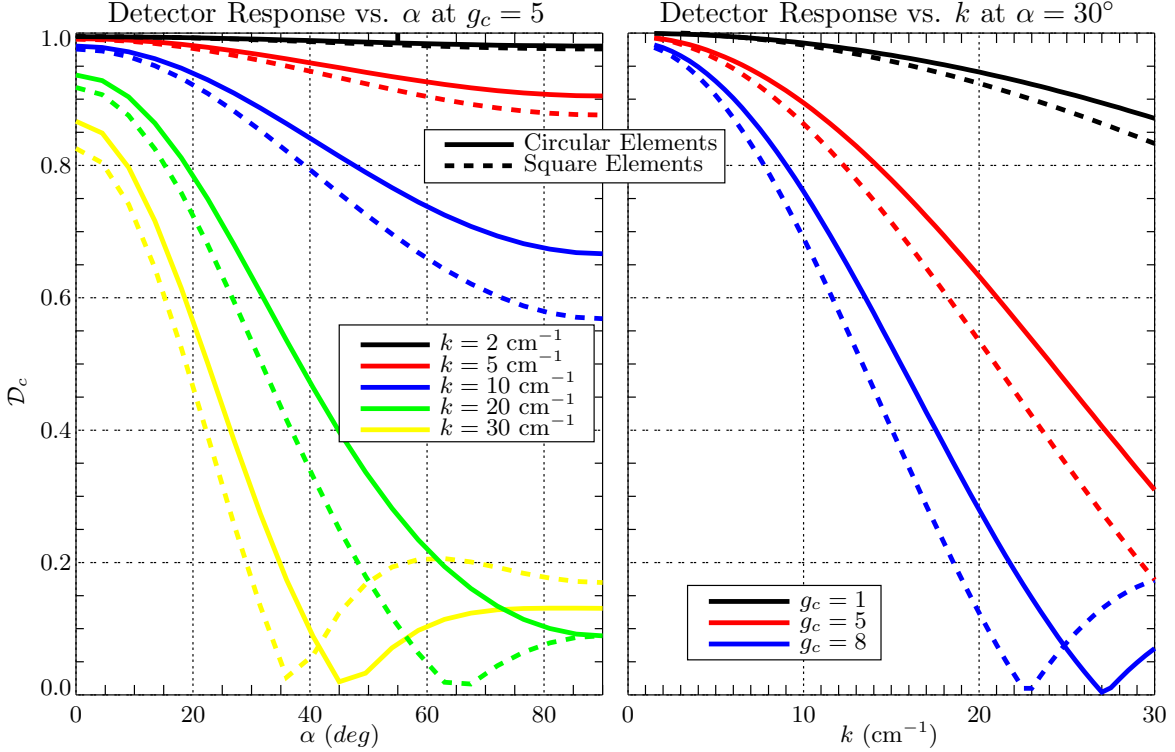
Figure 3-12: Left plot) Finite sized detection elements reduced the system response with increased propagation angle. The effect is more detrimental at higher wave-number. Right plot) The system response decreased with increased wave-number. The effect is more detrimental at higher cylindrical lens gain.

at a cylindrical lens gain factor of $g_c = 5$. We can see that at the maximum wave-number (yellow), the 1$^{\text{st}}$ zero in the response occurs at smaller propagation angle for the square detector elements (dashed lines) than for the circular detector elements (solid lines). The right plot shows the detector response vs. wave-number at a fixed propagation angle ($\alpha = 30°$). The effect of increased cylindrical lens gain increases the rate at which the response falls off with wave-number. Data analyzed for use in this thesis was collected with a maximum cylindrical gain $g_c = 5$ and propagation angle measurements are concerned with $|\alpha| \lesssim 20°$. Under these conditions, the effect of finite sized detector elements reduces the measured amplitude by a maximum of 30% as the measured wave-number is $|k| \lesssim 25$ cm^{-1}.

For all imaging configurations used to collect PCI data in this thesis, throwing out the terms proportional to (ϵ/r) is justified. Therefore, the PCI response for a given detector channel at the digitizer can be written as

$$V(\xi, t) = G\mathcal{R}(\xi)I_d A_e \mathcal{D}_c(k, g_c, \alpha) \cos(\zeta + \delta) \cos\left(\frac{k\cos\alpha}{M}\xi - \omega t\right) e^{-\left(\frac{\xi}{r}\right)^2}, \qquad (3.9)$$

where $\mathcal{R}(\xi)$ is the detector channel responsivity in units of [V/W] (*i.e.* the current produced per watt times the detector channel resistance), and G is the total gain including the gain factor of 20 in the system preamps, the amplification of the variable gain amplifiers, and fiber optic links.

3.4.2 Measurements

The DIII–D PCI uses two calibration systems to launch ultra sonic waves in air at frequencies from 20 kHz to 200 kHz. Under typical calibration conditions, the speed of sound is $C_s = 345$ m/s, and the calibration systems can launch waves with wave-numbers in the range of 3.5 - 35 cm^{-1}. These two systems operate in tandem, and together provide both the system response over a continuous range in frequency (and wave-number), and calibrated pressure waves.

CW Ultrasonic Loudspeaker

The first calibration system uses an ultrasonic loudspeaker manufactured by Ultra Sound Advice, Wimbledon UK, model S55/6. Originally developed for bat research, this loudspeaker is a variable frequency, CW device with a 5 cm diameter membrane, a frequency range from 15 kHz to better than 150 kHz, and a power output $85 < P < 105$ dB SPL or $0.5 < P < 5$ Pa peak amplitude. It is used for qualitative measurements as the power output is not guaranteed to be stable. It is highly valuable to use while sweeping the frequency to measure the system wave-number response. The PCI response to the CW loudspeaker is shown in Fig. 3-13, where the output frequency was ramped in time. Figure 3-13 a) shows the frequency chirp as a streaked line of high intensity in the power spectra. We can see the signal drop in power at
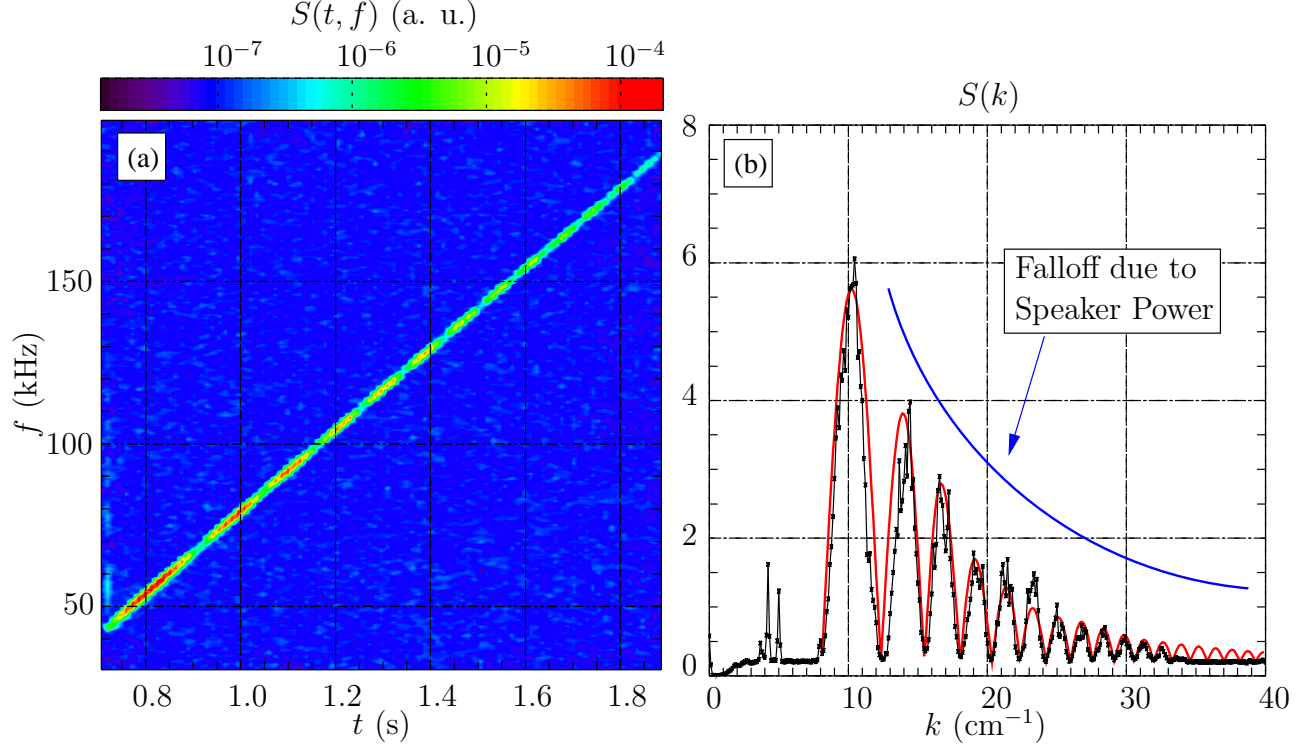
Figure 3-13: a) Chirped CW loudspeaker spectra as a function of time and frequency. The nulls are due to defocusing effects while the overall amplitude falloff is due to the non-uniform power output of the loudspeaker itself. b) Spectra $S(k)$ integrated over time, and the fit of the defocusing term.

regular intervals as the frequency is increased, this is due to the out-of-focus launch location used for the ultrasonic calibration signal. Integrating over time, we resolve the spectral response $S(f; \xi)$ or equivalently $S(k; \xi)$ of the PCI shown in Fig. 3-13 b). This data was collected by placing the CW loudspeaker outside the vacuum chamber, and therefore the speaker is not located an the appropiate object plane (or equivalently, the detectors are not located at an image of the CW loudspeaker). This causes zeros in the response due to the $\cos(\zeta + \delta)$ term in Eq. 3.2. By measuring the wave-number at which the zeros occur we can determine the values of $\zeta(k)$ and δ by fitting the data to

$$\frac{z}{2M^2 k_0} k^2 + \delta = n\pi + \frac{\pi}{2}, \tag{3.10}$$

where n is an increasing integer corresponding to the zeros. The fit is plotted in red in Fig. 3-13 b). Computing the value of δ for 9 test shots with the CW loudspeaker at

a variety of locations we get $\delta = -0.94 \pm 0.10$. This indicates that the groove depth of the original phase plate is off from the $\lambda/8$ spec reducing the system response to 60% of optimal.

Fixed Frequency Transducers

The second calibration system uses 4 fixed frequency ultrasonic transducers from Airmar Technology Corporation, Milford NH, models AR30, AT75, AT120, and AT200. These transducers are suitable for quantitative measurements as they are fired in 1 ms bursts with a 1% duty cycle to prevent reflected waves from interfering with measurements, and to prevent overheating of the transducer. The 4 transducers are fired sequentially starting at the lowest frequency with 10 ms intervals between transducers. This provides test data at fixed frequency (and thus wave-number) with a sound pressure profile that has been measured using a calibrated microphone [63, 64]. The transducer membrane amplitude is modeled as a sum of 0th Bessel function as

$$P_0(\rho) = \sum_{n=0}^{N} A_n J_0 \left(\frac{\rho}{r_m} r_n \right), \tag{3.11}$$

where r_m is the membrane radius, A_n are the complex coefficients, and r_n depends on the boundary conditions of the pressure field at the membrane edge - r_n is the nth root of the J_0 Bessel function for Dirichlet type boundary conditions ($P_0(r_m) = 0$) or r_n is the nth root of the J_1 Bessel function for Neumann type boundary conditions ($\frac{dP_0}{d\rho}(r_m) = 0$). The scalar diffraction equation [65, 66] is used to relate the pressure field at the transducer membrane surface to the pressure profile a distance (ρ, z) away,

$$P(\rho, z) = \frac{k}{2\pi i} \int_0^{r_m} d\rho' \int_0^{2\pi} d\theta' \frac{e^{ikR}}{R} \left(1 + \frac{i}{kR} \right) \frac{\hat{z}' \cdot \vec{R}}{R} \; P_0(\rho'). \tag{3.12}$$

Here $\hat{z} \cdot \vec{R} = z$, $R = \sqrt{\rho^2 + \rho'^2 - 2\rho\rho' \cos(\theta') + z^2}$, and $k = 2\pi f/C_s$ is the wave-number associated with the transducer frequency. The coefficients A_n in Eq. 3.11 are computed by fitting the modeled pressure field given in Eq. 3.12 to the calibrated
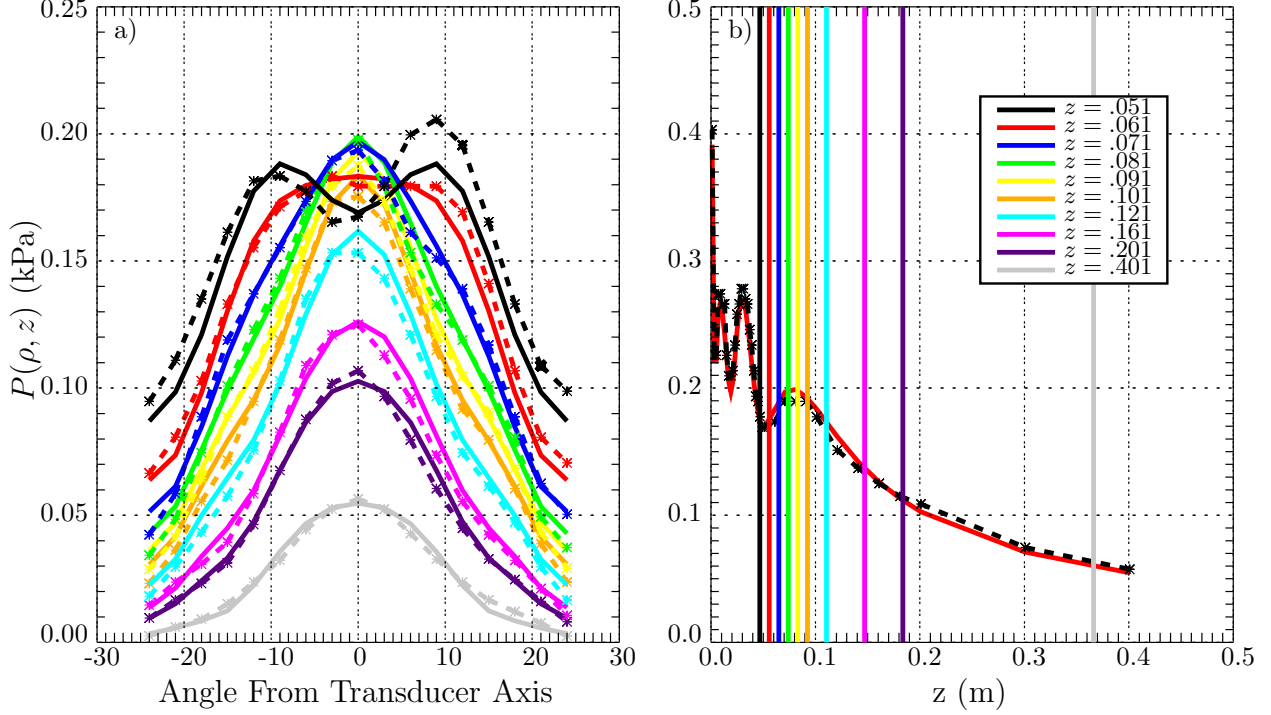
Figure 3-14: Transducer Field amplitude and model.

microphone measurements. Microphone measurements were performed by Nauto Tsujii at MIT along the transducer axis and as a function of angle from the axis $\phi = \tan^{-1}(\rho/z)$ at several locations along the axis. The measurements and fitted model are plotted in Fig. 3-14 showing good agreement. There are significant amplitude fluctuations in the near field that smooth out beyond $z > 9$ cm. Therefore, the transducers should be placed roughly 10 cm from the incident laser.

To use the fixed frequency transducers for absolute calibration of the DIII–D PCI we must compute the phase shift induced by the pressure field of each transducer. In essence, we must compute a (*i.e.* the amplitude of the fluctuation in index of refraction) as defined in Eq. 2.13. The relation from sound pressure to index of refraction is given by the Biot-Arago Formula [67]

$$\tilde{\Phi}(x,z) = \frac{k_0(N_0 - 1)}{\gamma p_0} \int dy \; \tilde{p}(x,y,z), \tag{3.13}$$

where the constants $(N_0 - 1) = 2.72613 \times 10^{-4}$, $p_0 = 1.01325 \times 10^5$ Pa, γ is the specific heat ratio $C_p/C_v = 1.403$, and k_0 is the incident laser wave-number. The coordinates

here are the same as used to describe the transducer sound pressure profile, with the laser beam propagating in the y-direction. Performing this integral for the sound pressure fields produced by the fixed frequency transducers gives the integrated phase shift after the laser passes through the sound wave field. As shown in Fig. 3-15, the
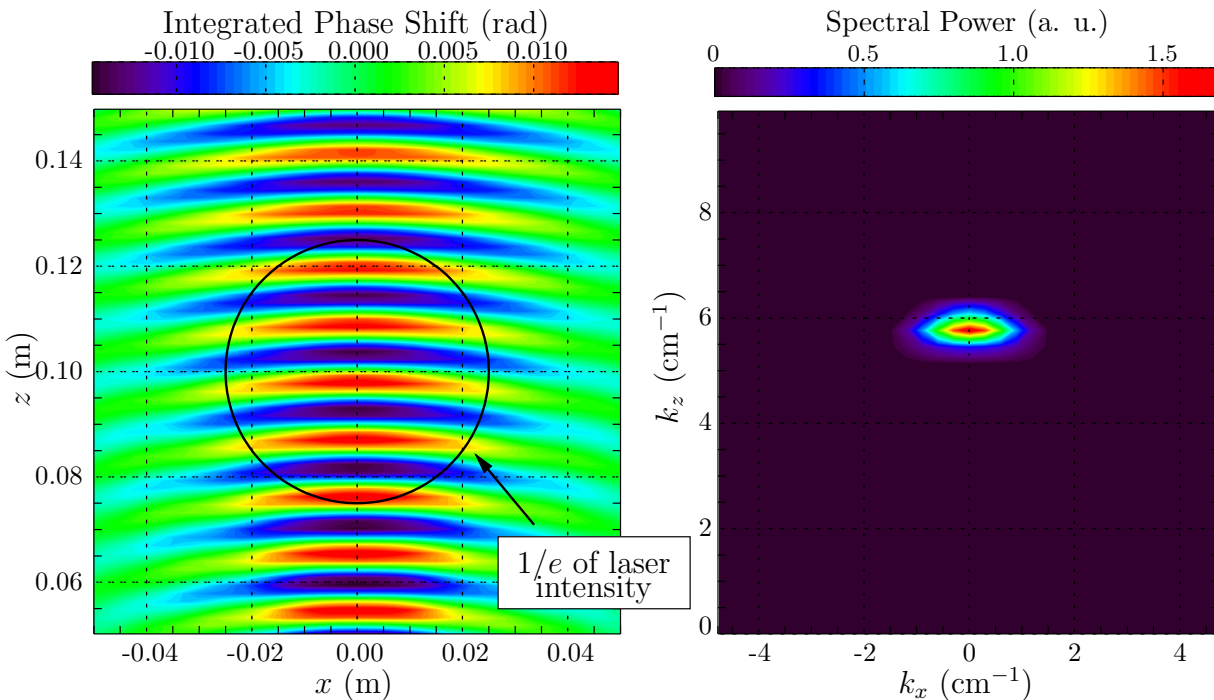
Figure 3-15: Integrated Pressure Profile for the 31.9 kHz Transducer

integrated phase shift is nearly a plane wave over the extent of the incident laser beam. The spectra is narrow in propagation angle $\alpha = \tan^{-1}(k_x/k_z)$, therefore the transducer is to good approximation described by a wave of the kind assumed in Eq. 2.10, ($i.e.$ $\tilde{\Phi} = a_s \cos(kz - \omega t)$). The amplitude of the transducer induced phase shift fluctuation (a in Eq. 2.13) is listed in Table 3.2. The sound wave induced phase

Table 3.2: Amplitude of the integrated phase shift fluctuation

Transducer	$\tilde{\Phi}$ Amplitude (a_s)
AR30	1.57×10^{-5}
AT75	3.20×10^{-5}
AT120	2.00×10^{-5}

shift can be connected to the PCI response equation Eq. 3.9 by writing the detector

intensity I_d in terms of a_s,

$$I_d = (2a_s) \left(\frac{2g_c}{\pi M^2 w^2} \right) \left(\eta_{opt} P_0 \sqrt{\mathcal{P}_r} \right). \tag{3.14}$$

Calibration data was collected with the fixed frequency transducers using an imaging system with magnification $M = 0.64$ in the Phase I beampath, with a beam $1/e$ radius in the vessel of w $= 2.5$ cm. The transducers were placed in the beampath just in front of the entrance window at the R-1 port. Chirped ultrasonic loudspeaker data was collected similar to that shown in Fig. 3-13) to compute the value of the defocusing term $\cos(\zeta + \delta)$ term in Eq. 3.9. The chirped loudspeaker data was collected both with and without the use of cylindrical lenses - together this data was used to estimate the angle of the launched sound wave relative to the detector axis and hence the value of $\mathcal{D}_c$. All data was collected with the same signal conditioning settings for the secondary amplifiers, $G = 20,000$. As given in Sec. 3.1.2, the laser power is measured to be $P_0 \sim 20$ W, and power measurements indicate that the system optical efficiency is $\eta_{opt} \sim 10\%$. The amplitude of the voltage fluctuation in each test condition at each channel is shown in Table 3.3 along with the values of the defocusing term $\cos(\zeta + \delta)$ and the detector response $\mathcal{D}_c$. The estimates of each detector element responsivity shown below assume $\eta_{opt} = 0.1$ and $P_0 = 20$ W, however these parameters are estimates and the actual detector responsivities would scale accordingly.

3.5 Rotating Mask Implementation

3.5.1 Placement in Optical Chain

The technique of using a rotating slit to mask scattered beams and therefore only allow fluctuations propagating at a specific angle to be detected was introduced in Sec. 2.2. In that description, and in particular in Fig. 2-4, the mask is depicted as sitting directly on top of the phase plate. That is, conceptually, the mask is imagined as coincident with the surface of the phase plate. Placing the mask in front of the

Table 3.3: Transducer calibration data collected with and without the cylindrical lenses

Detector Channel #	$V_{\max}(\xi)$ (mV)						Responsivity $\mathcal{R}(\xi)$ [V/W]
	($g_c = 8$)			($g_c = 1$)			
	AR30	**AT75**	**AT120**	**AR30**	**AT75**	**AT120**	
1	310.09	254.04	35.30	55.96	122.86	35.41	351.6 ± 93.5
2	0.94	0.94	0.93	0.93	0.93	0.94	4.3 ± 1.6
3	493.91	528.58	28.68	44.18	117.14	44.64	386.9 ± 83.5
4	472.59	365.57	61.79	71.78	111.49	47.63	382.0 ± 57.1
5	1.71	1.63	1.72	1.62	1.54	1.61	6.9 ± 2.5
6	387.50	175.06	45.71	34.12	36.65	24.10	189.7 ± 20.5
7	391.58	67.42	43.80	29.49	40.34	24.86	174.1 ± 33.1
8	10.26	10.64	10.21	10.02	9.95	10.09	41.0 ± 14.9
9	605.58	397.65	66.10	53.93	66.76	40.81	313.1 ± 25.3
10	734.29	957.10	157.13	34.91	78.75	42.52	450.3 ± 81.3
11	62.49	51.31	13.76	15.23	16.00	13.48	69.4 ± 15.6
12	864.40	1165.39	198.56	62.12	60.29	40.41	540.1 ± 110.4
13	643.61	443.34	123.23	37.89	25.80	28.36	318.5 ± 67.1
14	699.97	667.78	79.87	37.63	38.81	24.02	337.2 ± 62.1
15	171.09	261.55	51.55	18.36	10.99	12.29	146.4 ± 30.5
16	120.18	78.61	18.03	17.98	13.42	11.07	94.3 ± 10.1
Test Parameters							
$\cos(\zeta + \delta)$	0.99	0.51	0.52	0.99	0.51	0.52	
$\mathcal{D}_c$	0.99	0.87	0.23	1.0	0.98	0.79	

phase plate quickly becomes an engineering challenge due its reflective nature and practically, this cannot be realized because the mask must be slightly separated from the phase plate to allow rotation. This small offset would cause the mask to block all radiation because of the narrowness of the slit and the angle of reflection off the phase plate.

Fortunately, after every lens in the PCI optical system there is the chance of having a location that is optically identical to the location of the phase plate itself (*i.e.* locations where a perfectly collimated PCI laser would form a waist). These are all conjugate planes as described in Sec. A.1 and should be the locations of choice for mask placement. In fact, all subsequent conjugate planes can be thought of as image planes where the initial conjugate plane is the object plane. When installed, the mask is located as shown in Fig. 3-16, thus permitting proper operation of the

mask. This placement also provides an arbitrary magnification between the initial conjugate plane (the phase plate location) and the mask plane, allowing the beam focus spot size to be optimized for a given mask slit width.
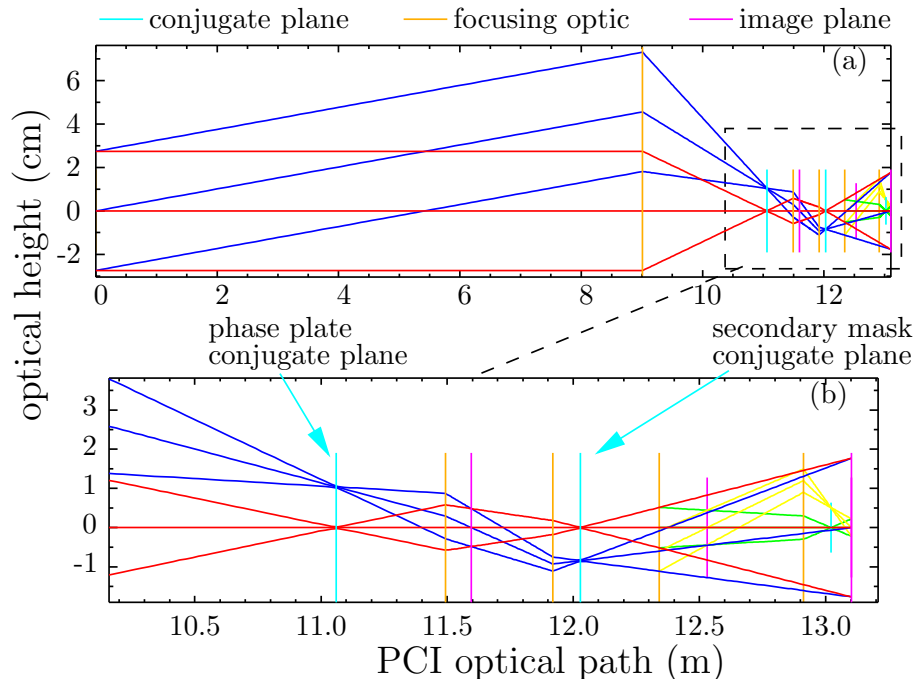
Figure 3-16: PCI optical layout showing unscattered (red) and one $k = 30 \text{ cm}^{-1}$ scattered (blue) beam composed of rays along the center-line of the beam and the $1/e$ electric field radii. (a) Full PCI optical path from plasma (object) to detector (image). (b) Imaging optics showing creation of secondary focal plane for rotating mask placement.

Placing the mask very close to the phase plate may be possible on systems that use a transmissive phase plate [28], but this is probably not practical on a tokamak PCI due to the small range in scattered pitch angle (see Eq. 2.42) and hence tight tolerances.

A similar localization technique is currently in use on the LHD heliotron, which has a poloidal field much larger than that in a tokamak. Rather than a mask, they use a 2-D detector to record the data and then fit the data to estimate $S(z, k)$ [34]. While LHD has a scattering pitch angle full range $\Delta\alpha \sim 80°$, this adaptation can operate in a region of smaller $\Delta\alpha$ using asymmetric magnification (the so-called "zoom" mode technique [34]) making it potentially tractable for a tokamak device. However, the

spatial resolution and wave-number resolution are directly related to the number of detector channels. For a tokamak with much smaller $\Delta\alpha$ (typically 12°), the rotating mask technique has the potential to achieve greater spatial resolution at high wave-numbers with more modest detector and digitizer requirements.

3.5.2 Mask Mapping

To use the rotating mask to localize turbulence as described in Sec. 2.2.2, it is important to recall that the assumption of drift-wave ($k_{||} \sim 0$) turbulence requires fluctuations to propagate perpendicular to the local magnetic field. This assumption produces the mapping from chord height to propagation angle, $\alpha(z)$ in Eq. 2.42. An understanding of the chord mapping is needed to translate between scattered pitch angle and plasma location, to calculate the mapping density $|dz/d\alpha|$, and to represent the PCI measured wave-vector (perpendicular to the chord) in terms of the more physically relevant (k_r, k_θ) components. The mapping from PCI chord height to propagation angle, $\alpha(z)$, depends on the specific magnetic geometry and is not always a monotonic function. Non-monotonic mappings are more pronounced as the PCI chord passes closer to the plasma core.

Figure 3-17a shows PCI chord mappings for two PCI chord locations in a lower single null L-mode plasma with $q_{95} = 5.5$. Here, q_{95} is the tokamak safety factor evaluated at the 95% flux surface. In use, for the collection of calibration and experimental data used in this thesis, is the PCI Phase I geometry, which is restricted to the outer plasma region while the current Phase II geometry reaches closer to the plasma interior (see Fig. 3-17c).

From the mappings shown in Fig. 3-17b, it is clear that the Phase II geometry suffers from non-monotonic mappings near the chord edges. This feature is worse for large q_{95} where the poloidal field becomes relatively weak due to peaked current profiles. However, even at $q_{95} = 5.5$, the mapping in the inner region of the PCI chord $0.4 < r/a < 0.55$ is single valued and the localization technique will be particularly useful in isolating turbulence from the shear regions of the ITB.

In the Phase I geometry, the mapping is generally well behaved for the lower
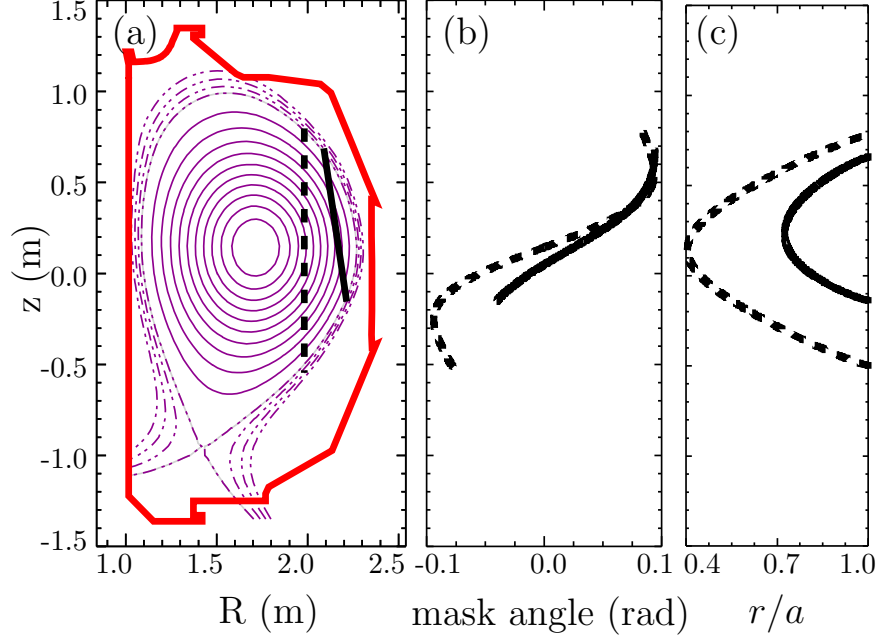
Figure 3-17: PCI chord mapping for both Phase I (solid line) and Phase II (dashed line) geometries during L-mode lower single null (LSN) discharge with $q_{95} = 5.5$. (a) Flux surfaces and chord locations. (b) Mask pitch angle as a function of chord height shows non-monotonic mapping for Phase II geometry but monotonic mapping for Phase I geometry. (c) Chord plasma location shows Phase I geometry $r/a > 0.7$ and Phase II geometry $r/a > 0.4$.

portion of the PCI chord while the upper portion of the chord ($z > 0.3$) can become difficult to resolve and even non-monotonic (see Fig. 3-18a). The best localization will be achieved where the PCI chord is tangent to flux surfaces and thus at the closest approach to the plasma core. As can be seen in Fig. 3-18b, the ability to localize fluctuations is better for lower q_{95}, due to fluctuations being spread over a larger range in scattered pitch angle in the focal plane. Here we define $\Delta\alpha$ as the full range of scattered pitch angle,

$$\Delta\alpha = \alpha_{\mathrm{max}} - \alpha_{\mathrm{min}}. \tag{3.15}$$

In the Phase I geometry, the upper edge of the PCI chord suffers from large chord mapping density per unit mask pitch angle $|dz/d\alpha|$ for many magnetic geometries. This feature is one reason the proper analysis based on Eq. 2.45 is essential to determining the spatial variation in the turbulence from the PCI data. Care is
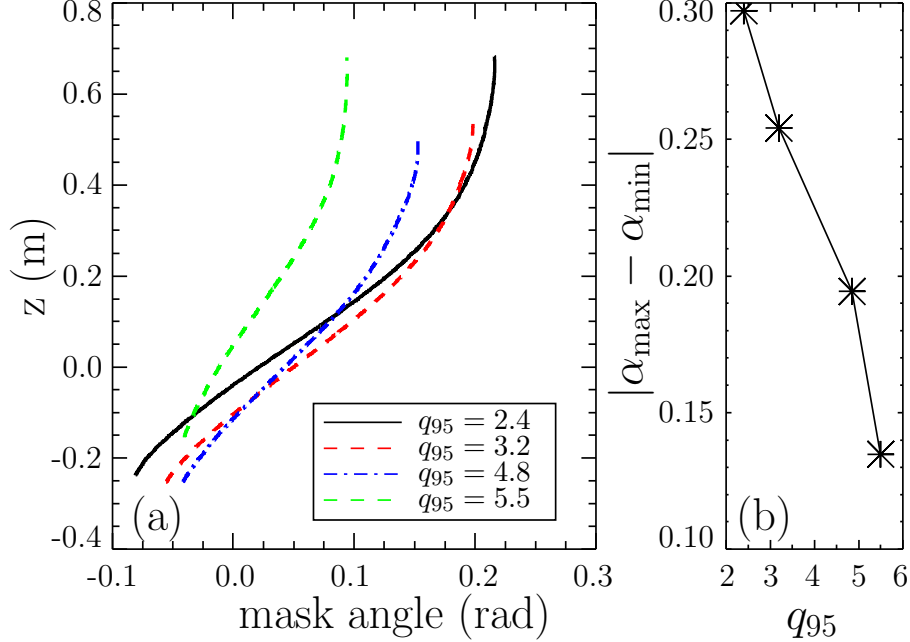
Figure 3-18: (a) PCI chord mapping of Phase I geometry for four different discharge geometries with increasing values of q_{95}. (b) Scaling of pitch angle full range shows better localization for low q_{95}.

thus needed when interpreting localized spectral measurements, as will be discussed further in Sec. 3.5.3.

3.5.3   Mask Calibration

As described in Sec. 2.2.2, the ability to properly interpret localized measurements made by a rotating mask system requires accurate knowledge of the mask response function $\mathcal{M}$ in Eq. 2.45. The mask response function is defined as the system response to a single plane wave mode in the plasma. This response is dependent on the focused beam structure (*e.g.* presence of higher order modes), the mask slit width, and the diffraction of both the scattered and unscattered beams through the mask slit.

The model used for computing $\mathcal{M}$ consists of the following assumptions: gaussian electric field profiles incident on the mask plate for both the scattered and unscattered beams, that the mask acts to zero the electric field where the incident beam profile is blocked by the mask plate, and that the mask plate is infinitely thin and the unblocked portion of the beam is not affected. With this as a starting point, the

electric field profile of the incident scattered beam can be written in the form $E_s = E_s(\mathbf{x}; \mathrm{w}_0, \Delta(k), \alpha(z))$ and the unscattered beam $E_0 = E_0(\mathbf{x}; \mathrm{w}_0)$ where $\Delta(k)$, w_0, and $\alpha(z)$ are previously defined in Eqs. 2.36 and 2.42. We introduce the clipping function $K = K(\mathbf{x}; \gamma, l)$ where γ is the mask plate angle (see Fig. 2-4) and l is the mask slit width. The value of the function K is unity over the region of the mask slit where the beam is not blocked and $K = 0$ where the beam is blocked by the mask plate.

Ignoring diffraction effects, the mask function is then simply the fraction of focused beam power passing through the rotating slit, $\mathcal{M}(\gamma - \alpha; k) = \int d^2x \, E_s^2 K / \int d^2x \, E_s^2$. With these simplistic assumptions, the mask response function can be expressed in terms of the error function $\mathrm{erf}(x) = \frac{2}{\sqrt{\pi}} \int_0^x e^{-t^2} dt$ and is proportional to the fraction of focused beam power passing through the rotating slit of width l

$$
\begin{aligned}
\mathcal{M}(\gamma - \alpha; k) = {} & \frac{1}{2}\mathrm{erf}\left(\frac{\sqrt{2}}{\mathrm{w}_0}\left[\Delta(k)\sin(\gamma - \alpha) + \frac{l}{2}\right]\right) \\
& -\frac{1}{2}\mathrm{erf}\left(\frac{\sqrt{2}}{\mathrm{w}_0}\left[\Delta(k)\sin(\gamma - \alpha) - \frac{l}{2}\right]\right).
\end{aligned}
\tag{3.16}
$$

While useful for understanding scalings with mask slit width and wave-number, ignoring diffraction is insufficient to properly characterize measurements of the mask response function because this effect tends to spread out the beam at the detector plane in the direction perpendicular to the mask slit.

To include diffraction effects, the scattered and unscattered beams are propagated from the mask focal plane to the detector plane using scalar diffraction theory [65]. We define a scalar diffraction operator $\hat{\mathcal{D}}$ as

$$
E_{\mathrm{det}}(\mathbf{x}) = \hat{\mathcal{D}}(E_{\mathrm{mask}}(\mathbf{x}')) = \frac{k}{2\pi i}\int d^2x' \, \frac{e^{ikR}}{R}\left(1 + \frac{i}{kR}\right)\frac{\mathbf{n}' \cdot \mathbf{R}}{R} \, E_{\mathrm{mask}}(\mathbf{x}'), \quad (3.17)
$$

where $\mathbf{x}'$ are coordinates in the mask focal plane, $\mathbf{x}$ are coordinates in the detector plane, $\mathbf{R} = \mathbf{x} - \mathbf{x}'$, $R = |\mathbf{R}|$, $\mathbf{n}'$ points along the beam direction of propagation, and the integral is performed over the mask focal plane. This is the same operator used to propagate the pressure amplitude from the transducer surface to a distance

away, only now written in rectangular coordinates. Thus the total electric field at the detector plane is the interference of the propagated scattered and unscattered beam electric fields $E_{\text{det}}^K = \hat{\mathcal{D}}(E_s K) + \hat{\mathcal{D}}(E_0 K)$. The resulting field in the detector plane has a sinusoidal intensity profile with amplitude A_K. We perform the same computation without the presence of the mask ($K = 1$) to obtain the total field at the detector $E_{\text{det}}^1 = \hat{\mathcal{D}}(E_s) + \hat{\mathcal{D}}(E_0)$ with intensity amplitude A_1. The mask response function is then simply the ratio $\mathcal{M}(\gamma - \alpha; k) = A_K/A_1$.

Measurements of the mask response were obtained by using the CW ultrasonic loudspeaker provided by Ultra Sound Advice, U.K. Recall that this loudspeaker is a broadband CW ultrasound device capable of 85 dB sound pressure level (SPL) from 30 kHz to greater than 150 kHz. Using ultrasound in air at these frequencies allows the launching of single wave-number modes from $6 - 40$ cm^{-1}. If the 5 cm diameter loudspeaker membrane is placed within 3 cm of the PCI laser beam, then the sound wavefront radius of curvature is large and the wavefronts are sufficiently planar to use for mask response function measurements. These data were obtained over a range in wave-numbers from $6 - 27$ cm^{-1}.

The scalar diffraction model agrees well with measurements of the mask response structure as shown in Fig. 3-19, where the symbols are the measured mask response function using the CW ultrasound loudspeaker and the solid line is the calculated response using the scalar diffraction model. While the calculated response scale is absolute, the data is fit using an arbitrary amplitude factor to account for the variations in response of the CW loudspeaker. The peak response of the 0.5 mm mask slit is $\sim 60\%$ of that of the 1.0 mm slit because the laser focal spot size (w_0) at the mask plane has a $1/e$ electric field radius of 0.28 mm. Thus, even when the response is maximum ($\alpha = \gamma$), the smaller 0.5 mm mask slit provides substantial clipping and diffraction that results in a lower system signal-to-noise ratio.

Figure 3-20 plots the measured and modeled full width at half maximum (FWHM) of the mask response function vs. wave-number for 3 different mask slit widths (2.0 mm, 1.0 mm, 0.5 mm). As expected, the measured widths for each wave-number scale as $1/k$. Solid lines are the calculated FWHM from the scalar diffraction model.
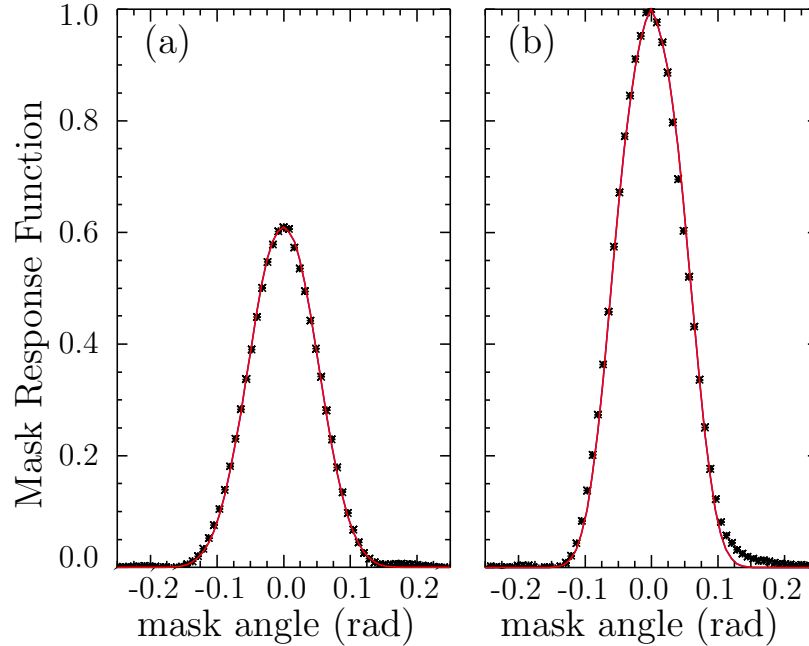
Figure 3-19: Measurements of the mask response function using (a) 0.5 mm slit at $k = 14$ cm^{-1} and (b) 1.0 mm slit at $k = 20$ cm^{-1} show good agreement between the scalar diffraction model (solid line) and measurements with the CW ultrasound loudspeaker (symbols). (a) shows that the peak response for the 0.5 mm slit is 60% of the system response without the mask slit.

Agreement is good with a relative error generally less than 5%. At higher frequencies, the loudspeaker membrane appears to vibrate in modes other than the fundamental making mask response measurements at high k difficult. The 2.0 mm mask slit provides poor resolution due to its broad response shown by the large FWHM measurements. While the 0.5 mm mask slit has the narrowest FWHM and therefore the best resolution, it causes an undesirable amount of diffraction and signal-to-noise is degraded as previously described. The 1.0 mm mask slit is generally used as it provides a good compromise between resolution and signal-to-noise.
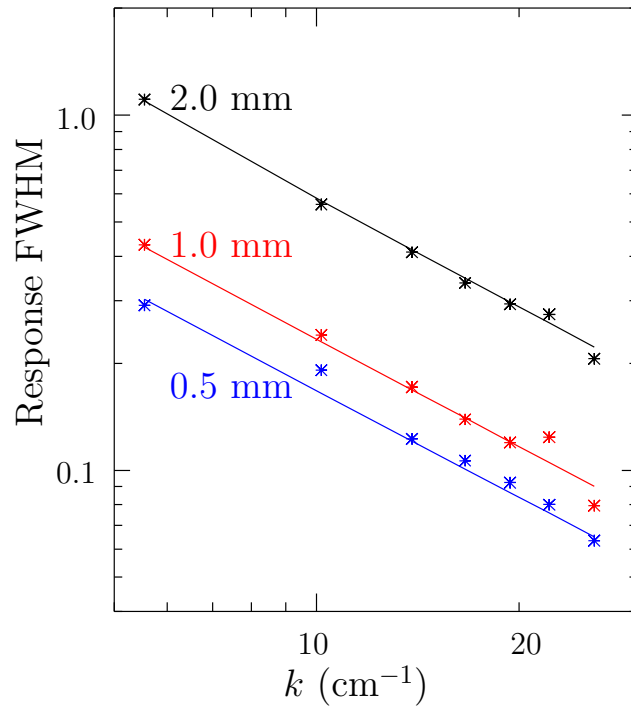
Figure 3-20: FWHM of mask response function over PCI wave-number range shows good agreement for all mask slit widths. Measurements using CW ultrasound loudspeaker shown as symbols and scalar diffraction model shown as solid lines.

THIS PAGE INTENTIONALLY LEFT BLANK

Chapter 4

Spectral Measurements of Turbulence with Upgraded PCI

Measurements of plasma turbulence using the DIII–D PCI diagnostic are typically described by computing estimates of the turbulence power spectra $S(k, \omega)$; however, other quantitative parameters such as correlation lengths, correlation times, and frequency spectra at fixed wave-number have been used for analysis [26, 68]. The conjugate space for spectral estimates of PCI data is wave-vector (k) and frequency (ω), where k is the wave-number corresponding to modes propagating perpendicular to the probe beam and ω is the angular frequency in radians/second.

In this chapter we define the PCI power spectrum in terms of a Fourier Transform of the plasma density fluctuation, and briefly describe how power spectra are estimated. We present an overview of the dominant features of such estimates in both wave-number and frequency. Large amplitude branches in the power spectrum with constant phase velocity propagating in both directions perpendicular to the PCI chord are ubiquitous across most plasmas. Power spectra of these branches are seen to scale with frequency as $1/k$ from low frequency to the peak branch frequency, and $1/k^2$ beyond. The phase velocity in the lab frame is highly dependent upon heating regime and plasma rotation. This dominant branch signal satisfies the assumption of near perpendicular propgation ($k_{||} \sim 0$) characteristic of drift-wave turbulence. We then discuss an approach to inverting Eq. 2.37 and making localized measurements

along the PCI chord, revealing that the large amplitude turbulence branches come from the edge of the plasma. Features in the data that do not adhere to the assumption of perpendicular propagation (finite $k_{||}$) are seen and limit the ability to make localized measurements.

4.1 Overview of DIII–D PCI Measurements

4.1.1 Power Spectra Estimates

The voltage output of each of the PCI detector elements is directly proportional to the line-integrated density fluctuation as given by Eqs. 3.3 and 3.9 (*i.e.* $V(\xi, t) \propto \tilde{n}(\xi, t)$). The PCI signal is sampled in space by the individual detector elements, each of which are sampled in time by the PCI digitizers. We can define the power spectra as the square magnitude of the two dimensional Fourier Transform of the density fluctuation

$$S(k, \omega) = \left| \int d\xi \int dt \ e^{ik\xi} \ e^{i\omega t} \ \tilde{n}(\xi, t) \right|^2 . \tag{4.1}$$

Typically, power spectra are estimated using the two dimensional complex correlation function as described in Appendix B.2; however there exist a multitude of techniques for estimating power spectra, each with their own benefits and limitations. Techniques relevant to PCI data and the work presented in this thesis are discussed in detail in Appendix B.

The DIII–D PCI is concerned with measuring short wavelength, high frequency turbulence. There is therefore a separation of timescales that is utilized to improve the signal-to-noise and make estimates of $S(k, \omega)$ as the plasma evolves in time. To see this, we note that the PCI data is high-pass filtered using the VGAF circuits described in Sec. 3.3.3 with a cutoff frequency $f_{\min} = 10$ or 100 kHz. This is performed because low frequency vibrational noise from the tokamak limits the measurement to $f \gtrsim 8$ kHz, and the lowest frequency cutoff was chosen accordingly. Therefore, power spectra are computed every 0.01 - 0.1 μs; if the plasma turbulence is evolving slowly with the background plasma profiles (typically timescales of order 10 ms) then each

estimate of the power spectra is considered an independent realization, and they are averaged for improved signal-to-noise. This process yields spectra estimates as a function of time $S(k, \omega, t)$.

During stationary plasma conditions (*i.e.* where the plasma is statistically invariant when shifted in time), the rotating mask is used to measure the turbulence power spectra as a function of mask angle, $S(k, \omega, \gamma)$. This is related to the turbulence propagation direction by Eq. 2.37. While calibration data can be collected under ideal conditions, plasma turbulence measurements have the contradictory requirements of long time averaging for improved signal-to-noise and short time averaging for responsiveness to changing plasma conditions. The rotating mask analysis technique thus requires a balancing of integration times to yield quality localized measurements. The practical rate at which localized measurements can be recorded is less than the hardware limitation of 100 profiles/sec and is set by system noise, the desired spatial resolution, and the desired frequency resolution.

4.1.2   Ubiquitous Features of PCI data

Power spectra estimates of DIII–D PCI data exhibit features that are ubiquitous across most plasma discharges (L-Mode, most H-Mode plasmas) and heating regimes (ohmic, neutral beam injection, ECH, Fast Wave). Analysis of PCI data is generally focused on changes in these ubiquitous features with plasma conditions, or on the appearance of unique structures in the PCI spectrum during specific plasma conditions.

Large Amplitude Branch Structures

The largest amplitude component can be described as a branch in wave-number and frequency space with roughly constant phase velocity that decays monotonically with increasing frequency. This branched structure is generally limited to wave-numbers $\lesssim$ $15\,\mathrm{cm}^{-1}$. The phase velocity is most closely tied to the plasma rotation suggesting that the mode frequency as measured in the lab frame is dominated by the Doppler shift; however, measurements also show that the branch phase velocity changes with plasma

temperature as a shift in the peak wave-number of $S(k)$ plotted at fixed frequency. This large amplitude branch signal satisfies the assumption of near perpendicular propgation ($k_{||} \sim 0$) characteristic of drift-wave turbulence.

To emphasize the branch structure at high frequency in the 2-D spectrogram, we can plot the conditional power spectrum (denoted as $\mathcal{C}(k; f)$ to avoid confusion with the actual power spectrum) which suppresses the decay with frequency and therefore has the disadvantage of losing all information about relative amplitude at different frequencies. The conditional power spectrum can trivially be defined as

$$\mathcal{C}(k; f) = \frac{S(k, f)}{\int dk \; S(k, f)}. \tag{4.2}$$

Figure 4-1 plots both a) the power spectrum (colors in log scale) and b) the conditional power spectrum (colors in linear scale) for a generic DIII–D L-Mode plasma
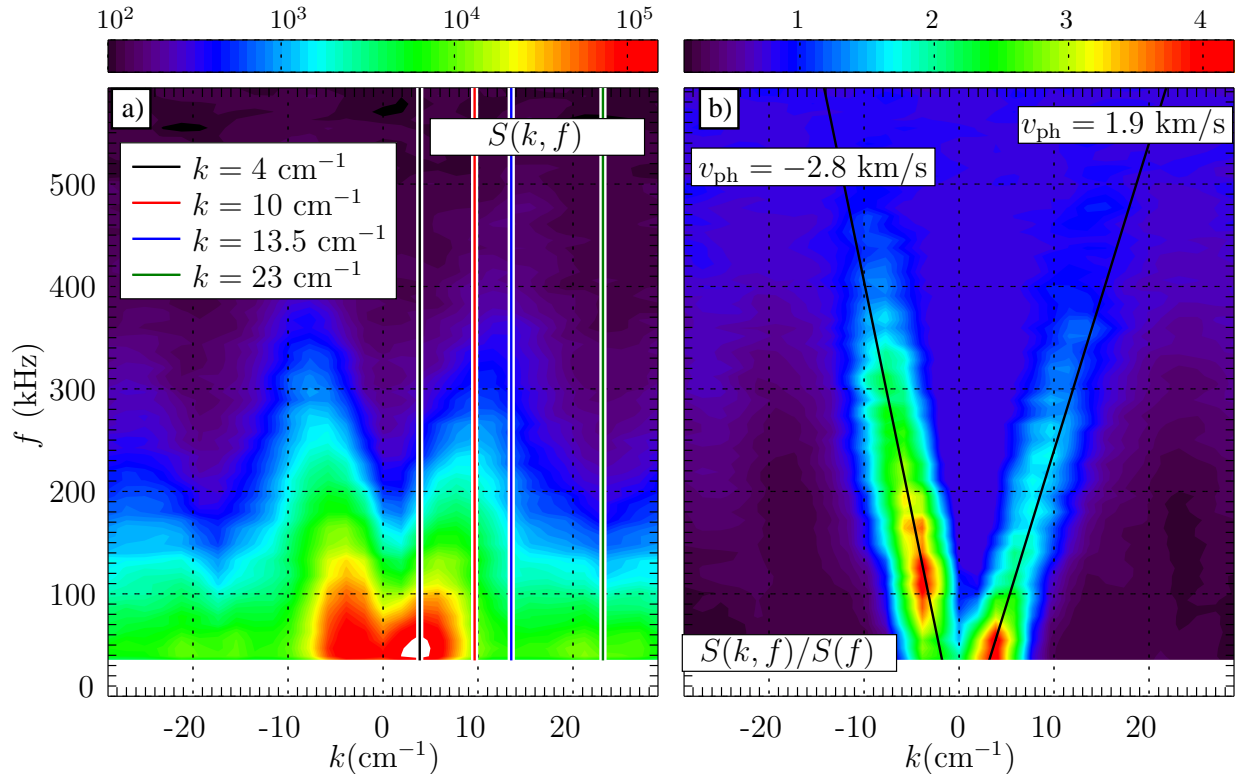
Figure 4-1: a) Power spectrum $S(k, f)$ plotted with colors in log scale for a typical L-Mode plasma in the DIII–D tokamak. b) Conditional power spectrum $\mathcal{C}(k; f)$ (with colors in linear scale) shows the structure of the main branches with roughly constant phase velocity.

with low power (2.8 MW) of neutral beam heating. Colored vertical lines are plotted corresponding to the wave-numbers 4, 10, 13.5, and 23 cm^{-1}. The lowest three wave-numbers cross the main branch while 23 cm^{-1} is chosen as it is well beyond the branch. The branch phase velocities are estimated to be -2.8 km/s and 1.9 km/s (in the lab frame) respectively and are indicated on the conditional power spectrum.

Spectral power is plotted as a function of frequency in Fig. 4-2 at each of the 4 wave-numbers previously described. The PCI noise level (integrated over a narrow wave-number band of 2 cm^{-1}) is roughly 0.02-0.03 (in the arbitrary units of Fig. 4-2) and S/N approaches unity for frequencies above 500-600 kHz. The power spectra decays monotonically; however the rate of decay increases to roughly $1/k^2$ beyond the branch frequency (indicated by the vertical lines). Therefore, seeing the branched structure is very difficult via measurements of turbulence as a function of frequency (at fixed wave-number).
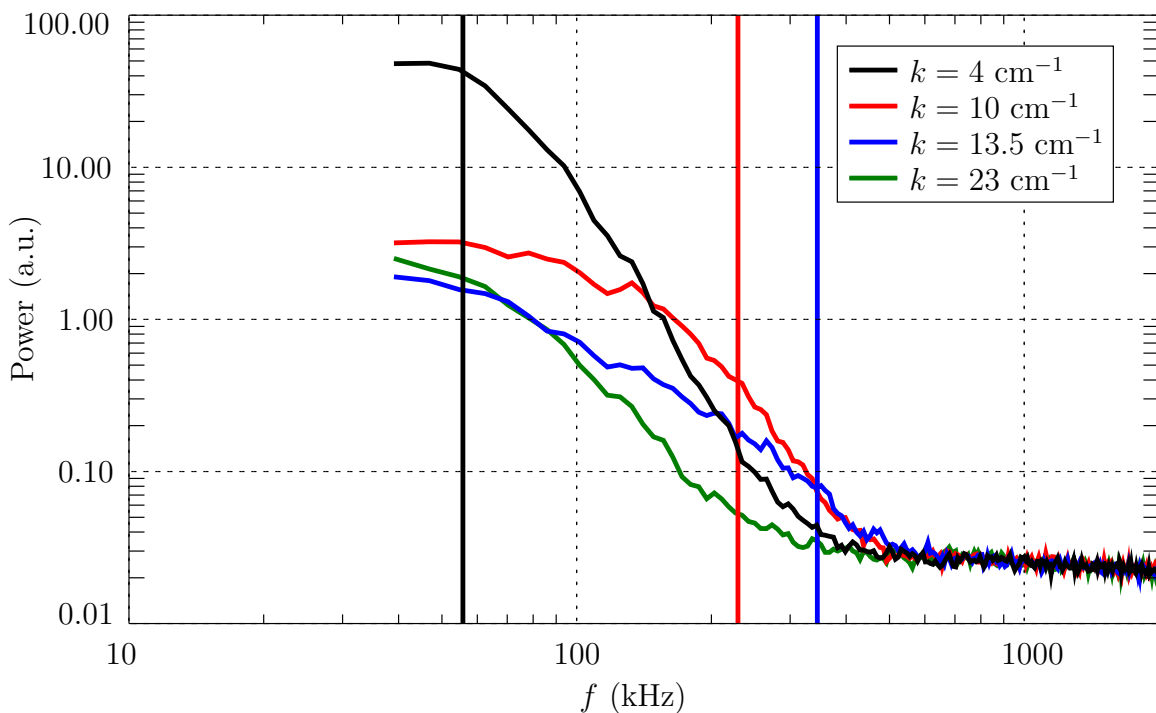
Figure 4-2: Typical L-Mode power spectrum vs. frequency at four fixed wave-numbers with integration width $\Delta k \sim 1.5$ cm^{-1}. Turbulence power is seen to scale as $1/k^2$ after the main branches. The branch frequency is plotted as a vertical line at each wave-number where the branch exists.

In Fig. 4-3, we plot both a) the power spectrum (colors in log scale) and b)
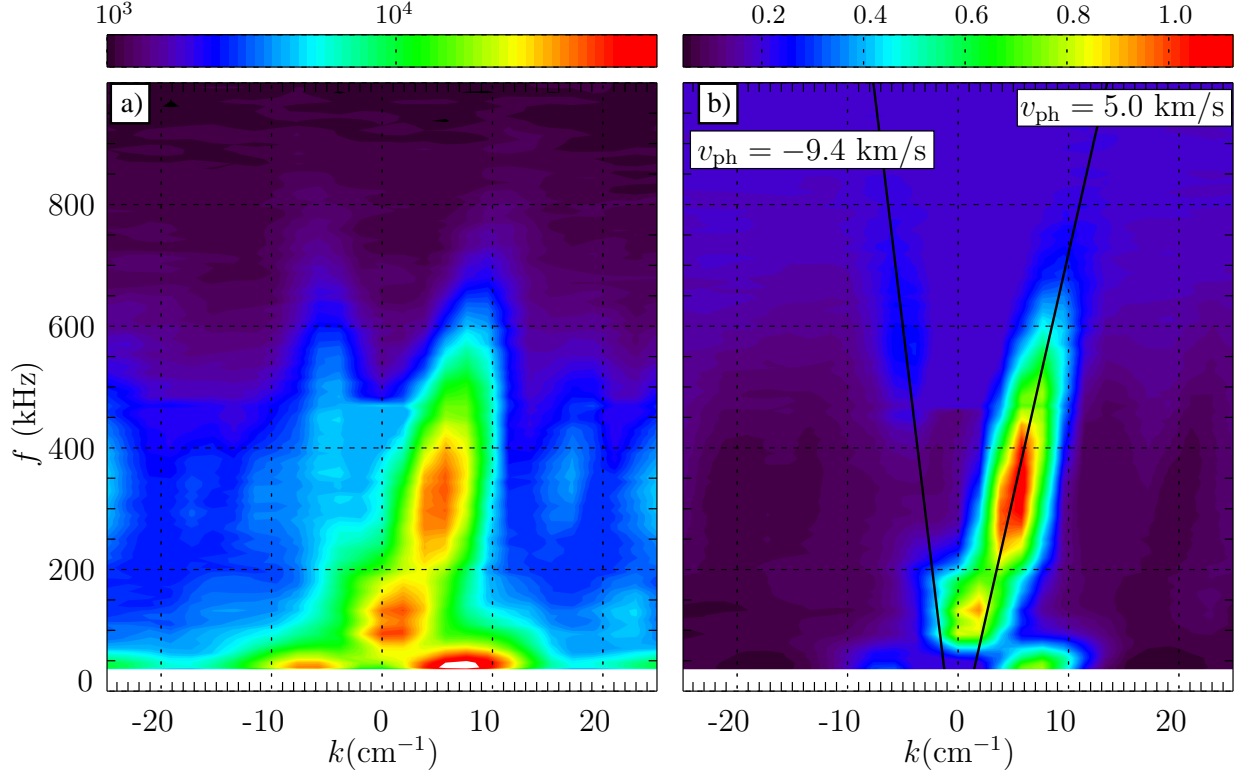
Figure 4-3: a) Power spectrum $S(k, f)$ plotted (colors in log scale) for the ELM-free period in a typical H-Mode plasma. b) Conditional power spectrum $\mathcal{C}(k; f)$ (colors in linear scale).

the conditional power spectrum (colors in linear scale) during the ELM-free period after an H-Mode transition. This H-Mode plasma is heated by roughly 5 MW of neutral beam heating. The branch phase velocities are estimated to be -9.4 km/s and 5.0 km/s, roughly a factor of 3 larger than for the L-Mode plasma presented in Fig. 4-1. This increase in mode phase velocity as measured in the lab frame is qualitatively consistent with the mode being Doppler shifted by the higher rotation of the H-Mode plasma. Plotted below in Fig. 4-4 is data from the Charge Exchange Recombination diagnostic (CER) used to measure the line of sight (LOS) velocity of carbon impurities in both the toroidal and poloidal planes. The data clearly shows that the plasma rotates faster in both the poloidal and toroidal directions in H-Mode than in L-Mode. The radial electric field is estimated [69, 70] and plotted in panel c) showing a larger $E \times B$ velocity over the PCI chord region (indicated by the gray box) in H-Mode than in L-Mode.
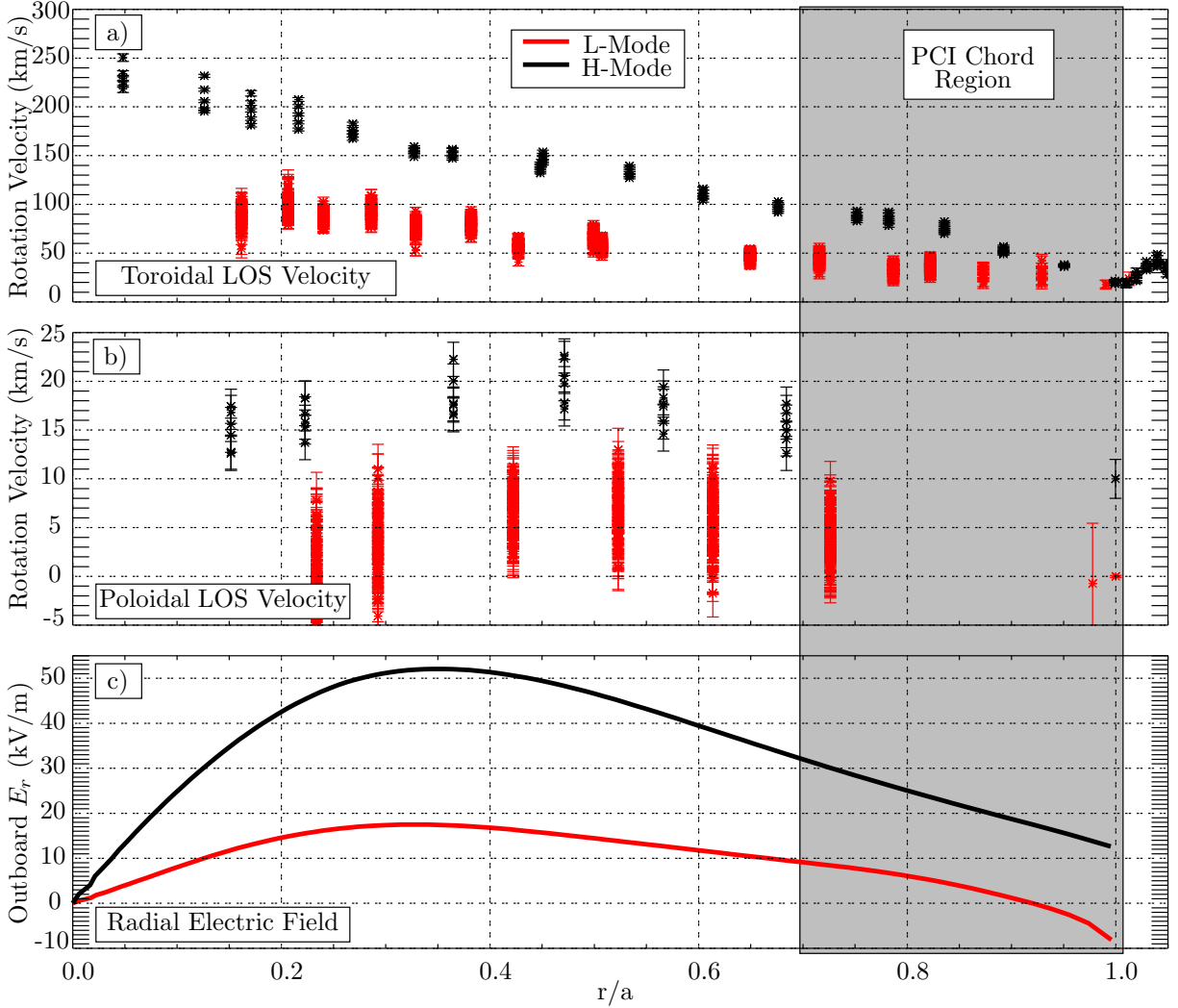
Figure 4-4: Carbon-VI rotation data from the DIII–D CER diagnostic showing increased plasma rotation in H-Mode from that of L-Mode. a) Line of sight velocity in the toroidal direction, b) Line of sight velocity in the poloidal plane, and c) The radial electric field estimate from CER data computed by solving the radial force balance.

High-k Signal at Large Propagation Angle

Another feature of DIII–D PCI data that is visible across a broad range of plasma shapes and heating regimes is a small amplitude component at relatively high-k. This feature is best described as a background level of turbulence because other more distinct features can be seen on top of and in addition to this background signal. While the background turbulence is most apparent at high-k and high frequency (due to the lack of other spectral features), it exists over a large range in frequencies. It is most

noticeable at frequencies in the range of 200 kHz and above, and at wave-numbers of 20 cm^{-1} and above. This feature will be described in more detail in Sec. 5.4.

Figure 4-5 plots the turbulence amplitude as a function of propagation angle obtained using the rotating mask system described in Sec. 2.2. These measurements of $S(\alpha)$ are integrated over the frequency range of 200 kHz $< f <$ 400 kHz and the wave-number range of $|k| > 20$ cm^{-1}. The green line is after a plasma disruption and represents the system noise level in the absence of plasma. The black line is during L-Mode with 2.5 MW of neutral beam heating, while the red line is during H-Mode with 5 MW of neutral beam heating. The background turbulence regularly appears to peak roughly at a propagation direction in the poloidal plane ($\alpha = 0$), extends to propagation angles up to $\pm 30°$, and is relatively symmetric.
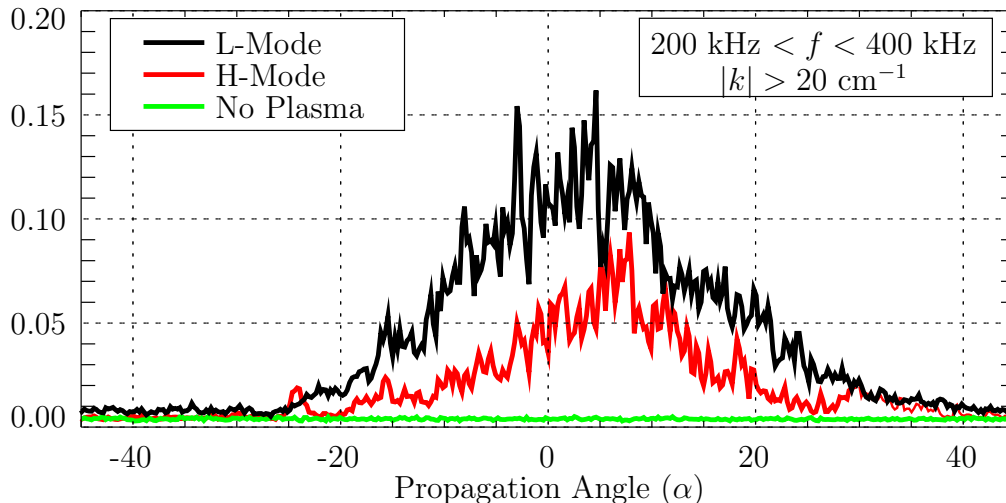
Figure 4-5: $S(\alpha)$ plotted during L-Mode, ELM free H-Mode, and after a plasma disruption in black, red, and green respectively. The signals are integrated over the frequency range of 200 kHz $< f <$ 400 kHz and the wave-number range of $|k| > 20$ cm^{-1}.

4.2 Localization of Turbulence

The rotating mask upgrade to the DIII–D PCI was implemented to provide localized measurements along the PCI chord as described in Sec. 2.2.2. This technique is useful only during stationary plasma conditions such that all variation of the turbulence is

due to the mask rotation and not to variations of the plasma itself. Recall that the rotating mask passes only scattered beams from a specific range in propagation angle, and that this corresponds to height along the chord *only* in the case that turbulence propagates near perpendicular to the magnetic field (*i.e.* that $k_{||}/k \lesssim 10^{-2}$). Power spectra are estimated as a function of time during the mask rotation, denoted as $S(k, f, \gamma)$ as described in Eq. 2.45 where γ is the mask rotation angle. Equation 2.45 must then be inverted to obtain the turbulence power spectra as a function of chord height $S(k, f, z)$.

4.2.1 Inversion of PCI Data

We will describe the process of computing power spectra and averaging over multiple realizations in Appendix B.1, and when computed during stationary plasma conditions, these measurements give power spectra as a function of mask rotation angle (γ). Therefore, power spectra are computed every $2/\delta f$ seconds, where δf is the desired frequency resolution. These power spectra are then averaged over multiple realizations, typically $2 < R < 16$. Sampling in the mask angle domain is therefore $\gamma_{i+1} - \gamma_i = 2\pi RF/\delta f$ where F is the mask rotation rate (typically 4-20 profiles/sec). This sets the grid on which Eq. 2.45 is inverted, and ultimately the maximum spatial resolution $\Delta z = z(\gamma_{i+1}) - z(\gamma_i)$. Further averaging can be performed over multiple mask profiles provided the plasma conditions remain stationary. The parameters δf and F are varied to optimize the analysis for each experiment so that better spatial and frequency resolution are produced for plasmas with long steady-state periods.

Measurements during various plasma conditions have been made with the new rotating mask system. Plasma data have been obtained that show $S/N > 1$ for $k \lesssim 25$ cm^{-1} and calibrations using ultrasonic waves have confirmed proper operation of the PCI to at least $k = 37$ cm^{-1}. While system signal-to-noise is the current limiting factor in spatial resolution of the localization technique, the DIII–D PCI shows unmistakable structure in the measured spectrum as a function of mask angle. The following data are presented to best illustrate the analysis procedure of this localization technique.
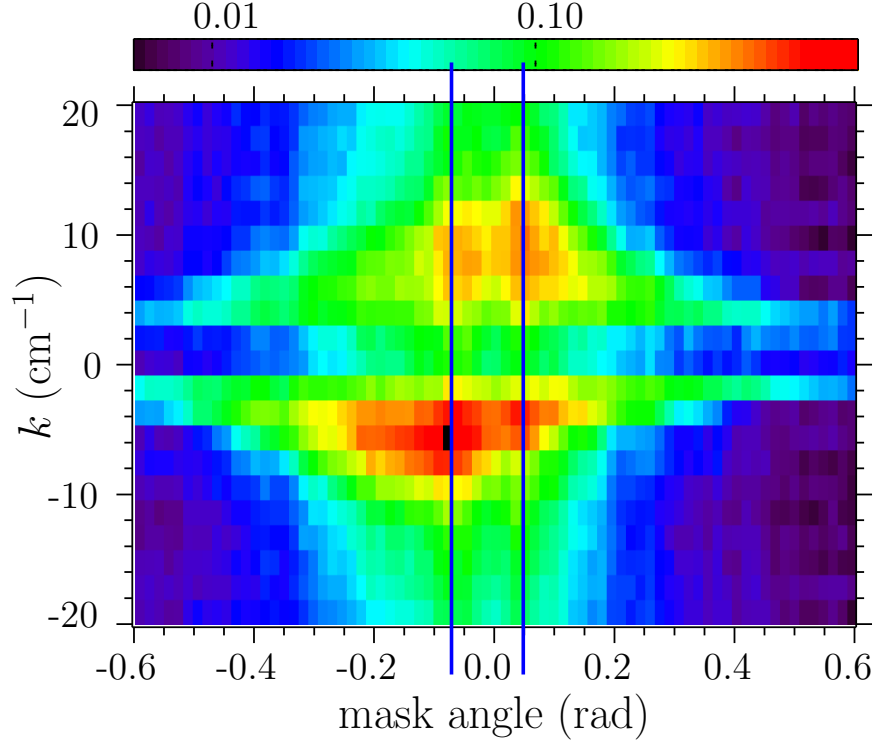
Figure 4-6: Measured spectrum of plasma turbulence (raw data before the inversion removes instrumental response) by the rotating mask system, integrated over frequency range $150 - 300$ kHz. Vertical blue lines represent mapping of LCFS locations in pitch angle space. By convention, $+k$ is defined as modes propagating approximately radially outward $(+\hat{R})$, and $-k$ is defined as modes propagating approximately radially inward $(-\hat{R})$. Colors in log scale.

Example of Inversion Technique

Figure 4-6 plots a measured fluctuation power spectrum $(S(\gamma, k)$ as in Eq. 2.37) during ECH heating of an L-mode discharge showing PCI signal integrated from $150 - 300$ kHz, and $S/N > 1$ for $k \lesssim 20$ cm^{-1}. The vertical lines represent the edges of the plasma. Two distinct features are immediately apparent: 1) The mask response does indeed get more narrow as k increases, and 2) turbulence is highly asymmetric with respect to inward/outward propagation. The measured power spectrum extends beyond the LCFS (shown by vertical lines in Fig. 4-6) due to the finite width of the mask response function. Recall that PCI measures wave-vectors perpendicular to the viewing chord and that the PCI beam is nearly vertical $(+\hat{z}$ direction); by convention we define positive k as approximately radially outward $(+\hat{R})$ and negative

k as radially inward $(-\hat{R})$. Inward propagating modes are particularly strong at the bottom of the PCI chord (negative mask angle edge). These features were verified by rotating the mask in the opposite direction during a repeat shot, thus instead of sweeping through the plasma from bottom to top of the PCI chord, the localized volume sweeps from top to bottom; the measured fluctuation power as a function of time reversed as expected.

The DIII–D PCI has previously measured turbulence power spectra to scale $\sim$ $1/k^2$ [71]. Since the localization becomes better at higher k, analysis of the rotating mask data is limited by low signal-to-noise at higher k. Currently, the inversion of Eq. 2.45 is being performed by choosing a parameterized trial function for $S(z;k)$ and varying the parameters to minimize the error between $S(\gamma, k)$ calculated from the trial function (via Eq. 2.37) and the observed $S(\gamma, k)$. The initial trial function $S(z, k)$ is chosen to be a sum of N Gaussians uniformly spaced in propagation angle (*i.e.* $\alpha_i = \alpha_{min} + i\delta\alpha$ where $\delta\alpha = \frac{\alpha_{max}-\alpha_{min}}{N-1}$ and $i = 0...N-1$). Therefore, the Gaussian widths become smaller as more Gaussians are introduced (by increasing N). The Gaussians located at $i = 0$ and $i = N-1$ are 'clipped' such that no fluctuation power is allowed beyond the mapping extrema α_{min} and α_{max}. Each Gaussians amplitude β_i is a parameter used in the fitting process. Therefore, the parameterized trial function is

$$S(z, k) = \begin{cases} \sum_{i=0}^{N-1} \beta_i e^{-\left(\frac{\alpha(z)-\alpha_i}{\delta\alpha/2}\right)^2} & \alpha_{min} \leq \alpha(z) \leq \alpha_{max}, \\ 0 & \alpha(z) < \alpha_{min}, \quad \alpha(z) > \alpha_{max}. \end{cases} \tag{4.3}$$

This process is necessary because the inversion of Eq. 2.37 is ill-conditioned; the spectral structure of $\mathcal{M}$ will lead to erroneous noise amplification even under a Weiner LTI filtering approach [72]. Figure 4-7 shows that $S(\gamma, k)$ reconstructed from the trial function accurately reproduces the observed $S(\gamma, k)$.

Examples of the turbulence power spectrum $S(z;k)$ calculated using this technique are shown in Fig. 4-8. It is clear that the peaking of power spectra at the mapping extrema $(\alpha_{\min}, \alpha_{\max})$ is not solely due to peaking in the chord mapping den-
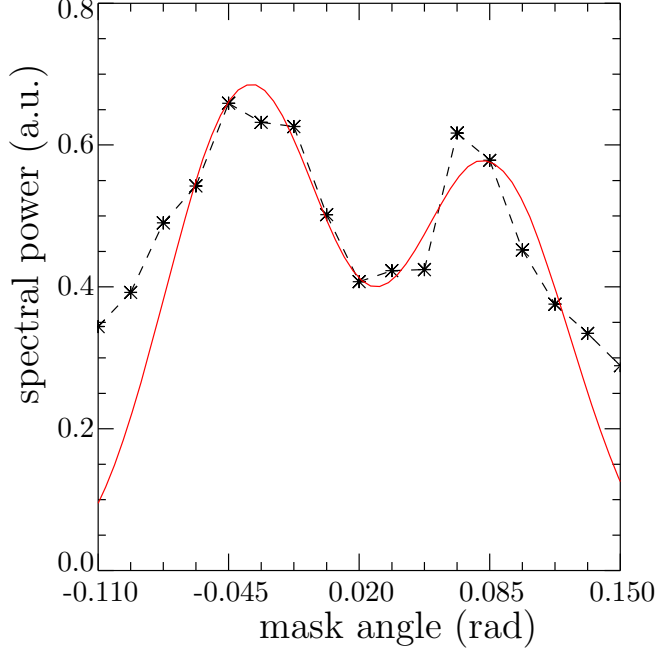
Figure 4-7: (Color online), Observed $S(\gamma, k)$ (dashed line with symbols) is a single slice of Fig. 4-6 at $k = -13.5$ cm^{-1} (raw data before inversion analysis). The reconstructed $\hat{S}(\alpha'; k)$ (solid line) is the best fit of the prototyped $S(z; k)$ convolved with the mask response function.

sity, $|dz/d\alpha|$. Figure 4-8 shows PCI turbulence power for $k = \pm 9.6$ cm^{-1} with and without ECH heating from the same discharge as Fig. 4-6. In both heating regimes, turbulence peaks at the plasma chord edges. ECH heating increases the outward propagating modes at both edges while marginally altering the inward propagating turbulence modes.

Difficulties with the Inversion

While the PCI signal-to-noise limits the resolution of the localization due to the inherent difficulties with deconvolving Eq. 2.45, the PCI data shows other features that further complicate the inversion, and are not consistent with the assumption that turbulent modes propagate near perpendicular to the local magnetic field ($k_{||} \sim 0$). While we have already shown very small amplitude signal at large propagation angle, the features we now describe exist at relatively low wave-numbers $5 \lesssim |k| \lesssim 15$ cm^{-1} (*i.e.* at the wave-numbers where the branches described in Sec. 4.1.2 exist).
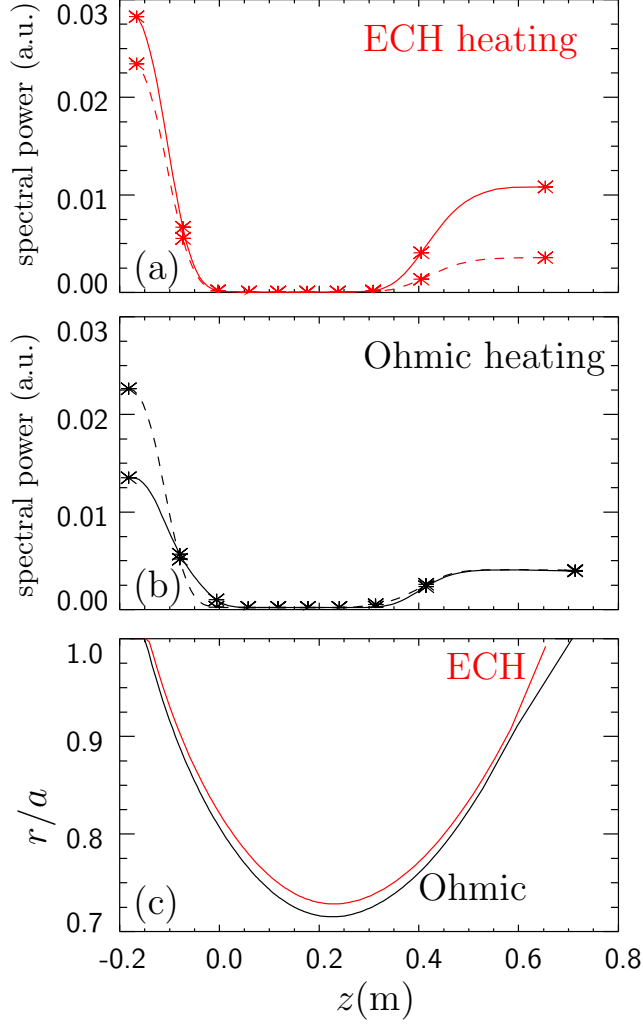
Figure 4-8: (Color online), Turbulence spectra $S(z; k)$ calculated for $k = -9.6$ cm^{-1} (dashed line) and $k = +9.6$ cm^{-1} (solid line) during (a) ECH heating and (b) Ohmic heating of a L-mode discharge. Turbulence is dominated by the plasma edge and increases in the outward propagating direction during the application of ECH heating. (c) Plasma radial location of PCI chord during both heating regimes.

Figure 4-9 plots (in symbols) the power spectra as a function of mask angle $S(\gamma; k)$ for a typical L-Mode DIII–D plasma. The signal is integrated over the frequency range of $300 < f < 450$ kHz and plotted at $k = \pm 11$ cm^{-1}. The green curves are the fit to the power spectra using the parametrized function for $S(z; k)$ given in Eq. 4.3. The red vertical lines show the mapping propagation angle corresponding to the LCFS of the PCI chord (*e.g.* no signal should come from propagation angles outside the red lines if the turbulence does indeed propagate near perpendicular to the local magnetic
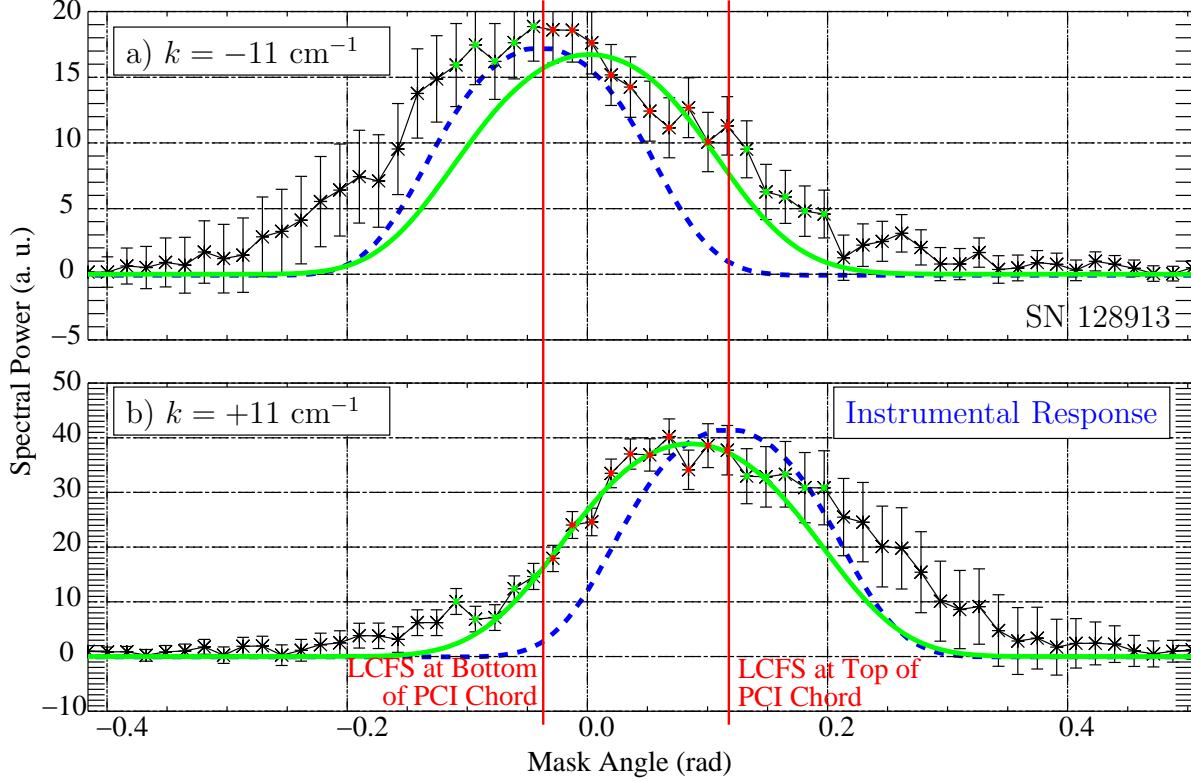
Figure 4-9: Turbulence amplitude plotted as a function of mask rotation angle γ at wave-numbers $k = -11$ cm^{-1} in panel a) and $k = +11$ cm^{-1} in panel b). Green curves are the fits computed for the parameterized function described in Eq. 4.3. Vertical red lines correspond to the propagation angles of $k_{||} \sim 0$ turbulence from the LCFS mappings.

field). Due to the finite width of the mask response function defined in Sec. 2.2.1 as $\mathcal{M}(\gamma - \alpha, k)$, the signal should extend beyond the LCFS mapping lines by as much as the half-width of the mask response function. However, the signal extends into the region beyond the LCFS mapping by as much as 10° further than the mask response function should allow. The mask response function is plotted in Fig. 4-9 as dashed blue lines aligned with the angular mappings of the LCFS.

These extra "wings" on the main branches of data extend to higher propagation angle than is expected; this brings into question the assumption that turbulence propagates near perpendicular to the local magnetic field ($k_{||} \sim 0$). Practically, this feature tends to pile up power at the apparent edges of the plasma while driving the solution negative in the central region of the plasma chord. The inversion procedure limits the solution $S(z; k)$ to be positive definite; however, the inversion technique

still suffers from fitting a model that is clearly based on an unsatisfied assumption.

THIS PAGE INTENTIONALLY LEFT BLANK

Chapter 5

Finite Parallel Wave-number Turbulence

This chapter presents results and analysis of DIII–D PCI measurements using the rotating mask system that show turbulence propagating at angles too large to be interpreted as electrostatic drift-wave modes with $k_{||} \sim 0$ (where parallel refers to the local magnetic field direction). Recall that we refer to such large parallel wave-numbers as "finite parallel wave-number" or "finite $k_{||}$", while we refer to the small parallel wave-number drift-wave modes as "propagating near perpendicular" or "$k_{||} \sim 0$". In Sec. 4.1.2, it was shown that near perpendicularly propagating turbulence is the source of the largest power main branch component of the PCI signal. Turbulence with finite $k_{||}$ is measured to be lower power than the main branch structure. The size of the wave-vector component parallel to the magnetic field is measured to be quite large, in the range $k_{||}/k \sim 0.1 - 0.4$.

First we will describe different techniques used for estimating turbulence power spectra, their trade-offs and performance. These estimates will be used to verify and benchmark our ability to pick out low amplitude spectral features from the higher power main branch features discussed in Sec. 4.1.2. Analysis of measurements that show turbulence with finite $k_{||}$ components are then presented. We measure three classes of turbulence with finite $k_{||}$, modes that are localized in wave-number and mask angle (described in Sec. 5.3), a broad background turbulence (described in

Sec. 5.4), and a low-k "wing" that smears the main branch structure (described in Sec. 5.5).

5.1 Spectral Analysis Techniques

Section 4.2.1 presented measurements of turbulence at propagation angles that can only be explained if the assumption that turbulence propagates near perpendicular to the local magnetic field ($k_{||} \sim 0$) is not satisfied. This finite $k_{||}$ component is often small in spectral amplitude compared with the large amplitude branch structures shown in Sec. 4.1.2. When a power spectrum consists of a large amplitude structure at one frequency (or wave-number) in the presence of secondary weak amplitude structures at another frequency (or wave-number), the technique used to estimate the power spectrum becomes critical and an understanding of the trade-offs between spectral resolution and spectral contamination (side-lobes) is required to have confidence in the spectral estimate. This section presents a brief discussion on two techniques used to estimate DIII–D PCI power spectra and quantitative measurements of their performance using both synthetic and calibration data. Further detail about the mathematical implementation of the following techniques can be found in Appendix B.

5.1.1 MEM and Fourier Spectral Techniques

Two techniques used in analysis of PCI data to estimate power spectra are the traditional windowed Fourier based estimates [73] and the Maximum Entropy Method (MEM) [74] (also called Maximum Entropy Spectral Estimation (MESE)). The literature on the subject of Fourier based spectral estimates is abundant and this is often thought to be the gold standard of spectral estimation since the advent of the Fast Fourier Transform (FFT). However, Ables [75] points out that the most rational approach to the spectral estimation problem should be that of the MEM since it introduces the least bias and often results in superior spectral resolution and lower spectral contamination, especially for datasets of limited extent.

The PCI power spectrum was defined in Eq. 4.1 using the continuous Fourier Transform. While this is a correct definition, in practice it is also of limited use. When making measurements of time series, we never have continuous sampling of a stationary signal for infinite duration. In reality, we sample a limited duration of the signal we hope to characterize using a finite sampling interval; we then hope to *estimate* the true power spectrum. By blindly taking the continuous Fourier Transform (FT) to a discrete Fourier Transform (DFT), we can attempt to estimate the power spectra. However, in so doing we also neglect to take fully into account the limitations imposed by the finite signal duration and finite sampling interval.

The DIII–D PCI signal is also limited in quality by imperfections of the system detectors and data transport system. The system detectors are 15 years old, and as pointed out in Sec. 3.1.2, certain detector channels are degraded in responsivity or completely inoperable. Therefore, the sampling in the spatial dimension suffers from non-uniform sampling (or missing samples). In fact, sampling in the spatial dimension has at most 16 spatial samples (corresponding to 16 digitizer channels), and often as few as 10-12 depending on the operation of the digitizers on any given day. The implications on the spectral estimates using a simple DFT cannot be overstated. By introducing the autocorrelation function (ACF) (described in detail in Appendix B.2) we can overcome the problem of missing samples.

In this section we've attempted to define the difficulties involved in estimating the power spectrum of PCI measurements. These are the problems introduced by finite signal duration, finite sampling interval, and non-uniform sampling (or missing data). A Fourier based spectral estimate can be obtained from both the raw time series as well as from the ACF. However, due to the problem of missing channels only the Fourier based estimate from the ACF is presented herein. In addition, we consider the use of windowing and Welch's Method [76], which again is described in detail in Appendix B.1. Similarly, the MEM spectral estimate can be obtained from both the raw time series as well as the ACF. In what follows we show estimates from both due to the fact that the estimate from the raw time series is a more robust and well known procedure [77].

Because sampling of PCI data in the time domain is generally performed at a rate above 4 MS/s, the performance of the Fourier based spectral estimate in the time dimension is generally very good. Therefore, when we refer to the MEM spectral estimate, we are actually performing a hybrid approach using a Fourier based estimate in the time domain, and the MEM estimate for the spatial domain - the details of such an approach are discussed in Appendix B.3.

5.1.2 Performance of MEM vs. Fourier Techniques

The performance of the power spectrum estimation techniques described above are measured in two ways. First, we consider the spectral resolution, here defined as the spectral width of the test signal given by Eq. 5.1 consisting of a mode at a single frequency and wave-number. The other performance figure of concern is spectral contamination (or side-lobe level), which we define as the spectral power density at frequencies and wave-numbers away from the test signal mode.

Power spectra were estimated using 4 Fourier based techniques of varied window combinations and 2 MEM based (in the spatial dimension) techniques. The Hann window was the chosen shape of the window as it balances the trade-off between spectral resolution and side-lobe level [77]. Therefore, the different spectral estimation techniques are described in Table 5.1, where "Rect" is a rectangular window, "Hann"

Table 5.1: Description of the 6 power spectra estimation techniques used in PCI data analysis.

Label	Time Domain			Spatial Domain		
	Window	Technique	Source	Window	Technique	Source
No Hann	Rect	FFT	ACF	Rect	FFT	ACF
Hann Time	Hann	FFT	ACF	Rect	FFT	ACF
Hann Space	Rect	FFT	ACF	Hann	FFT	ACF
Hann Space Time	Hann	FFT	ACF	Hann	FFT	ACF
MEM ACF	Hann	FFT	ACF	–	MEM	ACF
MEM Burg	Hann	FFT	time series	–	MEM	time series

is the Hann window, "FFT" is a Fourier based estimate, "MEM" is the maximum entropy method based estimate, and "ACF" is the autocorrelation function.

124

Synthetic Test Signal

To assess the performance of the various spectral estimation techniques described in the previous section, two approaches were undertaken. First, a synthetic PCI signal was used - this has the benefit of isolating the power spectra estimation numerics independently from the entirety of the PCI hardware. It also has the benefit of looking at the difference between using all 16 (synthetic) detector elements or a reduced subset, testing the technique's ability to handle missing spatial samples. The synthetic test signal used is

$$\frac{\tilde{n}_t(x, t)}{n_0} = \cos(kx - 2\pi f t) + 0.3 g(x, t), \tag{5.1}$$

where $k = 20$ cm^{-1}, $f = 50$ kHz, and $g(x, t)$ is the random white noise component generated from a Gaussian probability distribution.

The power spectra estimates are plotted vs. both frequency and wave-number in Fig. 5-1, where the colors are in log scale. Additionally, the color scale is the same across all 6 plots, therefore the spectral power density for a given shade of blue is the same for all panels a) - f). In these 2-dimensional color-scale plots we can see the qualitative effects of the Hann window, and the increased spectral resolution of the MEM spectra in the spatial domain. Panels a) and b) have rectangular windowing in the time domain while panels c) and d) have Hann windows used in the time domain. The level of the side-lobe (spectral contamination) is clearly decreased with the use of the Hann window. Similarly, panels a) and c) use a rectangular window in the spatial domain, while panels b) and d) use the Hann window. From the color level along $f = 50$ kHz, we can see the side-lobes reduced again by the Hann window. Panels e) and f) plot the MEM power spectra estimates computed from the ACF and raw time series, respectively. What is most noticeable are the narrower peaks along the wave-number axis indicating improved spectral resolution. What is also noticeable is that the MEM estimate computed from the raw time series has a higher background signal level across all frequencies. This is due to the choice of noise in the test signal. Because white random noise is completely uncorrelated, the process of computing the autocorrelation function suppresses this noise. However, in practice
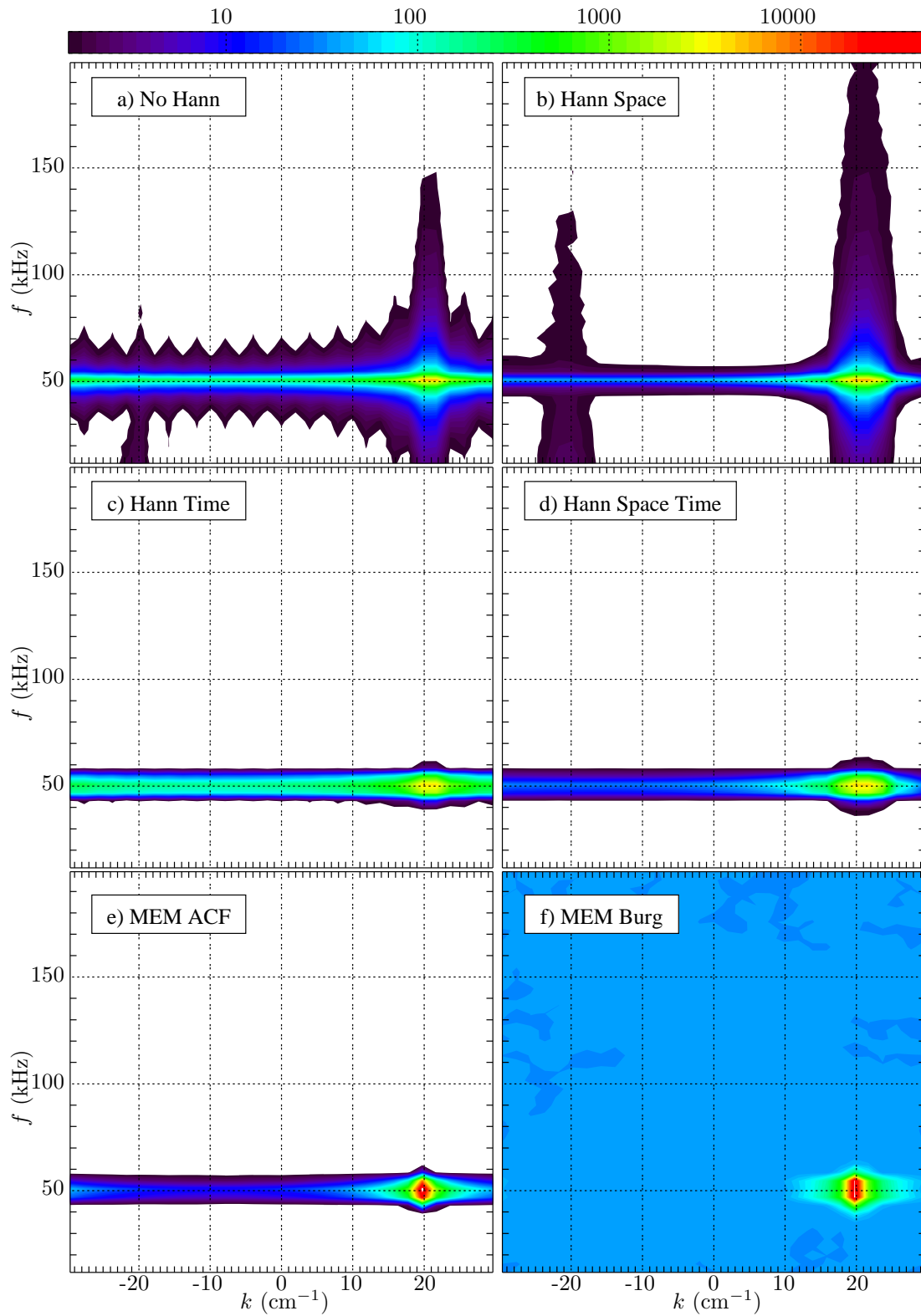
Figure 5-1: Estimates of the power spectra $S(k, f)$ using a plane wave test signal for the 6 estimation techniques. Colors use the same log scale across all panels.

the noise component of the PCI signal is highly complex, and is not eliminated as efficiently by the computation of the autocorrelation function.

A more quantitative measure of the performance of each of the spectral techniques is plotted in Fig. 5-2 where panels a) and b) plot the power spectra as a function of frequency and of wave-number, respectively. These data were obtained by integrating
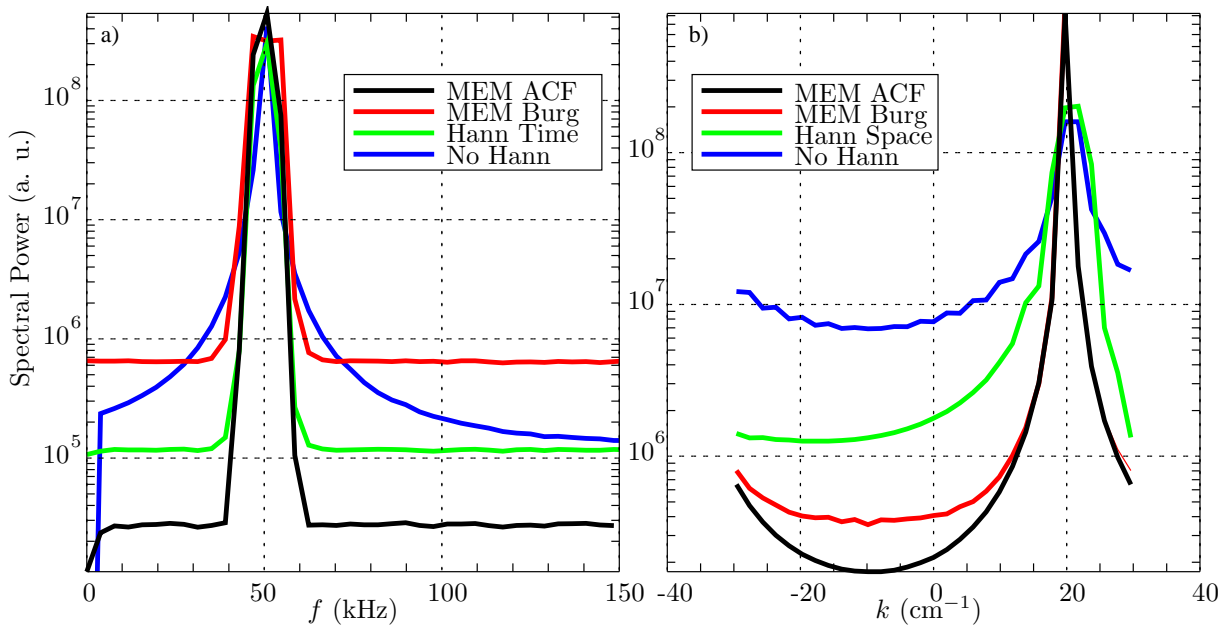
Figure 5-2: a) $S(f)$ integrated from $17 < k < 23$ cm^{-1} and b) $S(k)$ integrated from $45 < f < 55$ kHz. The spectral power plotted vs. wave-number shows that the Hann window trades off poorer spectral resolution for improved spectral contamination. MEM estimates outperform the Fourier based estimates in both resolution and contamination in the spatial domain.

the spectral power density over a band centered around the mode frequency and wave-number, $17 < k < 23$ cm^{-1} for panel a) and $45 < f < 55$ kHz for panel b). By defining the spectral resolution as the $1/e$ width of the peak of the spectral response, we can compare the effectiveness of each technique. We define the spectral contamination (or side-lobe level) as the ratio between the peak power density and the average power density outside of 1 spectral resolution from the peak. Table 5.2 lists the spectral resolution and contamination performance in both temporal and spatial domains for the cases of rectangular window, Hann window, MEM ACF, and MEM Burg.

By looking at the results of the Rectangular vs. the Hann window, we can see

Table 5.2: Estimates of Spectral Resolution and Spectral Contamination levels for Rectangular and Hann windowed Fourier based estimates, and both MEM estimates.

Technique	Resolution		Contamination	
–	Time	Space	Time	Space
Rect Window	5 kHz	7 cm^{-1}	60 dB	27 dB
Hann Window	8 kHz	9 cm^{-1}	80 dB	46 dB
MEM ACF	9 kHz	2 cm^{-1}	97 dB	76 dB
MEM Burg	10 kHz	2 cm^{-1}	62 dB	69 dB

the trade-off between resolution and contamination. The Hann window dramatically lowers the side-lobe level while decreasing the spectral resolution by less than a factor of 2. At the same time, by looking at the performance of the MEM estimates in the spatial domain, the spectral resolution is improved by roughly a factor of 4 over both Fourier based techniques, while providing the lowest contamination levels.

Using the same synthetic test signal, we can compute the spectral estimates from a *limited subset* that is typical of the more reliable PCI detector channels. This shows how robust and able to handle missing spatial samples each technique is. Only the spatial sampling is affected and the performance of each technique is roughly unchanged as can been seen in Fig. 5-3 a). The most noticeable effect is that the MEM spectra computed from the raw time series (MEM Burg) suffers from artifacts due to the missing spatial samples. The other techniques all use the autocorrelation function approach that compensates for missing spatial samples. The Hann window used in the spatial dimension is not as effective at suppressing the side-lobe level when missing samples are introduced, and the MEM spectra computed from the ACF have the best performance in both spectral resolution and contamination, both with and without missing spatial samples. This is the spectral estimation technique of choice when interested in fine scale spectral features, or when interested in small amplitude spectral features in the presence of larger amplitude modes.

Ultrasonic Calibration Test Signal

The power spectra estimation techniques were also bench-marked against one another using calibration measurements from the CW ultrasound loudspeaker tuned to
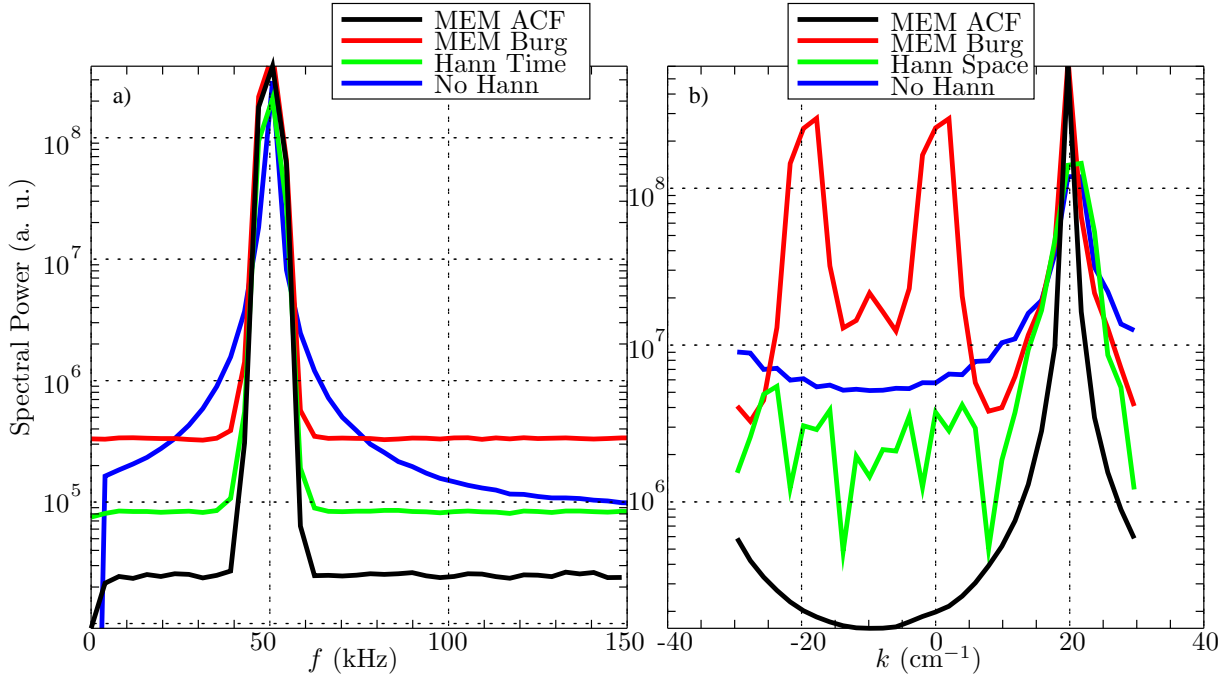
Figure 5-3: $S(f)$ integrated from $17 < k < 23$ cm^{-1} and b) $S(k)$ integrated from $45 < f < 55$ kHz computed using a reduced subset of spatial samples to simulate the actual PCI measurements. The MEM Burg estimate shows artifacts created by the missing spatial samples in combination of too high a pole order.

75 kHz (roughly 14 cm^{-1}). The MEM Burg estimate was not performed because the calibration data suffers from missing detector channels that can result in spectral artifacts as shown in Fig. 5-3 b). The other three spectral estimates are plotted in Fig. 5-4 below. The smallest spectral resolution in the spatial domain is still provided by the MEM ACF estimate; however, quantitatively the resolution is worse than for the synthetic data at only 3.5 cm^{-1}. This is an upper limit on the resolution as the test signal is not an infinite plane wave at a single wave-number, but has a finite width in wave-number due to the phase front structure launched by the loudspeaker. Again, the spectral contamination is lowest for the MEM ACF with a level of 46 dB, compared to 30 dB for the Fourier based estimates.
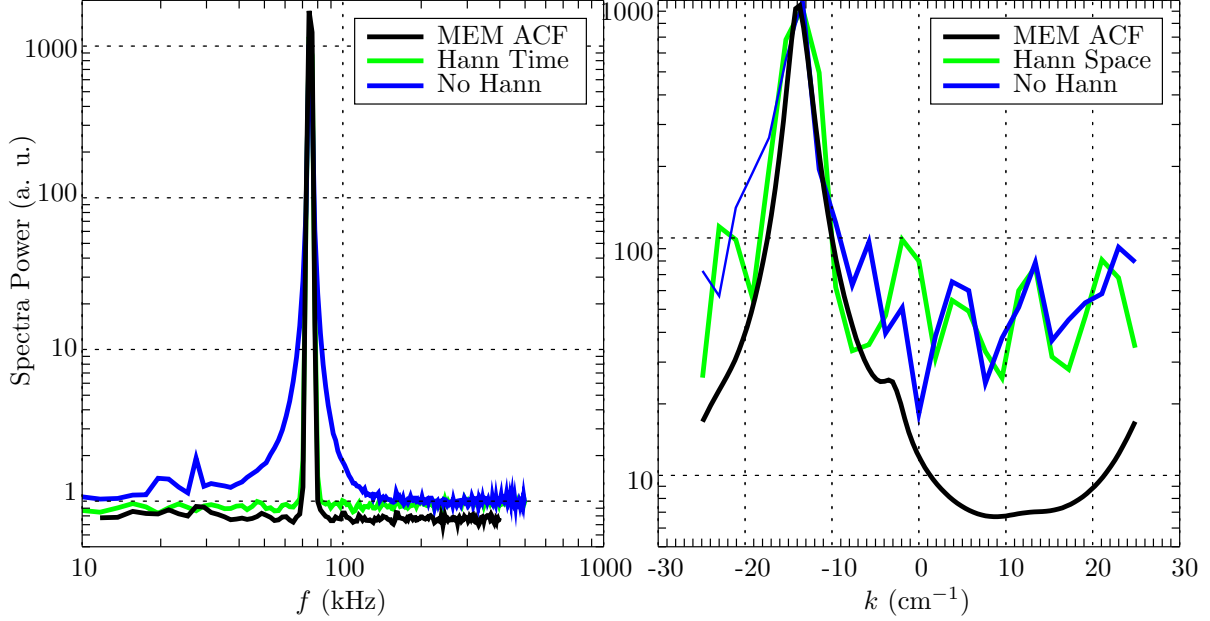
Figure 5-4: $S(f)$ integrated from $-17 < k < -11$ cm^{-1} and b) $S(k)$ integrated from $70 < f < 80$ kHz from the CW ultrasonic loudspeaker calibration data. The Hann window in space does not reduce the side-lobe contamination level. Again, the MEM ACF estimate outperforms the Fourier based estimates in both resolution and side-lobe level.

5.2 Introduction to Finite $k_{||}$ Turbulence

As discussed in Sec. 2.2 and depicted in Fig. 2-3, the rotating mask upgrade to the DIII–D PCI diagnostic enables us to measure turbulence as a function of propagation angle about the PCI chord. If turbulence propagates near perpendicular to the local magnetic field with $k_{||} \sim 0$ then there is a limited range in mask angle where $S(\alpha)$ is non-zero. This is due to the finite range in magnetic field pitch along the PCI chord and the finite width of the mask response function. In the sections that follow below, results are presented that show turbulence propagating at angles beyond the expected range that could be allowed by $k_{||} \sim 0$ modes. The implication is that these modes do not propagate near perpendicular to the local magnetic field and must have a finite and large wave-number component along the magnetic field, $k_{||}$.

Finite $k_{||}$ modes have been measured with the PCI diagnostic and the signals are observed to be relatively smaller in amplitude than the $k_{||} \sim 0$ main branch modes. Therefore we seek to verify that these measurements are indeed real plasma fluctua-

tions and not simply spectral contamination from the large amplitude main branch structures. The following data is presented from L-Mode plasmas during ohmic heating, neutral beam injection, and electron cyclotron heating (ECH) at various power levels. In Sec. 5.4, further data is presented from discharges before, and during, the ELM-free development of H-Mode plasmas.

The L-Mode plasma discharges used to study finite $k_{||}$ turbulence under different heating conditions are diverted in a lower single null configuration as shown in Fig. 5-5 a) from DIII–D run 20080624. This run day is of particular interest as there were
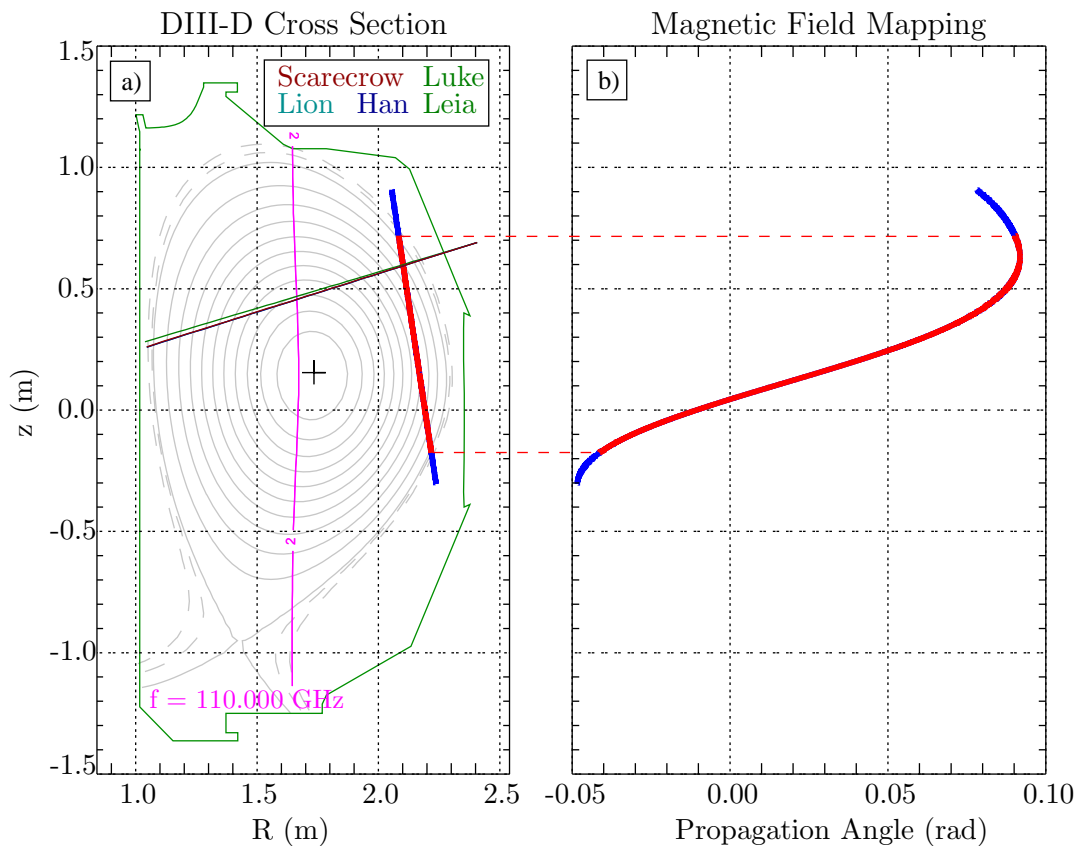
Figure 5-5: a) Plasma flux surfaces with PCI chord shown for lower single null diverted L-Mode discharge 133606. b) PCI chord mapping for $k_{||} \sim 0$ turbulence from chord height to propagation angle space. The mapping inside the LCFS is shown in red while outside is shown in blue. All ECH gyrotons aligned for deposition at $r/a \sim 0.3$.

many repeat shots with matched plasma conditions, and data was collected both with and without the rotating mask. Repeat shots allow averaging over multiple plasma discharges thereby improving power spectra estimations. The analyses presented

in the following sections use two mask sweeps during each plasma condition and are averaged over discharges 133606, 133609, and 133610. This results in improved signal-to-noise ratio of $\sqrt{6}$. These discharges also have a relatively low plasma current and thus weak poloidal field. The propagation angle of turbulence as a function chord height (if turbulence propagated near perpendicular to magnetic field) is plotted in Fig. 5-5 b) showing a narrow window in propagation angle of roughly 7.5°. By considering turbulence outside the LCFS, this total width in propagation angle can be increased by only 0.02 radians. This is because the decrease in poloidal field strength becomes more of a factor than the small change in geometry of the field lines.

The time evolution of shot 133606 is typical of this group of repeat shots (including 133609 and 133610) and is shown in Fig. 5-6. The main differences between these shots are in the details of the neutral beam heating segment, from roughly 3700-4200 ms, ranging from 2.5 MW of co-injection beams (133606) to balanced injection of 2.5 MW co and 2.5 MW counter (133609 and 133610). The timing of windows used for analysis are shown in shaded colors, gray during ohmic heating, green, blue and red during the three levels of increasing ECH heating (0.3, 1.3, and 1.6 MW respectively), and gold during neutral beam injection. Note that only shot 133606 stays in L-Mode during the NBI heating segment (this plasma condition is plotted as gold curves in what follows), and 133609 and 133610 are ELMing H-Modes. Due to nature of ELMs being large amplitude turbulence events localized in time, only data from the NBI heated discharge 133606 is presented.
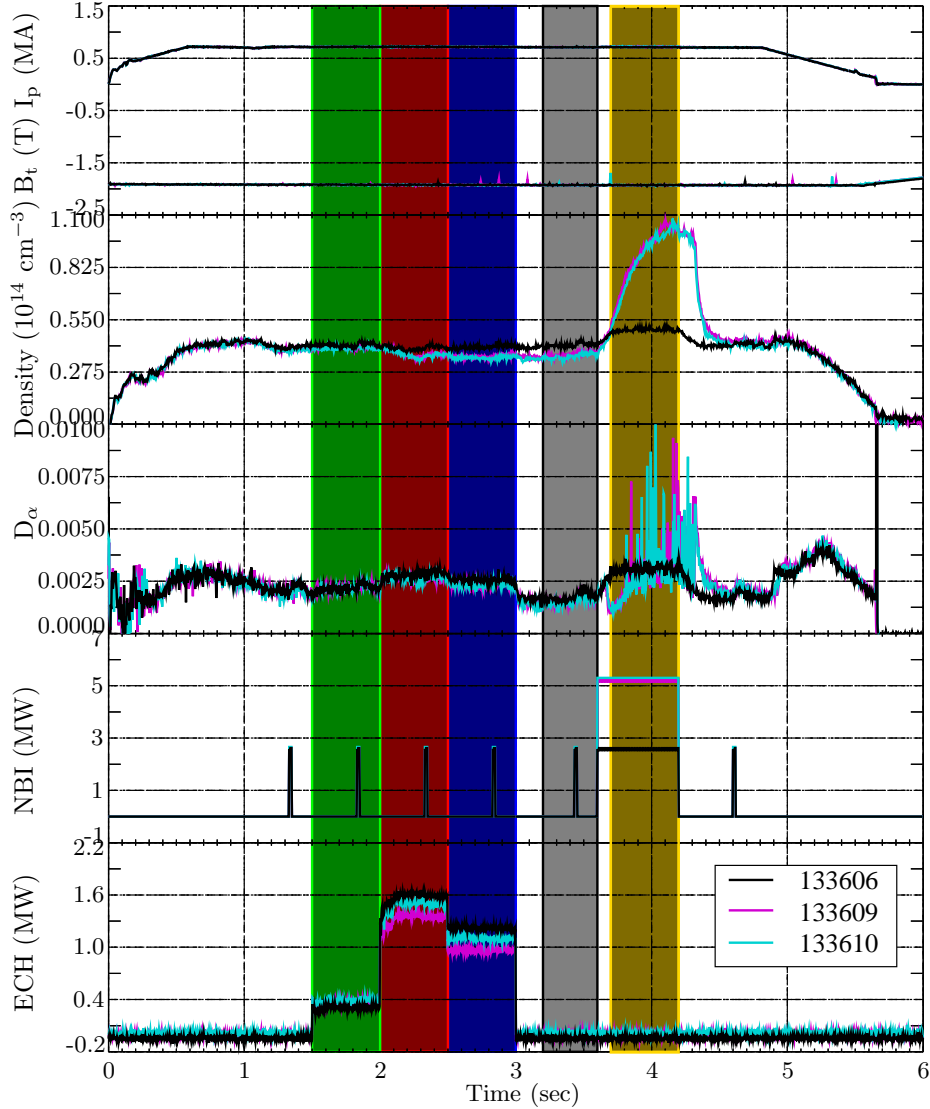
Figure 5-6: Plasma conditions during DIII–D discharges 133606, 133609, and 13310 shown in black, magenta, and cyan, respectively. Analysis windows shown in shaded boxes.

5.3 Localized Wave-number and Frequency Modes

One of the most striking features of the new PCI measurements that utilize the rotating mask upgrade is the increase in power of short wavelength turbulence ($|k| \gtrsim 15$ cm^{-1}) with both ECH and NBI heating in L-Mode plasmas. These modes appear to be localized in both wave-number and mask angle spaces, and somewhat loosely localized in frequency. This section presents measurements of two such modes during the set of lower single null L-Mode discharges shown in Figs. 5-5 and 5-6.

The first mode (referred to as the high-k mode) is most visible during the two highest levels of ECH heating as well as during NBI heating in L-Mode, however it is not present during NBI heating in H-Mode discharges. These high-k modes exists over roughly $-24 < k < -18$ cm^{-1} in wave-number, and $-0.3 < \alpha < 0.35$ radians in mask angle, and are visible from roughly 100 kHz to beyond 400 kHz where the PCI signal-to-noise ratio becomes unity.

The second mode (referred to as the medium-k mode) is only visible in the frequency range of $200 < f < 400$ kHz, and wave-number range $14 < k < 17$ cm^{-1}. What makes the medium-k modes particularly interesting is the high level of asymmetry with respect to mask angle, existing over $-0.40 < \alpha < -0.10$ radians. Such an asymmetry is in stark contrast to the mask angle response of the main branch features described in Sec. 4.1.2.

5.3.1   Observation of high-k modes

The high-k modes are seen during both ECH and NBI heating as an increase in turbulence power over the specific range in wave-number and mask rotation angle as previously described. Because this mode is asymmetrical in propagation direction ($\pm k$ direction), it is convenient to plot the relative power spectra of the positive and negative wave-numbers as shown in Fig. 5-7. For reference, panel a) plots the MEM power spectra at low-k showing the LCFS-aligned edge turbulence of the main branches. Panel b) plots the power spectra at medium-k showing the background turbulence structure (discussed further in Sec. 5.4) that is mostly symmetrical in propagation direction. Finally, panel c) plots the high-k response where we can see the increase in turbulence power (highlighted by the vertical blue lines) over the mask angle range $-0.3 < \alpha < 0.35$. This increase in turbulence power in the negative propagating direction scales with heating power as will be shown in what follows.

We show the high-k mode wave-number and frequency space ranges in Fig. 5-8 by the light blue and light red boxes with white borders. The mode amplitude increases with heating power, however the significance of the increase varies with mode frequency - we therefore perform analysis in two frequency ranges $100 < f < 200$ kHz
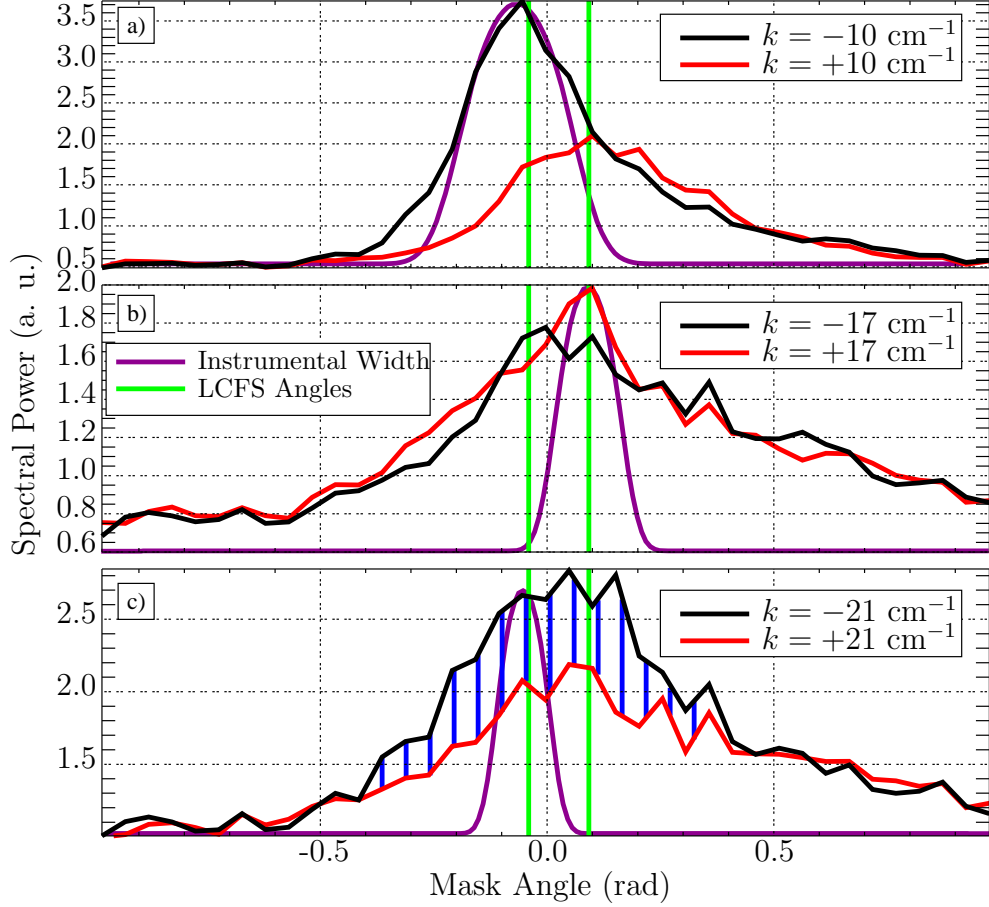
Figure 5-7: MEM power spectra plotted as a function of mask angle and integrated over frequencies $200 < f < 400$ kHz. a) low-k spectra showing edge aligned main branch turbulence, b) medium-k spectra showing symmetry between positive and negative propagating directions, and c) increase in turbulence power due to the high-k mode propagating in the negative direction. Vertical green lines show the LCFS mapping in mask angle, and vertical blue lines highlight the high-k mode extent in mask angle. Magenta curves are the mask response function at each wave-number.

and $200 < f < 400$ kHz. Figure 5-8 plots the MEM power spectrum estimate $S(k, f)$ integrated over the range in mask angle $-0.15 < \alpha < 0.25$ rad, for the Ohmic heating case in panel a) and the highest level of ECH heating (1.6 MW) in panel b). We can see the increase in mode amplitude both above and below 100 kHz when ECH heating is applied. As a function of frequency, the high-k mode remains at a relatively constant wave-number, indicating a group velocity of nearly zero. This is in clear contrast to the group velocity measurements of the main branches shown in Fig. 4-1. If this feature were due to spectral contamination or a harmonic from the main branches,
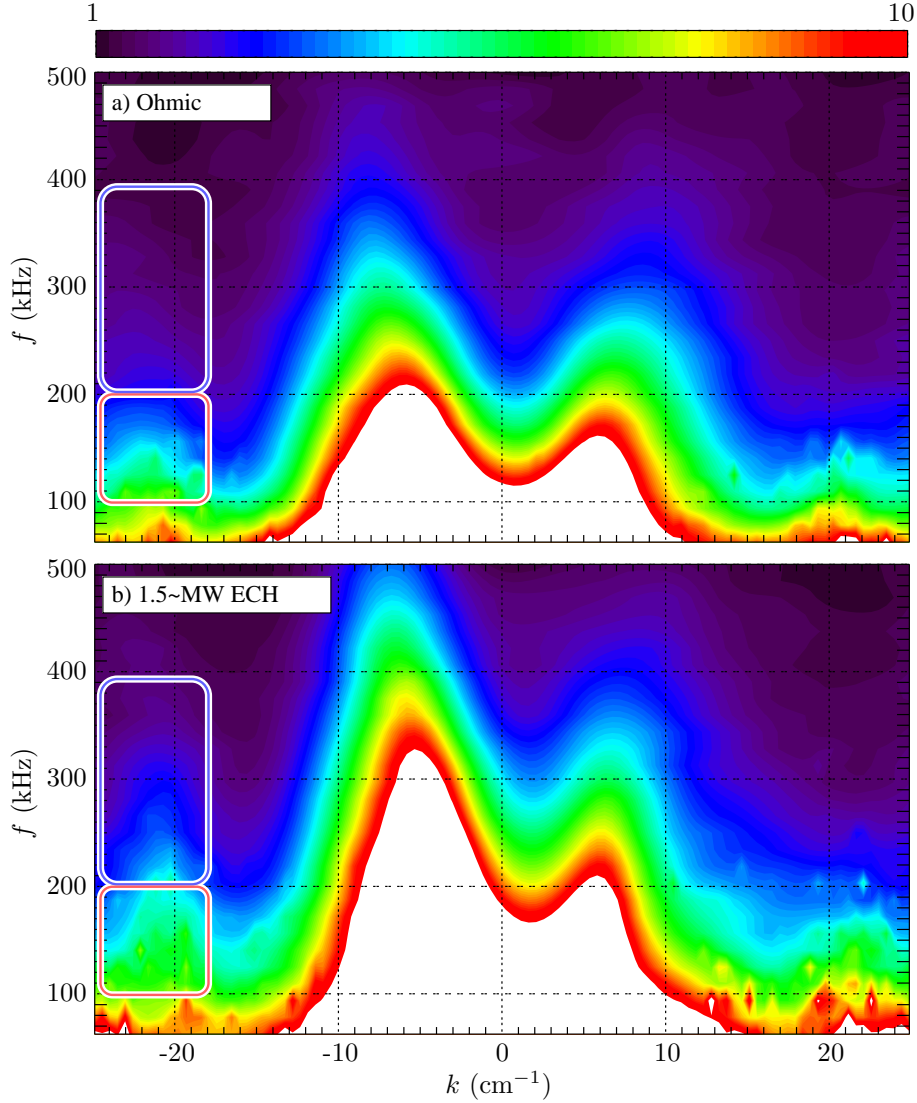
Figure 5-8: Power spectra computed using the MEM estimate during a) Ohmic heating and b) the high power ECH heating. Spectra are integrated over mask angle $-0.15 < \alpha < 0.25$ rad.

one would expect the mode to have a similar, or an integer multiple of, the main branch group velocity. This suggests that the high-k mode is unique and separate from the main branches.

In Fig. 5-9, we now plot the same MEM power spectra, during Ohmic heating in panel a) and 1.6 MW of ECH heating in panel b), as a function of wave-number and mask angle, integrated over the higher frequency range $200 < f < 400$ kHz. The black box with white border highlights the wave-number and mask angle ranges
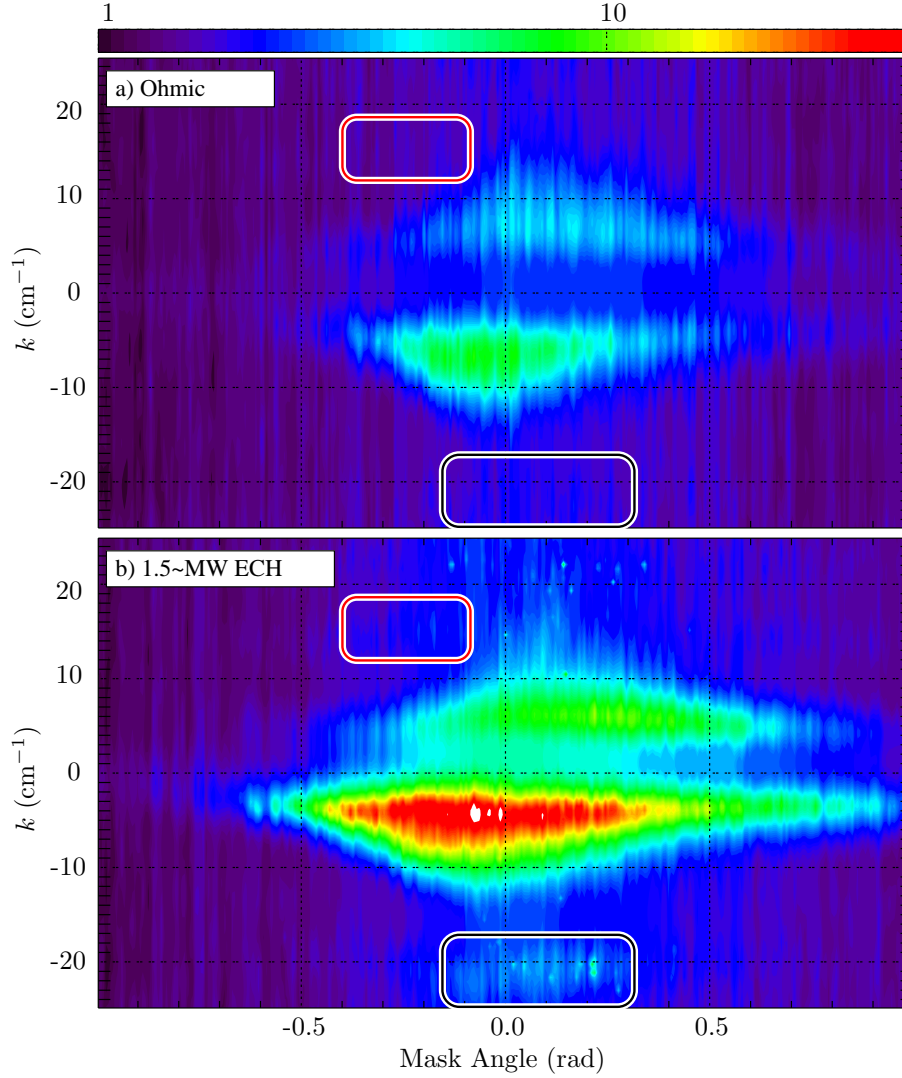
Figure 5-9: MEM power spectra estimate integrated over $200 < f < 400$ kHz shown during Ohmic and ECH heating in panel a) and b) respectively. The high-k and medium-k modes are shown in the black and red boxes, respectively.

of the high-k mode. We also highlight the medium-k mode with the red box with white border - the medium-k mode is discussed subsequently. Again, both plots use the same logarithmic color scale. As a side note, the ECH power increases the turbulence amplitude of the main branch structures, here at $|k| < 14$ cm^{-1}. The ECH heating also increases the turbulence amplitude of the high-k mode visible from $-24 < k < -18$ cm^{-1} and from $-0.15 < \alpha < 0.3$ radians - the apparent speckle is due to the color scale; the increase in amplitude is best seen in Fig. 5-7. The peak in the high-k response appears to be centered near mask angle of 0.1-0.2 radians while the

peak in the negative wave-number branch of the main branches is at a mask angle of -0.1 radians. If the high-k mode were due to spectral contamination, then we would expect these peaks to coincide. Again, this suggests that the high-k mode is unique from the low-k main branch structures.

The frequency response of the high-k mode is shown in Fig. 5-10 by plotting the
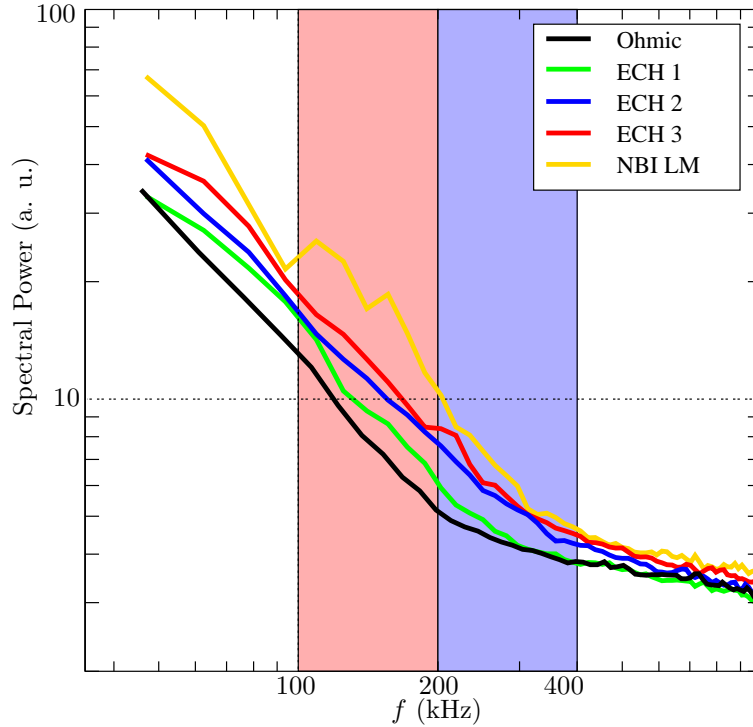
Figure 5-10: MEM power spectra estimates of all heating conditions integrated over mask angle $-0.15 < \alpha < 0.25$ radians and wave-number $-23 < k < -19$ cm^{-1}.

power spectra integrated over the ranges previously described in wave-number and mask angle. The light red background highlights the low frequency range $100 < f < 200$ kHz while the light blue highlights $200 < f < 400$ kHz. In the low frequency range the mode increases in amplitude with increasing heating power and furthermore, shows a dramatic increase in amplitude with NBI heating power in L-Mode. This shows how difficult it is to resolve spectral features based on frequency spectra alone, highlighting one of the strengths of PCI as a diagnostic technique - simultaneous measurements that span a range in wave-number space and, with the use of the rotating mask, mask angle space.

The high-k mode peak wave-number is roughly $k \sim -21$ cm^{-1}, as shown in

Fig. 5-11, where the power spectrum is plotted as a function of wave-number $S(k)$,
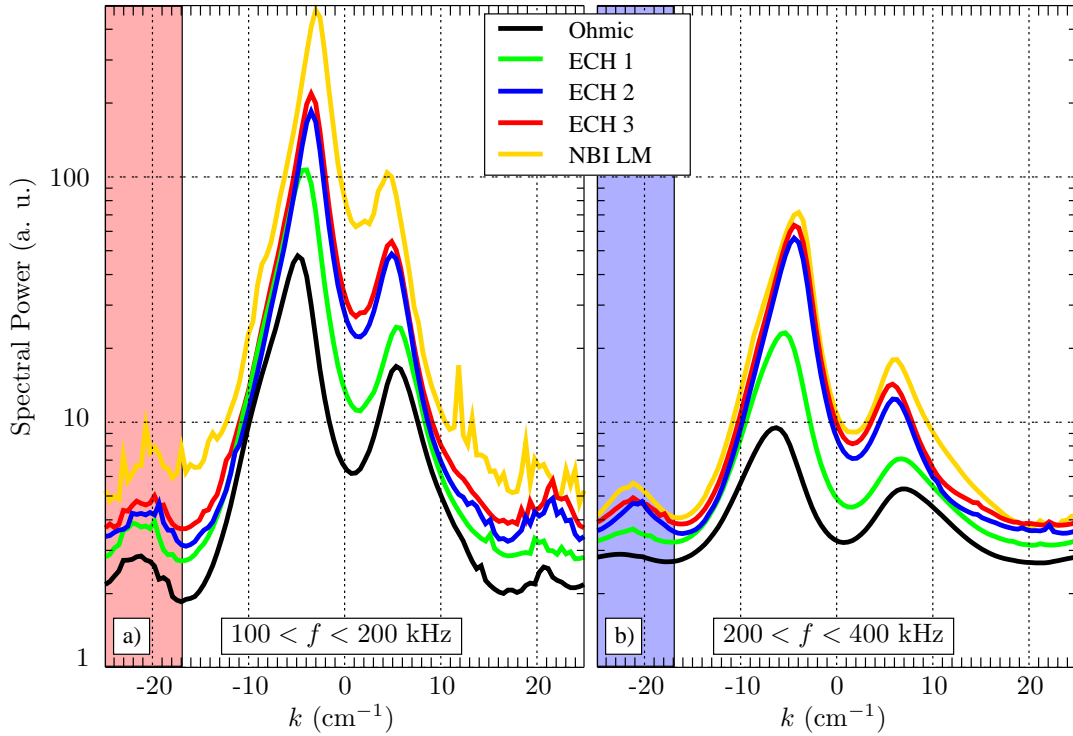
Figure 5-11: MEM power spectra estimates plotted vs. wave-number for mask angle of $-0.15 < \alpha < 0.25$, and frequency of a) 100-200 kHz and b) 200-400 kHz. The high-k mode region in wave-number is highlighted by the light red and blue backgrounds showing increased amplitude with increased levels of heating.

integrated over mask angle and frequency. Again, the light red background highlights the mode in panel a) integrated over the frequency range from 100 - 200 kHz while the light blue background in panel b) highlights the mode amplitude integrated over the frequency range from 200 - 400 kHz. In the lower frequency range, the mode is present during Ohmic heating and increases in amplitude with ECH heating. The same large amplitude response we saw in the frequency spectra plotted in Fig. 5-10 with NBI heating in L-Mode is also seen in the wave-number spectra. Panel b) shows that the high-k mode is small or barely present during ohmic heating but increases significantly in amplitude with applied ECH heating. In the higher frequency range, the NBI heated amplitude is significantly closer to that of the highest power of ECH heating.

Figure 5-12 plots the MEM power spectra estimates in plasmas with Ohmic and

ECH heating, along with the MEM estimate of the power spectra from calibration data (in dark magenta) using the CW ultrasonic loudspeaker. We see that the cal-
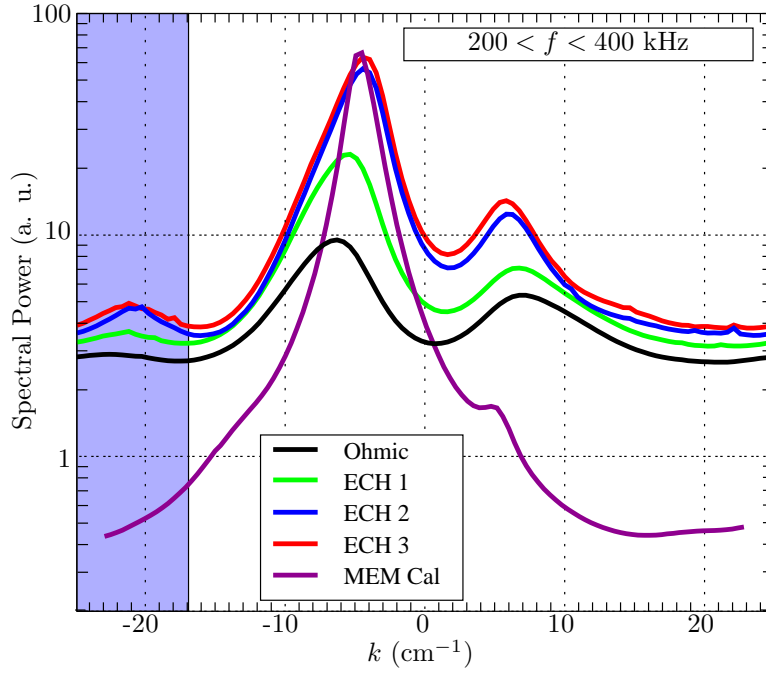
Figure 5-12: Comparison of Ohmic and ECH heating power spectra with MEM power spectra of a single frequency and wave-number mode generated using the CW ultrasound loudspeaker. Side-lobe levels from ultrasound calibration are an order of magnitude lower than the high-k mode power level, showing high-k mode is not due to spectral contamination.

ibration spectrum estimate of the side-lobe levels are an order of magnitude lower than the amplitude of the of the high-k mode measured in the presense of plasma.

To briefly summarize, we have shown that for the high-k modes, the group velocity (see Fig. 5-8) and mask angle range (Fig. 5-9) are starkly different from that of the main branch structure. We have also shown in Fig. 5-11, that the spectral power of the high-k modes respond to plasma conditions with increased amplitude associated with increased heating power levels. Finally, we have shown that the high-k mode power is an order of magnitude higher than the expected side-lobe level of the main branch. We therefore conclude that the high-k mode is real plasma turbulence and not an artifact or spectral contamination of the near perpendicularly propagating main branch structure.

5.3.2 Estimate of $k_\parallel$ for high-k modes

We now turn to estimating the magnitude of $k_\parallel$ needed to account for the large range in mask angle covered by the high-k mode. Figure 5-13 plots the MEM power spectra as a function of mask angle during the Ohmic and the 3 increasing power levels of ECH heating. Plotted as black lines are the power spectra estimates showing the
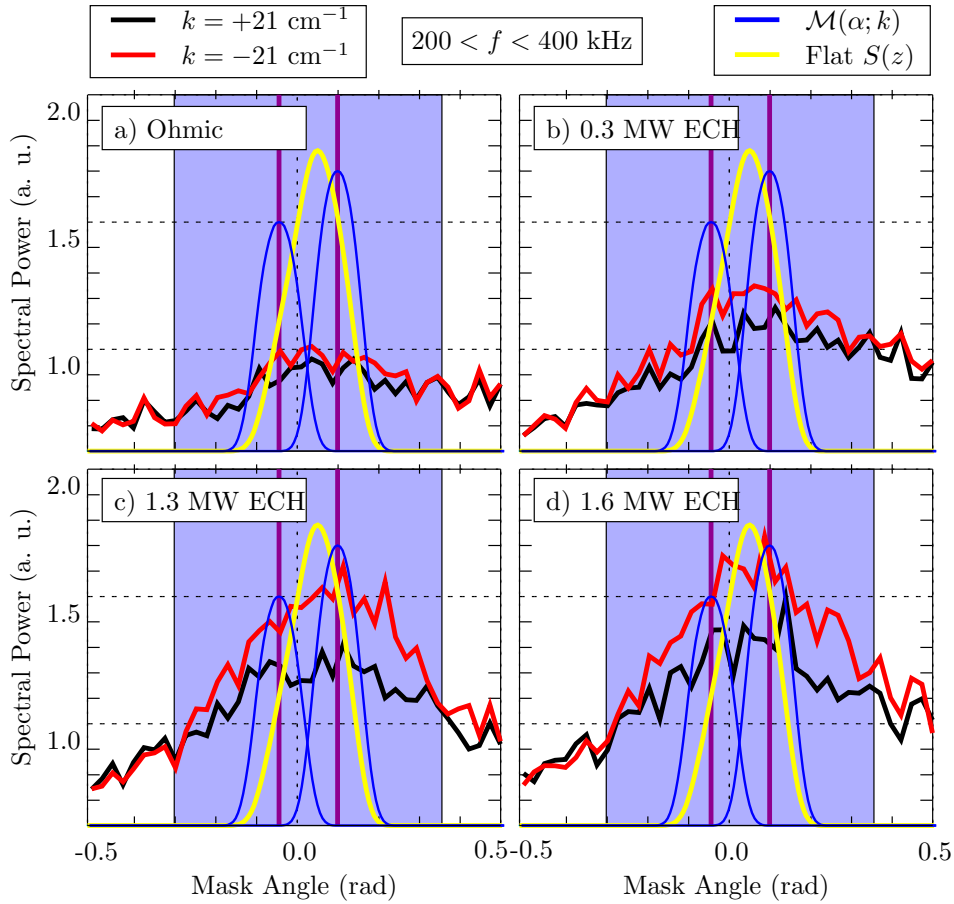
Figure 5-13: MEM power spectra as a function of mask angle during a) Ohmic and b)-d) the 3 power levels of ECH heating. Red lines are integrated over the wave-number range $-23 < k < -19$ cm^{-1} showing the high-k mode, while black lines show the response in the absence of the high-k mode and are integrated over $+19 < k < +23$ cm^{-1}. The high-k mode shows up as "bubble" on top of the broad background structure introduced in Sec. 4.1.2 and discussed in detail in Sec. 5.4. This bubble extends in mask angle from -0.3 to +0.35 radians, or roughly -13 to +15 degrees.

positive propagating wave-number response integrated from $+19 < k < +23$ cm^{-1}. This is useful because it enables us to see the difference between the broad background turbulence (that will be described in detail in Sec. 5.4) and the "bubble" on top of

this background that represents the high-k mode. By "bubble", we are referring to the increase in turbulence power indicated by the shaded region in Fig. 5-13 and the vertical blue lines in Fig. 5-7. Figure 5-13 plots the MEM power spectra estimate $S(\alpha)$ integrated over the high frequency range of 200 - 400 kHz. The black lines are the power spectra at $k \sim +21$ cm^{-1}; these spectra are nearly constant with wave-number as seen in Fig. 5-11 b), and therefore they represent an estimate of finite $k_{||}$ background turbulence spectra. The increased amplitude of the red lines ($k \sim -21$ cm^{-1}) above the background level is highlighted with the light blue box, and is due to the high-k mode. This "bubble" extends in mask angle over the range $-0.3 < \alpha < 0.35$ radians or approximately -13 to +15 degrees.

Figure 5-13 also plots the mask response function $\mathcal{M}(\alpha)$ centered at the LCFS's (blue curves) and also a model of the expected spectral response (yellow curve) that assumes that the turbulence amplitude is constant as a function of chord height (z). The comparison between the high-k mode in mask angle vs. what is expected if turbulence propagated near perpendicular to the magnetic field with $k_{||} \sim 0$ can be seen by comparing the flat $S(z)$ spectra with the ECH heated power spectra. The mask response function at $k = 21$ cm^{-1} falls to zero by 0.1 radians. The high-k mode extends from $-0.3 < \alpha < 0.35$ radians with the LCFS mapping at roughly -0.05 and 0.1 radians. This shows that the high-k mode extends in mask angle nearly 0.15 radians beyond what is possible if $k_{||} \sim 0$. This allows us to estimate the size of the parallel wave-number, $k_{||}/k \sim 0.15$.

For completeness, the NBI heated power spectra are shown as a function of mask angle in Fig. 5-14 during L-Mode (gold curve) while the ohmic and highest power level ECH heating responses are shown for reference. The high-k mode "bubble" indicates that the presence of the high-k mode is visible during NBI heating in L-Mode.
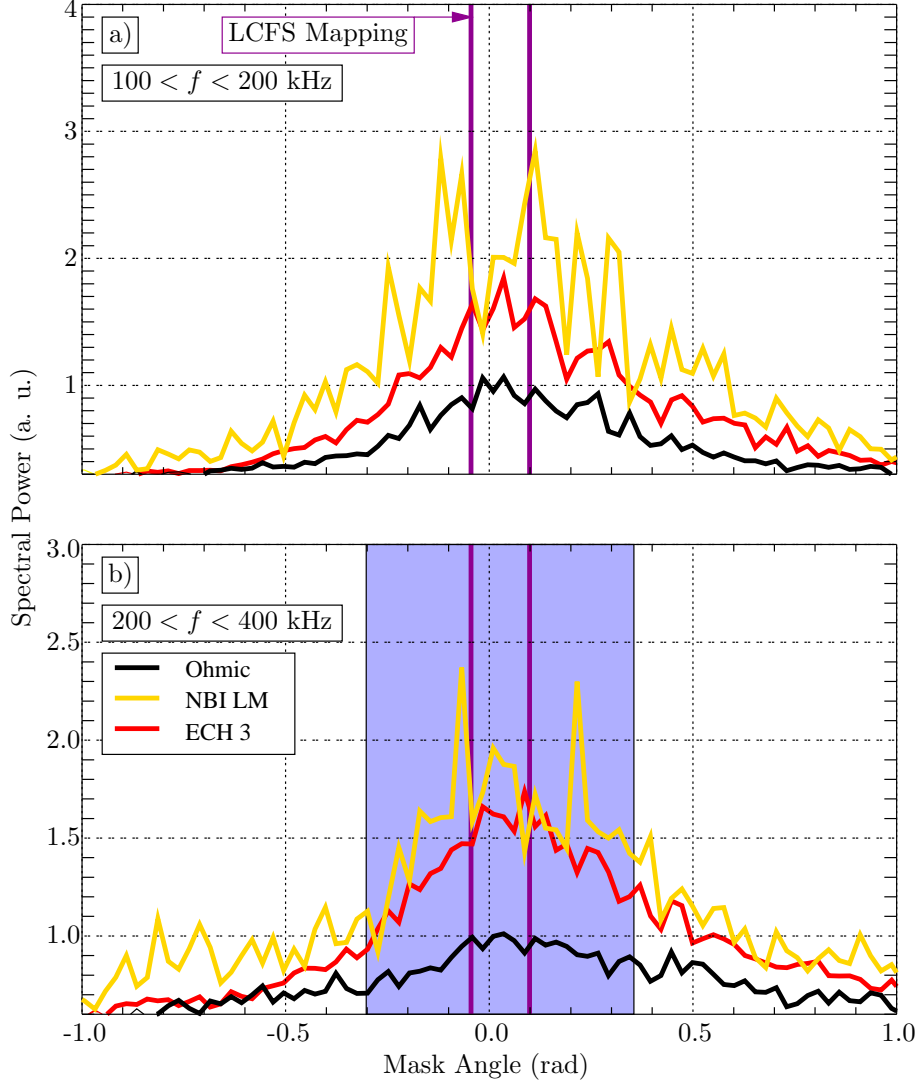
Figure 5-14: Power Spectra using MEM estimate showing the mask angle response of NBI heated plasma. The high-k "bubble" is present during the NBI heating at a similar level to the highest power level ECH heating.

5.3.3 Observation of medium-k modes and $k_{||}$ estimate

The medium-k mode regime, with the spectrum integrated over frequencies from $200 < f < 400$ kHz and wave-numbers from $+14 < k < +17$ cm^{-1}, is shown in Fig. 5-15. The region in wave-number and mask angle is shown in Fig. 5-9 using the red box. The dashed lines correspond to the spectra integrated over negative wave-numbers showing the background turbulence structure. The increase in turbulence level over $-0.4 < \alpha < -0.1$ rad in mask angle shows the asymmetrical region in mask
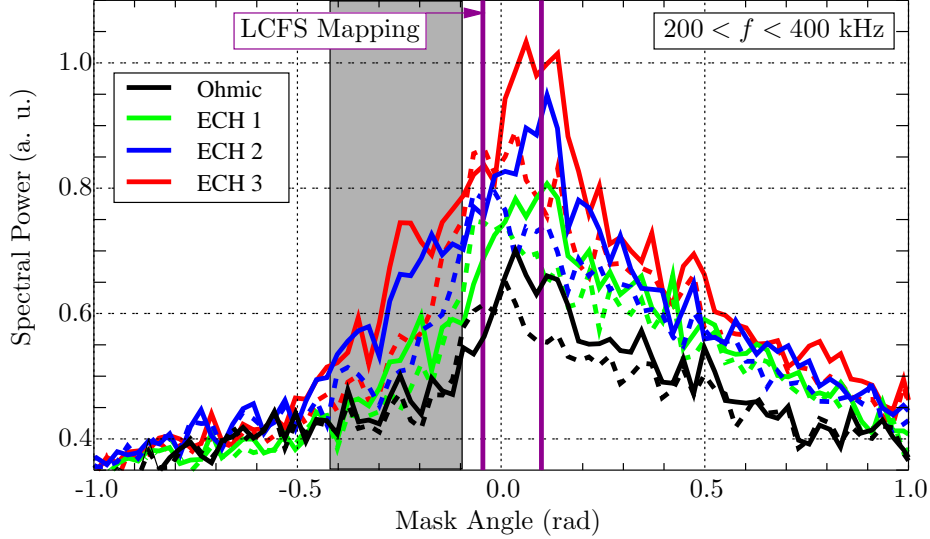
Figure 5-15: MEM power spectra estimate of ohmic and ECH heating of the medium-k mode plotted vs. mask angle. Data is integrated over $200 < f < 400$ kHz and wave-number from $+14 < k < +17$ cm^{-1} (solid lines) and $-17 < k < -14$ cm^{-1} (dashed lines). The dashed lines show the background turbulence response while the solid lines an asymmetrical increase in turbulence amplitude from $-0.4 < \alpha < -0.1$ radians.

angle where increased levels of heating result in enhancement of the medium-k mode.

5.4   Finite $k_{||}$ Background Turbulence

Section 4.1.2 introduced another example of PCI measurements that show significant signal at large mask angles. Indeed, these angles are larger than would be possible from turbulence propagating near perpendicular to the magnetic field, and therefore must have a wave-vector component along the local magnetic field ($k_{||}$). This background turbulence level is broad in mask angles and is seen to extend to angles as large as 0.5-0.8 rad. In this section we characterize the background turbulence structures as functions of the three dimensional PCI measurement space; frequency, wave-number, and mask angle. We find that the finite $k_{||}$ background turbulence does not scale with wave-number in any meaningful way, while the peak amplitude decreases and the width of the structure weakly decreases with increasing frequency.

The finite $k_{||}$ background is present throughout the wave-number space, including

the long wavelength ($|k| < 10$ cm^{-1}) region of the spectrum where the large amplitude main branch signal (discussed in Sec. 4.1.2) exists. The finite $k_{\parallel}$ background turbulence is shown with the blue curve in Fig. 5-16 along with the main branch signal plotted for $k = 10$ cm^{-1}. The background turbulence is a structure that peaks near
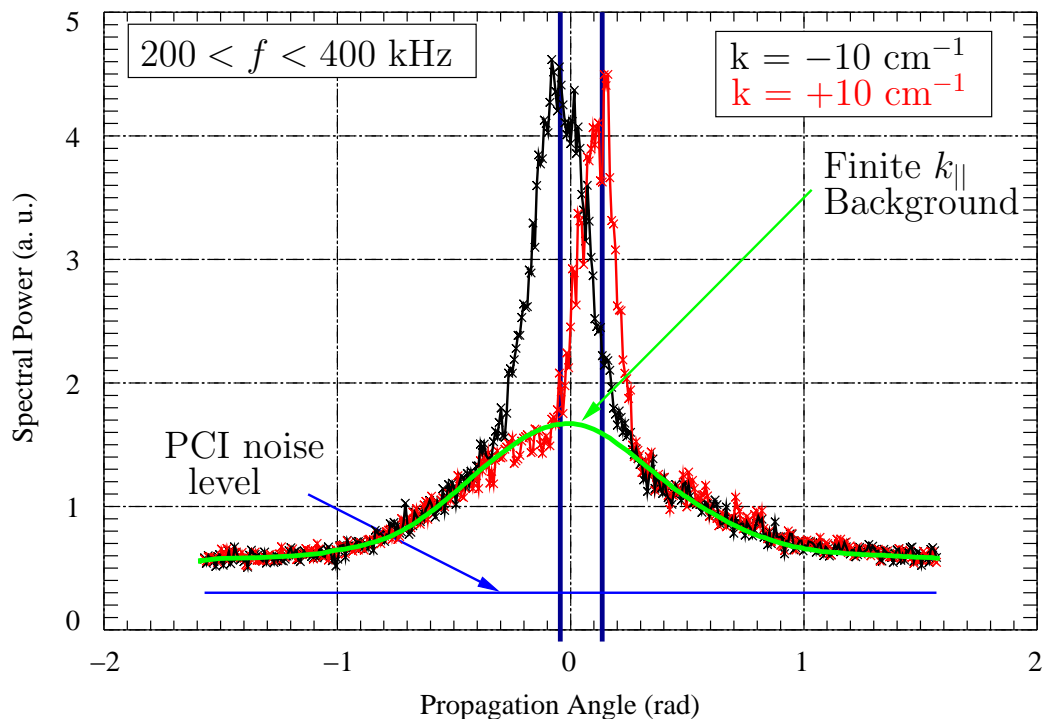
Figure 5-16: L-Mode turbulence power spectra integrated over frequencies $200 < f < 400$ kHz and plotted for $k = \pm 10$ cm^{-1} showing a broad, finite $k_{\parallel}$, background turbulence structure (shown in blue) with the edge aligned main branch structure on top.

the center of the plasma chord mapping, and decreases in amplitude with a full width at half maximum (FWHM) from 0.25-0.5 radians. The FWHM is more dependent upon plasma conditions than upon wave-number or frequency. In plasma conditions where the high-k and medium-k modes are not present, the finite $k_{\parallel}$ background turbulence is the dominant feature at short wavelengths (*i.e.* above the main branch maximum wave-number, $|k| \gtrsim 15$ cm^{-1}).

In Sec. 3.4.1, we computed the PCI signal response due to finite sized detector elements ($\mathcal{D}_c$) given by Eq. 3.6. This response was shown to decrease with increasing mask angle, the rate of decrease becoming stronger with increasing wave-number

and increasing cylindrical lens gain. In the same section, we also showed that wave-number measured by the PCI is given by $k_{PCI} = k \cos(\alpha)$ where k is the wave-number in the plasma. To determine how these effects vary with mask angle, we consider the response at fixed wave-number as measured by the PCI diagnostic, k_{PCI}.

The first effect is how the power spectra conserves power under the change of variables to k_{PCI}. This is given by $S(\alpha, k) \ dk = \bar{S}(\alpha, k_{PCI}) \ dk_{PCI}$. Therefore the measured power spectra $\bar{S}$ shows an apparent increase in power due to the larger differential width in wave-number at increased mask angle

$$\bar{S}(\alpha, k_{PCI}) = \frac{1}{\cos(\alpha)} S(\alpha, k) = \frac{1}{\cos(\alpha)} S\left(\alpha, \frac{k_{PCI}}{\cos(\alpha)}\right). \tag{5.2}$$

The second effect is that the mask response function becomes more narrow as the real wave-number increases with mask angle at fixed apparent wave-number k_{PCI}. The power spectra are computed at constant k_{PCI} and the width of the mask response function $\mathcal{M}$ scales with wave-number as $1/k$ as shown in Fig. 3-20. In the limit of narrow mask response ($k \gtrsim 20 \ \mathrm{cm}^{-1}$) $\mathcal{M}$ can be approximated as

$$\mathcal{M}(\gamma - \delta, k_{PCI}) \approx \frac{C_M}{k} \delta(\gamma - \alpha) = \frac{C_M \cos(\alpha)}{k_{PCI}} \delta(\gamma - \alpha), \tag{5.3}$$

where C_M is a constant and we use the Dirac delta-function to represent the mask response in the high-k limit, and the $\cos(\alpha)$ term shows the smaller mask response width.

Recalling Eq. 2.45, the power at the detector plane in a given mode propagating with wave-number in the plasma k and mask angle α is given by

$$\hat{S}(\gamma, k_{PCI}) = \int d\alpha \ \bar{S}(\alpha, k_{PCI}) \ \mathcal{M}(\gamma - \alpha, k_{PCI}) \approx \frac{C_M \hat{S}\left(\gamma, \frac{k_{PCI}}{\cos(\alpha)}\right)}{k_{PCI}}. \tag{5.4}$$

Therefore, the smaller width of the mask response function cancels with the larger differential width in wave-number space. Thus, the only effect of consequence is due to the finite sized detector elements $\mathcal{D}_c$.

Figure 5-17 compares the finite $k_\parallel$ background turbulence with the finite size de-

tector element term $\mathcal{D}_c$. The red and black curves are the positive and negative
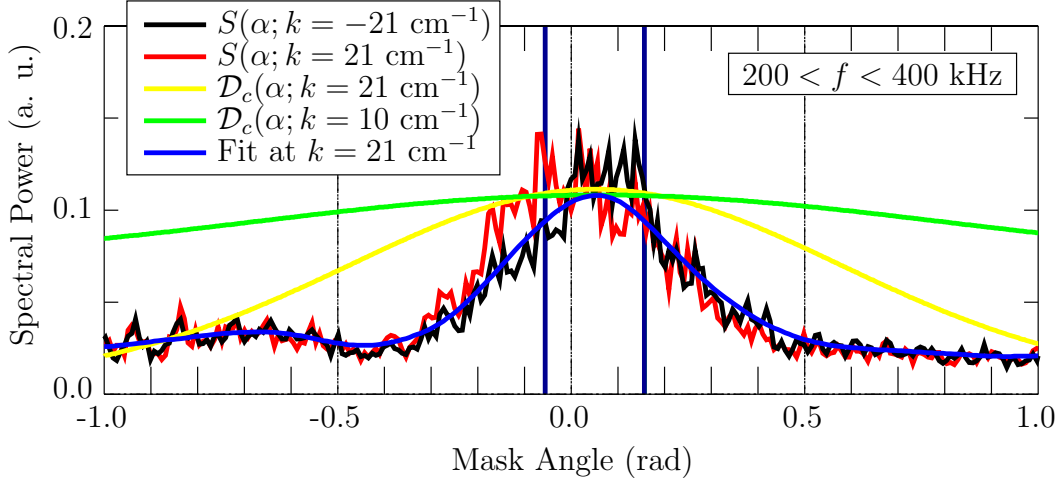
Figure 5-17: L-Mode turbulence power spectra (red and black curves) with broad finite $k_{||}$ background estimate (blue curve). The background turbulence is significantly more narrow than the width of the finite sized detector element effect ($\mathcal{D}_c$) plotted in green and yellow for $k = 10$ and $k = 21$ cm^{-1} respectively.

propagating directions at $k_{PCI} = 21$ cm^{-1} with the estimate of the background turbulence plotted in blue. The response due to the finite size of detector elements is plotted in green and yellow for wave-numbers $k = 10$ and $k = 21$ cm^{-1} respectively. The background turbulence response is significantly more narrow than the suppres-
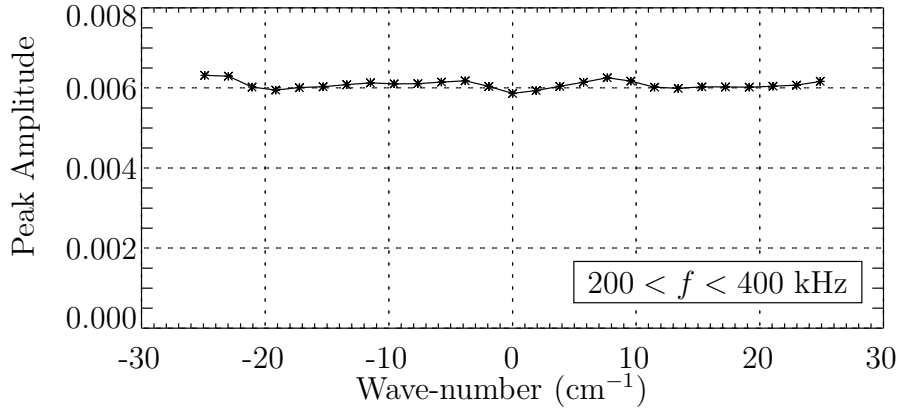
Figure 5-18: Peak amplitude of the finite $k_{||}$ background turbulence estimate plotted vs. wave-number and integrated over frequencies $200 < f < 400$ kHz.

sion imposed by finite sized detector elements. In addition, the peak amplitude of the finite $k_{||}$ background turbulence does not scale with wave-number as shown in

Fig. 5-18 (*i.e.* $\hat{S}(\gamma, k)$ does not depend on k). Therefore, the decrease in amplitude is due to the actual angular dependence of the turbulence itself.
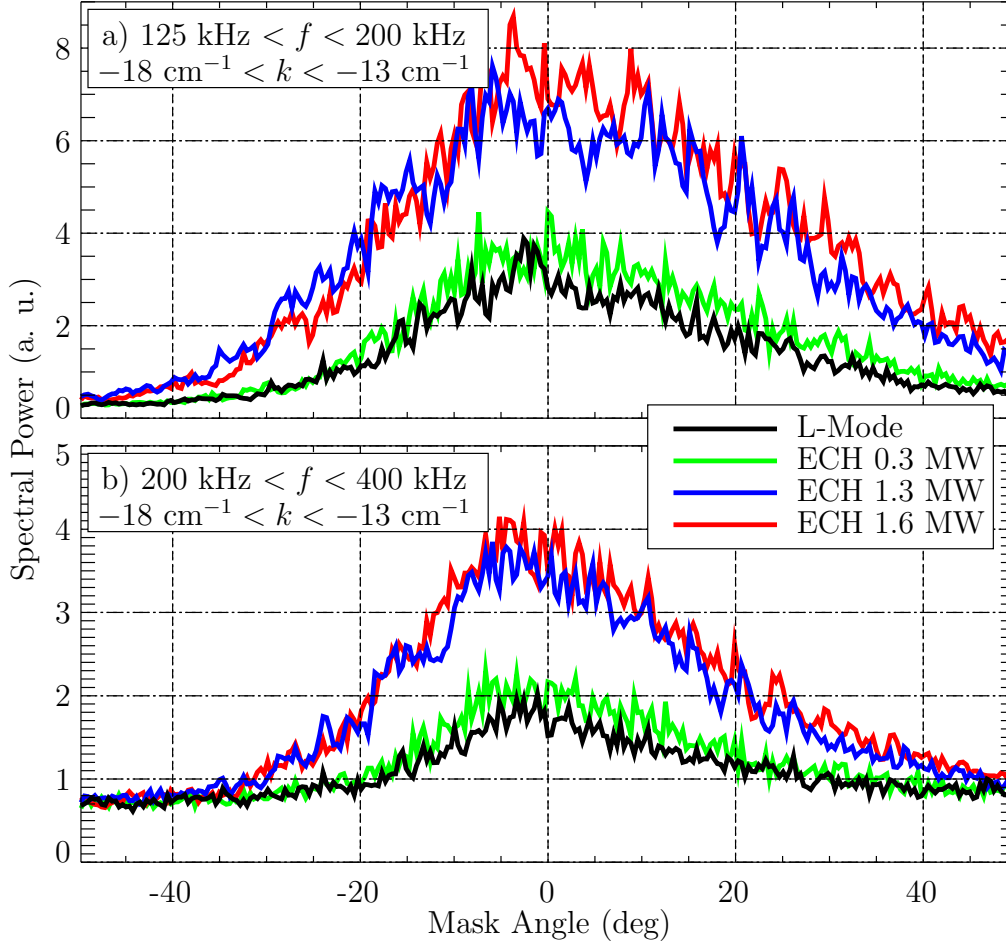
Figure 5-19: Finite $k_{||}$ background turbulence plotted during Ohmic and ECH heating plasma conditions. Background turbulence amplitude scales with applied ECH heating power.

The finite $k_{||}$ background turbulence increases in amplitude with applied electron heating. Using the same ECH heated plasma discharge as discussed previously (see Fig. 5-6), Fig. 5-19 plots the finite $k_{||}$ background turbulence vs mask angle during Ohmic, and three ECH power levels during an L-Mode plasma. The applied heating does not change the background turbulence structure, but causes an overall increase in turbulence amplitude.

5.4.1 Background turbulence during L-H transition

It is well known that turbulence is suppressed when the plasma undergoes an L-Mode to H-Mode transition [78]. We examine the suppression of the finite $k_{||}$ background turbulence over two frequency ranges, $125 < f < 200$ kHz and $200 < f < 400$ kHz in figure Fig. 5-21a and Fig. 5-21b respectively. Figure 5-20 plots the plasma parameters during the plasma discharge showing the L-H transition at 1.05 sec marked by the decrease in D_α emission and the rise in density. The finite $k_{||}$ background turbulence
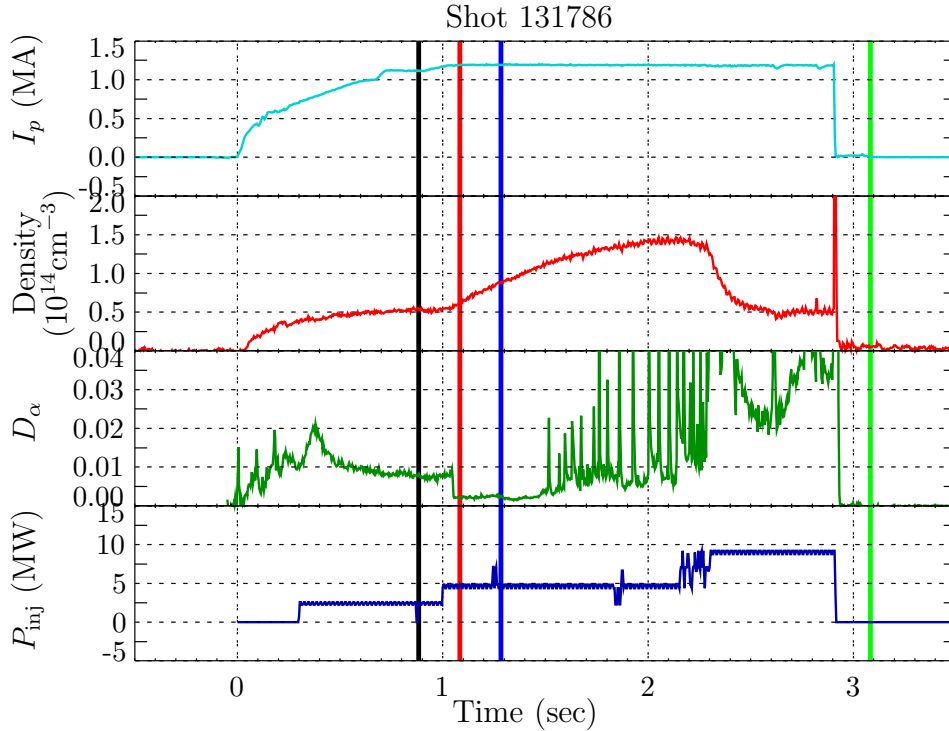
Figure 5-20: Plasma discharge used to study the finite $k_{||}$ background turbulence response to an L-H transition. Vertical lines indicate the plasma conditions where the background turbulence is estimated.

was estimated as a function of mask angle at 4 different times during the discharge shown with the vertical black, red, blue, and green lines corresponding to prior to the L-H transition, just after the L-H transition, as the H-Mode is developing before ELMs, and after the plasma disrupted. This allows us to compare the time evolution across the L-H transition of the background turbulence amplitude.

The finite $k_{||}$ background turbulence is plotted as a function of mask angle in Fig. 5-

21, shown for the 4 times corresponding to the vertical lines in Fig. 5-20. Panels a) and
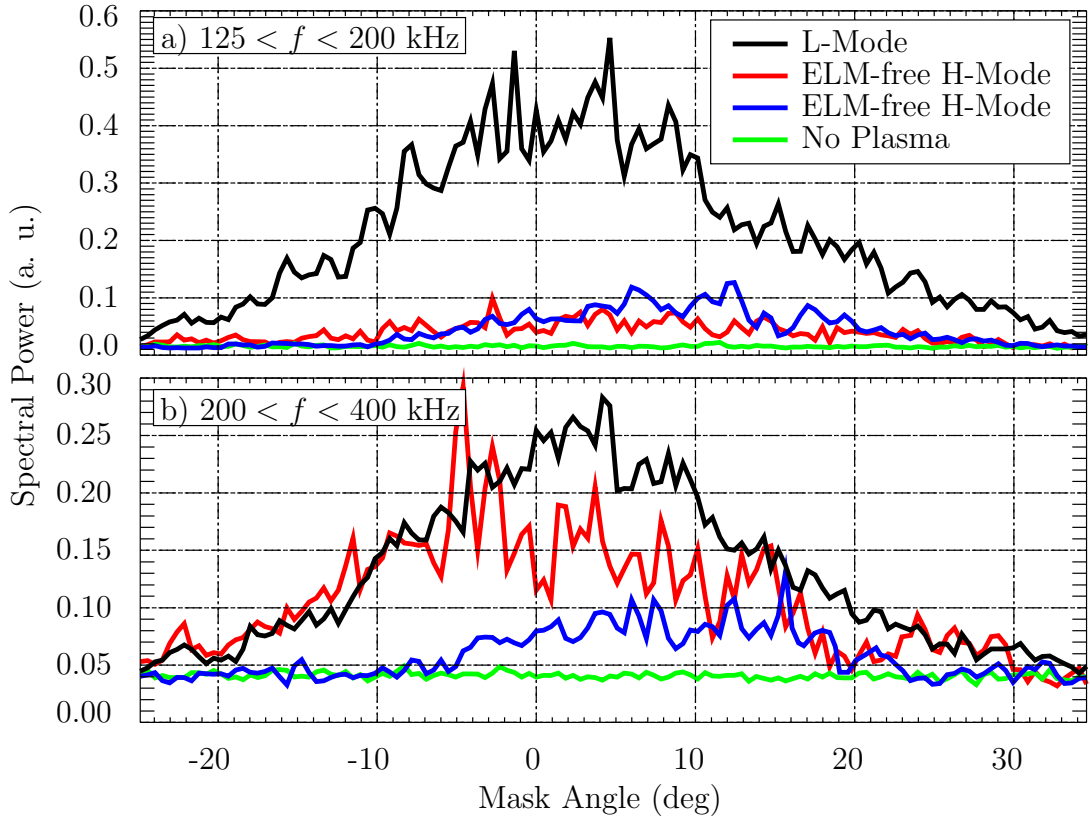
Figure 5-21: Finite $k_{||}$ background turbulence suppression due to the H-mode transition. Shown in black, red and blue are turbulence power spectra computed before the L-H transition, just after the transition, and as the ELM-free H-Mode evolves. The suppression rate is almost immediate in the low frequency response ($125 < f < 200$ kHz) and slower in the high frequency range ($200 < f < 400$ kHz).

b) plot the lower and higher frequency responses over the ranges $125 < f < 200$ kHz and $200 < f < 400$ kHz respectively. The low frequency response shows an immediate suppression of the turbulence amplitude of nearly a factor of 5 in both spectra from the H-mode shown in red and blue. The higher frequency background turbulence is suppressed more slowly; the red (immediately after the H-Mode transition) is down by less than a factor of 2 while the full suppression of nearly a factor of three occurs later in the transition as the H-mode evolves (shown in blue). For reference, the green is the system noise level computed after the plasma disruption.

To review, this section has shown that the finite $k_{||}$ background turbulence is more narrow than the suppression caused by the finite sized detector elements, that it re-

sponds to ECH heating with increased turbulence amplitude, and that the suppression caused by the L-H Mode transition is frequency dependent.

5.4.2 Background turbulence $k_{||}$ estimate

We now seek to determine the dependence of the width and peak of the turbulence level with frequency and wave-number. The background turbulence has a peaked
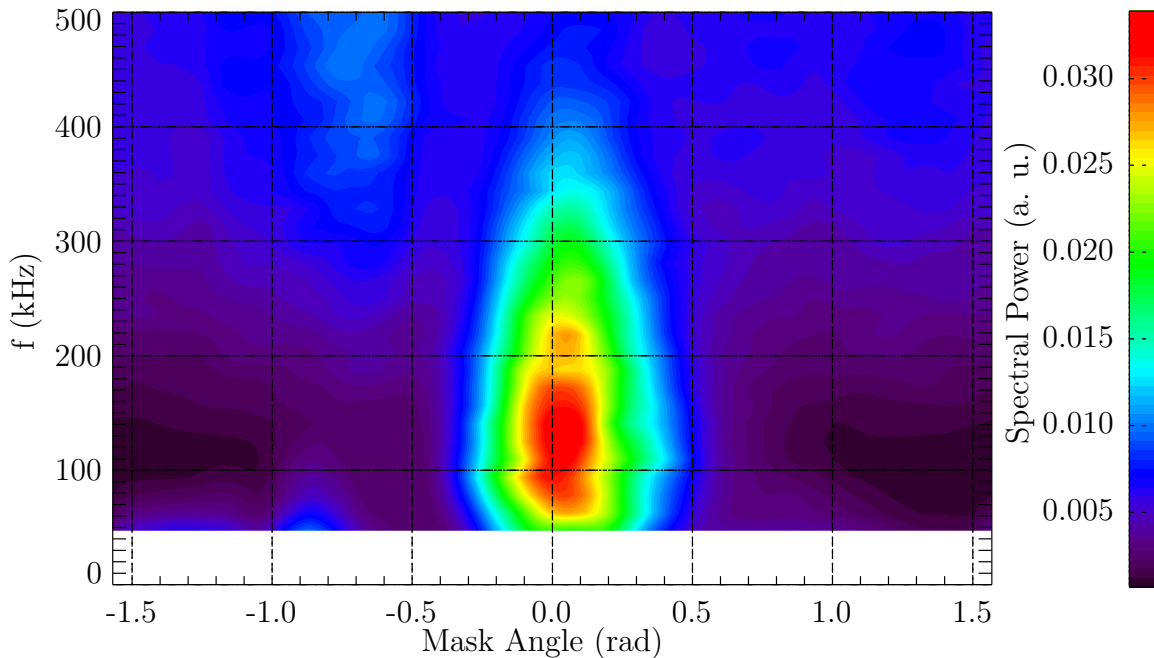
Figure 5-22: Conditional power spectra $\mathcal{C}(\alpha; f)$ of the finite $k_{||}$ background turbulence model shown for $k = 15$ cm^{-1}. The width of the structure is always peaked near the center of the chord mapping and the width only weakly depends upon frequency.

structure aligned with the center of the PCI chord mapping, with a FWHM anywhere between 0.25 and 0.5 radians, decreasing to the PCI noise floor at large mask angle. The conditional power spectra $\mathcal{C}(\alpha; f)$ (previously defined in Eq. 4.2) is plotted in Fig. 5-22 showing the peaked structure across the range in frequencies above the PCI system noise floor.

A quantitative measure of the peak amplitude and the FWHM of the finite $k_{||}$ background structure is plotted in Fig. 5-23 in panels a) and b) respectively. The peak amplitude decreases exponentially until $f \sim 450$ kHz where it becomes roughly the order of the PCI noise level. The FWHM is nearly constant over the frequency
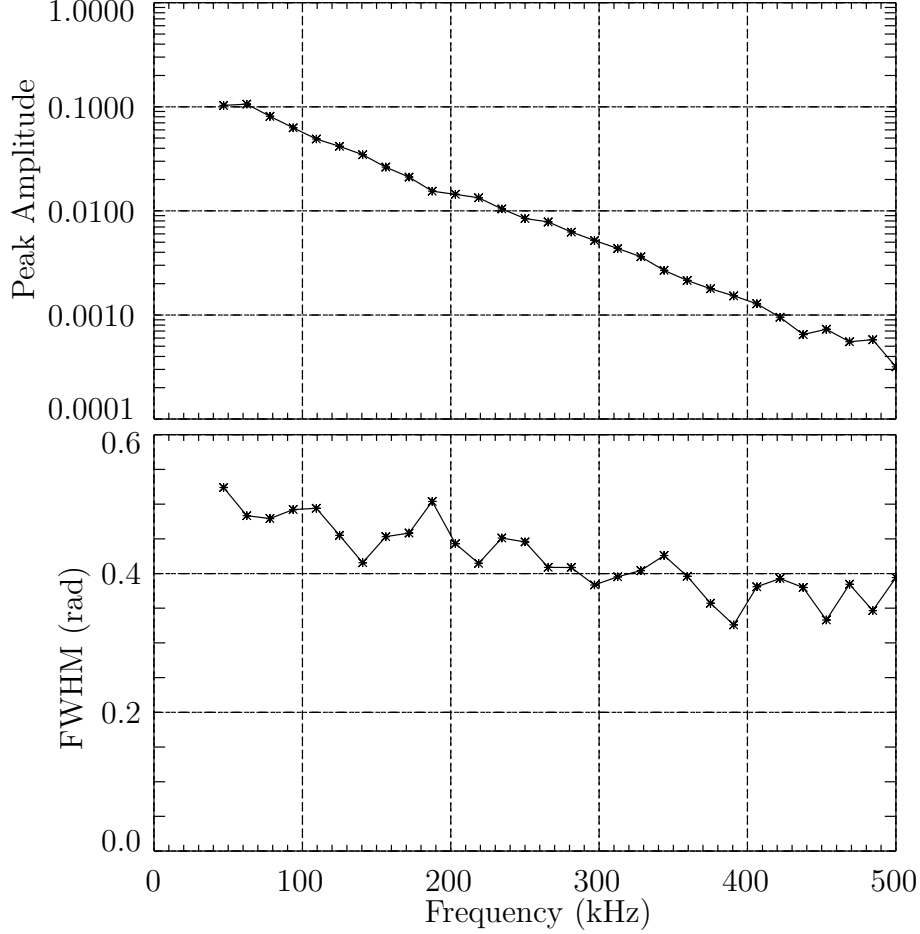
Figure 5-23: a) Finite $k_{||}$ background turbulence model peak amplitude variation with frequency shows an exponential decay with increasing frequency. b) FWHM of the background turbulence in mask angle only modestly decreases with increasing frequency.

range with only a modest decrease with increasing frequency. The width and peak amplitude do not scale with wave-number, and that is built into the model of the background turbulence estimation. With a FWHM between 0.3 and 0.55 radians, and a chord mapping width of nearly 0.1 radians, the parallel wave-vector component estimate is roughly $0.2 \lesssim k_{||}/k \lesssim 0.4$.

The previous sections describe the background turbulence level measured by the PCI and how it scales with wave-number, frequency, and mask angle. We find that the fall-off in mask angle is too rapid to be explained by the effects of finite sized detector elements, and that the width does not scale appreciably with wave-number.

The background turbulence extends to mask angles much too large to be explained by fluctuations propagating near perpendicular to the local magnetic field; we estimate the size of the parallel wave-number to be $0.2 \lesssim k_{\parallel}/k \lesssim 0.4$.

5.5 Low-k Wings

The third example of turbulence propagating at angles far too large to be explained by turbulence with $k_{\parallel} \sim 0$ was first introduced in Sec. 4.2.1. Again, we plot the turbulence power spectra as a function of mask angle in Fig. 5-24 for $|k| = 11$ cm^{-1}. At this wave-number, the turbulence is dominated by the main branch structure seen
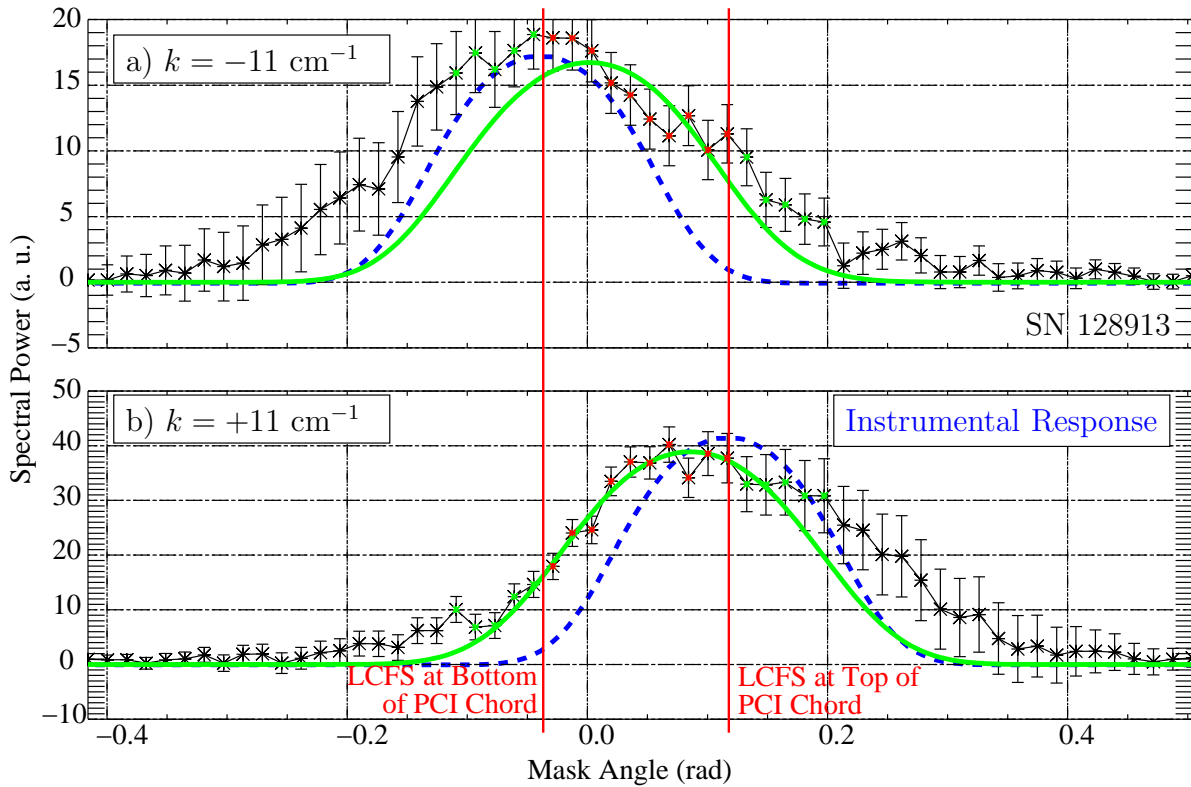
Figure 5-24: Turbulence amplitude plotted as a function of mask rotation angle γ at wave-numbers $k = -11$ cm^{-1} in panel a) and $k = +11$ cm^{-1} in panel b) with green curves showing the best estimate of the reconstructed fit using the parameterized function described in Eq. 4.3. Vertical red lines correspond to the mask angles of turbulence (with the assumption that $k_{\parallel} \sim 0$) from the LCFS. The decay on the left of panel a) and the right of panel b) is wider than can be achieved if the turbulence is aligned near perpendicular to the local magnetic field.

to align with the edges of the plasma (*i.e.* the mask angle corresponding to the LCFS, shown using the red vertical lines). The green lines are the best fit estimate of the reconstructed power spectra computed using the parametrized function in Eq. 4.3, and convolved with the mask response function $\mathcal{M}$.

The peak of the reconstruction does not align with the LCFS mapping because the best fit must have a finite amount of power elsewhere to fit the decay on the right of panel a) and left of panel b). The turbulence extends by roughly 0.05 - 0.1 radians beyond the LCFS mapping for it to be fit properly using the assumption of $k_{||} \sim 0$, near perpendicular propagation. Therefore, there must be a component of the turbulence propagating parallel to the local magnetic field with $k_{||}/k \sim 0.05 - 0.1$.

5.6   Summary of Finite $k_{||}$ Turbulence

This section described four examples of turbulence propagating at angles too large to be explained by turbulence propagating near perpendicular to the local magnetic field ($k_{||} \sim 0$). A summary of the size of the parallel wave-vector component needed to explain the above measurements is presented in Table 5.3.

Table 5.3: Summary of finite $k_{||}$ turbulence estimates

Mode	$k_{||}/k$ estimate
high-k Mode	0.15
medium-k Mode	0.2
background turbulence	0.2-0.4
low-k wings	0.05-0.1

Chapter 6

Interpretation of Finite $k_{||}$ Modes

In Ch. 5, we presented PCI measurements that cannot be explained by $k_{||} \sim 0$ turbulence because the propagation angles needed to result in the measurements are significantly larger than the variation of the magnetic field pitch along the PCI chord. The assumption that the drift-wave family of turbulence ($k_{||}/k \lesssim 10^{-2}$) is most relevant to plasma tranport is fairly ubiquitous across most modern theories of plasma turbulence. There is therefore not a reliable theory from which a quantitative comparison can be made to the measurements of finite $k_{||}$ turbulence. The current "gold standard" of plasma turbulence modeling is based on solutions to the gyrokinetic equations. In this chapter we begin discussing how modes with finite $k_{||}$ are ordered out of the gyrokinetic equations, thereby imposing an upper limit $k_{||}/k_{\theta} \sim 0.01$. Gyrokinetic simulation results are presented to verify that the modeled turbulence output is well within this regime (nominally $k_{||}/k_{\theta} \lesssim 10^{-4}$ for wave-numbers larger than 5 cm^{-1}). Then we present a discussion of how the plasma parameters of the PCI measurements relate to the parameters relevant to temperature gradient drift-wave turbulence. Lastly, we point out a possible mechanism by which these modes may interact with the plasma.

6.1 Gyrokinetics

To quantitatively model micro-turbulence in magnetically confined plasmas, one needs to address both the driving mechanism of the turbulence as well as the associated transport of particles and energy. While, in simplified geometry, analytic linear solutions of some micro-turbulence drives are possible, the quantitative analysis of the associated transport, supression mechanisms, and instability saturation levels are dependent on the long-time behavior and nonlinear interaction of the fluctuations with the rest of the plasma dynamics. Nonlinear gyrokinetic theory has become the most ubiquitous model used to study micro-turbulence across a broad range of plasma parameters. It has been used to study the family of drift-wave instabilities that include the universal drift-wave instability [79], the Ion Temperature Gradient (ITG) mode [80,81], the Electron Temperature Gradient (ETG) mode [47,82], coupled ITG-ETG turbulence [60,83], and the Trapped Electron (TEM) mode [62,84].

The theory of gyrokinetics has matured greatly since the development of the linear theory in 1968 by Rutherford and Frieman [85]. It was developed to address the need for a general theory to model a broad range of low frequency ($\omega < \Omega_i$) plasma phenomena that depend on a wide range of time and spatial scales. For example, the dynamics of micro-turbulence depend on scales from the gyro-motions of charged particles about magnetic fields (10's of ps and 10's of μm) to the long-time evolution and profile scale-lengths (100's of ms, 10's of cm). Such a system with important dynamics occurring across so many spatio-temporal orders of magnitude poses a very difficult problem to model. The approach taken by gyrokinetics to make this problem more tractable is to note that the spatio-temporal scales of the plasma phenomena are often larger and longer than the scales of a gyro-orbit. Therefore, in the perturbative solution to the Boltzmann-Maxwell set of equations, the 6-D phase space $(\vec{x}, \varepsilon, \mu, \varphi)$ is reduced to 5-D by analytically averaging over the gyro-angle φ, and introducing the new physical variables of total particle energy and magnetic moment.

Modern solutions of the gyrokinetic equations based upon relevant experimental devices require a numerical simulation. One of the great successes of modern theoret-

ical plasma physics is the development and benchmarking of a number of nonlinear gyrokinetic codes. These codes use methods to solve the gyrokinetic equations that fall into two techniques, the Lagrangian or particle-in-cell (PIC) codes and the Eulerian or continuum codes. Having multiple numerical methods to solve the complicated set of gyrokinetic equations is advantageous in that the codes can be bench-marked to one another for the purpose of verification. At present, the main gyrokinetic PIC codes in use today are GTC [86] and GEM [87], while the continuum codes are GS2 [47,88], GENE [12], and GYRO [4,89]. These codes are often executed on some of the largest computational facilities available today.

6.1.1 $k_{||}$ Ordering in Gyrokinetics

There are a multitude of references for the derivation of the gyrokinetic equations, some more theoretical [90] and some more physical [91,92]. In the latter, the perturbative solution is generated by expanding the Boltzmann equation in terms of the drift ordering parameter $\delta = \rho_j/L$, where L is the equilibrium scale-length, $\rho_j = v_{th,j}/\sqrt{2}|\Omega_j|$ is the Larmor radius, $v_{th,j} = \sqrt{2T_j/m_j}$ is the thermal velocity, and $\Omega_j = q_j B/m_j$ is the gyro-frequency. The gyrokinetic ordering results in the following consequence for the size of the parallel wave-number

$$\frac{k_{||}}{k_\perp} \sim \delta = \rho/L. \tag{6.1}$$

The drift ordering parameter implies an upper limit on the parallel wave-number included in the gyrokinetic equations. For the plasmas analyzed in Ch. 5, we find this ordering imposed limit to be roughly $k_{||}/k_\perp \sim 10^{-2}$. When compared to the size of $k_{||}$ as summarized in Sec. 5.6, the finite $k_{||}$ turbulence measured by the PCI has a parallel wave-number much larger (by at least a factor of 10) than what is valid for the gyrokinetic theory.

In addition to the ordering limit on $k_{||}$, the gyrokinetic equations also break down near the plasma edge as the scale-lengths become short. Near the edge, the expansion parameter can become $\delta \sim \mathcal{O}(1)$, and the entire gyrokinetic expansion is no longer

based on a small parameter.

6.1.2 $k_{||}$ studies from GYRO simulations

We have shown that the finite $k_{||}$ modes measured by the PCI have a parallel wave-number significantly larger than the largest parallel wave-number included in the derivation of the gyrokinetic equation. Still, it is useful to check the $k_{||}/k_\perp$ limit of the turbulence in gyrokinetic simulations and compare that to the limit imposed by the ordering of the gyrokinetic equations. If the parallel wave-number limit of the simulated turbulence is well below the limit imposed by the ordering, then the physics in the gyrokinetic equations does not contain fluctuations with large parallel wave-numbers. However, if the parallel wave-number limit of the simulated turbulence is of the same size as the limit imposed by the gyrokinetic ordering, then the suppression of finite $k_{||}$ modes in the simulation is due to the assumptions made in the derivation of the gyrokinetic model and not the underlying physics.

Gyrokinetic simulations were performed to determine whether the parallel wave-number response is limited by the gyrokinetic ordering or by the underlying physics, given that the plasma parameters of discharge 133609 show high-k mode activity that increases with increasing ECH heating power level. Due to the availability of detailed documentation in this work, the GYRO code was used to determine the linear parallel wave-number structure of plasma turbulence. The GYRO code uses spectral methods in the toroidal direction as it is a good quantum number for tokamak devices, and in what follows the toroidal mode number is given by ℓ.

$k_{||}$ structure in GYRO output

Linear GYRO simulations are generally performed at a fixed toroidal mode number ℓ and a particular radial location in the plasma. This allows the radial grid of the simulation to be optimized for the spatial scales for that particular toroidal mode.

The GYRO documentation [93] details the structure of the fluctuating density as

$$\tilde{n}(r, \theta, \varphi, t) = \bar{n}_e \mathrm{Re} \left[\sum_\ell \delta n_\ell(r, \theta, t) \ e^{-i\ell[\varphi + \nu(r, \theta)]} \right], \tag{6.2}$$

where $\tilde{n}$ is the total fluctuating density and δn_ℓ is the "coefficient" of the fluctuating density of the ℓth toroidal mode. Note that this coefficient is complex, and $\varphi + \nu = \alpha$ is the Clebsch angle, as GYRO uses the Clebsch representation for the magnetic field

$$\mathbf{B} = \nabla\alpha \times \nabla\psi \tag{6.3}$$

$$\alpha = \varphi + \nu(r, \theta), \tag{6.4}$$

where ψ is the poloidal flux (divided by 2π). Equation 6.3 implies $\mathbf{B} \cdot \nabla\alpha = 0$ and α is therefore constant along a field line. For further intuition, we point out that in the case of concentric (un-shifted) circular flux surfaces, ν becomes equal to $-q\theta$, again showing that α remains constant along the magnetic field. This representation is chosen such that the fluctuation of a mode propagating perpendicular to the local magnetic field is entirely contained in the exponent and δn_ℓ is not a function of θ. This implies that if the mode is not propagating perpendicular to the local magnetic field, then that information is contained in the $\theta-$dependence of δn_ℓ. The variation in δn_ℓ is never exactly zero because the plasma density is a real quantity and must be continuous in θ. This continuity constraint requires some variation with the poloidal angle θ in the coefficient δn_ℓ on non-rational flux surfaces. This small shift from perfectly perpendicular alignment to the magnetic field is of the order $k_\parallel/k \sim 10^{-4}$ for the parameters of fluctuations measured with the PCI.

We have shown above that a simulated toroidal mode in the GYRO simulation that propagates with a finite $k_\parallel$ will have a coefficient δn_ℓ that is dependent upon the poloidal angle θ. To analyze the spectral power response as a function of propagation angle, the coefficient δn_ℓ must be transformed into a conjugate space. However, because the component of the mode propagating parallel to the field is sampled along the θ-axis and not along a spatial path length coordinate parallel to the field, the

conjugate space is not the wave-number parallel to the field ($k_{||}$). Instead, we consider the conjugate variable ϱ as shown in Fig. 6-1, where the the blue phase fronts are due to the $e^{-il\alpha}$ term and propagate perpendicular to the field, and the green phase fronts represent the component of the fluctuation propagating parallel to the field. Therefore, the Fourier Transform of the coefficient $\delta n_\ell(r, \theta, t)$ gives the spectral
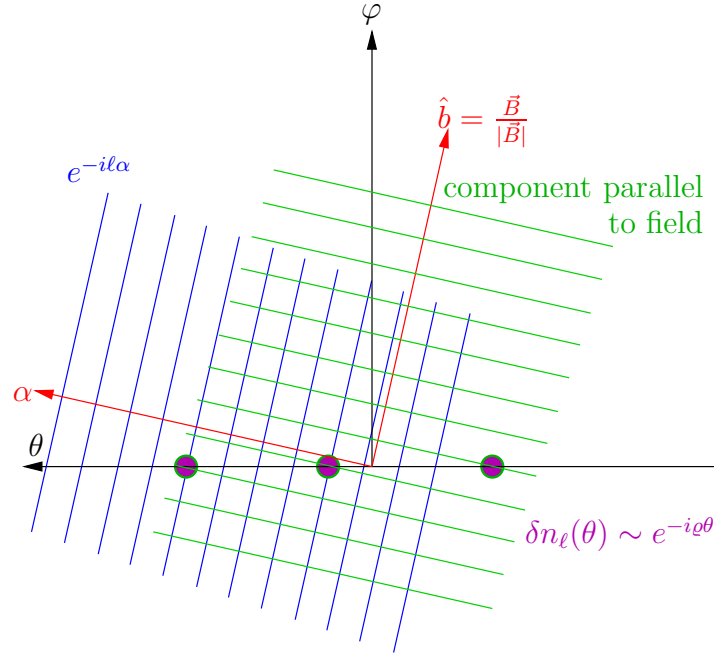
Figure 6-1: Diagram of the geometry of modes in GYRO simulations showing the modes propagating perpendicular to the magnetic field (along α in blue phase fronts), the modes propagating parallel to the local magnetic (along β in green phase fronts) and the way the parallel modes are sampled along the poloidal axis θ.

amplitude as a function of ϱ which is in essence a poloidal mode number (but not restricted to integer values) due to the component propagating parallel to the local field but sampled along the θ coordinate (the magenta samples in Fig. 6-1). The parallel wave-number $k_{||}$ is then related to transformed mode-number of the coefficient $\delta n_\ell(r, \theta, t)$ by $k_{||} = \frac{\varrho}{qR_0}$, which can be shown by considering how an incremental change in the poloidal angle relates to the path length along the field line, $ds \approx qR_0 d\theta$ (in the large aspect ratio limit).

The modes propagating perpendicular to the local magnetic field get projected onto the poloidal axis with ($k_\theta = \ell q/r$), and therefore we can transform the coefficient

into a conjugate space of the parallel wave-number

$$\delta n_\ell \left(r, \frac{k_{||}}{k_\theta}, t \right) = \int_0^{2\psi} d\theta \ \delta n_\ell(r, \theta, t) \ e^{-i\frac{k_{||}}{k_\theta}\frac{\ell q^2 R_0}{r}\theta}, \tag{6.5}$$

$$\frac{k_{||}}{k_\theta} = \frac{\varrho r}{\ell q^2 R_0}, \tag{6.6}$$

where we have chosen to write the transform as a function of propagation angle $k_{||}/k_\theta$ given the geometry shown in Fig. 6-1. The spectral power response as a function of propagation angle and frequency can now simply be written

$$S'_\ell \left(\frac{k_{||}}{k_\theta}, f; r_0 \right) = \left| \int_{r_0-\Delta r}^{r_0+\Delta r} dr \ \int_{-\infty}^{\infty} dt \ e^{i2\pi ft} \ \delta n_\ell \left(r, \frac{k_{||}}{k_\theta}, t \right) \right|^2, \tag{6.7}$$

where the prime indicates that this is the GYRO simulated power spectrum, so as not to confuse it with actual PCI measurements. The time domain is transformed to frequency, and the simulated power spectrum is integrated over a small annulus centered about the simulation radius r_0.

Propagation angle response in GYRO simulations

GYRO simulations were performed to estimate the spectral power response as a function of propagation angle $k_{||}/k_\theta$ for the highest level of ECH heating from discharge 133609 (discussed in Sec. 5.2). As an example of the linear GYRO results, Fig. 6-2 characterizes the fluctuating density of a single toroidal mode $\ell = 200$ ($k = 12$ cm^{-1}) from the simulation centered at $r/a = 0.7$, using plasma profiles from the highest level of ECH heating power. Panel a) plots the density fluctuation coefficient as a function of time, integrated over a small annulus centered about the simulation radius and integrated over poloidal angle. The mode is an unstable growing Fourier harmonic ($\delta n_\ell \propto e^{(\gamma+i2\pi f)t}$) with growth rate $\gamma = 170 \times 10^3$ rad/s shown with the red dashed curves, and frequency $f = 83$ kHz. Panel b) plots the 2-D structure (in poloidal angle and time) of the fluctuation with the exponential growth divided out. This shows that the dominant fluctuation is in time, while the variation with poloidal angle is a small amplitude perturbation combined with the broad ballooning structure envelope.
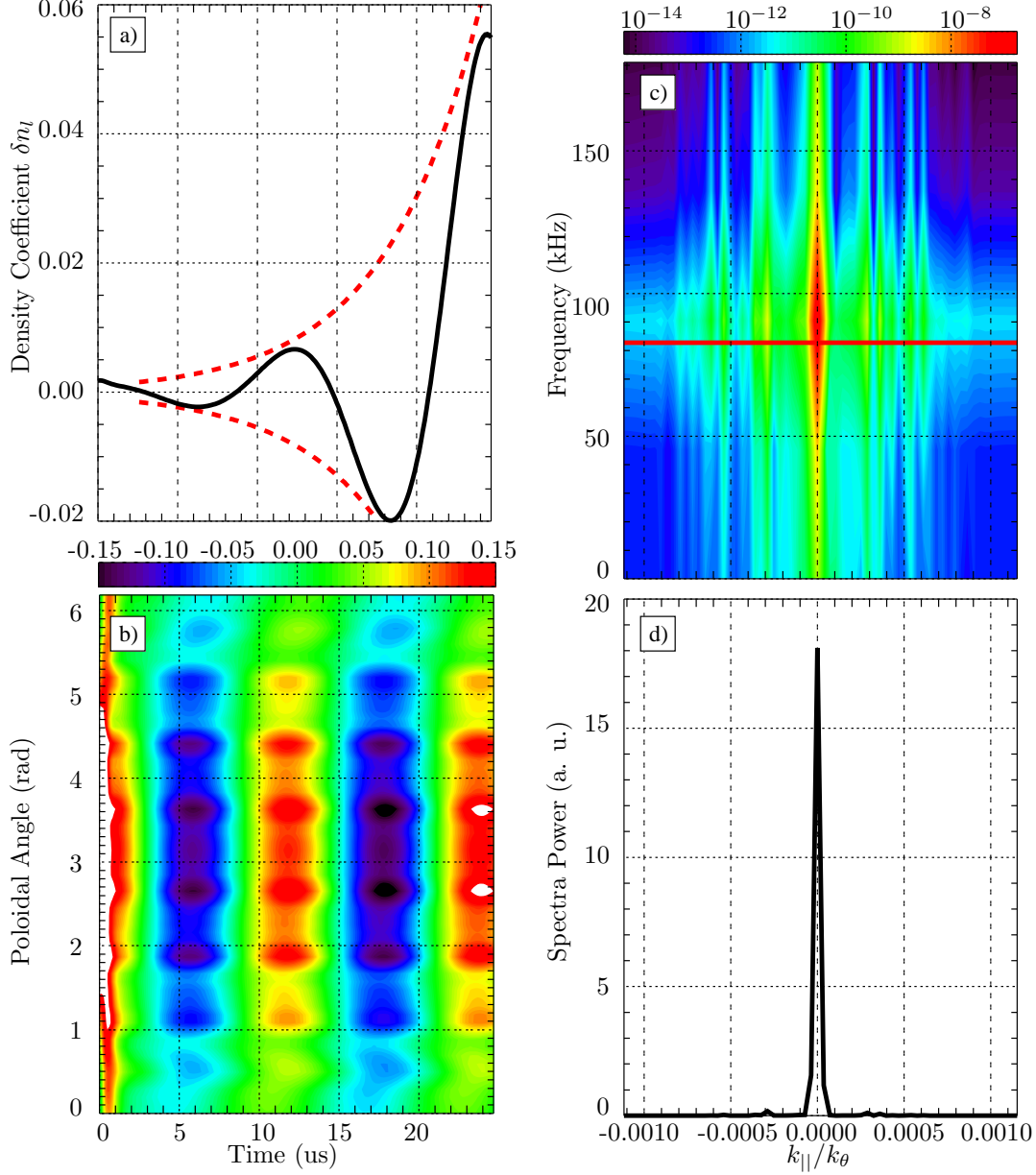
Figure 6-2: GYRO simulation of toroidal mode $\ell = 200$ at $r/a = 0.7$ during the highest level of ECH heating of plasma discharge 133609. a) $\delta n_\ell(t)$ integrated over poloidal angle and simulation radius showing the mode evolution (black curve), and the growth rate $\pm e^{\gamma t}$ (dashed red curve). b) $\delta n_\ell(t, \theta)/e^{\gamma t}$ integrated over the simulation radius showing the poloidal structure. c) Power spectrum of $\delta n_\ell(t, \theta)/e^{\gamma t}$ plotted vs the associated propagation angle $k_{||}/k_\theta$, colors in log scale. d) Power spectrum of mode $\ell = 200$ vs. propagation angle shown at the mode frequency (83 kHz, shown with solid red line in panel c).

Panel c) plots the spectral power as function of propagation angle and frequency as described in Eq. 6.7, where the colors are in log scale. The peak power is roughly

centered at the mode frequency (given the poor frequency resolution $\Delta f \sim 40$ kHz), and centered with propagation perpendicular to the local field. Panel d) plots quantitatively the spectral power as a function of propagation angle and shows a peaked structure with very narrow width (FWHM roughly $k_{||}/k_\theta \sim 5 \times 10^{-5}$). Outside the central peak, the spectral power is over two orders of magnitude lower than the peak power. The GYRO simulation at this radius and wave-number does not exhibit the large propagation angles measured by the PCI described in Ch. 5.

GYRO simulations were performed using profiles both during Ohmic heating and at the highest power level of ECH heating, and at radii $r/a = [0.6, 0.7, 0.8]$ and toroidal modes $\ell = 20, 40, 60, ..., 320$. Attempts were made to perform the simulation at $r/a = 0.9$, however the convergence was poor due to the large gradients and a subsequent breakdown of the gyrokinetic ordering. The widths of the central peak in the spectral power as a function of propagation angle (recall Fig. 6-2d) are plotted as a function of toroidal mode number (or equivalently wave-number k_θ) in Fig. 6-3. The FWHM spectral response in propagation angle is shown for both the Ohmic (dashed lines) and ECH (solid lines) heating conditions at each of the 3 simulation radii 0.6, 0.7 and 0.8 in black, red, and blue, respectively. The FWHM is seen to scale as $1/k_\theta$ (shown for comparison in the green curve) and no measurable difference is observed between Ohmic and ECH heating or with plasma radius.

The largest propagation angle contained in the GYRO simulation depends on the resolution of the poloidal grid. To extend these simulations to larger propagation angles, several GYRO simulation parameters must be adjusted. The internal poloidal grid resolution is controlled by the parameters BLEND_GRID and ORBIT_GRID, while the poloidal grid resolution of the density output is controlled by THETA_PLOT [93]. These parameters should be adjusted together with BLEND_GRID = ORBIT_GRID = 0.5 THETA_PLOT. Increasing the poloidal resolution of the simulation poses difficulties for the simulation to converge. This problem can be addressed by using fully gyro-kinetic electrons (and an explicit solver in time) as opposed to the drift-kinetic electrons (and the implicit solver in time) and keeping the time step short enough such that the Courant stability condition [94] is satisfied. However, such
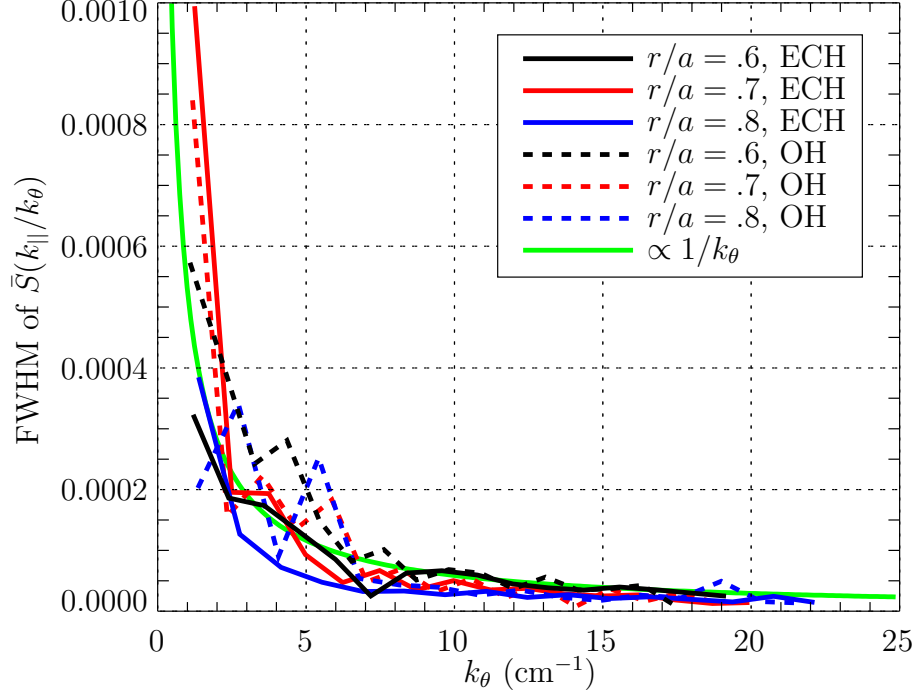
Figure 6-3: Width of spectral power peak in propagation angle plotted as a function of wave-number (k_θ) shown for simulations at $r/a = [0.6, 0.7, 0.8]$ and toroidal modes $\ell = 20, 40, 60, ..., 320$. It is seen that the width in propagation angle scales $\propto 1/k_\theta$ with no measurable difference between Ohmic and ECH heating or with simulation radius.

details are beyond the scope of this thesis.

Simulations were performed at $r/a = 0.7$ and toroidal modes $\ell = 100, 300$ for the highest power level of ECH heating, with increasing poloidal resolution (increased maximum $k_{||}/k$). Figure 6-4 plots the results for a) toroidal mode $\ell = 100$ and b) $\ell = 300$. Extending the simulation domain in propagation angle has no effect on the FWHM of the peak of the spectral response. Decreasing the poloidal resolution mildly truncates the spectral power roll-off at propagation angles outside the peak for $\ell = 300$, and barely affects the roll-off outside the peak for $\ell = 100$. The spectral power just outside the peak is more than 2 orders of magnitude lower than the peak response and decreases to 6 orders of magnitude lower near the propagation angle limit. Recall that the high-k mode spectral power is only a factor of ~ 15 lower than the main branch peak response as seen in Fig. 5-11.

To summarize, GYRO simulations do not contain modes propagating with signif-
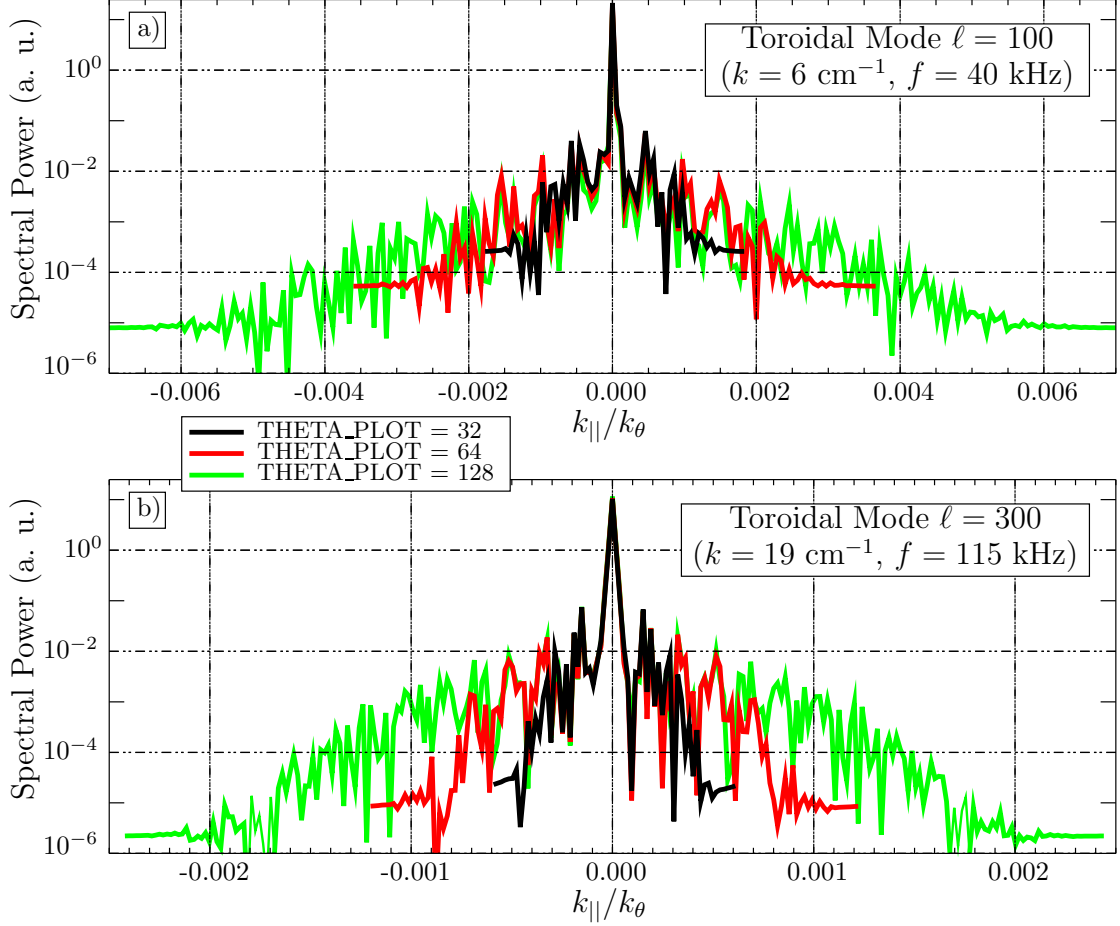
Figure 6-4: GYRO spectral response as a function of propagation angle with increased poloidal (and therefore propagation angle) resolution. The peak FWHM remains constant, the large propagation angle behavior is mildly truncated with decreased poloidal resolution for the $\ell = 300$ simulation and barely affected for the $\ell = 100$ simulation, and is 2-6 orders of magnitude lower in power than the mean response.

icant power outside propagation angles $k_{||}/k_\theta \sim 1 - 5 \times 10^{-5}$ at wave-numbers in the high-k and medium-k range $|k| \gtrsim 14$ cm^{-1}. The roll-off in amplitude is unchanged by increasing the poloidal resolution (and therefore the maximum propagation) of the simulation. Additionally, the width of the spectral power peak in propagation angle is significantly smaller than the maximum propagation angle assumed in the gyrokinetic ordering. This leads us to conclude that the simulation is self-consistent with respect to modes propagating at large angles from perpendicular to the magnetic field. The high-k and medium-k modes measured by the DIII–D PCI are thus ordered out of the gyrokinetic equations from the outset.

6.2   Drift-Wave Analysis

Tokamak transport is often believed to be governed by processes generated by micro-instabilities of the drift-wave family (ITG, ETG, and TEM) [95, 96]. While there has been agreement between transport models of drift-wave turbulence in the ion channel and experimental measurements in the plasma core [11], agreement in the electron channel and near the plasma edge are still not satisfactory [97–99]. For reference, we will show in Sec. 6.2.2 that linear GYRO simulations predict that these modes are unstable over a large portion of the plasma. Unfortunately, non-linear GYRO simulations, necessary to predict mode saturation and transport, have not been performed while preparing this thesis. For future reference, we will present the relevant plasma parameters and profiles that may be used for drift-wave turbulence studies without assuming gyrokinetics.

6.2.1   Plasma Profiles

To look at the finite $k_{||}$ turbulence in the context of drift-wave turbulence, we focus on the high-k mode because it is the strongest feature seen at mask angles too large to be explained by perpendicular propagation. Recall that the high-k mode wave-numbers are in the range $18 - 23$ cm^{-1}, frequencies in the range $100 - 400$ kHz, and propagation angles $k_{||}/k_\theta \lesssim 0.15$. The peak spectral power of these modes increases with increasing ECH heating power up to the highest levels, and during NBI heating.

In Fig. 6-5, the plasma profiles are plotted from discharge 133606 during Ohmic heating, 0.3, 1.3, 1.6 MW of ECH heating, and 2.5 MW of NBI heating. These profiles are fit using the standard tool for DIII–D profile estimation (gaprofiles), which uses a spline model for the profile. In panels (a-c) are plotted profiles of the electron density, the electron temperature, and the ion temperature over the range $0.2 < r/a < 0.9$. In panels (d-f) are plotted the associated gradient scale-lengths defined as, for example,

$$\frac{a}{L_n} = -\frac{a}{n(r)}\frac{\partial n(r)}{\partial r},$$

(6.8)
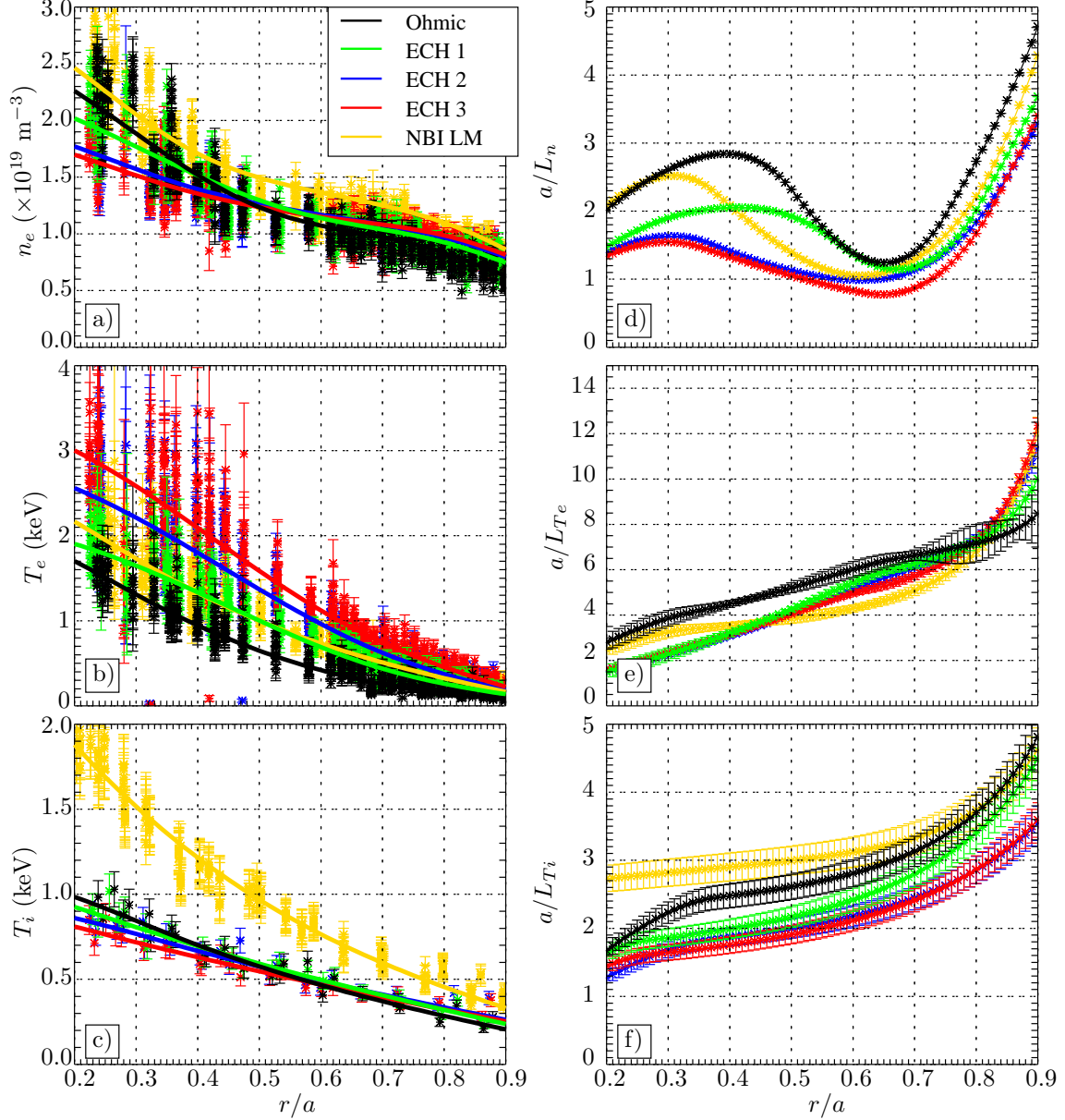
Figure 6-5: Plasma profiles of discharge 133606, during Ohmic heating (black), ECH heating with 0.3 MW (green), 1.3 MW (blue), 1.6 MW (red), and 2.5 MW of NBI heating (gold). T_e data is provided from the Thomson scattering diagnostic. Panels a)-c) plot the electron density, electron temperature, and ion temperature, respectively. Panels d)-f) plot the normalized inverse scale-lengths. All measurements are during L-Mode plasma conditions.

where r is the plasma minor radius. The quantity a/L_j (where j represents the plasma parameter, n, T_i, T_e) is a common non-dimensional normalization used in various theories which useful because it is proportional to the profile gradient (and therefore

167

the inverse of the scale-length). The drift-wave modes discussed at the beginning of this section (ITG, ETG, and TEM) are driven by gradients in the ion temperature, electron temperature, and the plasma density, respectively, and the larger the non-dimensional quantity a/L_j, the larger the associated instability drive.

The most interesting features displayed in the plasma profiles are how they are affected by ECH and NBI heating. The electron temperature, shown in panel b), increases in the core of the plasma when ECH heating is applied. In contrast, there is only a moderate increase of T_e with NBI heating at 2.5 MW, not unlike that during 0.3 MW of ECH heating. The ion temperature, shown in panel c), remains roughly at the Ohmic level during ECH heating, but it is increases by nearly a factor of 2 with NBI heating. The electron density, shown in panel a), decreases with ECH heating in the core ($0.2 < r/a < 0.4$) and marginally increases with ECH heating outside $r/a = 0.6$. NBI heating increases the density above the ohmic heating level throughout the entire plasma.

The most striking feature revealed by the inverse scale-length (drift-wave turbulence drives) is seen in the electron temperature inverse scale-length (a/L_{Te} shown in panel e). The response of this driving term to applied heating is dramatically different for the core plasma ($0.2 < r/a < 0.8$) vs. the edge region ($r/a > 0.85$). In the edge region, the electron temperature inverse scale-length (ETG drive) increases dramatically (by almost a factor of 3) for the highest level of ECH heating and NBI heating. The increase in the electron temperature inverse scale-length, during the lower power levels of ECH heating, scale proportionately to the applied ECH power. The other inverse scale-lengths (a/L_n and a/L_{Ti} in panels d and f, respectively) are perturbed by less than 50% and the drives are actually *decreased* with applied ECH heating, while the NBI heating appears to have little effect.

The electron temperature inverse scale-length profile is very stiff over the core of the plasma ($0.2 < r/a < 0.8$) in that there is little variation with applied heating, indicating that the profile is near marginal stability. However, there is a noticable scaling of a marginal decrease in ETG drive with increasing heating. The density and ion temperature drives (a/L_n and a/L_{Ti}) also decrease with ECH heating, however

168

the NBI heating increases the ion temperature inverse scale-length while decreasing the density inverse scale-length over the region $0.3 < r/a < 0.6$.

In this section, we have shown how the density and temperature profiles are modified during the various applied heating regimes, as well as their associated scale-lengths. The scale lengths are generally considered a proxy for the strength of the associated driving term behind ITG, ETG and TEM turbulence. We find that the application of heating *increases* the ETG drive (by decreasing the electron temperature scale-length) in the edge region of the plasma (where the PCI measurement is made but gyrokinetics may not be valid), while ECH heating *decreases* the density and ion temperature drives (by increasing the density and ion temperature scale-lengths) in the edge region. This implies that the electron temperature gradient may be an important mechanism for instability drive in the edge region.

6.2.2   Linear Stability Analysis

Linear gyrokinetic simulations were performed using the GYRO code with plasma profiles from the L-Mode discharges described in Sec. 5.2 and shown above in Sec. 6.2.1 during both the Ohmic and the highest power level of ECH heating. GYRO is an initial value code, meaning that it can only reveal the frequency (f_ℓ) and growth rate (γ_ℓ) of the fastest growing drift-wave fluctuation for a given toroidal mode number (ℓ). The poloidal wave-number (k_θ) is related to the toroidal mode number by

$$k_\theta = \frac{\ell q(r)}{r},\tag{6.9}$$

where $q(r) = rB_\phi/RB_\theta$ is the safety factor, r and R are the minor and major radii, and B_ϕ and B_θ are the toroidal and poloidal components of the magnetic field. Positive growth rates correspond to unstable modes, while negative growth rates correspond to damped modes. In addition, positive frequencies correspond to modes propagating (in the plasma frame) in the electron diamagnetic drift direction, while negative frequencies correspond to the ion diamagnetic drift direction.

Simulations were performed (using the Loki computational facility at MIT) for

toroidal modes $\ell = 20, 40, 60, ..., 320$ at plasma locations $r/a = 0.3, 0.4, 0.5, ..., 0.9$.
The frequency and growth rate of the most unstable modes are plotted in Fig. 6-6 as
a function of the normalized wave-number $k_\theta \rho_{si}$ for each radius, where $\rho_{si} = c_s/\Omega_i$
is the ion sound Larmor radius computed using the electron temperature. Panels a)
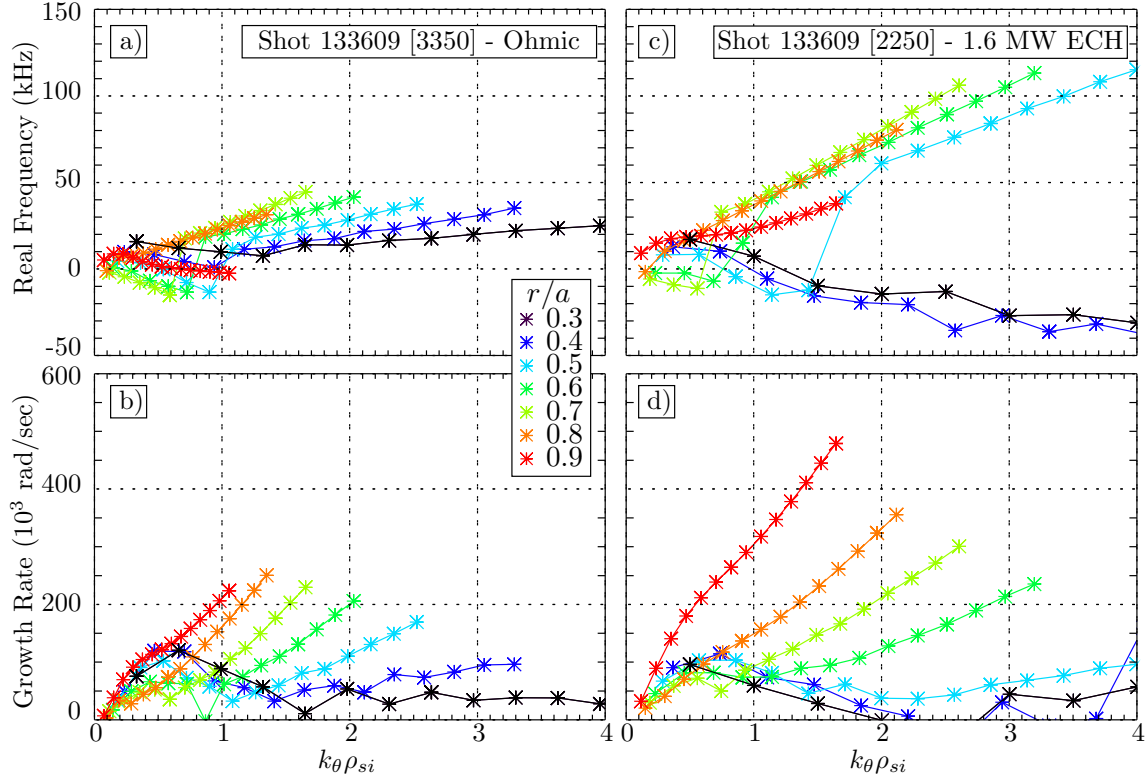
Figure 6-6: Linear GYRO stability analysis for both the Ohmic (panels a and b) and
highest level of ECH heating (panels c and d) using profiles from discharge 133609
described in Sec. 5.2. Frequencies are plotted in panels a) and c) while growth rates
in panels b) and d) as a function of normalized wave-number. Positive frequencies
correspond to modes propagating (in the plasma frame) in the electron diamagnetic
drift direction, while negative frequencies correspond to the ion diamagnetic drift
direction. Colors correspond to different radial locations in the plasma from $0.3 \leq r/a \leq 0.9$.

and b) plot the simulated frequencies and growth rates based on the Ohmic heating
profiles while panels c) and d) plot the frequencies and growth rates based on the
highest power level of ECH heating profiles.

For both heating regimes, the mid-radius of the plasma $r/a = [0.5, 0.6, 0.7]$ simula-
tions show ITG modes unstable (negative frequencies) in the long wavelength regime
and a switch to TEM/ETG dominant instabilities at high wave-number. In the ITG

range in ohmic plasmas, the growth rate peaks at $k_\theta \rho_{si} \simeq 0.5$ and then decreases as wave-number increases until the TEM mode dominates and the growth rates increase again at $k_\theta \rho_{si} > 1$. In the ECH plasmas, the ITG modes barely exist and TEM/ETG dominate.

The edge region of the plasma $r/a = [0.8, 0.9]$ shows instabilities in the electron direction with frequencies increasing with increasing wave-number, however at $r/a = 0.9$, the Ohmic heated plasma regime shows that the most unstable modes tend toward zero frequency. Recall that the gyrokinetic ordering breaks down near the plasma edge, and although the numerics of these simulations converge, the gyrokinetic equations may not contain the relevant physics this near to the plasma LCFS. In this region, the modes become more unstable with increasing wave-number, indicating the possible importance of ETG modes.

The core region of the plasma, $r/a = [0.3, 0.4]$, shows growth rates during ohmic heating that peak near $k_\theta \rho_{si} \sim 0.5$. The ohmic heating simulations also show that the dominant instabilities are in the electron direction (TEM/ETG) across the wavelength range. The simulations during the highest power level of ECH heating converge poorly in the core region due to short gradient scale-lengths (shorter than the ohmic case by nearly a factor of 2). While the peak in growth rate near $k_\theta \rho_{si} \sim 0.5$ makes sense for the long wavelength turbulence, the switch to ion direction and increase in growth rate at short wavelengths is due to poor convergence of these simulations and may not be reliable.

6.2.3 Analytic Model for Temperature Gradient Drive Without Gyrokinetic Assumptions

We revisit early analytic models [43, 44, 100, 101] for temperature gradient driven turbulence to point out terms that may be relevant to modes that propagate with parallel wave-numbers of the size measured by the PCI. These models assume a magnetized plasma in slab geometry with density and temperature gradients. A solution to the linearized Vlasov equation is obtained and used to compute the perturbed density for

species j due to an electrostatic mode with fluctuating potential $\tilde{\Phi}_1$

$$\tilde{n}_{1j} = -\frac{Z_j e}{T_j} n_0 \tilde{\Phi}_1 \left\{ 1 + \frac{\Gamma_m \mathcal{Z}}{k_\parallel v_{tj}} \left[\omega - \omega_{\star j} \left(1 - \eta_j \left[\frac{1}{2} - \frac{\zeta_{mj}}{\mathcal{Z}} - \zeta_{mj}^2 - b_j \frac{\Gamma_m'}{\Gamma_m} \right] \right) \right] \right\},$$
(6.10)

where Z_j is the mass number, T_j is the temperature, n_0 is the unperturbed density, $\Gamma_m = \Gamma_m(b_j)$ and $\mathcal{Z} = \mathcal{Z}(\zeta_{mj})$ are the plasma functions well known from wave theory [37], ω is the complex wave frequency, $\omega_{\star j} = k_\perp \frac{T_j}{eBL_n}$ is the drift frequency, $\eta_j = L_n/L_{Tj}$ is the density to temperature scale-length ratio (large when temperature gradient scale-lengths are shorter than density gradient scale-lengths), and $k_\parallel$ and $k_\perp$ are the wave-vector components parallel and perpendicular to the magnetic field. There is an implicit sum over the integer m, and b_j, ζ_{mj}, v_{tj} are defined as

$$b_j = \frac{k_\perp^2 v_{tj}^2}{2\Omega_j^2}$$
(6.11)

$$\zeta_{mj} = \frac{(w - m\Omega_j)}{k_\parallel v_{tj}}$$
(6.12)

$$v_{tj} = \sqrt{\frac{2T_j}{m_j}},$$
(6.13)

where m_j is the species mass, and Ω_j is the cyclotron frequency. A dispersion relation is formed by writing out Poisson's equation for an electrostatic mode

$$k^2 \tilde{\Phi}_1 = e\tilde{n}_{1i} - e\tilde{n}_{1e}.$$
(6.14)

Recall that the plasma dispersion function $\mathcal{Z}(\zeta_{mj})$ comes in from the Landau damping contour integral. When its argument is near unity, energy can be exchanged between particles and the plasma wave; this is the mechanism by which modes are destabilized or strongly damped. The function $\Gamma_m(b_j)$ contains finite larmor radius effects due to the finite plasma temperature.

The derivation of the gyrokinetic equation assumes that $k_\parallel$ is small and that the fluctuation frequency is small relative to the cyclotron frequency ($\omega \ll \omega_{ci}$). This implies that $|\zeta_{mj}| \gg 1$ and only the $m = 0$ term is retained in the sum over m. This

can be demonstrated by using the asymptotic limit of $\mathcal{Z}$ in Eq. 6.10; in this limit the largest terms are proportional to $-1/\zeta_{mj}$. However, when the parallel wave-number is large, it may be necessary to return terms with $m \neq 0$ as the argument $\zeta_{mj} \sim \mathcal{O}(1)$.

We now consider the parameters of the high-k mode ($k_\theta = 20$ cm^{-1} and $k_{||}/k_\theta = 0.15$) during plasma discharge 133606 (discussed in Sec. 5.2) to specify a regime in which the finite $k_{||}$ turbulence could be studied. Recall that turbulence with finite $k_{||}$ cannot be localized and could exist anywhere across the PCI chord, therefore, in Fig. 6-7 we plot the relevant parameters ($\omega_{\star j}/2\pi$, η_j, b_j, ζ_{mj}) as a function of normalized radius $0.6 < r/a < 1.0$ (recall that the PCI chord covers roughly $r/a \gtrsim 0.7$). Plotted are both ion and electron parameters during both Ohmic and the highest power level of ECH heating so as to contrast regimes in which the high-k mode changes from negligible amplitude to large amplitude. Black and blue curves are the ion and electron parameters during ohmic heating, while yellow and red curves are the ion and electron parameters during ECH heating. In panel b) we plot the ratio of the temperature gradient to the density gradient, a measure of the strength of the temperature gradient drive, showing that the most dramatic effect of the ECH heating is to increase η_e by a factor of 2 in the center of the PCI chord to as much as a factor of 4 at the edge. Panel e) plots the finite larmor radius parameter ($k_\perp \rho_j$) indicating that finite larmor radius effects are relevant for ions but not for electrons. Finally, panels c) and f) plot the Landau damping parameters ζ_{0j} and ζ_{1j} showing that, for electrons $\zeta_{0e} \ll 1$ and $\zeta_{1e} \gg 1$ so that electrons interact little with the wave and can be treated adiabatically, while the ion parameters are $\zeta_{0i} \ll 1$ but $\zeta_{1i} \sim 1$, and ions can interact with the wave producing an unstable mode.

To summarize, the parameter ranges relevant to the basic slab drift-wave model are listed in Table 6.1. While a solution to the slab geometry, temperature gradient driven, drift-wave model may be determined numerically, this framework does not include many features necessary for a proper analysis in modern fusion devices (toroidal effects, realistic geometry, and velocity or magnetic shear to name a few), many of which can have stabilizing or destabilizing results. Therefore, no stability analysis of Eq. 6.10 was performed in this thesis.
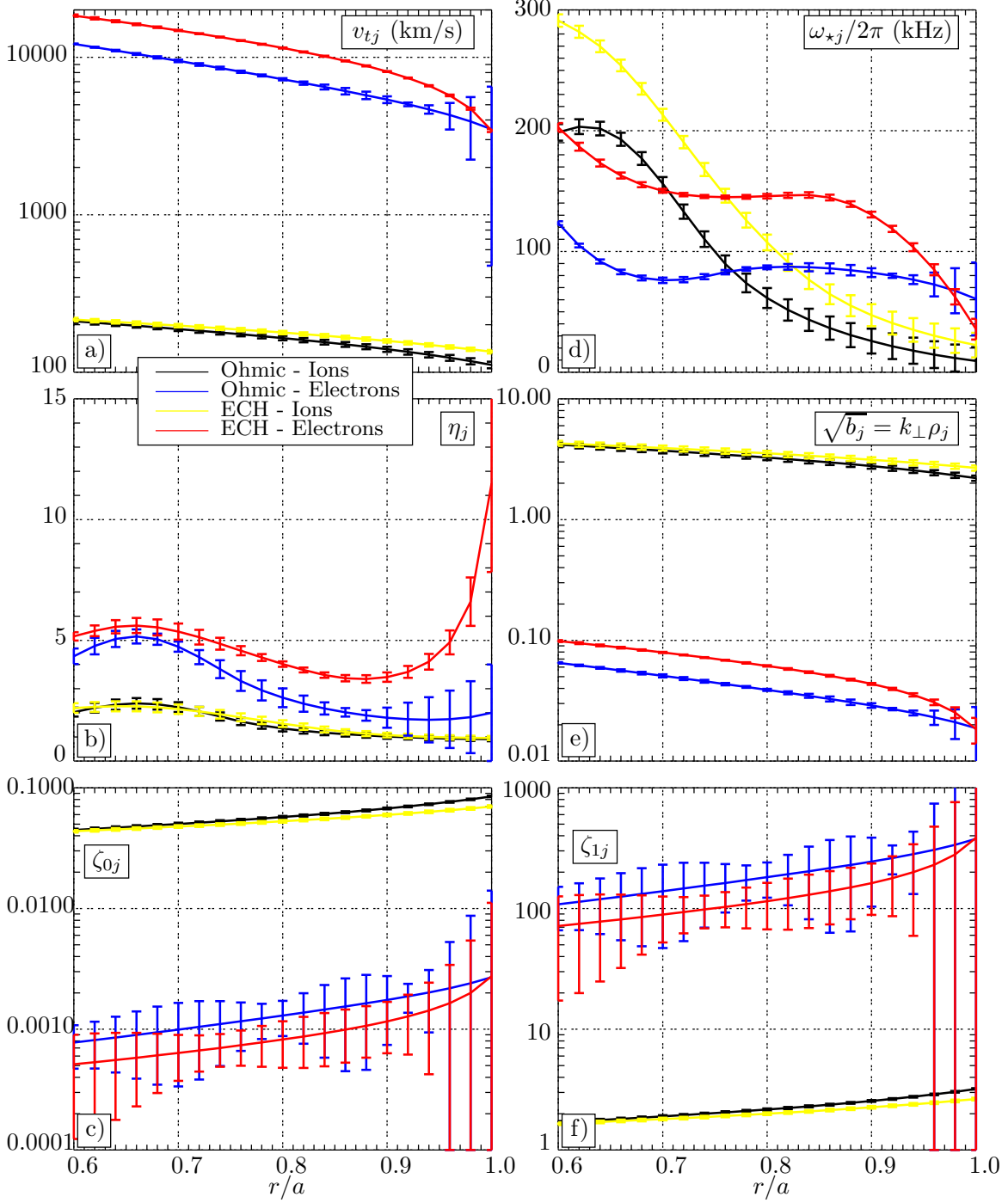
Figure 6-7: Drift-wave parameters plotted for $0.6 < r/a < 1.0$ over the PCI chord showing ion and electron parameters during ohmic heating in black and blue and ion and electron parameters during the highest power level of ECH heating in yellow and red. Calculations are performed for the high-k mode regime ($k_\theta = 20$ cm^{-1} and $k_{||}/k_\theta = 0.15$). The largest effect of the applied ECH heating is seen in η_e, and the Landau damping parameter ζ_{mj} is of $\mathcal{O}(1)$ for only ζ_{1i}.

Table 6.1: Drift-wave model parameters for ions and electrons during both Ohmic and ECH heating

	Ions		Electrons	
	Ohmic	ECH	Ohmic	ECH
v_{tj} (km/s)	100-200	100-200	4000-20000	4000-20000
$\omega_{\star j}/2\pi$ (kHz)	20-200	30-300	70-120	50-200
η_j	1-2	1-2	2-5	4-10
$\sqrt{b_j} = k_\perp \rho_j$	2-4	2-4	0.02-0.07	0.02-0.10
ζ_{0j}	0.04-0.08	0.04-0.09	0.001-0.003	0.001-0.003
ζ_{1j}	2-3	2-3	100-300	100-300

THIS PAGE INTENTIONALLY LEFT BLANK

Chapter 7

Conclusions and Future Work

7.1 Summary

Understanding particle and energy transport in modern fusion experiments and ultimately in reactor relevant regimes is a major thrust of the international fusion energy research community. Current experimental measurements reveal transport levels that are usually large compared to those predicted by collisional theories. This so-called anomalous transport is generally thought to arise from turbulent processes generated by micro-instabilities. Having a predictive theory, validated against experimental measurements, that models turbulence and the associated transport is a necessary step to improving the confinement of fusion devices. Therefore, this thesis is focused towards a comparison between experimental measurements and the simulation of short-wavelength turbulence. Upgrades to the diagnostic sensitivity, operational range, and measurement capacity have been designed, fabricated, and implemented as part of this work. The upper limits of the PCI operational range have been extended from 1 MHz and 8 cm^{-1} to 10 MHz and 40 cm^{-1} through new high speed digitizers, and a re-designed optical layout. In addition, the diagnostic sensitivity has been improved by nearly 10X through numerous improvements to the system conditioning and data transport electronics. The implementation of Phase Contrast Imaging (PCI) as a turbulence diagnostic is comparatively simple. The requirements for in-vessel equipment are minimal, it operates over a wide range of plasma param-

eters, it provides continuous measurements over a range of wave-numbers, and the diagnostic is completely non-perturbative. These factors should make PCI very useful for measuring turbulence in future reactor-relevant machines.

Following the approach by Raman and Nath, this thesis develops a simple framework for a mathematically rigorous treatment of the laser-plasma scattering interaction relevant for PCI measurements. This approach has the advantage of being relatively simple and intuitive. It yields details of the PCI operation such as the system response to modes propagating non-perpendicular to the PCI chord, and the system response to defocusing. The defocusing calculation takes into account potential fabrication errors in the phase plate groove depth, necessary to match calibration measurements. The theoretical framework is then extended to include the analysis of a rotating mask placed in any conjugate plane of the PCI optical system, and how this can be used to measure turbulence as a function of propagation angle about the PCI chord. Additionally, this work explains the assumptions that must be satisfied to interpret measurements as a function of propagation angle as being localized along the PCI chord. The difficulties in applying this technique to the small B_θ/B_ϕ plasmas in a tokamak require a novel version of the pitch angle masking technique.

Modifications to the DIII–D Phase Contrast Imaging diagnostic were designed and implemented to increase the frequency and wave-number range as well as the system signal-to-noise ratio. Many of the diagnostic improvements were performed as original work for this thesis. This includes design and analysis of new optical layouts to accommodate larger scattering angles of short wavelength turbulence and placement of the rotating mask. Circuit design, analysis, and prototyping, as well as contracting for PCB fabrication was performed during the development of the variable gain amplifier and filter (VGAF) circuits. The cylindrical lens technique was developed and implemented improving the signal-to-noise ratio by 5X. A fiber optic data transport system was implemented to provide a low noise solution to the PCI data transport from the DIII–D machine hall to the system digitizers. Additionally, the work in this thesis has provided absolute calibration measurements of the DIII–D PCI using both the ultrasonic CW loudspeaker and the fixed frequency transducers.

Calibrations using ultrasonic waves in air confirm that the upgraded PCI operates over the range $2 < k < 30$ cm^{-1}, and 10 kHz $< f < 10$ MHz; and analysis of magnetic field mappings show that the diagnostic covers roughly $0.7 < r/a < 1$. The mask response function was experimentally measured and is in excellent agreement with theoretical expectations.

Power spectra estimates of DIII–D PCI data exhibit features that are ubiquitous across most plasma discharges (L-Mode, most H-Mode plasmas) and heating regimes (ohmic, neutral beam injection, ECH). The largest amplitude turbulence structure seen with the PCI is a branch in wave-number and frequency space with roughly constant phase velocity that decays monotonically with increasing frequency. This branched structure is generally limited to wave-numbers $\lesssim 15$ cm^{-1}. The phase velocity is most closely tied to the plasma rotation, suggesting that the mode frequency as measured in the lab frame is dominated by the Doppler shift. The main branch feature is due to turbulence propagating perpendicular to the magnetic field, and is localized to the edge region of the plasma. A low power component of the signal is also common across many plasma discharges and appears as a broad structure in mask angle, indicating that these modes do not propagate perpendicular to the local magnetic field.

Analysis of PCI measurements using the rotating mask system shows a number of examples in which turbulence propagates at angles too large to be interpreted as modes propagating perpendicular to the local magnetic field. Many of these modes are low power spectral features that are best revealed using the Maximum Entropy Method (MEM) spectral estimation technique. We show that this spectral estimation technique is superior in both spectral resolution and sidelobe suppression to that of the typical Fourier spectral estimation technique. Three classes of turbulence with finite and large $k_{\parallel}$ are identified, modes that are localized in wave-number and mask angle (the high-k and medium-k modes), a broad (in mask angle) background turbulence, and a low-k "wing" that smears the main branch structure. These modes are seen to propagate at large angles corresponding to $k_{\parallel}/k \sim 0.1 - 0.4$.

The most common modern tools used to predict and model plasma turbulence

are complex nonlinear simulations built around the gyrokinetic theory. However, the assumption that the turbulent modes of interest propagate perpendicular to the magnetic field is made at the outset of the theoretical derivation. As a result, finite $k_{||}$ modes are ordered out of the gyrokinetic equations; this imposes an upper limit on the size of the parallel wave-number, $k_{||}/k_\theta \sim 0.01$. This is verified by linear simulations using the GYRO code in which the angular response in spectral power is a narrow peak limited to $k_{||}/k_\theta \lesssim 10^{-4}$ for wave-numbers larger than 5 cm^{-1}, and scales as $1/k_\theta$. In light of this fact, we have revisited a basic slab model drift-wave theory that will have to be extended in the future by including effects due to toroidal geometry. In addition, high power ECH heating increases the value of η_e by a factor of 2 in the interior region of the plasma and by nearly a factor of 4 at the edge, both regions intercepted by the PCI chord. The importance of such effects on plasma turbulence need to be explained in future theoretical efforts outside of the limitations of gyrokinetic theory.

7.2 Conclusions

The work in this thesis focused on experimental measurements of plasma density fluctuations in the DIII–D tokamak using the Phase Contrast Imaging diagnostic. These measurements are the first in the expanded operational regime that use the rotating mask to both localize turbulent fluctuations along the PCI chord, as well as provide measurements as a function of propagation angle about the PCI chord.

The work in this thesis has also led to further insights into the details and operation of the PCI as a plasma diagnostic. The assumption that the PCI is only sensitive to modes propagating perpendicular to the chord is valid only when the physical extent of the mode in the plasma is large (see Sec. 2.1.2). The notches with wave-number in PCI calibration measurements due to defocusing (the Talbot Effect) can be phase shifted by imperfections in the phase-plate groove depth. Dual cylindrical lenses (in one of two valid configurations) can be used to enhance the PCI signal-to-noise ratio by as much as a factor of 5 by effectively integrating the measurement

along the toroidal direction. The use of cylindrical lenses also degrades the ability to make measurements at large propagation angles. Power spectra estimates using the Maximum Entropy Method result in improved spectral resolution as well as improved side-lobe level spectral contamination over a basic Fourier based approach. In regard to turbulence measurements, we draw the following conclusions:

1. The largest amplitude turbulence structures measured by the PCI consist of branches in wave-number and frequency space with relatively constant phase velocity, referred to as the "main branches". These branches decrease in spectral power with frequency and wave-number $\propto 1/k^2$.

2. The main branch turbulence propagates perpendicular to the local magnetic field, and is localized to the plasma edge region ($r/a \gtrsim 0.9$) with the response peaking at the LCFS.

3. Three classes of turbulence have been measured with mask angle responses too large to be interpreted as propagating near perpendicular to the magnetic field, and therefore cannot be localized. The high-k and medium-k modes are localized in wave-number ($k \sim -21$ cm^{-1} and $k \sim +16$ cm^{-1}, respectively) and mask angle with $k_{||}/k \lesssim 0.15$. These modes exist over the frequency range from $100 - 400$ kHz and $200 - 400$ kHz respectively. The background turbulence is broad in mask angle with $k_{||}/k \lesssim 0.2 - 0.4$ depending on frequency, and the low-k wings exist to $k_{||}/k \lesssim 0.05 - 0.1$.

4. The high-k mode ($k\rho_i \sim 3$) spectral power increases with applied ECH and NBI heating. The applied heating is shown to *increase* the electron temperature gradient drive (inverse scale-length, $1/L_{Te}$) and *decrease* the ion temperature and density gradient drives ($1/L_{Ti}$ and $1/L_n$) in the edge region $r/a \gtrsim 0.8$ where the PCI measurements are made.

5. The derivation of the Gyrokinetic equations assumes an ordering such that $k_{||}/k_\perp \sim \rho/L \sim 0.01$. GYRO simulations produce self-consistent turbulence with $k_{||}/k_\theta \lesssim 10^{-4}$ for $k > 5$ cm^{-1} and scales like $1/k$.

6. A basic temperature-gradient driven drift-wave model in slab geometry shows that finite $k_{||}$ modes could interact resonantly with ions through the ion cyclotron Doppler resonance terms $\zeta_{\pm 1i} = (\omega \mp \Omega_i)/(k_{||}v_{ti}) \sim 1$. These $m \neq 0$ terms in the dispersion relation are not included in the derivation of the gyrokinetic equations.

The rotating mask technique for localizing measurements along the viewing chord was designed and implemented on the DIII–D PCI, allowing us to draw several conclusions. The rotating mask provides time-dependent measurements as a function of turbulence propagation angle convolved against a system transfer function as given in Eq. 2.37. The ability to interpret rotating mask measurements as localized along the PCI chord requires the assumption that turbulence propagates perpendicular to the local magnetic field and results in Eq. 2.45. The mask response function (system transfer function) peaks at $(\alpha - \gamma)$ and decreases monotonically to zero in both directions; the width of the peak decreases with increasing wave-number, thus improving the localization at high-k. Additionally, localization improves for plasma geometries with low q_{95}, as this increases the range in magnetic pitch across the PCI chord. Finally, the mask itself can be placed at any conjugate plane in the PCI imaging system provided the beam is sufficiently collimated in the plasma.

7.3   Future Work

The ability for the DIII–D PCI diagnostic to make short-wavelength, high-k measurements relies on the system having the best signal-to-noise ratio. Currently, the 15 year old HgMnTe detectors are the most limiting component of the PCI system and we estimate a factor of 5-10 improvement in signal-to-noise with a new detector array. Unfortunately, due to low demand, HgCdTe (the modern semiconductor material used at 10.6 μm) detector arrays produced in the photovoltaic (PV) configuration are difficult to find at an affordable price (Raytheon Vision Systems, Goleta, CA). A non-array PV HCT detector can be made from smaller individual elements (Teledyne Judson Technology, Montgomerville, PA). However, this approach would have

specifications (element size, spacing, alignment tolerance) that would result in lower S/N, and other degradations in performance. HgCdTe detectors can be acquired in a photoconductive (PC) configuration (InfraRed Associates Inc., Stuart, FL) with similar noise levels to that of the PV configuration, however the frequency response of the PC configuration is not as good, namely the PC response is flat to ~ 500 kHz and then falls off with 3dB/octave.

The rotating mask system has been shown to be able to localize measurements of the "main branch" structures to the plasma edge. With such an ability, one can determine the propagation direction of the mode around the tokamak, and in the Phase I geometry, can also use this technique to measure turbulence amplitude response at two different ballooning angles. This $k_{||} \sim 0$ turbulence is the largest amplitude structure measured with the PCI, and although edge turbulence is not well understood, it is thought to set the pedestal parameters and have a large impact on H-Mode performance. Therefore, studies to characterize scalings of the main branch turbulence with density, current, ECH heating power level, and other plasma parameters would be useful to establish a quantitative database to be compared to edge turbulence codes as they become more mature.

The basic slab geometry drift-wave model for temperature gradient driven turbulence was used in this work to merely point out a potential mechanism for interaction between modes with large parallel wave-numbers and the plasma through the ion channel. Solutions to the dispersion relation in this basic model would determine whether the mode is unstable, however a more robust model including toroidal effects, realistic geometry, velocity and magnetic shear as well as other important factors need to be included beyond the limitations of gyrokinetic theory. Such work was not attempted in this thesis.

THIS PAGE INTENTIONALLY LEFT BLANK

Appendix A

Optical Techniques

The Phase Contrast Imaging diagnostic is just that, an imaging system much like that of an early camera. For anyone who has used a manual 35 mm camera, the wave-number of fluctuation is similar to different f# rays in the paraxial limit. Just as lowering the f-stop (low f# cutoff) on a camera decreases the depth of focus in the resulting image, so too the high-k are more readily out of focus than the lower scattering angle low-k fluctuations. A fraction of the PCI optical analysis is handled accurately in the geometric optics regime (*i.e.* the paraxial limit of rays, and focusing optics treated as thin lenses). These geometric optics considerations define the object, image, and conjugate planes. The object plane is the PCI chord center of the intersection with the plasma, the image plane is where the detector array is placed, and the conjugate plane is where the phase plate is located.

The PCI also uses a CO_2 laser, operating in the TEM_{00} mode. Thus the beam intensity profile is Gaussian, and the beam propagation through the optics is governed by Gaussian beam propagation laws. Gaussian beams can be described in terms of laser waists, the Rayleigh range, and the phase front radius of curvature.

The following appendix gives a review of geometric optics and Gaussian beam propagation laws.

A.1 Geometric Optics

The locations of both the phase plate (conjugate plane) and detector array (image plane) are defined by purely geometric optic considerations. An **image plane** is defined by the location after a lens where the distance of a given ray from the optical axis depends **only on the distance from the optical axis at the object plane** and not the angle of the ray at the object plane. Conversely, the **conjugate plane** is defined by the location after a lens where the distance of a given ray from the optical axis depends **only on the angle of the ray at the object plane** and not the distance from the optical axis at the object plane. Figure A-1 depicts the geometric optic focusing of a single lens using two sets of parallel rays. We say that the image plane is "optically equivalent" to the object plane in that all rays from a specific location in the object plane meet at a specific location at the image plane. Thus some intensity distribution $S^{\text{object}}(x, y) = S^{\text{image}}(Mx, My)/M^2$, where M is the magnification of the imaging system and x and y are dimensions perpendicular to the optical axis.
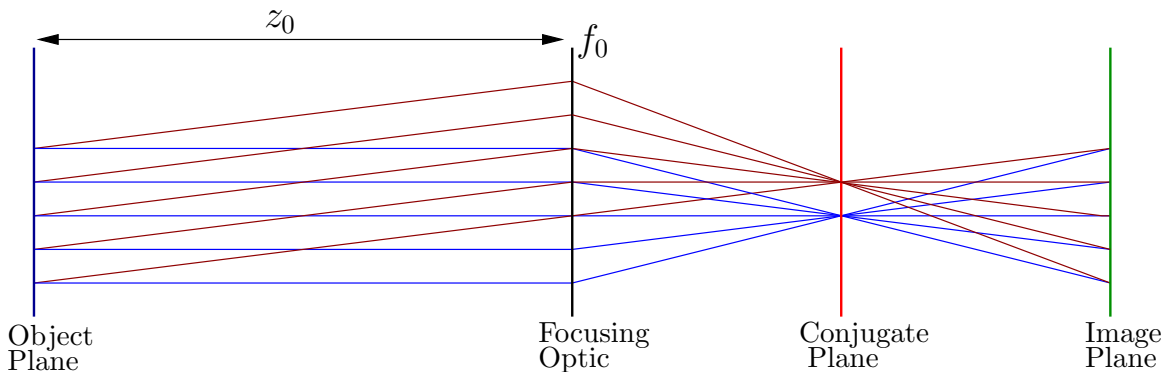
Figure A-1: Geometric Optics Description of Image and Conjugate Planes

Calculations of how rays propagate when governed by geometric optics are most easily performed by using the ABCD matrix representation of optical components. In this approach, each ray is described by a vector where the top index, r, is the distance measured from the optical axis, and the lower index, r', is the slope of the ray. When optical systems operate in the paraxial limit ($r' \ll 1$), rays propagate near horizontal and the curvature of optical components is similarly small. In this representation the

free-space propagation matrix $\mathcal{F}(z)$ and the thin lens transformation matrix $\mathcal{L}(f)$ are given by Eq. A.1

$$\mathcal{F}(z) = \begin{bmatrix} 1 & z \\ 0 & 1 \end{bmatrix} \qquad \mathcal{L}(f) = \begin{bmatrix} 1 & 0 \\ -\frac{1}{f} & 1 \end{bmatrix}. \qquad (A.1)$$

Applying these two matrices to the above single lens imaging system depicted in Fig. A-1 we get

$$\begin{bmatrix} r(z) \\ r'(z) \end{bmatrix} = \begin{bmatrix} 1 & z \\ 0 & 1 \end{bmatrix} \begin{bmatrix} 1 & 0 \\ -\frac{1}{f_0} & 1 \end{bmatrix} \begin{bmatrix} 1 & z_0 \\ 0 & 1 \end{bmatrix} \begin{bmatrix} r_0 \\ r'_0 \end{bmatrix}$$
$$= \begin{bmatrix} r_0(1 - \frac{z}{f_0}) + r'_0(z_0 - z(1 - \frac{z_0}{f_0})) \\ r_0(-\frac{1}{f_0}) + r'_0(1 - \frac{z_0}{f_0}) \end{bmatrix}. \qquad (A.2)$$

The above simple calculation shows the propagation of rays through the optical system in Fig. A-1. It starts with a ray (in the object plane) with a height from the optical axis r_0, and slope r'_0. It then propagates a distance z_0 through free space, encounters a lens of focal length f_0, and finally propagates a distance beyond the lens z. Generically, the resulting ray has the form (as a function of z away from the lens) as given in Eq. A.3.

$$\begin{bmatrix} r(z) \\ r'(z) \end{bmatrix} = \begin{bmatrix} r_0(A + zC) + r'_0(B + zD) \\ r_0(C) + r'_0(D) \end{bmatrix}. \qquad (A.3)$$

At this point it should be clear that the image plane (defined where r is not dependent on r'_0) is located at $z_{\text{image}} = -\frac{B}{D}$. The conjugate plane (defined where r is not dependent on r_0) is located at $z_{\text{conj}} = -\frac{A}{C}$. It doesn't matter how many lenses you would like to propagate through. Next, we consider a multiple lens system, z_0 to the first lens of focal length f_0, then z_1 to the second lens of focal length f_1, ..., finally propagating a distance z after the final lens. The ray will again be given by an equation identical to Equation A.3 where A, B, C, D will now depend on z_0, f_0, z_1, f_1, ... but the image plane will still be located at $z_{\text{image}} = -\frac{B}{D}$ and the conjugate

plane at $z_{\text{conj}} = -\frac{A}{C}$. It should now be obvious that after every lens in the imaging system there exists an image plane and a conjugate plane. However, if z_{image} or z_{conj} are negative then these planes are said to be *virtual*, and are therefore not useful to us as designers of imaging systems.

One can iteratively update the parameters A^i-D^i for every free space propagation and lens pair. The parameters start at $A^0 = 1, D^0 = 1$ the rest start equal 0. Then for every z_i, f_i pair, the parameters are updated as follows:

$$
\begin{aligned}
A^i &= A^{i-1} + z_i C^{i-1} \\
B^i &= B^{i-1} + z_i D^{i-1} \\
C^i &= C^{i-1} - \frac{A^{i-1}}{f_i} - \frac{z_i C^{i-1}}{f_i} \\
D^i &= D^{i-1} - \frac{B^{i-1}}{f_i} - \frac{z_i D^{i-1}}{f_i},
\end{aligned}
\tag{A.4}
$$

or in matrix form,

$$
\begin{bmatrix} A^i & B^i \\ C^i & D^i \end{bmatrix} = \begin{bmatrix} 1 & z \\ -\frac{1}{f_i} & 1 - \frac{z_i}{f_i} \end{bmatrix} \begin{bmatrix} A^{i-1} & B^{i-1} \\ C^{i-1} & D^{i-1} \end{bmatrix}.
\tag{A.5}
$$

The properties of the A^i, B^i, C^i, D^i parameters relate to the system magnification. Since after every lens of focal length f_i there exists the ith image plane, there must also be a magnification between that image plane and the object plane. It is simply $r(z_{\text{image}}^i)/r_0$ or

$$
M = \frac{r(z_{\text{image}}^i)}{r_0} = \frac{A^i D^i - B^i C^i}{D^i} = \frac{1}{D^i},
\tag{A.6}
$$

where in the final equality we've used the fact that the determinant of the free space propagation and lens matrices are unity.

A final relation is useful when computing the change of wave-vector direction from the scattered beams generated at the object plane, where the PCI probe beam scatters off density fluctuations, to the scattered beams at the image plane, where the PCI beams are interfered for detection. Considering rays scattered with $r_0 = 0$, as is the case for PCI scattered beams, the slope of the ray at the image is $r'_{\text{img}} = D\, r'_0 = r'_0/M$.

If we think in terms of wave-vectors to represent the rays where k_r is the radial component at the object plane and k is the magnitude of the wave-vector at the object plane, then the wave-vector at the image is

$$\vec{k}_{\text{img}} = \frac{k_r}{M}\hat{r} + \sqrt{k^2 - \frac{k_r^2}{M^2}}\hat{z}. \qquad (A.7)$$

The rotation of the wave-vector from object plane to image plane depends solely on the overall system magnification and *not* on the details of the imaging system.

A.2 Gaussian Laser Optics

This section will review the properties of Gaussian beam propagation through an optical system assumed to operate in the paraxial limit defined in Sec. A.1. The probe beam used in the DIII–D PCI Diagnostic, a CO_2 laser operating in the TEM_{00} Gaussian mode, is focused to a minimum spot size in the conjugate plane of the imaging system. At this minimum spot size, the scattered beams are filtered for measurements of propagation direction as described in Sec. 2.2. If the spot is not of minimum size at this location, the resolution of such measurements are directly degraded. Therefore, it is important to understand how Gaussian beams propagate through focusing optics. The electric field of a Gaussian beam is a solution to the Helmholtz equation in the paraxial limit

$$E(x, y, z) = E_0 \, \frac{\text{w}_0}{\text{w}(z)} \, e^{-\left(\frac{r^2}{w^2(z)}\right)} \, e^{-i\left[kz - \tan^{-1}\left(\frac{z}{z_0}\right)\right]} \, e^{-i\left(\frac{kr^2}{2R(z)}\right)}. \qquad (A.8)$$

where $r = \sqrt{x^2 + y^2}$ is the radial distance from the optical axis, w is the beam waist $(1/e$ radial distance of the electric field profile), z is the distance along the direction

of propagation from the beam waist minimum (w_0), and the beam parameters

$$z_0 = \frac{k w_0^2}{2}$$

$$w(z) = w_0 \sqrt{1 + \left(\frac{z}{z_0}\right)^2} \tag{A.9}$$

$$R(z) = z \left[1 + \left(\frac{z_0}{z}\right)^2\right]$$

are all specified in terms of the minimum spot size (w_0). Therefore, a Gaussian beam is defined by knowledge of the minimum spot size, location of the minimum beam waist ($z \equiv 0$), and the beam wave-number in the medium k as shown in Fig. A-2. The beam expands with an angle $\theta \simeq \frac{2}{k w_0}$, and this can be verified by evaluating $w(z)$ in the limit $z \gg z_0$ as given in Eq. A.9.
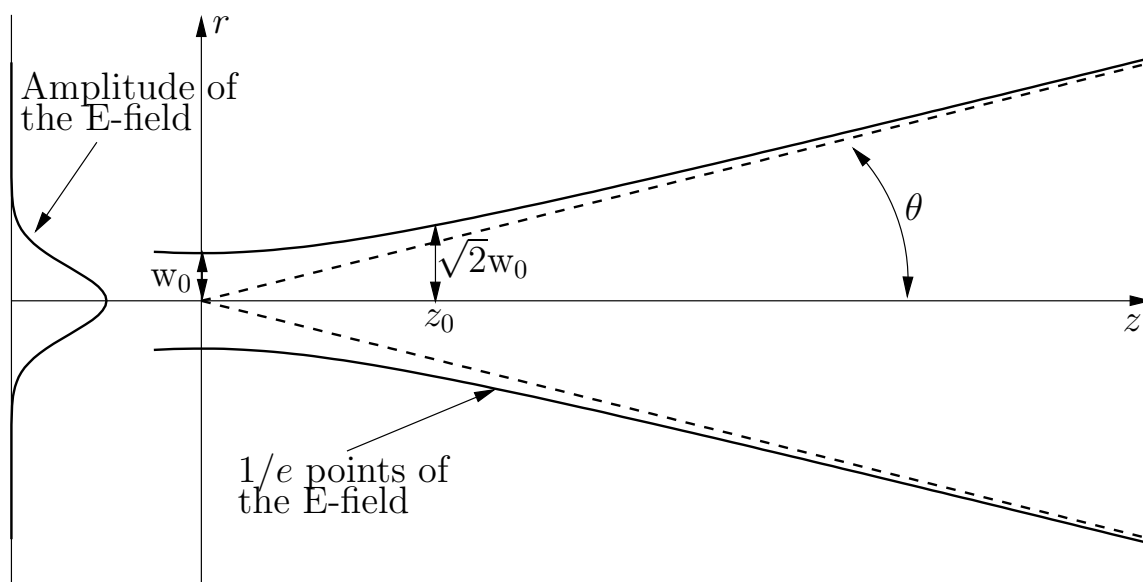
Figure A-2: Beam expansion of a TEM_{00} laser mode.

A well known and quite astounding relationship holds for Gaussian beam propagation similar to that used for geometric rays described in Sec. A.1 [102]. Just as a geometric ray is specified by its parameters (r, r') which transform simply through free space and thin lenses, the Gaussian beam is specified by its parameters (w, R) at every location along the beam. These parameters also transform simply through free space and thin lenses. This is performed through the definition of the complex

190

beam parameter (sometimes called the complex radius of curvature) q, defined as

$$\frac{1}{q} = \frac{1}{R} - i\frac{2}{k\mathrm{w}^2}. \tag{A.10}$$

What is astounding is that the complex beam parameter transforms using the same ABCD propagation parameters as used for geometric rays. It is no longer a matrix transformation, but given by

$$\frac{1}{q} = \frac{C + D(1/q_0)}{A + B(1/q_0)}. \tag{A.11}$$

That is, if we know the initial Gaussian beam waist size (w_i) and its radius of curvature (R_i) at the starting location, we can compute the initial complex beam parameter (q_i) and propagate it through an arbitrary set of optical components as before. If we consider the parameters ABCD as containing the information of propagating through a set of distances and focusing optics $(z_0, f_0, z_1, f_1, ...)$, then we can compute the complex beam parameter at a distance z after the last lens.

$$\frac{1}{q(z)} = \frac{C + D(1/q_i)}{(A + Cz) + (B + zD)(1/q_i)}. \tag{A.12}$$

The real part of Eq. A.12 gives an expression for the radius of curvature at a distance z from the last lens, while the imaginary part gives an expression for the waist. Solving for the beam parameters,

$$R(z) = \frac{\left[\left(A + \frac{B}{R_i}\right) + z\left(C + \frac{D}{R_i}\right)\right]^2 + (B + zD)^2\frac{4}{k^2\mathrm{w}_i^4}}{\left(C + \frac{D}{R_i}\right)\left[\left(A + \frac{B}{R_i}\right) + z\left(C + \frac{D}{R_i}\right)\right] + D(B + zD)\frac{4}{k^2\mathrm{w}_i^4}}, \tag{A.13}$$

$$\mathrm{w}^2(z) = \mathrm{w}_i^2 \frac{\left[\left(A + \frac{B}{R_i}\right) + z\left(C + \frac{D}{R_i}\right)\right]^2 + (B + zD)^2\frac{4}{k^2\mathrm{w}_i^4}}{D\left[\left(A + \frac{B}{R_i}\right) + z\left(C + \frac{D}{R_i}\right)\right] - \left(C + \frac{D}{R_i}\right)(B + zD)}. \tag{A.14}$$

After the last lens, the above equations describe the beam parameters. The beam

minimum waist size will occur at $R(z) \rightarrow \infty$ or

$$z_{\text{waist}} = -\frac{\frac{4DB}{k^2 \text{w}_i^4} + \left(C + \frac{D}{R_i}\right)\left(A + \frac{B}{R_i}\right)}{\frac{4D^2}{k^2 \text{w}_i^4} + \left(C + \frac{D}{R_i}\right)^2}. \tag{A.15}$$

To summarize, a Gaussian laser beam is specified as it propagates through free space by its radius of curvature and waist (R, w), or equivalently the minimum waist size (w_0) and the location at which the spot is minimum $(z \equiv 0)$. The beam transforms as it passes through focusing optical components through the complex beam parameter and Eq. A.11.

Appendix B

Spectral Estimation Techniques

A problem common to many branches of science and engineering is that of estimating the frequency content of a time-domain signal. In other fields the problem presents itself in spatial domains, the problem being how one accurately estimates the power spectrum of a real world signal. It is true, by definition, that the time/frequency or space/wave-number domains are linked by the Fourier Transform, but only in the case where the signal is known completely and in the absence of noise. This is, of course, never the case in the real world, and therefore a signal's power spectrum is never truly *known*, but is instead *estimated*. The deviations from complete knowledge of a real world signal are the presence of noise in any real world process, the fact that the duration of the signal is only known over a limited domain, and (in the case of modern experiments) the signal is almost always sampled at discrete intervals. There are a multitude of methods to estimate power spectra (a review of which is beyond the scope of this work), each with their own assumptions, trade-offs and benefits, and what may be the best technique for dataset A may not be the best technique for dataset B. This appendix reviews two approaches to computing power spectra and how they are applied to the DIII–D PCI data.

B.1 Basic Fourier Analysis

The most common approach to estimating a signal's power spectrum is to convert the Fourier Transform into the discrete domain, and truncate the transform to the limited region of space that has been sampled. Computationally, we often default to the Fast Fourier Transform (FFT) as the benefits of speed, efficiency, and wide-spread use are difficult to ignore. This is not to say that the FFT approach is without its merits, and we use it regularly with PCI data. To adress the issue of noise in any real world signal, the proper way to estimate the power spectrum is to average the power spectra of an ensemble of estimates of the noisy signal. To begin, we start by defining a time-domain signal as

$$
\begin{aligned}
s_j(t) = & s(t_j) \rightarrow \{s_0, s_1, s_2, ..., s_{N-1}\} \\
t_j = & j\Delta t \text{ and } j = 0, 1, 2, ..., N-1,
\end{aligned}
\tag{B.1}
$$

where generally, for the PCI data analyzed in this thesis, $N = 48 \times 1024 \times 1024$ and $\Delta t = 2.5 \times 10^{-7}$ sec. We use the FFT approach in a method similar to that of Welch [76], where overlapping windows are used to improve the estimate by averaging over multiple realizations of the data as depicted in Fig. B-1. Hann windows are used as the FFT assumes that the data is circular (*i.e.* the Hann window avoids artifacts imposed by the edge discontinuities of the circular wrapping). By denoting $\mathcal{F}_\mathcal{D}$ as the
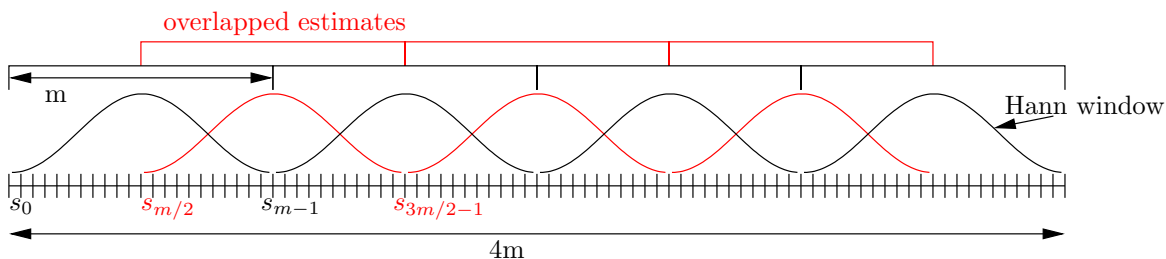
Figure B-1: Graphical depiction of Welch's Method using overlapping, windowed segments of data in the estimation of power spectra. Here, the overlap is 50%, and a Hann window is shown.

discrete FFT operator, a typical power spectrum estimate (as shown above in Fig. B-

1) comprised of 4 spectral windows with 3 overlapping windows can be written

$$S_j(f) = \sum_{i=0}^{2R-2} \left| \mathcal{F}_{\mathcal{D}}\{s_{j+id}, s_{j+id+1}, s_{j+id+2}, ..., s_{j+(i+1)d-1}\} \right|^2, \qquad \text{(B.2)}$$

where R is the number of non-overlapped realizations (in the above example $R = 4$), $d = m/2$ is the amount of overlap, in the case shown 50%. For typical DIII–D PCI data, this process is performed with $m = 128 - 1024$ and $R = 2 - 16$, giving power spectra estimates as a function of time throughout the discharge.

The PCI signal is composed of time series samples from 16 detector elements each corresponding to a particular spatial location in the plasma. With the 1-D FFT technique described above, the frequency domain power spectra can be estimated for any of the 16 detector elements. One might be tempted to apply such an approach to the spatial dimension as well, however this would be foolhardy as we will discuss in the following section.

B.1.1 Complications in DIII–D PCI Data

The DIII–D PCI data suffers from a number of complicating factors. First, with only 16 samples, breaking the spatial domain into multiple realizations would reduce the wave-number resolution to unacceptable levels. Therefore, no ensemble averaging is possible in this dimension. The PCI detector array is 15 years old, and 4 channels are degraded or inoperable. This results in a non-uniform multiplicative coefficient in front of each spatial sample, some of which are 0 for channels that are non-functional. This coefficient results in the problem of missing spatial samples, and by blindly taking the FFT in the spatial dimension, the coefficients distort the actual underlying wave-number spectra. Fortunately, computing the power spectra from the autocorrelation function (described in the next section) reduces the impact of these imperfections on the resulting power spectra.

B.2 2-D Autocorrelation Function Approach

The autocorrelation function (ACF) can be used as an intermediary step on the road to computing power spectra. This is useful because accurate estimates of the ACF are still possible in the presence of the complications of missing spatial samples and non-uniform responsivity for each detector channel. The relationship between the ACF and the power spectra is easily derived by considering, for example, a 2-D signal of time and space $f(x,t)$ for which we seek to estimate the power spectra $S(k,\omega)$. We define the ACF as

$$C(\chi, \tau) = \int_{-\infty}^{\infty} dt \int_{-\infty}^{\infty} dx \ f(x,t) f(x+\chi, t+\tau). \tag{B.3}$$

By operating on both sides with a 2-D Fourier transform we get

$$
\int_{-\infty}^{\infty} d\chi \int_{-\infty}^{\infty} d\tau \ C(\chi, \tau) e^{-ik\chi} e^{-i\omega\tau} =
$$
$$
\int_{-\infty}^{\infty} d\chi \int_{-\infty}^{\infty} d\tau \int_{-\infty}^{\infty} dt \int_{-\infty}^{\infty} dx \ f(x,t) f(x+\chi, t+\tau) e^{-ik\chi} e^{-i\omega\tau}. \tag{B.4}
$$

To get to a definition of the ACF in terms of the autocorrelation function, we focus on the RHS of Eq. B.4 above. By multiplying the RHS by $e^{-ikx}e^{+ikx}$ and $e^{-i\omega t}e^{+i\omega t}$, and defining the dummy variables $\xi = x + \chi$ and $\lambda = t + \tau$, we get

$$\int_{-\infty}^{\infty} dt \int_{-\infty}^{\infty} dx \ f(x,t) e^{+ikx} e^{+i\omega t} \int_{-\infty}^{\infty} d\xi \int_{-\infty}^{\infty} d\lambda f(\xi, \lambda) e^{-ik\xi} e^{-i\omega\lambda}, \tag{B.5}$$

which we can recognize as the complex conjugate of the Fourier transform of the function f multiplied by the Fourier transform of the function f. This is, by definition, the power spectra $S(k,\omega) = \mathcal{F}[f] \times \mathcal{F}^{\star}[f]$. This leaves us with the result that the Fourier transform of the autocorrelation function is the power spectrum of the underlying signal, or

$$S(k,\omega) = \int_{-\infty}^{\infty} d\chi \int_{-\infty}^{\infty} d\tau \ C(\chi, \tau) e^{-ik\chi} e^{-i\omega\tau}. \tag{B.6}$$

The relation between the power spectrum and correlation function was shown using a continuous signal. The relation also holds in the discrete domain, that the Fourier transform of the correlation function is the power spectrum. For PCI data we can define a 2-D autocorrelation function in the discrete domain as

$$C_{m,n} = \sum_{i=0}^{N_t-1} \sum_{j=0}^{N_s-1} s_{i,j} \ s_{i+m,j+n},$$
(B.7)

where N_t and N_s are the number of temporal and spatial samples, $i+m \to i+m-N_t$ for $i + m \geq N_t$, and $j + n \to j + n - N_s$ for $j + n \geq N_s$ making the correlation functions circular.

The relation between the autocorrelation function and the power spectrum is highly useful for handling missing spatial samples in PCI data because the ACF is only a function of *channel separation*. Therefore, one missing channel only reduces the number of estimates one can form of a given channel separation and does not entirely remove a given sample in channel separation. For example, if all 16 channels were available, this would allow us to compute the ACF at channel separations of $0, \pm 1, \pm 2, ..., \pm 15$, with $16, 15, 14, ..., 1$ estimates of each separation. If instead of all 16 channels we have only the typical subset $[1, 3, 4, 6, 7, 9, 10, 12, 13, 14, 15, 16]$ (*i.e.* missing channels 2,5,8,11) then we can still compute the ACF at all 16 channel separations $[0, \pm 1, \pm 2, ..., \pm 15]$ with $[12, 7, 7, 9, 5, 5, 7, 4, 4, 5, 3, 3, 3, 2, 1, 1]$ estimates of the corresponding channel separation. Additionally, the non-uniform responsivity of each detector channel can be estimated by normalizing each pair of correlations by the root mean squared of each channel in the given realization. The resulting power spectra can be re-normalized to the proper total power through Parseval's well-known theorem.

In this sense, the autocorrelation function is estimated over multiple realizations using Hann windows in both space and time as was laid out in Sec. B.1. If the correlations are computed via the FFT (a well known trick in signal processing), the computation is extremely fast, and only the final FFT of the resulting ACF is necessary to result in an accurate 2-D power spectra estimation.

B.3   MEM Spectral Analysis

The Maximum Entropy Method for power spectra estimation has been in use since Burg in the 1960s [74]. One of the best pedagogical explanations of the merits of the MEM spectral estimation technique can be found with Ables [75]. Computation of the MEM spectral estimate can be performed based on the raw time series $s_j(t)$ or from the estimate of an autocorrelation function.

B.3.1   MEM from Time Series

The MEM spectral estimate can be computed from the time series data without first estimating the autocorrelation function. This is useful in many applications and produces a robust solution. When the power spectrum of a real valued time series is needed (and thus there is no phase information), the solution need only produce a power spectrum for positive frequencies. Such a solution is given in Numerical Recipes [77]. In the case of complex signals where phase information is available, a MEM spectral estimation can be computed for both positive and negative frequencies [74]. Details of the time-series MEM estimates are beyond the scope of this work as the MEM spectral estimate based on the correlation function is more usefully applied to PCI data. By computing the power spectrum from the autocorrelation function, the issues of missing spatial samples due to inoperable detector channels do not distort the spectral estimate.

B.3.2   MEM from Autocorrelation Function

The MEM spectral estimate can be computed from the autocorrelation function by setting up a matrix equation. To demonstrate this, we consider a 1-D time series of complex data similar to that in Eq. B.1. The autocorrelation function can be written as

$$C_j = \sum_{i=0}^{N-1} s_i^\star\, s_{i+j}, \tag{B.8}$$

where $i + j \rightarrow i + j - N$ for $i + j \geq N$ making the correlation function circular, and $\star$ denotes the complex conjugate. The correlation function can also be easily computed from the FFT for computational efficiency. The Maximum Entropy (all-pole) power spectra is then defined as [103–105]

$$S_{\mathrm{MEM}}(f) = \frac{\sigma_p^2 \Delta t}{\left| 1 - \sum_{j=1}^{p} a_j^p e^{-i2\pi f j \Delta t} \right|^2} \tag{B.9}$$

where a_j^p is the jth coefficient of a p pole autoregressive model, and σ_p is called the "innovations variance," or the variance in the signal noise. The coefficients a_j^p are defined in terms of the *Yule-Walker* equation that relates them to the autocorrelation function C_j

$$\begin{bmatrix} C_0 & C_1 & \cdots & C_{p-1} \\ C_1 & C_0 & \cdots & C_{p-2} \\ \vdots & \vdots & \ddots & \vdots \\ C_{p-1} & C_{p-2} & \cdots & C_0 \end{bmatrix} \begin{bmatrix} a_1^p \\ a_2^p \\ \vdots \\ a_p^p \end{bmatrix} = \begin{bmatrix} C_1 \\ C_2 \\ \vdots \\ C_p \end{bmatrix}. \tag{B.10}$$

Note that there can only be as many poles in the model as there are offsets in the correlation function minus one. For a model of only 3 poles, one only need to compute 4 offsets in the autocorrelation function $[C_0, C_1, C_2, C_3]$. The matrix formed by the correlation function in Eq. B.10 is a Toeplitz matrix, and the solution of such an equation is efficiently solved using the Levinson-Durbin recursion algorithm [104, 106]. The form of the recursion presented below follows Burgs modification to the standard algorithm [104].

The recursion solves for the pth order σ_p^2 and set of $[a_1^p, a_2^p, ..., a_p^p]$ given the previous order σ_{p-1}^2, $[a_1^{p-1}, a_2^{p-1}, ..., a_{p-1}^{p-1}]$ and the autocorrelations $[C_0, C_1, ..., C_p]$ using the following relations

$$a_p^p = \frac{C_p - \sum_{j=1}^{p-1} a_j^{p-1} C_{p-j}}{\sigma_{p-1}^2}, \tag{B.11}$$

$$a_j^p = a_j^{p-1} - a_p^p \, a_{p-j}^{p-1}, \tag{B.12}$$

$$\sigma_p^2 = \sigma_{p-1}^2 \left(1 - \left| a_p^p \right|^2 \right), \tag{B.13}$$

where $|a|^2 = a^{\star}a$ is the square of the magnitude. The recursion is started with the solution to the Yule-Walker equation for $p = 1$ giving the following initialization

$$a_1^1 = C_1/C_0, \tag{B.14}$$

$$\sigma_1^2 = C_0 \left(1 - \left| a_1^1 \right|^2 \right). \tag{B.15}$$

The solution to the MEM spectral estimation described in this section was based on an example autocorrelation function computed for a time series of complex data. That is, the Yule-Walker equations and Levinson-Durbin recursion algorithm are general and apply to complex autocorrelation functions, thereby retaining directionality in the conjugate space.

B.4 Hybrid MEM/Fourier Spectral Estimate

The PCI data samples plasma fluctuations as a function of both space and time; the above MEM spectral estimate was given for only a 1-D signal. A full 2-D MEM spectral estimate is a non-linear problem requiring complex iterative solutions [107–109]. The Fourier based spectral estimate works very well in the time-domain because the sampling is fast and uniform, and the responsivity of the detector elements do not change in time. The spatial dimension suffers for sparse sampling, missing samples, and spatially dependent responsivity of the different detector elements. Therefore, a hybrid Fourier in time, MEM in space spectral estimate is used for analyzing low power regions of the spectrum (to avoid large side-lobe contamination). The procedure is as follows:

1. For each spatial sample (detector channel), break the time series into multiple overlapped windows as depicted in Fig. B-1.

2. Compute the normalized autocorrelation function in both space and time, retaining only the positive spatial lags.

3. Use the FFT to transform in time, leaving a complex valued correlation function

at each frequency.

4. For each frequency, use the 1-D MEM solution described in Sec. B.3.2 to transform the correlation function at each frequency into wave-number space.

THIS PAGE INTENTIONALLY LEFT BLANK

Bibliography

[1] J. D. Lawson, *Some Criteria for a Power Producing Thermonuclear Reactor*, Proceedings of the Physical Society B **70**, 6 (1957).

[2] M. Shimada, D. Campbell, V. Mukhovatov, M. Fujiwara, N. Kirneva, K. Lackner, M. Nagami, V. Pustovitov, N. Uckan, J. W. ley, N. Asakura, A. Costley, A. Donne, E. Doyle, A. F. i, C. Gormezano, Y. Gribov, O. Gruber, T. Hender, W. H. a nd S. Ide, Y. Kamada, A. Leonard, B. Lipschultz, A. Loarte, K. M. yamoto, V. Mukhovatov, T. Osborne, A. Polevoi, and A. Sips, *Chapter 1: Overview and summary*, Nuclear Fusion **47**, S1 (2007).

[3] J. L. Luxon, *Overview of the DIII–D Fusion Science Program*, Nucl. Fusion **42**, 614 (2002).

[4] J. Candy and R. E. Waltz, *Anomalous Transport Scaling in the DIII-D Tokamak Matched by Supercomputer Simulation*, Phys. Rev. Lett. **91**, 045001 (2003).

[5] P. W. Terry, M. Greenwald, J.-N. Leboeuf, G. R. McKee, D. R. Mikkelsen, W. M. Nevins, D. E. Newman, D. P. Stotler, T. G. on Verification Validation, U. B. P. Organization, , and U. T. T. Force, *Validation in fusion research: Towards guidelines and best practices*, Phys. Plasmas **15**, 062503 (2008).

[6] A. J. Wootton, B. A. Carreras, H. Matsumoto, K. McGuire, W. A. Peebles, C. P. Ritz, P. W. Terry, and S. J. Zweben, *Fluctuations and anomalous transport in tokamaks*, **2**, 2879 (1990).

[7] B. A. Carreras, *Progress in anomalous transport research in toroidal magnetic confinement devices*, IEEE Trans. Plasma Sci. **25** (1997).

[8] A. M. Dimits, G. Bateman, M. A. Beer, B. I. Cohen, W. Dorland, G. W. Hammett, C. Kim, J. E. Kinsey, M. Kotchenreuther, A. H. Kritz, L. L. Lao, J. Mandrekas, W. M. Nevins, S. E. Parker, A. J. Redd, D. E. Shumaker, R. Sydora, and J. Weiland, *Comparisons of Physics Basis of Tokamak Transport Models and Turbulence Simulations*, Phys. Plasmas **7**, 969 (2000).

[9] M. Kotschenreuther, W. Dorland, G. W. Hammett, and M. A. Beer, Phys. Plasmas **2**, 2381 (1995).

[10] A. E. White, L. Schmitz, G. R. McKee, C. Holland, W. A. Peebles, T. A. Carter, M. W. Shafer, M. E. Austin, K. H. Burrell, J. Candy, J. C. DeBoo, E. J. Doyle, M. A. Makowski, R. Prater, T. L. Rhodes, G. M. Staebler, G. R. Tynan, R. E. Waltz, and G. Wang, *Measurements of core electron temperature and density fluctuations in DIII-D and comparison to nonlinear gyrokinetic simulations*, Phys. Plasmas **15**, 056116 (2008).

[11] C. Holland, A. E. White, G. R. McKee, M. W. Shafer, J. Candy, R. E. Waltz, L. Schmitz, and G. R. Tynan, *Implementation and application of two synthetic diagnostics for validating simulations of core tokamak turbulence*, Phys. Plasmas **16**, 052301 (2009).

[12] F. Jenko, W. Dorland, M. Kotschenreuther, and B. N. Rogers, *Electron temperature gradient driven turbulence*, Phys. Plasmas **7**, 1904 (2000).

[13] W. M. Nevins, J. Candy, S. Cowley, T. Dannert, A. Dimits, W. Dorland, C. Estrada-Mila, G. W. Hammett, F. Jenko, K. J. Pueschel, and D. E. Shumaker, *Characterizing electron temperature gradient turbulence via numerical simulation*, Phys. Plasmas **13**, 122306 (2006).

[14] G. Wang, E. J. Doyle, W. A. Peebles, L. Zeng, T. L. Rhodes, S. Kubota, X. Nguyen, and N. A. Crocker, *High-resolution dual-polarization frequency modulated reflectometer density profile measurements on DIII-D*, Rev. Sci. Instrum. **75**, 3800 (2004).

[15] C. L. Rettig, S. Burns, R. Philipona, W. A. Peebles, and J. N. C. Luhmann, *Development and operation of a backward wave oscillator based FIR scattering system for DIII–D*, Rev. Sci. Instrum. **61**, 3010 (1990).

[16] D. K. Gupta, R. J. Fonck, G. R. McKee, D. J. Schlossberg, and M. W. Shafer, *Enhanced sensitivity beam emission spectroscopy system for nonlinear turbulence measurements*, Rev. Sci. Instrum. **75**, 3493 (2004).

[17] T. L. Rhodes, W. A. Peebles, X. Nguyen, M. A. VanZeeland, J. S. deGrassie, E. J. Doyle, G. Wang, and L. Zeng, *Millimeter-wave backscatter diagnostic for the study of short scale length plasma fluctuations*, Rev. Sci. Instrum. **77**, 10E922 (2006).

[18] T. L. Rhodes, W. A. Peebles, J. C. DeBoo, R. Prater, J. E. Kinsey, G. M. Staebler, J. Candy, M. E. Austin, R. V. Bravenec, K. H. Burrell, J. S. deGrassie, E. J. Doyle, P. Gohil, C. M. Greenfield, R. J. Groebner, J. Lohr, M. A. Makowski, X. V. Nguyen, C. C. Petty, W. M. Solomon, H. E. St. John, M. A. VanZeeland, G. Wang, and L. Zeng, *Broad wavenumber turbulence and transport during Ohmic and electron cyclotron heating in the DIII–D tokamak*, Plasma Phys. Control. Fusion **49**, B183 (2007).

[19] T. L. Rhodes, W. A. Peebles, M. A. VanZeeland, J. S. deGrassie, G. R. McKee, G. M. Staebler, J. C. DeBoo, E. J. Doyle, M. Gilmore, P. Gohil, C. M. Greenfield, R. J. Groebner, X. V. Nguyen, G. Wang, and L. Zeng, *Broad wavenumber turbulence measurements during neutral beam injection on the DIII–D Tokamak*, Nucl. Fusion **47**, 936 (2007).

[20] I. H. Hutchinson, *Principles of Plasma Diagnostics*, pages 341–348, Cambride University Press, Cambridge, UK, 2nd edition, 1987.

[21] F. Zernike, *Beugungstheorie des Schneidenverfahrens und Seiner Verbesserten Form, der Phasekontrastmethode*, Physica **1**, 689 (1934).

[22] F. Zernike, *Phase Contrast, a New Method for the Microscopic Observations of Transparent Objects*, Physica **9**, 686 (1942).

[23] H. M. Presby and D. Finkelstein, *Plasma Phasography*, Rev. Sci. Instrum. **38**, 1563 (1967).

[24] H. Weisen, *Imaging methods for the observation of plasma density fluctuations*, Plasma Phys. Control. Fusion **28**, 1147 (1986).

[25] S. Coda, M. Porkolab, and T. N. Carlstrom, *A phase contrast interferometer on DIII–D*, Rev. Sci. Instrum. **63**, 4974 (1992).

[26] S. Coda, *An Experimental Study of Turbulence by Phase-Contrast Imaging in the DIII–D Tokamak*, PhD thesis, Massachusetts Institute of Technology, 1997.

[27] K. Matsuo, K. Tanaka, and K. Muraoka, *Development of Laser Imaging Method for Measurements of Electron Density Fluctuations in Plasmas*, Japanese Journal of Applied Physics **30**, 1102 (1991).

[28] S. Kado, T. Irie, K. Muraoka, K. Matsuo, K. Tanaka, K. Kondo, F. Sano, and T. Obiki, *Improvement of the Laser Phase Contrast Method for Measuring the Spatial Distribution of Electron Density Fluctuations in Heliotron E*, Jpn. J. Appl. Phys. **34**, 6492 (1995).

[29] R. Chatterjee, G. A. Hallock, and M. L. Gartman, *Phase contrast imaging system for TEXT-U*, Rev. Sci. Instrum. **66**, 457 (1995).

[30] A. Mazurenko, M. Porkolab, S. J. Wukitch, G. Hallock, and A. Shugart, *New Results from the Phase Contrast Imaging on Alcator C-Mod*, Bull. Am. Phys Soc. **44**, 257 (1999).

[31] A. Mazurenko, *Phase Contrast Imaging on the Alcator C-Mod tokamak*, PhD thesis, Dept. of Physics, Massachusetts Institute of Technology, 2001.

[32] A. Mazurenko, M. Porkolab, D. Mossessian, X. Xu, and W. Nevins, An experimental and theoretical study of the quasi-coherent fluctuations in high density tokamak plasmas, In preparation for Phys. Rev. Lett., 2001.

[33] A. L. Sanin, K. Tanaka, L. N. Vyacheslavov, K. Kawahata, and T. Akiyama, *Two-dimensional phase contrast interferometer for fluctuations study on LHD*, Rev. Sci. Instrum. **75**, 3439 (2004).

[34] C. A. Michael, K. Tanaka, L. Vyacheslavov, A. Sanin, K. Kawahata, and S. Okajima, *Upgraded two-dimensional phase contrast imaging system for fluctuation profile measurement on LHD*, Rev. Sci. Instrum. **77**, 10E923 (2006).

[35] C. V. Raman and N. S. Nath, *The Diffraction of Light by High Frequency Sound Waves*, Proc. Ind. Acad. Sci. (A) **2**, 406 (1935).

[36] F. F. Chen, *Introduction to Plasma Physics and Controlled Fusion*, Plenum Press, New York, NY, 2$^{\mathrm{nd}}$ edition, 1984.

[37] T. H. Stix, *Waves in Plasmas*, American Institude of Physics, New York, NY, 1992.

[38] C. V. Raman and N. S. Nath, *The Diffraction of Light by High Frequency Sound Waves*, Proc. Ind. Acad. Sci. (A) **3**, 75 (1936).

[39] A. Korpel, *Acousto-Optics – A Review of Fundamentals*, Proc. IEEE **69**, 48 (1981).

[40] M. Abramowitz and I. A. Stegun, *Handbook of Mathematical Function with Formulas, Graphs, and Mathematical Tables*, Dover Publications, New York, NY, 1970.

[41] C. R. Scott, *Field Theory of Acousto-Optic Signal Processing Devices*, chapter 8, Artech House, Inc., Norwood, MA, 1992.

[42] R. L. Miller, M. S. Chu, J. M. Greene, Y. R. Lin-Liu, and R. E. Waltz, *Noncircular, finite aspect ratio, local equilibrium model*, Phys. Plasmas **5**, 973 (1998).

[43] B. Coppi, M. N. Rosenbluth, and R. Z. Sagdeev, *Instabilities due to Temperature Gradients in Complex Magnetic Field Configurations*, Phys. Plasmas **10**, 582 (1967).

[44] M. Porkolab, *Plasma Instabilities due to Ion Temperature Gradients*, Nucl. Fusion **8** (1968).

[45] B. Coppi and G. Rewoldt, *New Trapped Electron Instability*, Phys. Rev. Lett. **33**, 1329 (1974).

[46] B. Coppi and B. Pegoraro, *Theory of the Ubiquitous Mode*, Nucl. Fusion **17** (1977).

[47] W. Dorland, F. Jenko, M. Kotschenreuther, and B. N. Rogers, *Electron temperature gradient turbulence*, Phys. Rev. Lett. **85**, 5579 (2000).

[48] A. Truc, A. Qumneur, P. Hennequin, D. Grsillon, F. Gervais, C. Laviron, J. Olivain, S. K. Saha, and P. Devynck, *ALTAIR: An infrared laser scattering diagnostic on the TORE SUPRA tokamak*, Rev. Sci. Instrum. **63**, 3716 (1992).

[49] S. C. Coda, M. Porkolab, and K. H. Burrell, *Decorrelation of Edge Plasma Turbulence at the Transition from Low- to High-Confinement Mode in the DIII–D Tokamak*, Phys. Letters A **273**, 125 (2000).

[50] S. Coda, M. Porkolab, and K. H. Burrell, in *Proc. of 22nd European Conf. on Controlled Fusion and Plasma Physics, Bournemouth*, volume 19C, part 1, pages I–297, European Physical Society, 1995.

[51] S. Coda, M. Porkolab, and K. H. Burrell, *Characterization of density fluctuations during ELMs in the DIII–D tokamak*, Nucl. Fusion **41**, 1885 (2001).

[52] J. C. Rost, M. Porkolab, B. J. Youngblood, G. R. McKee, T. L. Rhodes, R. A. Moyer, and K. H. Burrell, *Comparison of Fluctuations in Lower and Upper Single Null Plasmas in DIII–D*, Bull. Am. Phys. Soc. **46**, 220 (2001).

[53] S. Coda, M. Porkolab, and K. Burrell, *Signature of Turbulent Zonal Flows Observed in the DIII–D Tokamak*, Phys. Rev. Lett. **86**, 4835 (2001).

[54] P. H. Diamond, M. N. Rosenbluth, F. L. Hinton, M. Malkov, J. Fleischer, and A. Smolyakov, Dynamics of zonal flows and self-regulating drift-wave turbulence, in *Proceedings of the 17th IAEA Fusion Energy Conference, Yokohama, Japan*, 1998, IAEA-CN-69/TH3/1.

[55] K. H. Burrell, M. E. Austin, D. P. Brennan, J. C. DeBoo, E. J. Doyle, C. Fenzi, C. Fuchs, P. Gohil, C. M. Greenfield, R. J. Groebner, L. L. Lao, T. C. Luce, M. A. Makowski, G. R. McKee, R. A. Moyer, C. C. Petty, M. Porkolab, C. L. Rettig, T. L. Rhodes, J. C. Rost, B. W. Stallard, E. J. Strait, E. J. Synakowski, M. R. Wade, J. G. Watkins, and W. P. West, *Quiescent double barrier high-confinement mode plasmas in the DIII–D tokamak*, Phys. Plasmas **8**, 2153 (2001).

[56] E. M. Edlund, *A Study of Reversed Shear Alfvén Eigenmodes in Alcator C-Mod With Phase Contrast Imaging*, PhD thesis, Massachusetts Institute of Technology, 2009.

[57] E. Nelson-Melby, M. Porkolab, P. T. Bonoli, Y. Lin, A. Mazurenko, and S. J. Wukitch, *Experimental Observations of Mode-Converted Ion Cyclotron Waves in a Tokamak Plasma by Phase Contrast Imaging*, Phys. Rev. Lett. **90**, 155004 (2003).

[58] R. E. Waltz, J. Candy, and M. Fahey, *Coupled Ion Temperature Gradient and Trapped Electron Mode to Electron Temperature Gradient Mode Gyrokinetic Simulations*, Phys. Plasmas **14**, 056116 (2007).

[59] R. Waltz, J. Candy, F. Hinton, C. Estrada-Mila, and J. Kinsey, *Advances in Comprehensive Gyrokinetic Simulations of Transport in Tokamaks*, Nucl. Fusion **48**, 741 (2005).

[60] J. Candy and R. Waltz, Coupled ITG/TEM-ETG gyrokinetic simulations, in *Proc. of 21st IAEA Fusion Energy Conference, Chengdu, China*, pages TH/2–1, 2006.

[61] F. Jenko, T. dannert, and C. Angioni, *Heat and particle transport in a tokamak: advances in nonlinear gyrokinetics*, Plasma Phys. Control. Fusion **47**, B195 (2006).

[62] D. R. Ernst, N. Basse, W. Dorland, C. L. Fiore, L. Lin, A. Long, E. Marmar, M. Porkolab, K. Zeller, and K. Zhorovich, Identification of tem turbulence through direct comparison of nonlinear gyrokinetic simulations with phase contrast imaging density fluctuation measurements, in *Proc. of 21st IAEA Fusion Energy Conference, Chengdu, China*, pages TH/1–3, 2006.

[63] N. Tsujii, M. Porkolab, E. M. Edlund, and L. Lin, *Development of Absolute Calibration of the Phase Contrast Imaging Diagnostic and Experimental Tests in Alcator C–Mod*, Bull. Am. Phys. Soc. **52**, 215 (2007).

[64] L. Lin, *Turbulence and Transport Studies with Phase Contrast Imaging in Alcator C-Mod Tokamak and Comparisons with Gyrokinetic Simulations*, PhD thesis, Massachusetts Institute of Technology, 2009.

[65] C. J. Bouwkamp, *Diffraction Theory*, Rep. Prog. Phys. **17**, 35 (1954).

[66] J. D. Jackson, *Classical Electrodynamics*, John Wiley & Sons, Inc., New York, NY, 3$^{\text{rd}}$ edition, 1999.

[67] D. E. Gray, editor, *American Institute of Physics Handbook*, McGraw-Hill Book Company, New York, NY, 3$^{\text{rd}}$ edition, 1972.

[68] A. Mazurenko, M. Porkolab, D. Mossessian, J. A. Snipes, X. Q. Xu, and W. M. Nevins, *Experimental and Theoretical Study of Quasicoherent Fluctuations in Enhanced D[sub alpha] Plasmas in the Alcator C-Mod Tokamak*, Phys. Rev. Lett. **89**, 225004 (2002).

[69] K. H. Burrell, M. E. Austin, C. M. Greenfield, L. L. Lao, B. W. Rice, G. M. Staebler, and B. W. Stallard, *Effects of $E \times B$ velocity shear and magnetic shear in the formation of core transport barriers in the DIII–D tokamak*, Plasma Phys. Control. Fusion **40**, 1585 (1998).

[70] K. H. Burrell, W. P. West, E. J. Doyle, J. S. deGrassie, P. Gohil, C. M. Greenfield, R. J. Groebner, R. Jayakumar, D. H. Kaplan, L. L. Lao, A. W. Leonard, M. A. Makowski, G. R. McKee, W. M. Solomon, D. M. Thomas, T. L. Rhodes, M. R. Wade, G. Wang, J. G. Watkins, and L. Zeng, *Edge Radial Electric Field*

Structure in Quiescent H-Mode Plasmas in the DIII–D Tokamak, Plasma Phys. Control. Fusion **46** (2004).

[71] J. C. Rost, M. Porkolab, and J. R. Dorris, *Analysis of High Frequency and Wavenumber Measurements from the DIII–D Phase Contrast Imaging Diagnostic*, Bull. Am. Phys. Soc. **51**, 112 (2006).

[72] R. Neelamani, H. Choi, and R. Baraniuk, *ForWaRD: Fourier-Wavelet Regularized Deconvolution for Ill-Conditioned Systems*, IEEE Trans. Signal Proc. **52**, 418 (2004).

[73] R. B. Blackman and J. W. Tukey, *The Measurement of Power Spectra: From the Point of View of Communication Engineering*, Dover Publications, New York, NY, 1959.

[74] J. P. Burg, Maximum entropy spectral analysis, in *Proceedings of the 37th Meeting Society of Exploration Geophysicists*, Society of Exploration Geophysicists, Oklahoma City, OK, 1967.

[75] J. G. Ables, *Maximum Entropy Spectral Analysis*, Astron. Astrophys. Suppl. **15**, 383 (1974).

[76] P. D. Welch, *The Use of Fast Fourier Transform for the Estimation of Power Spectra: A Method Based on Time Averaging Over Short, Modified Periodograms*, IEEE Trans. Audio Electroacoust. **AU-15**, 70 (1967).

[77] W. H. Press, B. P. Flannery, S. A. Teukolsky, and W. T. Vetterling, *Numerical Recipes in C: The Art of Scientific Computing*, chapter 13, pages 572–575, Cambride University Press, Cambridge, UK, 2$^{\text{nd}}$ edition, 1992.

[78] E. J. Doyle, R. J. Groebner, K. H. Burrell, P. Gohil, T. Lehecka, N. C. Luhmann, Jr., H. Matsumoto, T. H. Osborne, W. A. Peebles, and R. Philipona, *Modifications in turbulence and edge electric fields at the L–H transition in the DIII-D tokamak*, Phys. Fluids B **3**, 2300 (1991).

[79] E. A. Frieman and L. Chen, *Nonlinear gyrokinetic equations for low-frequency electromagnetic waves in general plasma equilibria*, Phys. Fluids **25**, 502 (1982).

[80] T. S. Hahm and W. M. Tang, *Weak turbulence theory of ion temperature gradient modes for inverted density plasmas*, Phys. Fluids B **2**, 1815 (1990).

[81] P. H. Diamond, S. I. Itoh, K. Itoh, and T. S. Hahm, *Zonal flows in plasma–a review*, Plasma Phys. Control. Fusion **47**, R35 (2005).

[82] F. Jenko, W. Dorland, and G. Hammet, *Critical gradient formula for toroidal electron temperature gradient modes*, Phys. Plasmas **8**, 4096 (2001).

[83] A. Dimits, W. Nevins, D. Shumaker, G. Hammett, T. Dannert, F. Jenko, W. Dorland, J. Leboeuf, T. Rhodes, J. Candy, and C. Estrada-Mila, *Gyrokinetic simulations of ETG and ITG turbulence*, in *Proc. of 21st IAEA Fusion Energy Conference, Chengdu, China*, pages TH/P2–3, 2006.

[84] D. R. Ernst, P. T. Bonoli, P. J. Catto, W. Dorland, C. L. Fiore, R. S. Granetz, M. Greenwald, A. E. Hubbard, M. Porkolab, M. H. Redi, J. E. Rice, K. Zhurovich, and Alcator C–Mod Group, *Role of trapped electron mode turbulence in internal transport barrier control in the Alcator C-Mod Tokamak*, Phys. Plasmas **11**, 2637 (2004).

[85] P. H. Rutherford and E. A. Frieman, *Drift Instabilities in General Magnetic Field Configurations*, Phys. Fluids **11**, 569 (1968).

[86] Z. Lin, Y. Nishimura, Y. Xiao, I. Holod, W. L. Zhang, and L. Chen, *Global gyrokinetic particle simulations with kinetic electrons*, Plasma Phys. Control. Fusion **49**, B163 (2007).

[87] Y. Chen and S. E. Parker, *Electromagnetic gyrokinetic δf particle-in-cell turbulence simulation with realistic equilibrium profiles and geometry*, J. Comput. Phys. **220**, 839 (2007).

[88] M. Kotschenreuther, W. Dorland, M. A. Beer, and G. W. Hammett, *Quantitative predictions of tokamak energy confinement from first-principles simulations with kinetic effects*, Phys. Plasmas **2**, 2381 (1995).

[89] J. Candy and R. E. Waltz, *An Eulerian gyrokinetic-Maxwell solver*, J. Comput. Phys. **186**, 545 (2003).

[90] A. J. Brizard and T. S. Hahm, *Foundations of Nonlinear Gyrokinetic Theory*, Rev. Mod. Phys. **79**, 421 (2007).

[91] P. J. Catto, W. M. Tang, and D. E. Baldwin, *Generalized gyrokinetics*, Plasma Phys. **23**, 639 (1981).

[92] H. Sugama and W. Horton, *Nonlinear Electromagnetic Gyrokinetic Equation for Plasmas with Large Mean Flows*, Phys. Plasmas **5**, 2560 (1998).

[93] J. Candy and E. Belli, *GYRO Technical Guide*, `http://fusion.gat.com/theory/Gyrodoc`, 2009.

[94] R. Courant, K. Friedrichs, and H. Lewy, *On the partial difference equations of mathematical physics*, IBM Journal **11**, 215 (1967).

[95] W. Horton, *Drift waves and transport*, Rev. Mod. Phys. **71**, 735 (1999).

[96] E. J. Doyle (Chair Transport Physics), W. A. Houlberg (Chair Confinement Database and Modelling), Y. Kamada (Chair Pedestal and Edge), V. Mukhovatov (co-Chair Transport Physics), T. H. Osborne (co-Chair Pedestal and Edge),

A. Polevoi (co-Chair Confinement Database and Modelling), G. Bateman, J. W. Connor, J. G. Cordey (retired), T. Fujita, X. Garbet, T. S. Hahm, L. D. Horton, A. E. Hubbard, F. Imbeaux, F. Jenko, J. E. Kinsey, Y. Kishimoto, J. Li, T. C. Luce, Y. Martin, M. Ossipenko, V. Parail, A. Peeters, T. L. Rhodes, J. E. Rice, C. M. Roach, V. Rozhansky, F. Ryter, G. Saibene, R. Sartori, A. C. C. Sips, J. A. Snipes, M. Sugihara, E. J. Synakowski, H. Takenaga, T. Takizuka, K. Thomsen, M. R. Wade, H. R. Wilson, ITPA Transport Physics Topical Group, ITPA Confinement Database and Modelling Topical Group, and ITPA Pedestal and Edge Topical Group, *Chapter 2: Plasma confinement and transport*, Nucl. Fusion **47**, S18 (2007).

[97] L. Lin, M. Porkolab, E. M. Edlund, J. C. Rost, C. L. Fiore, M. Greenwald, Y. Lin, D. R. Mikkelsen, N. Tsujii, and S. J. Wukitch, *Studies of turbulence and transport in Alcator C-Mod H-mode plasmas with phase contrast imaging and comparisons with GYRO*, Physics of Plasmas **16**, 012502 (2009).

[98] J. C. Deboo, *Probing Plasma Turbulence by Modulating the Electron Temperature Gradient*, Bull. Am. Phys. Soc. **54** (2009).

[99] E. Mazzucato, D. R. Smith, R. E. Bell, S. M. Kaye, J. C. Hosea, B. P. LeBlanc, J. R. Wilson, P. M. Ryan, C. W. Domier, N. C. Luhmann, H. Yuh, W. Lee, and H. Park, *Short-Scale Turbulent Fluctuations Driven by the Electron-Temperature Gradient in the National Spherical Torus Experiment*, Phys. Rev. Lett. **101**, 075001 (2008).

[100] M. Porkolab, *Plasma drift instabilities with phase velocities below the ion thermal velocity*, Phys. Lett. **22**, 427 (1966).

[101] M. Porkolab, *Kinetic Theory of Plasma-Wave Motion in the Presence of Collisions*, Phys. Fluids **17**, 834 (1968).

[102] J. T. Verdeyen, *Laser Electronics*, chapter 3, pages 63–79, Prentice-Hall, Inc., Englewood Cliffs, NJ, 3$^{\text{rd}}$ edition, 1995.

[103] A. Oppenheim, *Lecture 12: Linear Prediction and All–Pole Modeling*, MIT OpenCourseWare 2006 - `http://mitocw.vocw.edu.vn/NR/rdonlyres/83179A58-06AA-4EB1-A1C7-4B3D3DABAB67/0/lec12.pdf`, 2006.

[104] D. B. Percival and A. T. Walden, *Spectral Analysis for Physical Applications: Multitaper and Conventional Univariate Techniques*, chapter 9, pages 392–420, Cambridge University Press, Cambridge, UK, 1998.

[105] A. Van Den Bos, *Alternative Interpretation of Maximum Entropy Spectral Analysis*, IEEE Trans. Information Theory **17**, 493 (1971).

[106] A. Oppenheim, *Lecture 13: The Levinson–Durbin Recursion*, MIT OpenCourseWare 2006 - `http://mitocw.vocw.edu.vn/NR/rdonlyres/34D979AD-0B93-4F4A-B4F4-8CC0A9465736/0/lec13.pdf`, 2006.

[107] J. S. Lim and N. A. Malik, *A New Algorithm for Two-Dimensional Maximum Entropy Power Spectrum Estimation*, IEEE Transactions on Acoustics, Speech, and Signal Processing , 401 (1981).

[108] N. Srinivasa, K. R. Ramakrishnan, and K. Rajgopal, *Two-Dimensional Spectral Estimation: A Radon Transform Approach*, IEEE Journal of Oceanic Engineering **OE-12**, 90 (1987).

[109] N. Srinivasa, K. R. Ramakrishnan, and K. Rajgopal, *On Two-Dimensional Maximum Entropy Spectral Estimation*, IEEE Trans. Signal Proc. **40**, 241 (1992).